Universiteit Gent
Faculteit Toegepaste Wetenschappen
Vakgroep Civiele Techniek
Laboratorium voor Hydraulica

Bloedstroming en gastransport in een kunstlong: in numero en in vitro analyse

Blood flow and gas transport in artificial lungs: in numero and in vitro analysis

ir. Peter Dierickx

Promotor: Prof. dr. ir. Pascal Verdonck

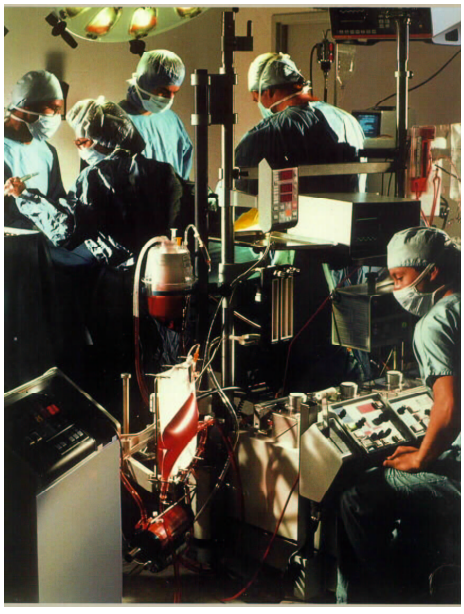

Proefschrift tot het verkrijgen van de graad van
Doctor in de Toegepaste Wetenschappen
Academiejaar 2000-2001

Universiteit Gent
Faculteit Toegepaste Wetenschappen
Vakgroep Civiele Techniek
Laboratorium voor Hydraulica

Bloedstroming en gastransport in een kunstlong: in numero en in vitro analyse

Blood flow and gas transport in artificial lungs: in numero and in vitro analysis

ir. Peter Dierickx

Promotor: Prof. dr. ir. Pascal Verdonck

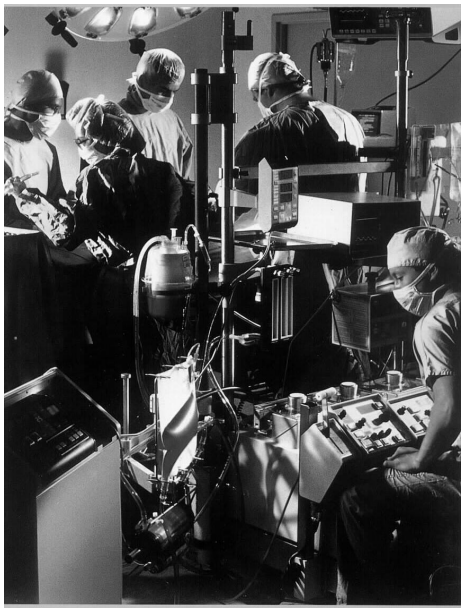

Proefschrift tot het verkrijgen van de graad van
Doctor in de Toegepaste Wetenschappen
Academiejaar 2000-2001

Promotor:
Prof. dr. ir. Pascal Verdonck

Vakgroep Civiele Techniek

St. Pietersnieuwstraat 41

B-9000 Gent

Dit onderzoek is uitgevoerd in het kader van een IWT-specialisatiebeurs (Instituut voor de aanmoediging van Innovatie door Wetenschap en Technologie in Vlaanderen, projectnummer 961181).

New Gold Dream
She Is The One In Front Of Me
The Science And The Ecstacy
She is your friend
Until the bitter end
And when you dream
Dream in the dream with me

vrij naar Simple Minds

aan onze ouders
voor Katrien, Emilyn en Sybelle

VOORWOORD

Het schrijven van een proefschrift is als het bewandelen van een berg. Naarmate het einde nadert, wil je sneller je doel bereiken, maar steile hellingen en een kronkelig pad vormen hindernissen die niet altijd vlot te overbruggen zijn.
Prof. dr. ir. Pascal Verdonck nodigde me uit voor een wandeling in het multidisciplinair landschap van de biomedische ingenieurswetenschappen. Dr. ir. Dirk De Wachter werd mijn gids. Hij introduceerde mij in verschillende vakgebieden en samen met mijn gastheer begeleidde hij mij zeer gedreven en vakkundig doorheen het labyrint van modellering, stroming, massatransport, ... en ja, zelfs informatica.
Tijdens zo een wandeling kom je nogal wat boeiende mensen tegen. Neem nu Filip De Somer, dé man die ik nodig had om mijn reis verder te zetten. Door zijn enorme ervaring in de klinische praktijk en zijn gevoel voor wetenschap, ben ik steeds bij hem te rade kunnen gaan. Ik meen dat we kunnen terugblikken op een mooie en vruchtbare samenwerking.
Prof. dr. Guido Van Nooten dank ik van harte voor het ter beschikking stellen van het dierexperimenteel laboratorium en de bijbehorende meetapparatuur.
De tocht verloopt echter niet altijd van een leien dakje. Af en toe raak je vermoeid en wil je er eens uit. Gelukkig waren er dan Patrick en Stefaan. Dankzij hun morele steun en aangenaam gezelschap hebben zij mij kunnen overtuigen om de moed niet op te geven. Er is tussen ons een hechte vriendschap gegroeid die, nadat we elk onze eigen weg zijn ingeslaan, zal blijven voortduren.
Ik besef dat de resultaten die onderweg geboekt zijn, tot stand zijn gekomen door de medewerking van velen. In het bijzonder wil ik mijn thesisstudenten Nico, Guy, Gerd en Tom bedanken voor hun inspanningen. Ik dank ook alle medewerkers van het Laboratorium voor Hydraulica dat steeds een thuisbasis is geweest.
Mijn welgemeende dank gaat naar Prof. dr. ir. Ronny Verhoeven voor de goede zorgen die hij aan zijn nat labo besteedt en voor de gemoedelijke sfeer die hij samen met het fantastische personeel weet op te bouwen.
Het einde van de tocht is nabij.
Weliswaar enigszins vermoeid kijk ik tevreden en toch ook wel opgelucht terug op de voorbije jaren van “zoeken”. De drukte die mijn zoektocht wel eens met zich meebracht, kan nu luwen. Ik besef dat ik ook de mensen vlak naast mij mijn zware rugzak mee liet dragen.
Ook voor mijn echtgenote Katrien en dochtertjes Emilyn en Sybelle wogen de laatste loodjes zwaar. De dagen doorbrengen met een ernstige papa achter de computer is niet zo gemakkelijk. Het was voor mij wel fijn te midden van hen te kunnen werken.
Ook onze ouders hebben steeds langs de kant van mijn traject gestaan en mijn avontuur met veel interesse en aanmoedigingen gevolgd. Dankzij hun steun kan ik dit proefschrift uiteindelijk toch bundelen als een vlag die op de top van de berg wordt neergeplant.
Graag draag ik dit werk aan hen allen op.
Hartelijk en welgemeende dank aan Pascal en Dirk voor het vertrouwen dat zij in mij hebben gesteld. Hun inzet, eindeloos geduld en goede raad zijn, naast de samenwerking, voor mij zeer waardevol geweest. De opdracht was niet altijd even gemakkelijk maar uiteindelijk is mijn thesis er toch gekomen op mijn manier.
Ik hoop dat dit verslag van mijn wandeling op zijn beurt een gids mag zijn voor anderen ...

Peter
Hamme – St.-Anna, maart 2001

STRUCTUUR VAN HET PROEFSCHRIFT

Het proefschrift omvat een Nederlandstalige synthese, acht Engelstalige hoofdstukken en één appendix. De Nederlandstalige synthese geeft een overzicht van de probleem- en doelstelling van het proefschrift. Ze biedt tevens een inleiding tot de werking en geometrie van de kunstlong (§3.1 en §3.2), het zuurstoftransport in bloed (§3.3 en §3.4) en een beschrijving van dimensieloze ontwerpparameters voor een kunstlong (§3.7). §4 biedt een overzicht van de wetenschappelijke numerieke ("*in numero*") en experimentele ("*in vitro*") resultaten, zowel voor de hydrodynamica van de kunstlong als het massatransport ervan. Ten slotte wordt in §5, respectievelijk §6, een overzicht van originele bijdragen en van toekomstig onderzoek gegeven.

Het Engelstalige deel start met een Engelstalig abstract waarin de doelstellingen en de structuur van het proefschrift worden uiteengezet. De Engelstalige hoofdstukken bieden de lezer een uitgebreid overzicht van de historiek van de kunstlong (Chapter I), de modellering van het zuurstoftransport in de kunstlong (Chapter II) en een bundeling van de belangrijkste gepubliceerde of ingediende wetenschappelijke publicaties. In het besluit wordt een overzicht van originele bijdragen en van het toekomstig onderzoek gegeven.

In de appendix vindt men een summier overzicht van *in numero* resultaten van de hemodynamica en het zuurstoftransport in bloed voor verschillende vezelconfiguraties.

Het proefschrift is dus als volgt ingedeeld:

- Nederlandstalige synthese
- Engelstalige abstract
- Acht Engelstalige hoofdstukken:

I Introduction to and History of Cardiopulmonary Bypass and Artificial Lungs
II Introduction to and Modeling of Oxygen Transfer in Artificial Lungs
III Hydrodynamic Characteristics of Artificial Lungs
IV Blood Flow around Hollow Fibers
V Mass Transfer Characteristics of Artificial Lungs
VI Two-dimensional finite element model for oxygen transfer in cross-flow hollow fiber membrane artificial lungs
VII Air-Handling Characteristics of Pediatric Artificial Lungs
VIII Conclusion

- Appendix

INHOUDSTAFEL

SYMBOLENLIJST†

Afkortingen

AAMI	"Association for the Advancement of Medical Instrumentation"
ARF	"Acute Respiratory Failure"
CPB	"CardioPulmonary Bypass"
ECC	ExtraCorporele Circulatie
ECMO	ExtraCorporele Membraan Oxygenatie
ET	vezelconfiguratie "gelijkzijdige driehoek"
GME	Gasvormige Microembolen
HLM	HartLongMachine
IL	vezelconfiguratie "vierkant in lijn"
IVOX	IntraVeneuze Oxygenatie
RBC	Rode Bloed Cel
SI	"Système Internationale d'Unités"
SS	vezelconfiguratie "gekanteld vierkant"

Symbolen

a	nat oppervlak per eenheidsvolume [mm^{-1}]
A	uitwisselingsoppervlakte [m^2]
$\overline{\mathbf{A}}$	afschuifsnelheidstensor [s^{-1}]
A_f	doorstroomoppervlakte [cm^2]
B_{O_2}	bindingscapaciteit van zuurstof aan hemoglobine [ml/g]
CO_2	koolstofdioxide
C_{Hb}	hemoglobine massaconcentratie [g/l]
C_{O_2}	totale zuurstofconcentratie [ml/l]

† Op het einde van deze symbolenlijst is een lijst met conversiefactoren toegevoegd om niet-S.I.-eenheden in SI-eenheden om te zetten. Deze kunnen dan worden aangewend in de definities / berekeningen van de dimensieloze grootheden.

$C_{O_2 b}$	gebonden zuurstofconcentratie [ml/l]
$C_{O_2 d}$	opgeloste zuurstofconcentratie [ml/l]
$C_{O_2 g}$	zuurstofconcentratie aan de gaszijde [ml/l]
d	vezeldiameter [mm]
d_c	capillairdiameter [mm]
D_i	inwendige diameter [cm]
D_o	uitwendige diameter [cm]
D_{O_2}	diffusiecoëfficiënt voor zuurstof [cm²/s]
$D_{O_2 eff}$	effectieve diffusiecoëfficiënt voor zuurstof in bloed [cm²/s]
f	wrijvingsfactor
H’	hoogte [*L*]
Hb	hemoglobine
Hct	hematocriet
j	Chilton-Colburn j-factor
K	massatransportcoëfficiënt [cm/s] [ml/s/cm²]
L	lengte van het membraancompartiment [cm]
L	lengte-eenheid
L’	lengte [*L*]
L_b	bloedpadlengte [cm]
L_m	stroomverdelerlengte [cm]
L_{Hg}	verplaatsing van kwik [mm]
m	parameter
m′	parameter
M	massa-eenheid
n	parameter
n	Hill parameter
$\bar{\mathbf{n}}$	normaalvector
N_{Eu}	Eulergetal
N_L	aantal vezels longitudinaal
N_{Pe}	Pécletgetal
N_{Re}	Reynoldsgetal
N_{Sc}	Schmidtgetal

N_{Sh}	Sherwoodgetal
O_2	zuurstof
p	druk [Pa]
pH	zuurtegraad
P_{O_2}	zuurstofpartieeldruk [mmHg]
$\overline{P_{O_2}}$	gemiddelde zuurstofpartieeldruk [mmHg]
P_{O_2g}	zuurstofpartieeldruk aan gaszijde [mmHg]
P_{50}	zuurstofpartieeldruk bij S_{O_2} =50 % [mmHg
Q	bloeddebiet [l/min]
q	debiet per eenheidslengte [mm³/s/mm]
Q’	debiet door het membraan per eenheidsbreedte [l/cm/min]
R^2	correlatiecoëffiiciënt
S_L	longitudinale afstand [mm]
S_{O_2}	zuurstofsaturatie
S_{O_2in}	inlaatzuurstofsaturatie
S_{O_2out}	uitlaatzuurstofsaturatie
S_T	transversale afstand [mm]
$\bar{\mathbf{t}}$	spanningstensor [$M/L/T^2$]
T	temperatuur [°C]
T	tijdseenheid
$\bar{\mathbf{u}}$	snelheidsvector [*L/T*]
U_m	gemiddelde snelheid [*L/T*]
U_s	superficiële snelheid [L/T]
V_{air}	volume lucht [ml]
V_{bed}	volume van het compartiment [ml]
V_{void}	leeg volume [ml]
$\dot{V}_{O_2}$	zuurstofmassadebiet [ml/min]
W’	breedte [*L*]
x	cartesische coördinaat [*L*]
y	cartesische coördinaat [*L*]
z	cartesische coördinaat [*L*]

Griekse symbolen

α	parameter
α'	parameter
α_{O_2}	Bunsen oplosbaarheidscoëfficiënt [ml/ml/mmHg]
β	parameter
β'	parameter
$\dot{\gamma}$	afschuifsnelheid [s^{-1}]
Γ	rand
Γ_{per}	periodieke randvoorwaarde
Γ_{sym}	symmetrische randvoorwaarde
ε	porositeit
λ	bindingscapaciteit van zuurstof aan het hemoglobine
μ	dynamische viscositeit [*M/L/T*]
μ_∞	dynamische bloedviscositeit [mPa·s]
μ_p	dynamische plasmaviscositeit [mPa·s]
Π	tweede invariant van de afschuifsnelheidstensor
ρ	dichtheid [kg/m^3]
τ_o	vloeigrens [mPa]
υ	kinematische viscositeit [cm^2/s]
φ	parameter
φ'	parameter
ξ	dimensieloze karakteristieke lengte

Subscripts

b	bloed
b	gebonden
c	capillair
d	opgelost
eff	effectief
f	frontaal
g	gasfase
Hg	kwik

i	inwendig
i	iteratie
i	nummer eenheidscel
in	inlaat
L	longitudinaal
m	gemiddelde
max	maximum
o	uitwendig
o	subscript vloeigrens
out	uitlaat
p	plasma
per	periodiek
s	superficieel
sym	symmetrie
T	transversaal
w	water

Superscripts

k	iteratie
T	transponering

Wiskundige operatoren

d	differentiaal
Δ	Laplace operator [L^{-2}]
$\overline{\overline{\nabla}}$	gradiënt [L^{-1}]
$\bar{}$	gewogen gemiddelde
$\int$	integraal

Eenheden

mm	[L]	millimeter	10^{-3} m
ml	[L]	milliliter	10^{-6} m³
cm	[L]	centimeter	10^{-2} m
l	[L³]	liter	10^{-3} m³
min	[T]	minuut	60 s

s	[T]	seconde	1 s
mPa	[M/T²/L]	milliPascal	10^{-3} Pa
g	[M]	gram	10^{-3} kg
kg	[M]	kilogram	1 kg
K		Kelvin	
°C		graad Celsius	
mmHg	[L]	millimeter kwik	133.3 Pa

SYNTHESE "BLOEDSTROMING EN GASTRANSPORT IN EEN KUNSTLONG: IN NUMERO EN IN VITRO ANALYSE"

1 Probleemstelling van het proefschrift

De hartlongmachine (HLM) wordt gebruikt tijdens openhartchirurgie om tijdelijk de pompwerking van het hart en de gasuitwisseling in de longen van de patiënt over te nemen. Door middel van een bloedpomp wordt veneus bloed van de patiënt doorheen de HLM tot in de hoofdslagader gepompt. De kunstlong in deze HLM bevat enerzijds een microporeus polypropyleenmembraan voor de gasuitwisseling, en anderzijds een warmtewisselaar die het mogelijk maakt de bloedtemperatuur te regelen.

Ondanks het hoge aantal succesvolle openhartoperaties jaarlijks (USA: 750000; UK: 24000; België: 12000) [1,2] (en een geleidelijke evolutie van de kunstlong), worden nog steeds regelmatig problemen beschreven die een verhoogde patiëntenmortaliteit veroorzaken (nl. in 1 op 4000 gevallen). Minstens een deel van deze problemen zijn te wijten aan onvoldoende kennis van de stromingskarakteristieken van het bloed (hemodynamica) in de kunstlong, hetzij bij de perfusionist, hetzij bij de fabrikant. De hemodynamica heeft immers een rechtstreekse invloed op het ontstaan van bloedstolling en bloedbeschadiging (hemolyse, plaatjesactivatie). Ook het warmtetransport en de gasuitwisseling met het bloed van de patiënt worden mee bepaald door de lokale convectiestroming en -gradiënt in de kunstlong. Een betere kennis van de hemodynamica in de kunstlong is absoluut vereist als uitgangspunt voor de verdere optimalisatie van de operationele karakteristieken van de kunstlong, onder andere om de therapeutische slaagkansen te verhogen bij de pediatrische hartchirurgie en bij de niet-invasieve ademhalingsondersteuning (ExtraCorporele Membraan Oxygenatie-techniek (ECMO) en Intravasculaire Oxygenatie (IVOX)).

Bij kleine kinderen en baby's zal een ontwikkeling van compactere eenheden een verminderd gebruik van bloedproducten tot gevolg hebben en een kleiner risico op post-operatoire

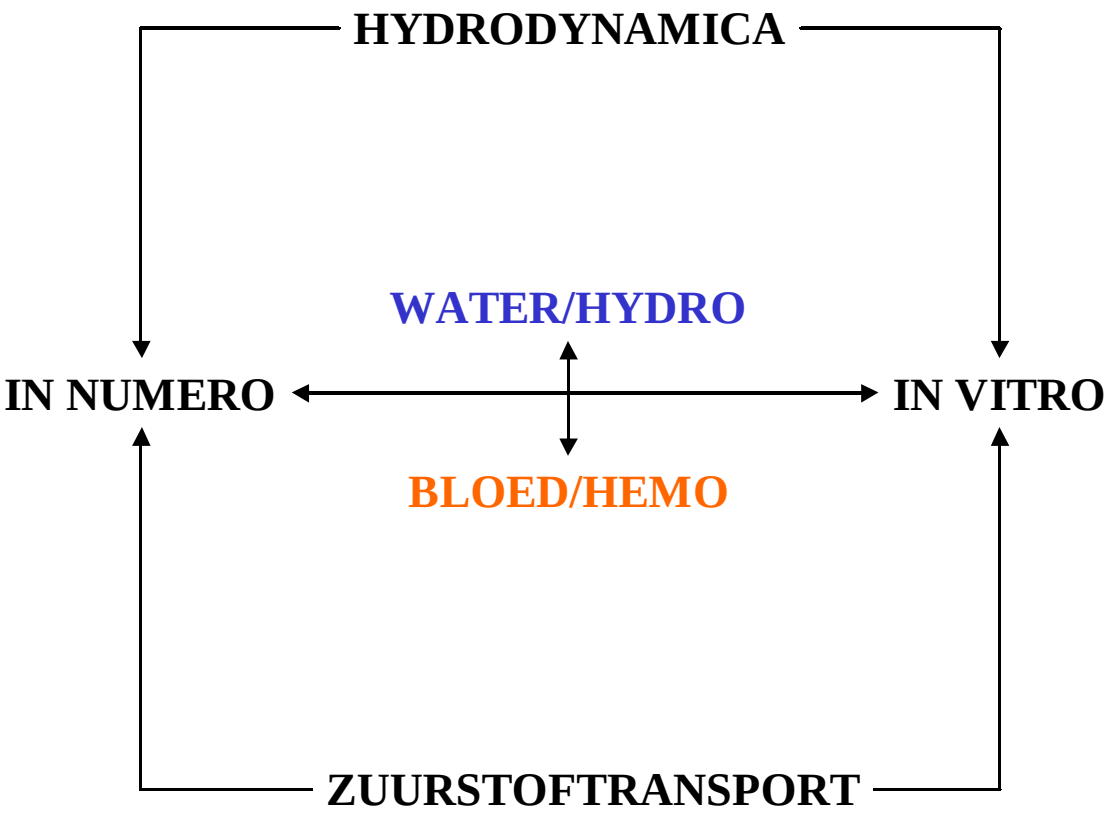

Figuur 1: Schematisch overzicht van de doelstellingen van het proefschrift.

oedeemvorming mogelijk maken. Door de verlaging van het lichaamsvreemd oppervlak kan tevens de immunologische respons afnemen.

ECMO en IVOX hebben tot doel de longfunctie gedurende een langere tijd door middel van een kunstlong te ondersteunen of te vervangen. Vanwege de langere toepassingsduur (dagen tot weken in plaats van uren) en de verschillende bloeddebieten, spreekt het vanzelf dat zowel de hemocompatibiliteit als de efficiëntie van de kunstlong moeten verbeteren ten opzichte van de kunstlong in de hartchirurgie. Ook de beoogde implanteerbaarheid van de kunstlong stelt nieuwe uitdagingen.

Een optimalisering van de hemodynamica in en het ontwerp van de kunstlong zal tevens toelaten de ontluchtingskarakteristieken van de kunstlong te verbeteren. Ten slotte is er nood aan een aantal ontwerpregels waaraan een kunstlong op stroomtechnisch gebied minimaal zou moeten voldoen.

Het recentste technisch onderzoek op het gebied van de kunstlong concentreert zich rond de beschrijving van het gastransport met behulp van eendimensionale modellen voor permanente bloedstroming, met de bedoeling de ontwerpkarakteristieken voor gastransport vast te leggen <3,4>. Dit onderzoek wordt voornamelijk uitgevoerd aan de North Western University (USA) en

ook aan de University of Strathclyde (Schotland). Daarnaast wordt aan de University of Pittsburgh, de University of Michigan en de Politecnico di Milano vergelijkbaar onderzoek verricht. Vanwege de kruisstroming in de huidige kunstlongen (zie infra), zijn deze modellen slechts een eerste benadering. Vooral voor de modellering van de afvoer van koolstofdioxide zijn deze modellen niet verfijnd genoeg.

Vele nieuwe principes worden klinisch of met behulp van diertesten uitgetest zonder een grondige kennis en analyse van de bepalende hemodynamica in de kunstlong. Een numeriek tweedimensionaal onderzoeksmodel voor stroming en massatransport kan hierbij helpen om zwakke en sterke punten in de verf te zetten, vooraleer de eigenlijke testen aangevat worden. Daardoor kan tevens het aantal diertesten beperkt worden.

2 Doelstelling van het proefschrift

Het doel van het proefschrift bestaat erin om de stromingsweerstand en het zuurstoftransport in het membraancompartiment van een holle vezel membraankunstlong met kruisstroming enerzijds numeriek (“*in numero*”) te modelleren en anderzijds experimenteel (“*in vitro*”) te bepalen. De fluïda in het numerieke model en de experimenten zijn water (“hydro”) en bloed (“hemo”), met als doel de resultaten bekomen met water om te kunnen rekenen naar resultaten voor bloed. Figuur 1 geeft een schematisch overzicht van de doelstellingen en de structuur van het proefschrift.

Binnen dit proefschrift is een numeriek tweedimensionaal model opgesteld dat toelaat de stroming en het zuurstoftransport rond één enkele vezel in het membraancompartiment van de holle vezel mebraankunstlong met kruisstroming te modelleren. De integratie van deze resultaten over een volledige membraanmat laat toe de resultaten te valideren met experimentele metingen van zowel stroming van water en bloed als zuurstoftransport in water en bloed. Deze validatie is uitgevoerd voor drie commercieel beschikbare holle vezel membraankunstlongen met kruisstroming.

De analyse heeft geleid tot het opstellen van unieke relaties voor zowel stroming als massatransport in een kunstlong. Deze kunnen worden aangewend voor een optimaal hydrodynamisch ontwerp van nieuwe kunstlongen.

3 Inleiding

3.1 Openhartchirurgie: historiek van de kunstlong

De natuurlijke long voorziet het zuurstofarm bloed uit het rechter hart van zuurstof, O_2, en wisselt koolstofdioxide, CO_2, uit met de omgeving. Dit zuurstofrijk bloed wordt door het linker hart in de systeemcirculatie (vasculair systeem) gepompt waar zuurstof wordt opgenomen door de lichaamsweefsels voor de nodige stofwisseling en energietoevoer. Wanneer de longfunctie faalt, kan men deze tijdelijk vervangen door het inschakelen van een kunstlong, die instaat voor

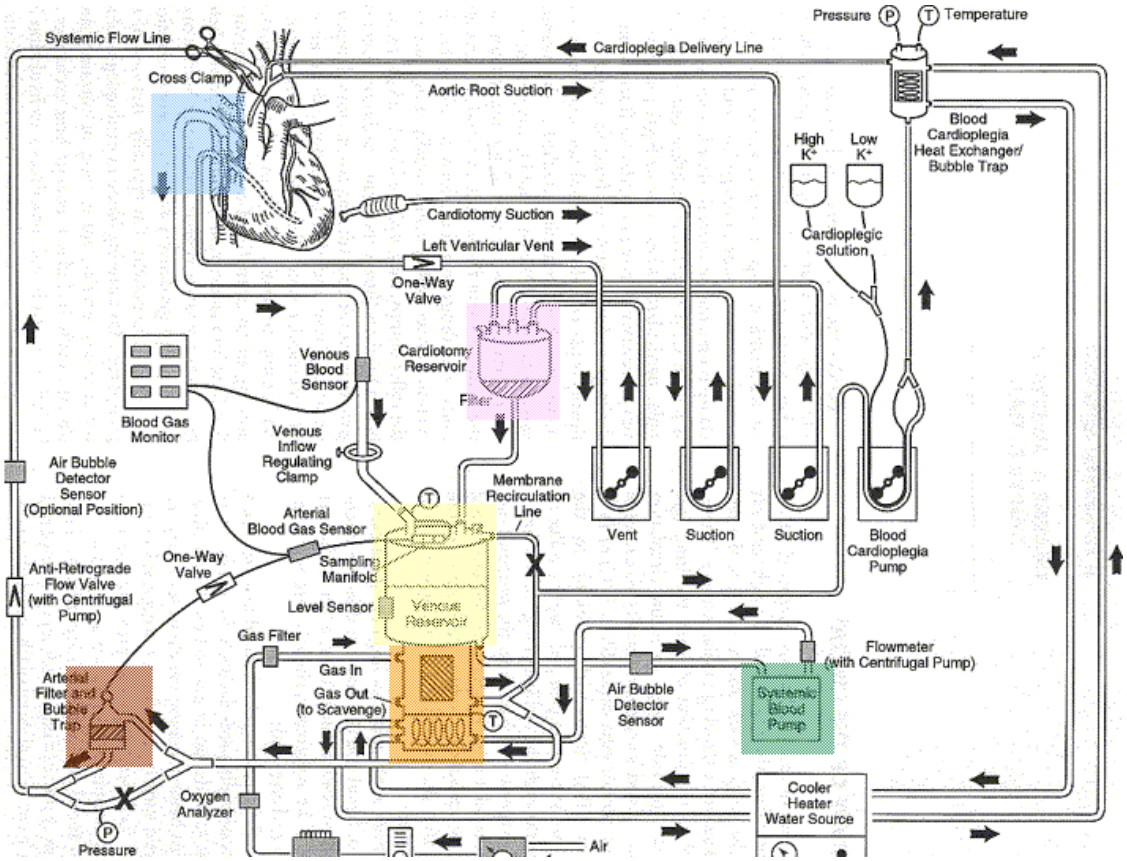

Figuur 2: Schema van een typisch extracorporeel circuit voor openhartchirurgie. In dit circuit wordt gebruik gemaakt van een membraankunstlong met rigied veneus reservoir (open systeem) (geel) en extern cardiotomie reservoir (magenta). Veneus bloed wordt via een veneuze canule (blauw) vanuit de vena cava en het rechter atrium tot in het veneus reservoir (geel) gedraineerd. Het veneuze bloed wordt vervolgens door een bloedpomp (groen) doorheen de kunstlong (oranje) gepompt waarin het eerst de warmtewisselaar doorstroomt voor de regeling van de bloedtemperatuur, en vervolgens het membraancompartiment doorstroomt voor de gasuitwisseling. Een externe warmtewisselaar regelt de temperatuur van het water dat de warmtewisselaar van de kunstlong doorstroomt. Het zuurstofrijk gas wordt via een menger en debietmeter en na doorstroming door een gasfilter in het membraancompartiment van de kunstlong gebracht. Nadat het bloed een arteriële filter (rood) heeft doorstroomd, wordt het bloed via een arteriële canule tot in de hoofdslagader van de patiënt geleid. <5>

de zuurstof- en koolstofdioxide-uitwisseling. Een kunstlong wordt gebruikt:

- tijdens openhartchirurgie waarbij de pompfunctie van het hart en de gasuitwisseling door de longen wordt overgenomen door de hartlongmachine (E: “cardiopulmorary bypass” (CPB))
- bij de behandeling van acute ademhalingsstoornis (E: “acute respiratory failure” (ARF))

De hartlongmachine is een onderdeel van een veno-arterieel extracorporeel circuit (ECC) om het hart (en bijgevolg de longen) te overbruggen. Het extracorporeel circuit is in serie verbonden met de systeemcirculatie van de patiënt. Het bloed tijdens openhartchirurgie wordt verdund (hemodilutie) en gekoeld (hypothermie) waarbij een niet-pulsatiele doorstroming en continue circulatie van het bloed in het extracorporeel circuit wordt voorzien. De gaszijde wordt, onder lage druk, continu door een zuurstofrijk gasmengsel doorstroomd en staat aan de uitlaatzijde bloot aan de omgeving. Door middel van een bloedpomp wordt veneus bloed van de patiënt doorheen de machine tot in de hoofdslagader (aorta) gepompt.

Het bloed wordt gedraineerd met behulp van canules geplaatst in de vena cava en/of het rechter atrium. Een goede canulatie zorgt voor een volledige drainage met voldoende debiet, een perfusie van alle organen en een bloedvrij operatieveld. De hartlongmachine bevat een veneus reservoir om als buffer plotse veranderingen in de bloedtoevoer op te vangen. De perfusionist, die de hartlongmachine bedient, heeft zo meer tijd om de situatie te kunnen controleren. Het veneus reservoir kan bestaan uit een collabeerbare polyvinylchloridezak (gesloten systeem) of een rigied reservoir (open systeem). Een arteriële filter zorgt voor de verwijdering van luchtembolen en partikels uit het bloed voordat het bloed de patiënt bereikt. Figuur 2 geeft een overzicht van een typisch extracorporeel circuit voor openhartchirurgie.

Tijdens openhartchirurgie wordt een lagere temperatuur (hypothermie) aangewend aangezien dit het metabolisme (zuurstofopname) beperkt. Dit heeft als voordeel dat de totale zuurstofconsumptie voldoende laag blijft en de zuurstofbehoefte door de kunstlong kan gedekt worden. Uiteraard moet bij het einde van de perfusiefase de patiënt langzaam terug op temperatuur gebracht worden. Een lagere temperatuur doet evenwel de viscositeit van het bloed toenemen. Met behulp van een warmtewisselaar in de kunstlong, waarbij als koelvloeistof water op kamertemperatuur wordt gebruikt, wordt het bloed op de juiste temperatuur gebracht. Het bloed wordt verdund met een fysiologische oplossing (hemodilutie) die bij aanvang van de bypass de hartlongmachine vult ten einde luchtbelletjes in de circulatie van de patiënt te voorkomen en embolie te vermijden. Terzelfdertijd doet die oplossing de viscositeit van het bloed afnemen <6>. Tijdens niet-invasieve ademhalingsondersteuning moet de patiënt slechts op lichaamstemperatuur gehouden worden. Het bloed dat zich in het extracorporeel circuit bevindt

zal lichtjes afkoelen, vooral door het contact met het koude gas in de kunstlong. In vivo varieert de bloedtemperatuur tussen 37 en 26 °C met een ingangssaturatie tussen de 26 en 75 %, waarbij ook het hematocriet sterk afneemt door hemodilutie (27 %) <6>†.

Een eerste poging om de functie van de natuurlijke long door een kunstlong te vervangen werd reeds ondernomen op het einde van de 19de eeuw, doch de eerste betrouwbare resultaten werden slechts bereikt rond 1950. Een groot uitwisselingsoppervlak voor de gasuitwisseling in de kunstlong werd ofwel verwezenlijkt door het opborrelen van zuurstof in circulerend bloed in een reservoir, ofwel door een dunne bloedfilm rechtstreeks in contact te brengen met een zuurstofrijke omgeving. Als gevolge van het directe, zeer bio-incompatibel contact tussen bloed en gas, en de grote moeilijkheid om een stabiel uitwisselingsproces te bekomen gedurende langere periodes, past men nu wereldwijd membraan-gemedieerde uitwisselingsprocessen toe <7>.

Tussen de gas- en de bloedzijde wordt een gaspermeabel kunststofmembraan geplaatst. In eerste instantie (1970) werden silicone membranen toegepast om de natuurlijke long gedurende een langere periode te ondersteunen. De hoge kosten van Silicone membranen en het uitblijven van positieve klinische resultaten <8,9> brachten de silicone membraankunstlong op de achtergrond. De ontdekking van hydrofobe microporeuze membranen die onder meer toelaten dat het gas vrij diffundeert, en de mogelijkheid om dergelijke membranen (goedkoop en betrouwbaar) op grote schaal te produceren en in te bouwen in een kunstlong, effenden de weg naar de holle vezel membraankunstlong rond 1980 <7,10>. Binnen deze groep kunstlongen zijn er drie weerstanden voor het gastransport: de gaszijde, het membraan en de vloeistoffase. Bij microporeuze membranen vervallen de eerste twee en spreekt men van vloeistofgelimiteerde systemen. Immers, door het poreuze karakter van het membraan is de permeabiliteit voor zuurstof en koolstofdioxide hoog, waardoor het massatransport aan de bloedzijde de grootste weerstand in het massatransport vormt. Vandaar het belang bij deze kunstlongen om het massatransport aan de bloedzijde te verhogen door convectie (secundaire stromingen).

Een gedetailleerde beschrijving van de geschiedenis van de kunstlong is weergegegeven in Chapter I “Introduction to and History of Cardiopulmonary Bypass and Artificial Lungs”.

---

† Bloed met een temperatuur van 37 °C (normotherm) en een hematocriet van 45 % wordt in dit proefschrift omschreven als normaal bloed.

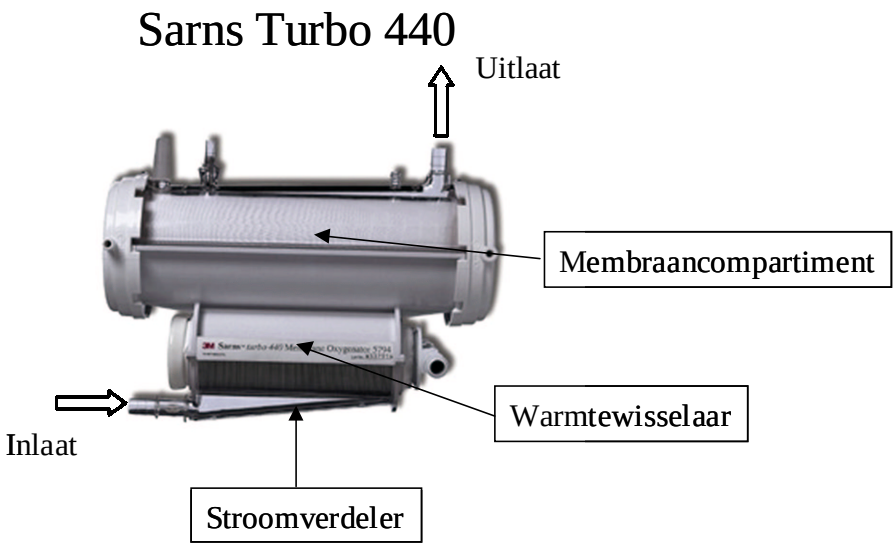

Figuur 3: De commerciële holle vezel membraankunstlong met kruisstroming "Sarns Turbo 440" met aanduiding van de stroomverdeler, de warmtewisselaar en het membraancompartiment. De pijlen duiden de stromingsrichting aan van het bloed.

3.2 Type membraankunstlongen

Momenteel zijn twee types membraankunstlongen commercieel beschikbaar, namelijk de platenmembraankunstlong en de holle vezel membraankunstlong met kruisstroming.

De platenmembraankunstlong maakt gebruik van het afwisselend stapelen van een membraan en een rooster. Het rooster biedt verscheidene voordelen waaronder de steun voor het dunne membraan en een periodiek stromingspatroon dat door zijn convectief karakter de gasuitwisseling bevordert. In een holle vezel membraankunstlong met kruisstroming stroomt het bloed rond holle, microporeuze polypropyleen- of polyethyleenvezels, terwijl het gas in het lumen van de vezels stroomt. Deze techniek heeft als voordeel dat het convectieve karakter van de stroming de gasoverdracht verhoogt, en er bijgevolg compacte eenheden (kleine, beperkte uitwisselingsoppervlakte) mogelijk zijn.

De kunstlong is opgebouwd uit twee modules (Figuur 3): een warmtewisselaar die toelaat de bloedtemperatuur te regelen en een membraancompartiment dat is opgebouwd uit een tienduizendtal holle, microporeuze, polypropyleenvezels, samengeweven in een matstructuur, die instaan voor de opname van zuurstof en afgave van koolstofdioxide (gasuitwisseling). Het bloed stroomt eerst door de warmtewisselaar en daarna extraluminaal en in kruisstroming met de vezels door het membraancompartiment.

In dit proefschrift wordt de holle vezel membraankunstlong met kruisstroming† zowel numeriek (“*in numero*”) als experimenteel (“*in vitro*”) bestudeerd voor wat betreft de hydrodynamica en het zuurstoftransport. De volgende drie commerciële holle vezel membraankunstlongen met kruisstroming komen aan de orde: Sarns Turbo 440 (Terumo, voorheen 3M), Cobe Optima (Sorin Biomedica, voorheen Cobe Cardiovascular) en Dideco Compactflo (Sorin Biomedica, voorheen Dideco Cardiovascular) (Figuur 4).

3.3 Fysische eigenschappen van bloed

Stroming van bloed verschilt grondig van homogene waterstroming. Zo is bloed onder bepaalde voorwaarden een niet-newtoniaanse vloeistof met een viscositeit die minstens 4 keer zo hoog ligt als die van water <11>.

De specifieke samenstelling van bloed en zijn rheologie spelen ook een rol bij het massatransport van en naar het bloed. Zo is er een verschil tussen de fysische transportconstanten (dichtheid, viscositeit, oplosbaarheid en diffusiecoëfficiënt) van plasma en van rode bloedcellen. De opname

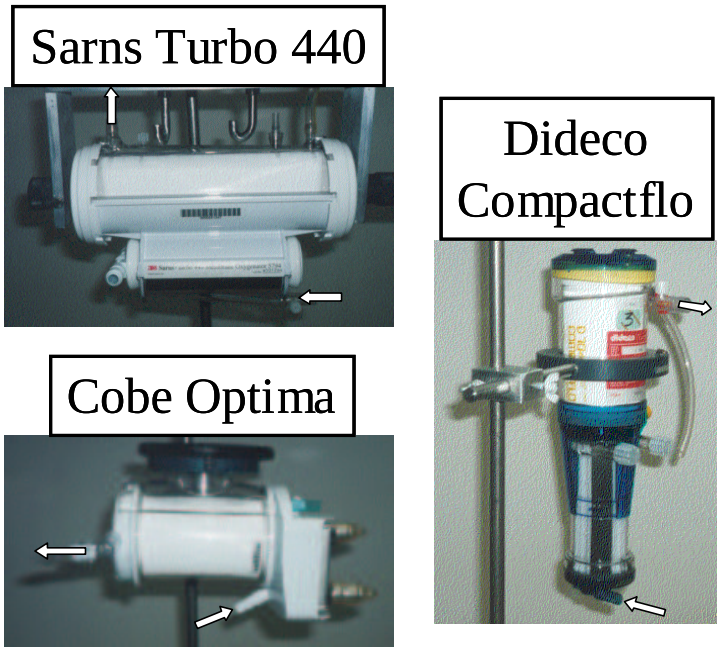

Figuur 4: De drie commercieel beschikbare holle vezel membraankunstlongen met kruisstroming die in dit proefschrift zijn bestudeerd. **Links boven:** Sarns Turbo 440 (Terumo, voorheen 3M); **Links onder:** Cobe Optima (Sorin Biomedica, voorheen Cobe Cardiovascular); **Rechts:** Dideco Compactflo (Sorin Biomedica, voorheen Dideco Cardiovascular). De pijlen duiden de stromingsrichting aan van het bloed.

† Tenzij expliciet anders vermeld, wordt hierna met kunstlong de holle vezel membraankunstlong met kruisstroming bedoeld.

en afgifte van zuurstof door het bloed gebeurt slechts gedeeltelijk door oplossing. De biochemische binding van zuurstof aan het hemoglobine in de rode bloedcellen voegt een extra complexiteit toe aan het fysiologische uitwisselingsproces.

De dynamische viscositeit, μ_∞, is onder andere afhankelijk van de hoeveelheid rode bloedcellen (hematocriet, Hct) <12> en de temperatuur, T <13>:

$$\mu_\infty = \mu_p \cdot e^{2.34 \cdot Hct} \qquad [1]$$

waarin μ_p de absolute plasmaviscositeit voorstelt <3,14>. Het plasma is een newtoniaanse vloeistof waarvan de viscositeit afneemt bij toenemende temperatuur, T, uitgedrukt in Kelvin:

$$\mu_p = e^{-5.54+\frac{1800}{T+273}} \qquad [2]$$

Bij lage afschuifsnelheden neemt de viscositeit van bloed toe: het gedraagt zich pseudoplastisch. Dit effect kan beschreven worden volgens Casson <15-17> met deze vergelijking:

$$\sqrt{\tau} = \sqrt{\tau_o} + \sqrt{\mu_\infty \cdot \dot{\gamma}} \qquad [3]$$

Hierin is τ_o de vloeispanning ("yield stress"), de minimale schuifspanning vooraleer er stroming kan gebeuren. τ en $\dot{\gamma}$ zijn respectievelijk de schuifspanning en de afschuifsnelheid.

De dichtheid van bloed, ρ, neemt lineair toe met het hematocriet volgens een eenvoudige mengregel:

$$\rho = 1090 \cdot Hct + 1035 \cdot (1 - Hct) \qquad [4]$$

De Bunsen oplosbaarheidscoëfficient van zuurstof in bloed, α_{O_2}, is afhankelijk van de temperatuur en het hematocriet <18,19>. Ook de diffusiecoëfficiënt van opgeloste zuurstof in het bloed, D_{O_2}, is temperatuursafhankelijk en kan worden beschreven volgens de theorie van Fricke <20-22>.

3.4 Zuurstoftransport

De natuurlijke long voorziet het zuurstofarm bloed uit de rechterhelft van hart van zuurstof en wisselt koolstofdioxide uit met de omgeving. Dit zuurstofrijk bloed wordt door de linkerhelft van het hart in de systeemcirculatie (vasculair systeem) gepompt waar zuurstof wordt opgenomen door de lichaamsweefsels voor de nodige stofwisseling en energietoevoer.

Bloed is een biologische vloeistof die enkele specifieke kenmerken heeft voor wat betreft het zuurstoftransport. Zuurstof wordt slechts in zeer geringe mate opgelost in plasma. Het grootste deel van de zuurstof in het bloed is gebonden aan één van de heem-moleculen die deel uitmaken van het hemoglobine (Hb) uit de rode bloedcel. De totale hoeveelheid zuurstof is een functie van

de zuurstofpartieeldruk in het bloed. De zuurstofconcentratie[†] in het bloed, C_{O_2}, is de som van de opgeloste hoeveelheid zuurstof, $C_{O_2 d}$, en de gebonden hoeveelheid zuurstof, $C_{O_2 b}$:

$$C_{O_2} = C_{O_2 d} + C_{O_2 b} \qquad [5]$$

De totale hoeveelheid zuurstof in het bloed is een functie van de zuurstofpartieeldruk, P_{O_2}. Voor opgeloste zuurstof is dit een lineaire functie (Henry's wet <23>):

$$C_{O_2 d} = \alpha_{O_2} \cdot P_{O_2} \qquad [6]$$

De oxyhemoglobine-dissociatiecurve of saturatiecurve beschrijft het chemisch bindingsgedrag van zuurstof met Hb door de saturatie van bloed uit te zetten als een niet-lineaire functie van de zuurstofpartieeldruk. De saturatie drukt de verhouding uit van de hoeveelheid hemoglobine, Hb, die gebonden is met zuurstof tot de totale hoeveelheid Hb. De curve is o.a. afhankelijk van de temperatuur, T, en de zuurtegraad, pH <24-26>. Een veelgebruikte formule die de zuurstofsaturatie

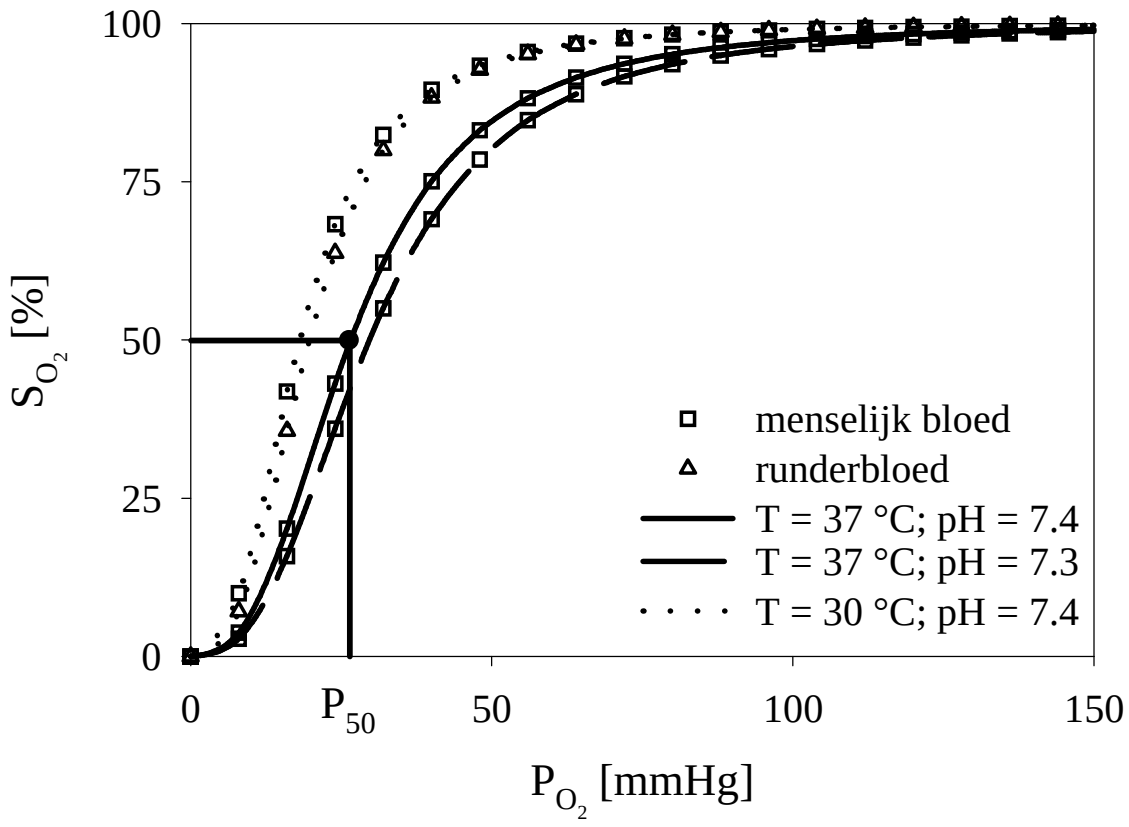

Figuur 5: De oxyhemoglobine-dissociatiecurve voor bloed van mensen en runderen bij verschillende temperatuur, T, en zuurtegraad, pH. Het niet-lineaire, sigmoïdale karakter van de hemoglobine saturatie en de zuurstofpartieeldruk is duidelijk zichtbaar. Er treedt een verschuiving naar rechts op bij toenemende temperatuur en dalende zuurtegraad. De Hill-vergelijking beschrijft de oxyhemoglobine-dissociatiecurve voor menselijk bloed en runderbloed.

[†] De zuurstofconcentratie wordt in dit proefschrift uitgedrukt in [ml O_2/l] of kortweg [ml/l].

benaderend beschrijft in functie van de zuurstofpartieeldruk is de formule van Hill <26> (Figuur 5):

$$S_{O_2} = \frac{\left(\frac{P_{O_2}}{P_{50}}\right)^n}{1+\left(\frac{P_{O_2}}{P_{50}}\right)^n} \qquad [7]$$

waarin n afhankelijk is van het bloedtype (menselijk bloed of runderbloed†) en P_{50} de zuurstofpartieeldruk bij een saturatie van 50 %. P_{50} is afhankelijk van het bloedtype, de temperatuur en de zuurtegraad. Tijdens rust is de gasuitwisseling minimaal. Door koeling van de patiënt (hypothermie) wordt de stofuitwisseling eveneens sterk verminderd.

De gebonden hoeveelheid zuurstof wordt beschreven door de oxyhemoglobine-dissociatiecurve, S_{O_2} (Figuur 5):

$$C_{O_2 b} = B_{O_2} \cdot C_{Hb} \cdot S_{O_2}\left(P_{O_2}\right) \qquad [8]$$

Hierin is B_{O_2} de bindingscapaciteit van zuurstof aan hemoglobine en C_{Hb} de hoeveelheid hemoglobine per volume-eenheid bloed.

Het zuurstofmassadebiet, $\dot{V}_{O_2}$, in de kunstlong kan worden begroot door aan de bloedzijde, zowel aan de inlaat als de uitlaat, de zuurstofconcentratie te meten en het behoud van massa toe te passen <27>. Dat geeft volgende vergelijking:

$$\dot{V}_{O_2} = \alpha_{O_2} \cdot Q \cdot \left(P_{O_2 out} - P_{O_2 in}\right) + B_{O_2} \cdot C_{Hb} \cdot Q \cdot \left(S_{O_2 out} - S_{O_2 in}\right) \qquad [9]$$

waarin de indices “in” en “out” verwijzen naar respectievelijk de inlaat en de uitlaat van de kunstlong. Q stelt het bloeddebiet voor.

3.5 Theoretische beschouwingen

3.5.1 Stroming: de Navier-Stokes vergelijkingen

We beschouwen een tweedimensionale isotherme, laminaire, onsamendrukbare, permanente stroming in het membraancompartiment. De warmteoverdracht tussen de gas- en bloedfase in het membraancompartiment is verwaarloosbaar klein, zodat de energievergelijking niet moet in rekening gebracht worden. De lage Reynoldsgetallen (§3.7) in het membraancompartiment rechtvaardigen laminaire stroming. We veronderstellen eveneens dat een constant debiet doorheen de kunstlong stroomt.

---

† Runderbloed wordt in het numeriek model en in de bloedexperimenten gebruikt als testfluïdum.

De vergelijkingen die de vloeistofstroming beschrijven zijn de continuïteits- en momentumvergelijking. Bloed kan behandeld worden als een onsamendrukbare vloeistof zodat de vergelijkingen vereenvoudigd kunnen worden. De Navier-Stokes vergelijkingen drukken het behoud van massa:

$$\bar{\nabla} \bullet \bar{\mathbf{u}} = 0 \qquad [10]$$

en momentum uit:

$$\rho \bar{\mathbf{u}} \bullet \bar{\nabla} \bar{\mathbf{u}} + \bar{\nabla} p = \bar{\nabla} \bar{\mathbf{t}} \qquad [11]$$

waarin $\bar{\mathbf{u}}$ de vloeistofsnelheid voorstelt, ρ de dichtheid, p de lokale hydrostatische druk en $\bar{\mathbf{t}}$ de schuifspanningstensor. $\bar{\nabla}$ is de gradiënt. Men veronderstelt dat de zwaartekracht geen invloed heeft. De schuifspanningstensor wordt beschreven in functie van de snelheidsgradiënten net als de constitutieve vergelijking voor de viscositeit (bv. Casson):

$$\bar{\mathbf{t}} = \mu\left(\bar{\nabla} \bar{\mathbf{u}}\right)\left(\bar{\nabla} \bar{\mathbf{u}} + \bar{\nabla} \bar{\mathbf{u}}^{T}\right) \qquad [12]$$

waarin μ de dynamische viscositeit voorstelt en T het superscript voor transponering van de snelheidsgradiënttensor. In het geval van een newtoniaanse vloeistof is de viscositeit onafhankelijk van de snelheidsgradiënt:

$$\mu\left(\bar{\nabla} \bar{\mathbf{u}}\right) = \mu_{\infty}$$

De invloed van het niet-newtoniaanse karakter laat zich pas voelen bij lagere Reynoldsgetallen, N_{Re} ($N_{Re} < 10$) (§3.7)

Een van de eenvoudigste manieren om een stroompad te karakteriseren is de stromingsweerstand bepalen. De stromingsweerstand van een kunstlong (hetzij het membraancompartiment, hetzij de warmtewisselaar, hetzij de kunstlong in haar geheel) wordt bepaald door in het toestel de relatie tussen het stromingsdebiet, Q, en de bijhorende drukval, Δp, te bepalen. Aldus bekomt men de druk-debietrelatie, Q-Δp. Druk en debiet zijn de bepalende factoren voor de andere stromingsparameters waaronder de lokale schuifspanningen.

3.5.2 Het zuurstoftransport: de convectie-diffusie vergelijking

Het zuurstoftransport in de kunstlong kan beschreven worden met behulp van de convectie-diffusievergelijking. De convectie-diffusievergelijking drukt het behoud van massa uit waarbij rekening wordt gehouden met het diffusief massatransport (wet van Fick), $D_{O_2} \cdot \Delta C_{O_2}$, en het convectief massatransport, $\bar{\mathbf{u}} \bullet \bar{\nabla} C_{O_2}$:

$$\bar{\mathbf{u}} \bullet \bar{\nabla} C_{O_2} = D_{O_2} \cdot \Delta C_{O_2} \qquad [13]$$

met Δ de Laplaciaan.

De niet-lineaire chemische binding van zuurstof in het bloed is in de convectie-diffusievergelijking gebracht en gelineariseerd. Dit kan door de convectie-diffusievergelijking te herschrijven in functie van de zuurstofpartieeldruk, in plaats van in functie van de zuurstofconcentratie. De afgeleide van de zuurstofsaturatie wordt gesplitst naar de partieeldruk. Linearisatie van de partiële differentiaalvergelijking is dan mogelijk door de afgeleide van de saturatie naar de partieeldruk te benaderen als een vooraf te berekenen waarde <26>. De diffusieterm werkt enkel in op de opgeloste hoeveelheid zuurstof. De gebonden zuurstof wordt er niet rechtstreeks door beïnvloed.

Als we enerzijds rekening houden met de chemische binding van zuurstof en hemoglobine, en anderzijds met het feit dat de diffusie van hemoglobine kan worden verwaarloosd, kan de convectie-diffusievergelijking voor het zuurstoftransport in bloed worden herschreven in functie van de zuurstofpartieeldruk. Dit geeft:

$$\bar{\mathbf{u}} \bullet \overline{\nabla} P_{O_2} = D_{O_2 eff} \cdot \Delta P_{O_2} \qquad [14]$$

waarin $D_{O_2 eff}$ de effectieve diffusiecoëfficiënt voorstelt en gelijk is aan:

$$D_{O_2 eff} = \frac{D_{O_2}}{1 + \lambda(P_{O_2})} \qquad [15]$$

$\lambda(P_{O_2})$ is een maat voor de bindingscapaciteit van zuurstof in de rode bloedcel.

De efficiëntie van het zuurstoftransport in de kunstlong kan worden begroot met behulp van de massatransportcoëfficiënt, K:

$$K = \frac{\text{massaflux}}{C_{O_2 g} - C_{O_2}} \qquad [16]$$

De massatransportcoëfficiënt drukt de hoeveelheid massaflux uit per eenheid concentratieverschil en is gedefinieerd als de reciproke van de massatransportweerstand, R. De massaflux is het massadebiet per tijdseenheid en per eenheid uitwisselingsoppervlakte:

$$\text{massaflux} = \frac{\dot{V}_{O_2}}{A} \qquad [17]$$

De drijvende kracht voor het massatransport is het zuurstofconcentratieverschil dat over het membraan heerst:

$$C_{O_2 g} - C_{O_2} \qquad [18]$$

waarin $C_{O_2 g}$ de zuurstofconcentratie aan de gaszijde voorstelt.

3.5.3 De eindige elementenmethode

De resulterende niet-lineaire partiële differentiaalvergelijkingen zijn over het algemeen te complex om een algemeen geldende analytische oplossing te berekenen. Met numerieke methoden is het mogelijk om particuliere oplossingen te berekenen bij gegeven randvoorwaarden. Naargelang van de gebruikte numerieke techniek, de resolutie van de discretisatie, de relatieve grootte van de fysische constanten van het wiskundig probleem ten opzichte van elkaar en de randvoorwaarden zal de bereikte oplossing meer of minder nauwkeurig zijn. De eindige elementenmethode <28-30> wordt gebruikt om het stelsel van partiële differentiaalvergelijkingen die de vloeistofstroming en het massatransport beschrijven, op te lossen. Een voordeel van de eindige elementenmethode is de mogelijkheid om complexe configuraties te modelleren. Voor de toepassing van eindige elementen bij de oplossing van partiële differentiaalvergelijkingen wordt in dit proefschrift het eindige elementen softwarepakket SEPRAN <30,31> gebruikt dat een stromingsmodule en een module voor tweede-orde lineaire elliptische en parabolische vergelijkingen met één vrijheidsgraad bevat, waarmee deze vergelijkingen kunnen opgelost worden.

3.6 Geometrische kenmerken van de kunstlong

3.6.1 Macroscopisch geometrische kenmerken

Het membraancompartiment van de kunstlong wordt gekenmerkt door enkele geometrische karakteristieken: de diameter van de holle vezels (0.380 mm), de afstand tussen de vezels in de verschillende richtingen, de stromingsrichting, de bloedpadlengte en de porositeit. Idealiter tracht men een maximaal bloeddebiet te realiseren met een lage drukval over de kunstlong en met een voldoende transportcapaciteit ten behoeve van zowel de warmtewisseling als de gasuitwisseling in een zo compact mogelijk geheel. Gezien het belang van de structuur van de membraanmat ligt de focus van de studie daar.

Een kunstlong kan worden gekarakteriseerd met verschillende geometrische parameters <3,4,32-34> (Figuur 6): uitwisselingsoppervlakte, A, vezeldiameter, d, lengte van het membraancompartiment, L, doorstroomoppervlakte, A_f, inwendige diameter, D_i, en uitwendige diameter, D_o, van de cilindervormige behuizing (annulus) van het membraancompartiment. Het membraancompartiment van de kunstlong bevat een zekere porositeit, ε, gedefinieerd als de verhouding tussen het lege volume, V_{void}, tot het volume van de behuizing, V_{bed}. Het lege volume is het volume van de behuizing, V_{bed}, verminderd met het vezelvolume, V_{fiber}:

$$\varepsilon = \frac{V_{void}}{V_{bed}} = \frac{V_{bed} - V_{fiber}}{V_{bed}} \qquad [19]$$

Als karakteristieke lengte voor stroming doorheen een poreus medium kan de hydraulische straal, R_h, worden genomen. R_h is gedefinieerd als de verhouding van de porositeit, ε, tot het nat oppervlak per volume-eenheid, a:

$$R_h = \frac{\left(\frac{V_{void}}{V_{bed}}\right)}{\left(\frac{A}{V_{bed}}\right)} = \frac{\varepsilon}{a} = \frac{\varepsilon \cdot d}{4 \cdot (1-\varepsilon)} \qquad [20]$$

De stroomverdelerlengte, L_m, is gedefinieerd als de lengte dat het gehele debiet verdeeld per eenheidsbreedte van het membraancompartiment. De gemiddelde bloedpadlengte, L_b, is de gemiddelde afstand die het bloed aflegt door de vezelbundel. Bijgevolg kan men een dimensieloze karakteristieke lengte, ξ, definiëren als de verhouding van L_b tot L_m:

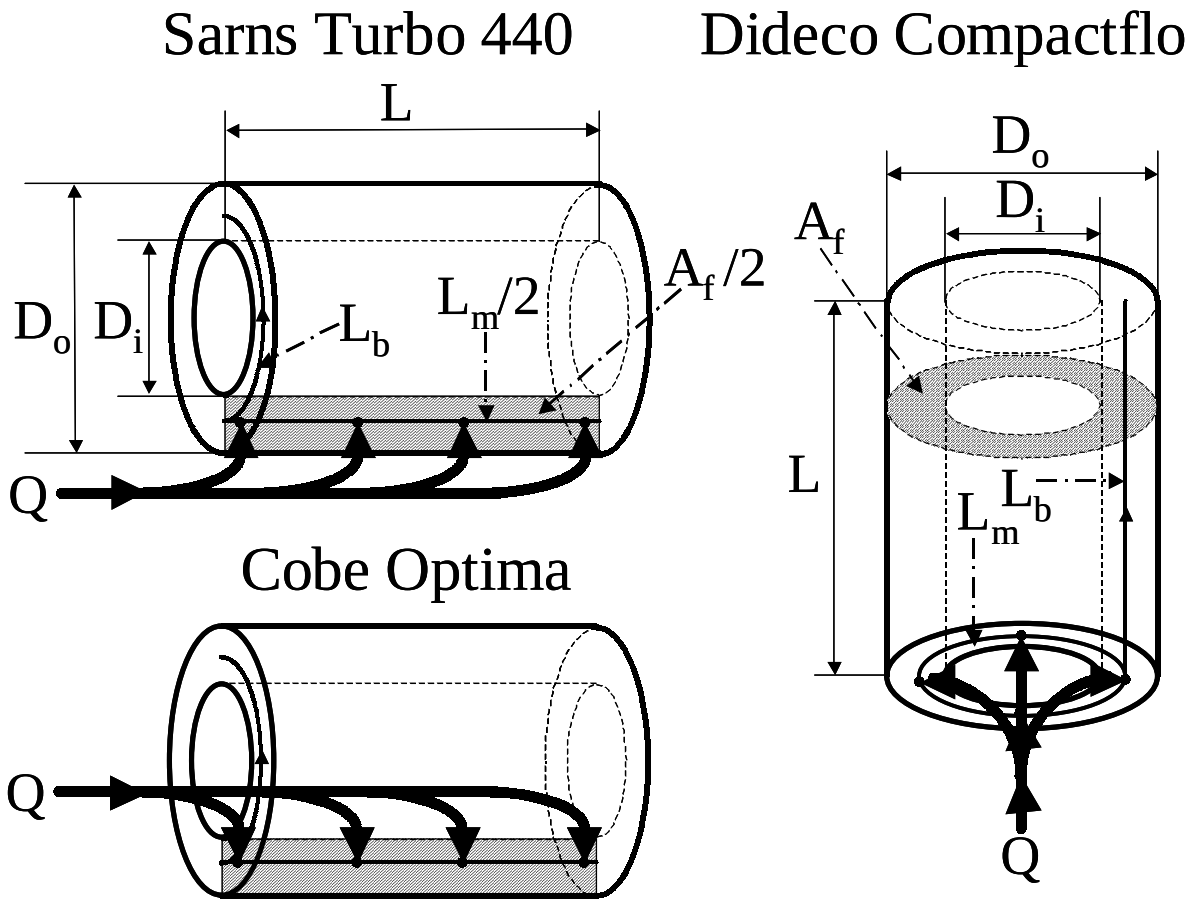

Figuur 6: Schematische voorstelling van de geometrie voor verschillende types commercieel beschikbare kunstlongen. **Links boven:** Sarns Turbo 440; **Links onder:** Cobe Optima; **Rechts:** Dideco Compactflo.

Tabel 1: Geometrische kenmerken van de commercieel beschikbare holle vezel membraankunstlongen met kruisstroming: Sarns Turbo 440, Cobe Optima en Dideco Compactflo.

	Sarns Turbo 440	***Cobe Optima***	***Dideco Compactflo***
uitwisselingsoppervlakte, A [m²]	1.6	1.7	2
vezeldiameter, d [µm]	380	380	380
inwendige diameter behuizing, D_i [cm]	5.0	4.4	5.0
uitwendige diameter behuizing, D_o [cm]	7.0	7.3	7.8
lengte membraancompartiment, L [cm]	20.5	12.4	12
porositeit membraancompartiment, ε	0.61	0.51	0.44
karakteristieke lengte, ξ	0.23	0.37	0.60

$$\xi = \frac{L_b}{L_m} \qquad [21]$$

We onderstellen dat het bloed uniform wordt verdeeld over de vezelbundel.

In Figuur 6 worden L_m en L_b weergegeven voor Sarns Turbo 440 (Figuur 6, links boven) en Optima (Figuur 6, links onder). Het bloed wordt uniform verdeeld over de lengte van het membraancompartiment, L, en wordt opgesplitst in twee voor het linker en rechter deel van het membraancompartiment. Het bloeddebiet, Q´, per eenheidsbreedte vezelbundel is:

$$Q' = \frac{Q}{L_m} = \frac{Q}{2 \cdot L} \qquad [22]$$

De bloedpadlengte wordt als volgt berekend:

$$L_b = \frac{\pi}{2} \cdot \left(\frac{D_i + D_o}{2} \right) \qquad [23]$$

In Dideco Compactflo wordt het bloed circumferentieel verdeeld over de vezelbundel (Figuur 6, rechts). De stroomverdelerlengte is hier gedefinieerd als volgt:

$$L_m = \pi \cdot \left(\frac{D_i + D_o}{2} \right) \qquad [24]$$

Voor de bloedpadlengte van Dideco Compactlfo geldt:

$$L_b = L \qquad [25]$$

Tabel 1 geeft een overzicht van de geometrische kenmerken van de drie kunstlongen die in dit proefschrift worden bestudeerd.

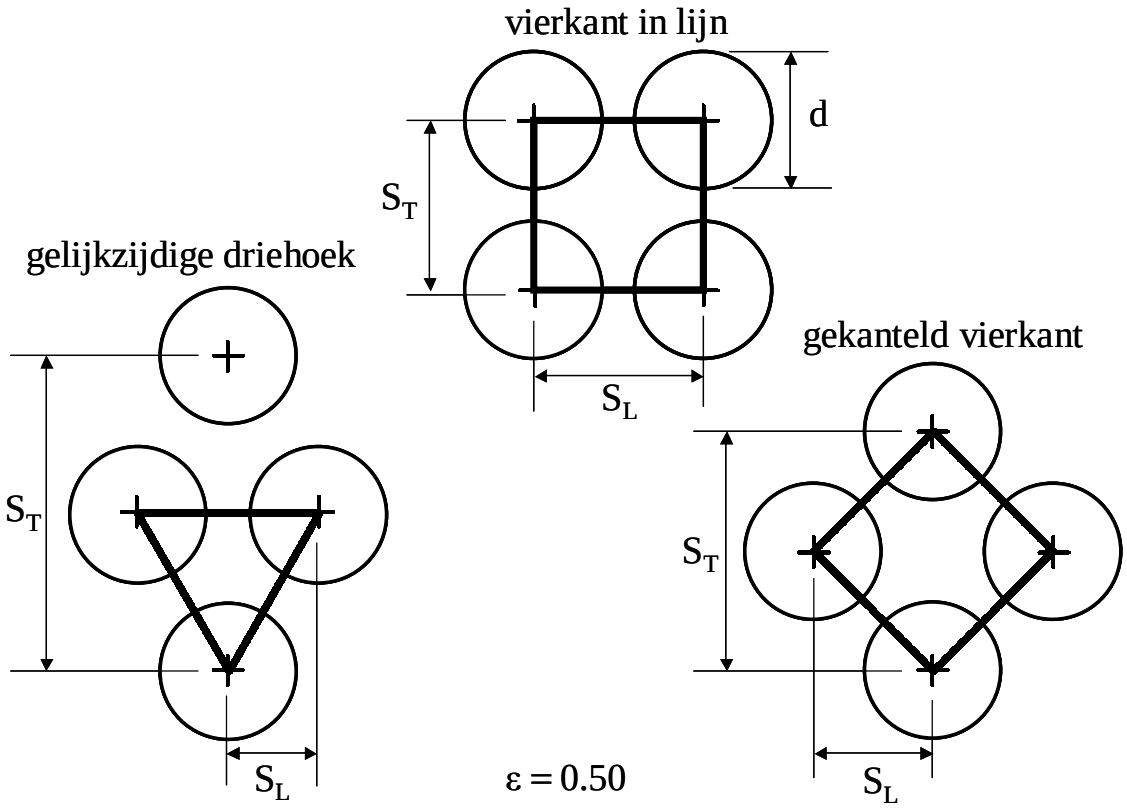

Figuur 7: De drie vezelconfiguraties met een porositeit, ε, van 0.5 en een vezeldiameter van 0.380 mm. **Boven:** het vierkant in lijn "inline square"; **Links onder:** de gelijkzijdige driehoek "equilateral triangle": **Rechts onder:** het gekanteld vierkant "staggered square".

De snelheid in een poreus medium kan worden gekenmerkt door enerzijds de superficiële snelheid, U_s, en anderzijds de gemiddelde snelheid, U_m <35>. De superficiële snelheid of Darcysnelheid wordt gedefinieerd als de gemiddelde snelheid in de stromingsrichting die zou optreden indien er geen vezels in het membraancompartiment aanwezig zouden zijn:

$$U_s = \frac{Q}{A_f} \qquad [26]$$

De gemiddelde snelheid wordt gedefinieerd als de gemiddelde snelheid doorheen de poriën van het poreus medium, i.e. doorheen de vrije ruimtes in het membraancompartiment:

$$U_m = \frac{Q}{\varepsilon \cdot A_f} \qquad [27]$$

zodat:

$$\varepsilon = \frac{U_s}{U_m} \qquad [28]$$

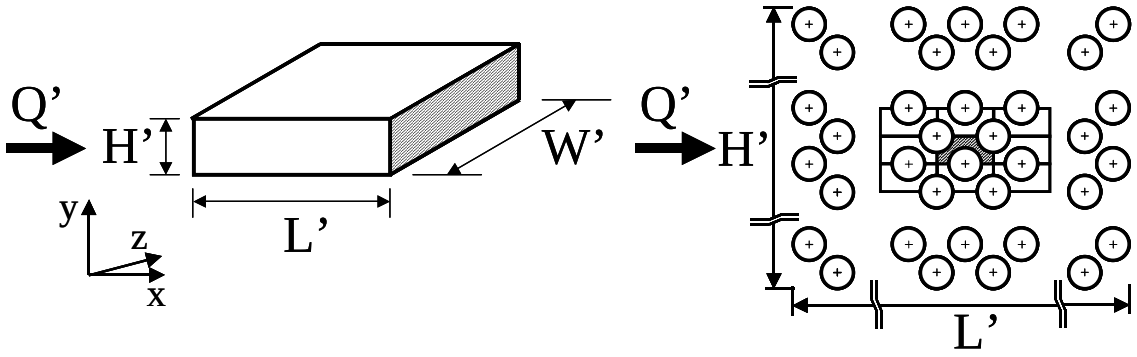

Figuur 8: Links: Schematische voorstelling van een vezelbank met hoogte, H’, lengte, L’, en diepte, W’. x duidt de stromingsrichting aan (longitudinaal), y is de transversale richting en z ligt volgens de lengteas van de vezels. Q’ stelt het debiet doorheen de vezelbank voor. **Rechts:** De vezelbank wordt hier voorgesteld als een geïdealiseerde bundel vezels die loodrecht op de stromingsrichting zijn geplaatst. De eenheidscellen zijn in een rechthoekig rooster geschikt.

3.6.2 Microscopisch geometrische kenmerken

Het membraan van de kunstlong is opgebouwd uit duizenden holle vezels die tot een structuur zijn samengeweven. Afhankelijk van het gebruikte weefpatroon en de plaatsing van het membraan in de behuizing van de kunstlong, zullen de vezels op een verschillende manier tegenover elkaar georiënteerd staan. Indien men enerzijds de invloed op de stroming van de inlaat, de uitlaat en de wand van het membraancompartiment verwaarloost en anderzijds een volledig ontwikkelde, tweedimensionale, constante stroming doorheen het membraancompartiment veronderstelt, kan men ervan uitgaan dat de stroming volledig ontwikkeld en periodiek is. Het membraancompartiment kan dan worden onderverdeeld in een (groot) aantal eenheidscellen die elk één enkele vezel bevatten.

Een vezelbank kan worden gekenmerkt door de transversale, S_T/d, en longitudinale, S_L/d, afstand (S) tot diameter (d) verhouding (Figuur 7).

Figuur 7 toont drie verschillende vezelconfiguraties met een porositeit van 0.5 en een diameter, d, van 0.380 mm: “vierkant in lijn” (E: “in line square” (IS)), “gelijkzijdige driehoek” (E: “equilateral triangle” (ET)) en “gekanteld vierkant” (E: “staggered square” (SS)). Men herkent hierin S_L als de afstand tussen twee opeenvolgende vezelkolommen en S_T als de afstand tussen twee opeenvolgende vezelrijen.

Figuur 8 stelt een vezelbank met hoogte, H’, lengte, L’, en breedte, W’ voor (links) als een bundel van vezels die loodrecht op de stromingsrichting zijn geplaatst (rechts). Deze vezelbank is een geïdealiseerde voorstelling van het membraancompartiment van een commercieel beschikbare holle vezel membraankunstlong met kruisstroming in Figuur 6:

$$H' = \frac{D_o - D_i}{2}$$
$$L' = L_b \qquad [29]$$
$$W' = L_m$$

Vertrekkende van een tweedimensionale eenheidscel kan na een integratie in de lengterichting (x-richting) en na transversale extrapolatie een membraancompartiment worden geconstrueerd dat het membraancompartiment van de kunstlong benadert, rekening houdend met de geometrische kenmerken (bloedpadlengte, vezellengte, dikte, …). De drukval en het zuurstofmassadebiet kan aldus berekend worden voor een volledig membraancompartiment.
In dit proefschrift zijn de drie voorgestelde karakteristieke configuraties (Figuur 7) gebruikt om de stroming en het massatransport in de kunstlong te bestuderen. Deze drie configuraties beslaan slechts enkele van de mogelijke configuraties, maar zijn hier gekozen omwille van hun specifieke stromingseigenschappen en symmetrie. Algemeen kan men er van uitgaan dat een mix van deze configuraties in staat is de stromingseigenschappen van een gehele kunstlong te modelleren.

3.7 Gelijkvormigheidsanalyse en dimensieloze getallen

Bij de beschrijving van transportverschijnselen kunnen de resultaten bekomen met behulp van verschillende fluïda met elkaar vergeleken worden. Dat gebeurt met behulp van de gelijkvormigheidsanalyse, die gebruik maakt van dimensieloze getallen. Elk van deze getallen is meestal opgebouwd uit de verhouding van twee fysische fenomenen en geeft bijgevolg uitdrukking aan het respectieve belang van beide fenomenen voor de bestudeerde kunstlong. Tabel 2 geeft een overzicht weer van de voornaamste parameters die in de stromingsleer en het massatransport worden gebruikt.
Door het toepassen van gelijkvormigheidsanalyse op druk-debiet data, kan men de *in vitro* resultaten, bekomen met water, berekenen naar druk-debietrelaties voor bloed.
Het Reynoldsgetal, N_{Re}, is de verhouding van de inertiekrachten tot de viskeuze krachten. In formule uitgedrukt geeft dat:

$$N_{Re} = U \cdot \frac{4 \cdot R_h \cdot \rho}{\mu} \qquad [30]$$

Tabel 2: Overzicht van de voornaamste parameters die in de stromingsleer en het massatransport worden gebruikt. Door een combinatie van deze getallen kan men dimensieloze grootheden samenstellen die de verhouding van twee fysische fenomenen weergeven. (*L*, lengte-eenheid; *T*, tijdseenheid; *M*, massa-eenheid)

parameter	***symbool***	***dimensie***
karakteristieke lengte: hydraulische diameter	$4 \cdot R_h$	*L*
karakteristieke snelheid *in numero* analyse: *superficiële snelheid, U_s*	$U_s = \frac{Q}{A_f}$	*L/T*
karakteristieke snelheid *in vitro* analyse: *gemiddelde snelheid, U_m*	$U_m = \frac{Q}{\varepsilon \cdot A_f}$	*L/T*
dichtheid	ρ	M/L^3
dynamische viscositeit	μ	*M/L/T*
kinematische viscositeit	υ	L^2/T
drukval	Δp	$M/L/T^2$
diffusiecoëfficiënt	D_{O_2}	L^2/T
massatransportcoëfficiënt	K	*L/T*

waarin U de karakteristieke snelheid voorstelt, hetzij U_s voor de *in numero* modellering, hetzij U_m voor de *in vitro* analyse. Voor normaal bloed (Hct = 45 % en T = 37 °C waarvoor ρ = 1060 kg/m³ en μ = 3.76 mPa· s) met een debiet van 5 l/min ligt N_{Re} tussen 2.1 en 3.3 bij de meeste kunstlongen ($0.4 < \varepsilon < 0.6$), waarbij de superficiële snelheid, U_s, is gebruikt als karakteristieke snelheid (*in numero*). Wanneer de gemiddelde snelheid, U_m, als karakteristieke snelheid wordt gebruikt (*in vitro*) ligt N_{Re} tussen 4.7 en 5.5. Voor bloed met een hematocriet van 30 % en een temperatuur van 30 °C (ρ = 1052 kg/m³ en μ = 3.02 mPa· s) en met een debiet van 5 l/min ligt N_{Re} tussen 2.6 en 4.2 met U_s als karakteristieke snelheid en tussen 5.8 en 6.8 met U_m als karakteristieke snelheid. Voor water met een temperatuur van 20 °C (ρ = 998 kg/m³ en μ = 1.00 mPa· s) en een debiet van 5 l/min ligt N_{Re} tussen 7.4 en 12.2 (*in numero* analyse) en tussen 17.0 en 20.2 (*in vitro* analyse) met U_m als karakteristieke snelheid.

Het gebruik van de superficiële snelheid in het *in numero* model laat toe de verschillende vezelconfiguraties met elkaar te vergelijken op basis van eenzelfde snelheid.

Het Eulergetal, N_{Eu}, drukt de verhouding van de drukval tot de kinetische energie uit:

$$N_{Eu} = \frac{\Delta p}{\rho \cdot U^2} \qquad [31]$$

Het Schmidtgetal, N_{Sc}, is gedefinieerd als de verhouding van het momentum tot het diffusief transport en is een karakteristiek van massatransport voor de vloeistof zoals het Prandtlgetal, N_{Pr}, dat is in de warmtewisseling:

$$N_{Sc} = \frac{\mu}{\rho \cdot D_{O_2}} = \frac{\upsilon}{D_{O_2}} \qquad [32]$$

Wanneer zowel een convectief als diffusief massatransportproces tegelijkertijd plaatsvinden in de vloeistoffase, zal het fysische proces zich, afhankelijk van de relatieve invloed van beide fenomenen, eerder convectief, gemengd of diffusief gedragen. Dit kan nagegaan worden met behulp van het dimensieloze Pécletgetal, N_{Pe}. N_{Pe} is het product van N_{Re} met N_{Sc} en drukt de verhouding van de convectieve stroming tot het diffusief massatransport uit:

$$N_{Pe} = N_{Re} \cdot N_{Sc} = \frac{4 \cdot R_h \cdot U}{D_{O_2}} \qquad [33]$$

In analogie met de warmtewisseling kan voor het massatransport een Nusseltgetal of Sherwoodgetal, N_{Sh}, worden gedefinieerd. N_{Sh} drukt het relatief belang van het convectief transport tot het diffusief transport uit met betrekking tot het transport doorheen het membraan.

$$N_{Sh} = \frac{K \cdot 4 \cdot R_h}{D_{O_2}} \qquad [34]$$

4 Wetenschappelijke resultaten

Het experimenteel (*in vitro*) onderzoek concentreert zich enerzijds op de hydrodynamische weerstand van de kunstlong (§4.1.1) en anderzijds op het zuurstoftransport in de kunstlong (§4.2.1). Het heeft de bedoeling de ontwerpkarakteristieken voor de hydrodynamische weerstand en het zuurstoftransport in de kunstlong te beschrijven. Hiertoe is gebruik gemaakt van experimentele en numerieke modellering.

Als testfluïdum in de *in vitro*-opstellingen is meestal gebruik gemaakt van gedistilleerd water. Voor de validatie van het transportmodel zijn een aantal *in vitro* metingen met stollingsvrij runderbloed uitgevoerd. In tegenstelling tot bloed kan er bij water geen stolling optreden en is de viscositeit ook beduidend lager. Hierdoor treden er verschillen op in de fysische constanten van de gebruikte testfluïda. Dimensie-analyse en het gebruik van dimensieloze getallen, karakteristiek voor het beschouwde probleem, moeten er dan voor zorgen dat de bereikte resultaten conform het gebruikte fluïdum zijn.

Daarnaast is er een numeriek tweedimensionaal model ontwikkeld dat toelaat de stroming (§4.1.2) en het zuurstoftransport (§4.2.2) rond een enkele vezel in het membraancompartiment in

detail te modelleren. De resultaten bekomen uit dit model kunnen geïntegreerd worden in een volledig membraancompartiment. De aldus verkregen resultaten kan men dan vergelijken met die resultaten, die proefondervindelijk bij bestaande kunstlongen werden vastgesteld.
De resultaten van de experimentele en numerieke modellering zijn geanalyseerd voor drie commercieel beschikbare kunstlongen.
In eerste instantie zijn de hydrodynamische karakteristieken bestudeerd (§4.1). Vervolgens zijn met behulp van het numerieke model <36> deze karakteristieken gesimuleerd en vergeleken met de gemeten waarden. Tenslotte zijn een aantal metingen uitgevoerd met water en bloed als testfluïdum om de efficiëntie van het zuurstoftransport te begroten met behulp van eendimensionale semi-empirische modellen voor permanente stroming <3>. Deze studie heeft geleid tot het opstellen van een unieke relatie voor de hydrodynamische weerstand van een kunstlong en haar geometrische karakteristieken <34,37>.
In een tweede fase is voor de drie bestudeerde kunstlongen een unieke relatie voor het zuurstoftransport in functie van de geometrische kenmerken van de kunstlong opgesteld (§4.2). Het zuurstoftransport is eveneens gemodelleerd in het numerieke model en de resultaten voor water zijn vergeleken met de metingen. Simulaties met bloed laten toe de bloedpadlengte te bepalen die nodig is om het bloed voldoende te satureren.
Het derde en laatste deel bespreekt de ontluchtingskarakteristieken van pediatrische <38> kunstlongen (§4.3). Het ontwerp en de wijze van doorstroming doorheen de kunstlong kan namelijk een rol spelen als men het ontstaan van gasvormige microemboli (GME) (E: “gaseous microemboli”) of kleine gasbellen wil vermijden. Een goed inzicht in enerzijds de risico’s die tot GME leiden en anderzijds de mogelijkheid tot het verwijderen van GME, is noodzakelijk om een minimale luchtintrede in het extracorporele circuit te bekomen en om de patiënt maximaal te beschermen.

4.1 Hydrodynamica van een kunstlong

Een deel van het onderzoek bestaat er in een zo efficiënt mogelijke doorstroming van de kunstlong te realiseren. Dit wil zeggen dat er wordt gestreefd naar een grote bloeddoorstroming, gecombineerd met een aangepaste drukval. De drukval over de kunstlong treedt op over de warmtewisselaar en het membraancompartiment. In het membraancompartiment is de drukval een functie van twee parameterreeksen. Een eerste reeks parameters wordt gegeven door de geometrische afmetingen van het membraan die bepalend zijn voor de drukval bij een gegeven debiet: de diameter van de holle vezels, de afstand tussen de vezels in verschillende richtingen, de richting waarin het membraan wordt doorstroomd en de lengte van het stroompad

(bloedpadlengte). Belangrijk is op te merken dat het bloed in kruisstroming met de vezels door het membraan stroomt. De tweede reeks parameters die de drukval bepaalt, is verbonden met de gelijkmatigheid van de instroming. Dit laatste aspect is niet bestudeerd in dit proefschrift.

4.1.1 Experimentele bepaling van de druk-debietrelatie

4.1.1.1 Meetopstelling water en bloed

Om een idee te verkrijgen van de hydrodynamica in de kunstlong, is het nodig het debiet en de drukken aan de in- en uitlaat van de warmtewisselaar en membraancompartiment te meten. Het grootste drukverschil over de kunstlong situeert zich in het membraancompartiment. Deze drukval is een functie van enerzijds de porositeit en anderzijds de karakteristieke lengte van de kunstlong.

Een experimentele meetopstelling is gerealiseerd om druk-debietrelaties *in vitro* vast te leggen bij permanente stroming (Figuur 9). Permanente stroming vindt plaats onder invloed van de zwaartekracht vanuit een opwaarts reservoir met overlaat, zodat een constante opwaartse druk gerealiseerd wordt. Een afwaarts reservoir met overlaat zorgt voor een tegendruk van 150 mmHg aan de uitlaat van de kunstlong bij een debiet van 2 l/min. De tegendruk vermijdt het aanzuigen van lucht door het membraan ten gevolge van een onderdruk aan de vloeistofzijde in het membraancompartiment. Het afwaarts reservoir doet dienst als nabelasting.

De reservoirs zijn door middel van een normale perfusiedarm (3/8 inch) verbonden met de kunstlong. Het debiet wordt geregeld door middel van een kraan en verloopt gradueel van 0 l/min tot een maximum debiet van 6 l/min om vervolgens te dalen tot 0 l/min. Het debiet wordt gemeten met behulp van een ultrasone debietmeter die volumetrisch is geijkt. De druk opwaarts, de druk tussen de warmtewisselaar en het membraancompartiment, en de druk afwaarts van de kunstlong worden simultaan gemeten met medische druksensoren. Voor en na elke meting worden de druksensoren gekalibreerd. De stromingsweerstand wordt dan bepaald bij verschillende debieten (0 – 6 l/min). Na gebruik worden de kunstlongen gedroogd met perslucht om de hydrodynamische eigenschappen te bewaren.

In totaal zijn 3 types kunstlongen getest (Sarns Turbo 440, Cobe Optima, en Dideco Compactflo) met minstens twee longen per type en drie onafhankelijke metingen per long.

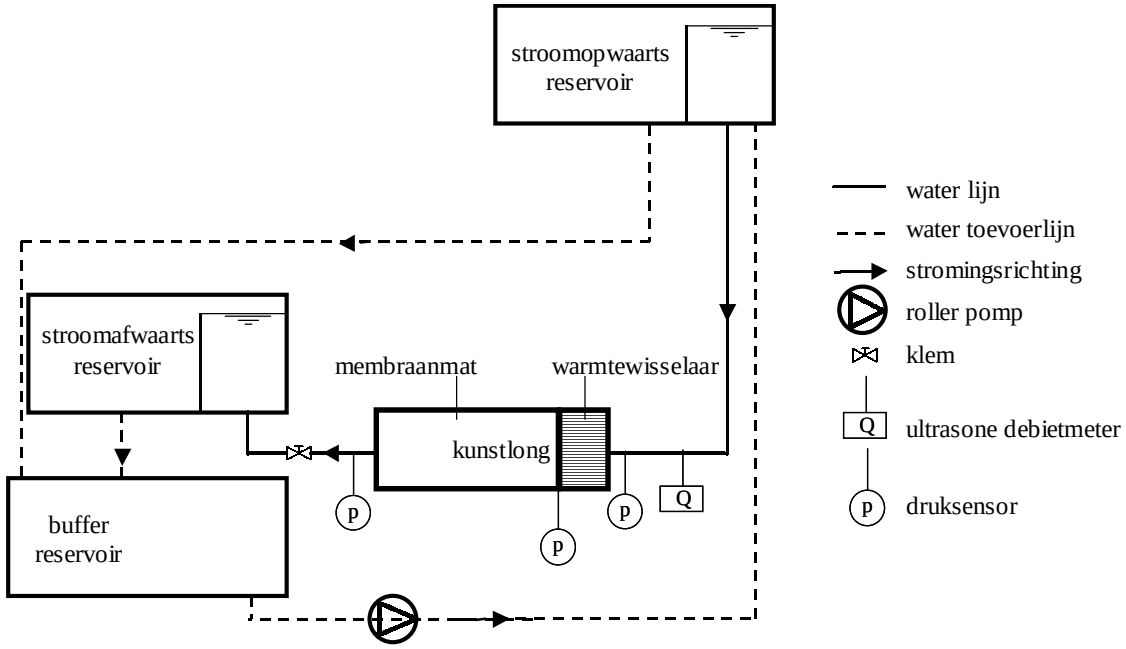

Figuur 9: Schematische voorstelling van de experimentele opstelling (*in vitro*) voor het bepalen van de druk-debietrelatie in een kunstlong bij permanente stroming. Vloeistofgevulde piëzoresistieve druksensoren worden geplaatst aan de inlaat, tussen het membraancompartiment en de warmtewisselaar en aan de uitlaat van de kunstlong. Een klem laat toe het debiet te moduleren. Een ultrasone debietmeter begroot het debiet. Een rollerpomp wordt gebruikt om de vloeistof vanuit het bufferreservoir naar het opwaartse reservoir te pompen. Pijlen duiden de stromingsrichting aan.

4.1.1.2 Resultaten

Figuur 10 toont de druk-debietrelaties voor de drie kunstlongen met water als fluïdum, gemeten over zowel het membraancompartiment als de warmtewisselaar. Men herkent hierin een parabolisch verloop van de drukval in functie van het debiet:

$$\Delta p = a' \cdot Q^2 + b' \cdot Q \qquad [35]$$

De verschillen tussen de druk-debietrelaties van de kunstlongen kunnen worden toegeschreven aan de onderlinge verschillen in constructie van de warmtewisselaar, het membraancompartiment of een combinatie van beide. Sarns Turbo 440 en Cobe Optima geven vergelijkbare hoge drukvallen over de gehele kunstlong terwijl Cobe Optima en Dideco Compactflo een vergelijkbare drukval hebben over de warmtewisselaar. Figuur 10 toont aan dat het grootste deel van de drukval over de kunstlong kan worden toegeschreven aan het membraancompartiment. Dit is vrij logisch aangezien het membraancompartiment een lagere porositeit bevat, een langer bloedpad en een minder gestroomlijnde doorstroming dan de warmtewisselaar. Sarns Turbo 440 vertoont de laagste drukval in de warmtewisselaar.

Figuur 11 (boven) geeft de druk-debietrelatie met water als fluïdum voor het membraancompartiment in de drie kunstlongen weer. Met behulp van de

gelijkvormigheidsanalyse kan de druk-debietrelatie voor water worden omgezet in een N_{Eu}-N_{Re} relatie (Figuur 11, middenste paneel):

$$N_{Sh} = \alpha' + \frac{\beta'}{N_{Re}} \qquad [36]$$

waarin N_{Re} en N_{Eu} zijn berekend op basis van de gemiddelde snelheid, U_m, doorheen het membraancompartiment. α' en β' zijn voor de drie kunstlongen gegeven in Tabel 3.

Rekening houdend met de geometrische kenmerken van de drie kunstlongen in Tabel 1 kan men een verband tussen de parameters (α' en β') en de geometrische kenmerken (porositeit, ε, en dimensieloze karakteristieke lengte, ξ) van de kunstlongen opstellen (Figuur 13). Aldus bekomt men een unieke relatie voor N_{Eu} en N_{Re} in functie van ε en ξ (Figuur 11, onderste paneel):

$$N_{Eu} \cdot \frac{\xi}{\varepsilon^2} = \alpha + \frac{\beta}{N_{Re} \cdot \varepsilon \cdot (1-\varepsilon)} \qquad [37]$$

met $\alpha = 2365 \pm 52$ en $\beta = 8509 \pm 25$.

De unieke relatie in vgl. [37] kan vervolgens worden aangewend om de druk-debietrelatie van het membraancompartiment in een kunstlong te bepalen en te vergelijken met de meetresultaten (Figuur 12).

De druk-debietrelaties voor de gehele kunstlong, zoals bekomen met water en met runderbloed, worden met elkaar vergeleken door de theorie van de dynamische gelijkvormigheid (§3.7) toe te passen. Dit laat toe de resultaten bekomen met water om te rekenen naar bloed.

Voor een gegeven druk-debietrelatie water, $(\Delta p)_w - Q_w$, met dichtheid ρ_w en viscositeit μ_w, kan men bijhorende $(N_{Re})_w$ en $(N_{Eu})_w$ berekenen. Indien men bloed beschouwt met dichtheid ρ_b en viscositeit μ_b (functie van hematocriet en temperatuur), kan men - door gelijkstellen van $(N_{Re})_b$ aan $(N_{Re})_w$, respectievelijk $(N_{Eu})_b$ aan $(N_{Eu})_w$ - bijhorend debiet, Q_b, en drukval, $(\Delta p)_b$, voor bloed berekenen.

Het resultaat van een dergelijke omrekening voor bloed met een hematocriet van 34.9 ± 1.3 % en een temperatuur van 36.7 ± 0.8 °C is weergegeven in Figuur 14. Uit Figuur 14 blijkt dat de omrekening van water naar bloed het drukverloop voor bloed onderschat. Dit kan worden toegeschreven aan het feit dat de viscositeit van het bloed in de experimenten niet gemeten is, maar berekend is op basis van vgl. [2]. Onderzoek heeft aangetoond dat de berekende viscositeit de werkelijke viscositeit overschat <39>.

Voor bloeddebieten tussen 3 en 5 l/min bedraagt de afwijking maximaal 10 % voor de Sarns Turbo 440 en Cobe Optima. De grote afwijking voor Dideco Compactflo kan worden toegeschreven aan de grote spreiding tussen de kunstlongen onderling, zoals uit Figuur 10 (boven) kan worden afgeleid.

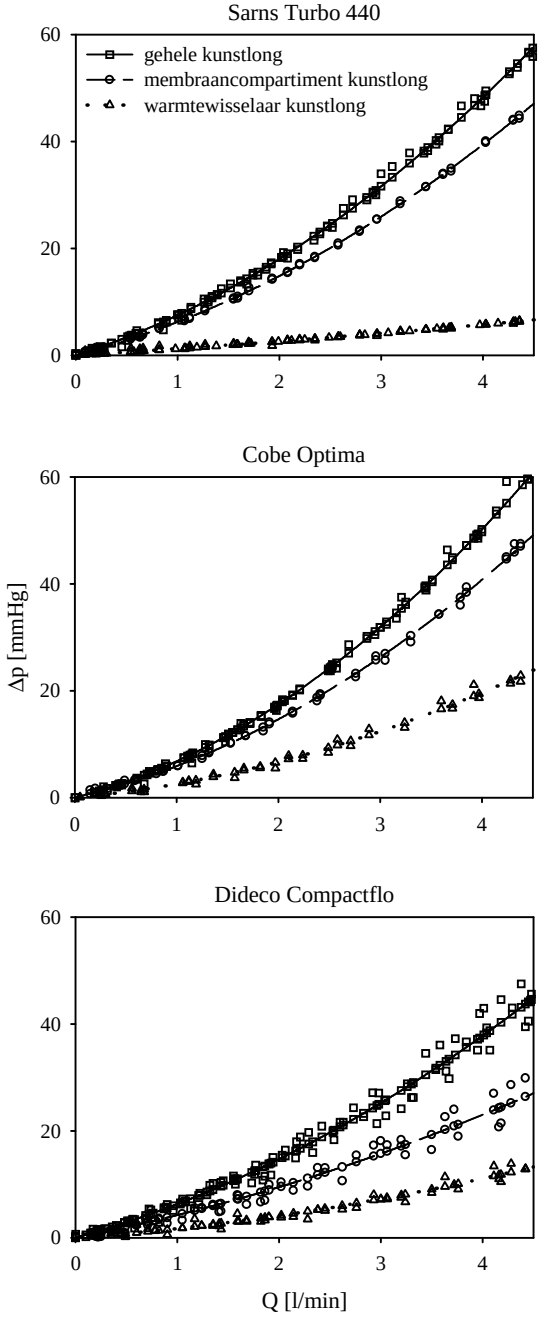

Figuur 10: Gemeten druk-debietrelaties voor de drie commercieel beschikbare kunstlongen met water als fluïdum. **Boven:** Sarns Turbo 440; **Midden:** Cobe Optima; **Onder:** Dideco Compactflo. De druk-debietrelaties voor het membraancompartiment, de warmtewisselaar en de kunstlong in zijn geheel zijn weergegeven.

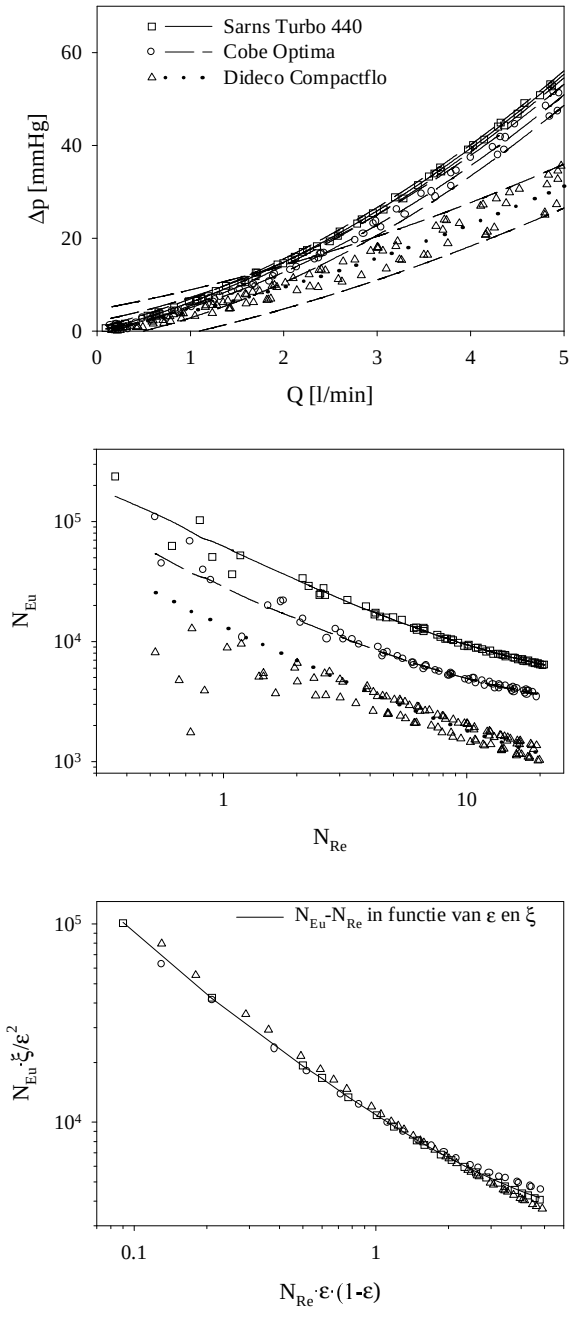

Figuur 11: Voor de drie kunstlongen Sarns Turbo 440, Cobe Optima en Dideco Compactflo zijn de volgende figuren weergegeven: **Boven:** Druk-debietrelaties met betrouwbaarheidsintervallen voor het membraancompartiment met water als fluïdum; **Midden:** N_{Eu}-N_{Re} voor het membraancompartiment op basis van voormelde druk-debietrelatie; **Onder:** Unieke N_{Eu}-N_{Re} relatie in functie van porositeit en dimensieloze karakteristieke lengte.

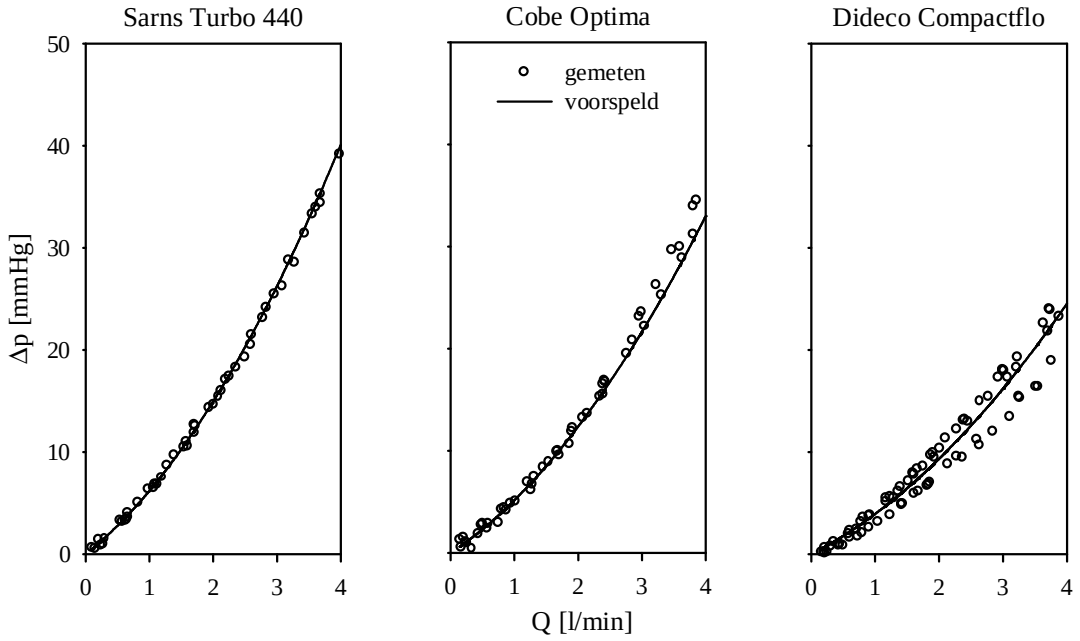

Figuur 12: Vergelijking tussen de berekende en gemeten druk-debietrelaties voor het membraancompartiment in de drie kunstlongen met water als fluïdum. **Boven:** Sarns Turbo; **Midden:** Cobe Optima; **Onder:** Dideco Compactflo.

4.1.2 Numerieke modellering van de hemodynamica in het membraancompartiment van een kunstlong

4.1.2.1 Tweedimensionaal stromingsmodel

In (§3.6.2) is reeds aangehaald dat het membraancompartiment van de kunstlong is opgebouwd uit duizenden holle vezels die tot een structuur zijn samengeweven. Indien men enerzijds de invloed op de stroming van de inlaat, de uitlaat en de wand van het membraancompartiment verwaarloost en anderzijds een volledig ontwikkelde, tweedimensionale, constante stroming doorheen het membraancompartiment veronderstelt, kan men ervan uitgaan dat de stroming volledig ontwikkeld en periodiek is. Het membraancompartiment kan dan worden onderverdeeld

Tabel 3: Model parameters α' en β' uit vgl. [36] voor de drie kunstlongen.

	Sarns Turbo 440	***Cobe Optima***	***Dideco Compactflo***
model parameter α'	3686	2076	514
model parameter β'	57450	22050	12930

in een (groot) aantal eenheidscellen die elk één enkele vezel bevatten.

Een vezelbundel kan worden gekenmerkt door de transversale, S_T/d, en longitudinale, S_L/d, afstand (S) tot diameter (d) verhouding (Figuur 7).

Als gevolg van het periodiek karakter van de vezelbundel zullen de stromingsparameters, met name de snelheid en de drukval, een typisch periodiek patroon vertonen [40,41] en volstaat het de stroming in een eenheidscel (Figuur 15) te berekenen. Symmetrie-randvoorwaarden, Γ_{sym}, worden opgelegd op de symmetrie-assen terwijl de snelheid aan de oppervlakte van de vezel nul is. Doordat de snelheidsverdeling (maar niet het drukverloop noch de verdeling van de

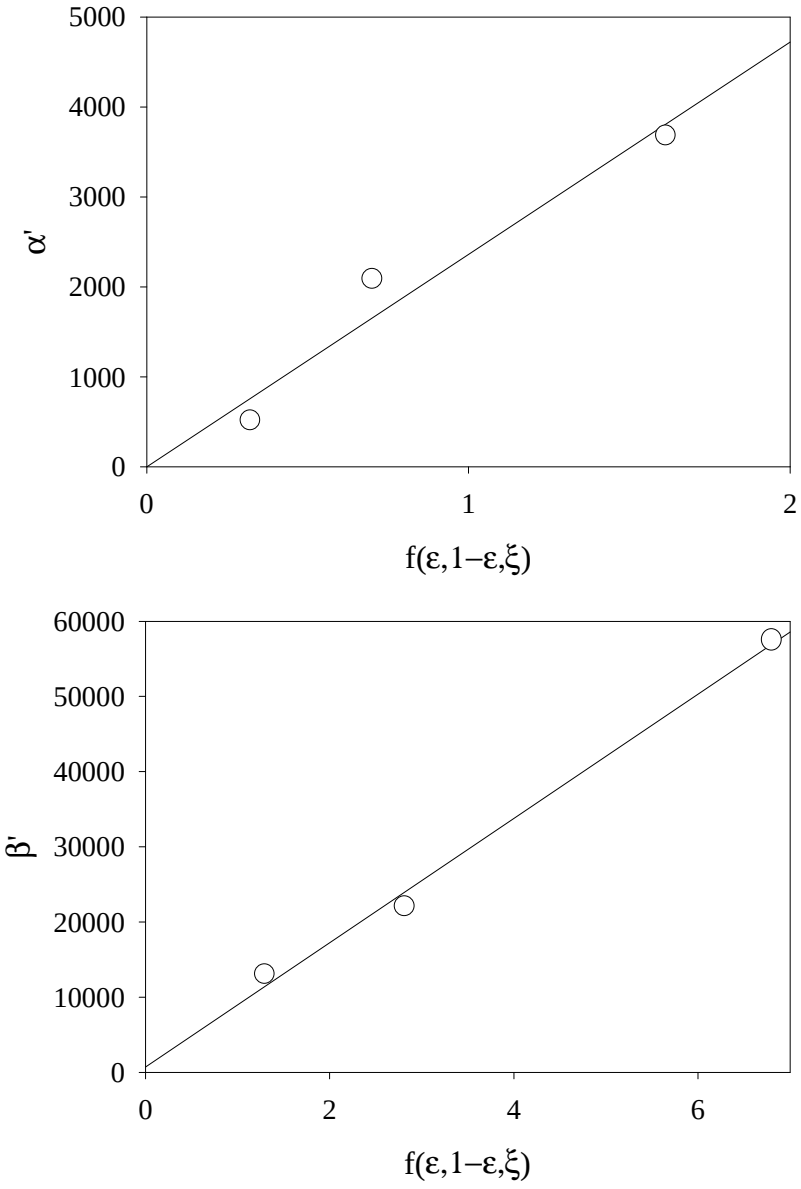

Figuur 13: Parameters α' (**boven**) en β' (**onder**) in functie van porositeit, ε, en dimensieloze karakteristieke lengte, ξ. De volle lijn duidt de gefitte relatie aan, (o) de punten uit Tabel 3.

zuurstofpartieeldruk) in alle eenheidscellen identiek is, kunnen periodieke randvoorwaarden, Γ_{per}, aan de ingang en uitgang van de eenheidscel worden aangewend <41> (Figuur 15). De periodieke randvoorwaarden leggen zowel de instroom- als uitstroomrandvoorwaarden vast. Symmetrisch periodieke randvoorwaarden kunnen in SEPRAN enkel worden geïmplementeerd door het invoeren van een gegeven (instroom)debiet, q, per eenheidslengte <31,41>. Dit debiet is afgeleid uit de lokale superficiële instroomsnelheid, U_s, die is berekend uit de doorstromingsoppervlakte van het membraancompartiment en het gemodelleerde instroomdebiet van de kunstlong:

$$q = U_s \cdot S_T \qquad [38]$$

Deze (extra) randvoorwaarde laat toe de drukval te berekenen. Het instroomdebiet in dit rekendomein kan berekend worden uitgaande van het instroomdebiet in de kunstlong en enkele onderstellingen die hierna worden opgesomd:

- een gelijkmatige, uniforme instroming via het instroomkanaal. Het bloed wordt aan de ingang van de kunstlong axiaal en radiaal uniform verdeeld over de vezelbundel. Doorheen elke eenheidscel stroomt dan eenzelfde debiet.
- alle vezels hebben dezelfde geometrie, ze zijn recht en evenwijdig. De parallelle

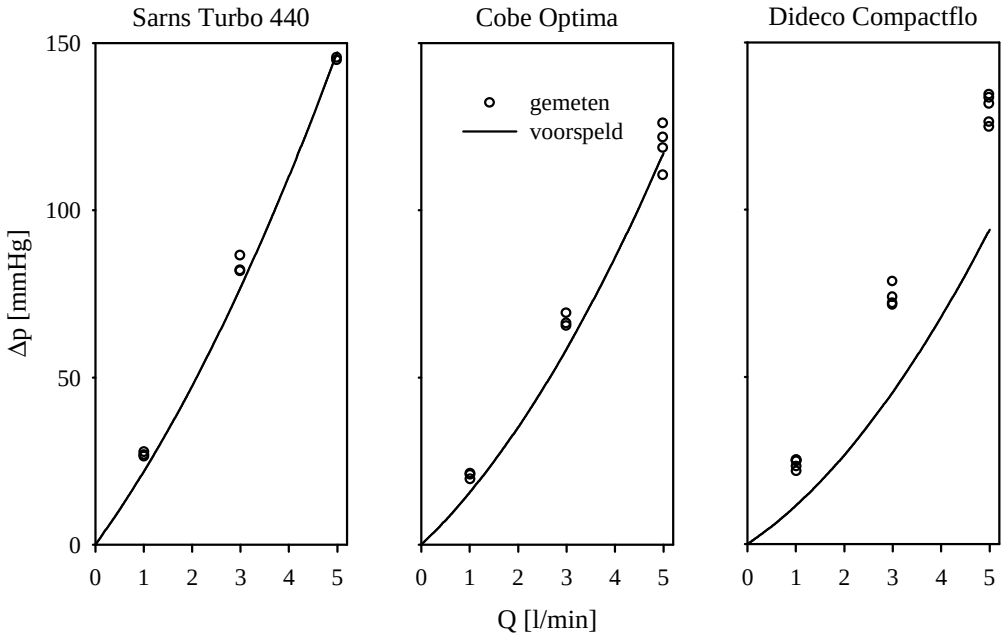

Figuur 14: Vergelijking tussen de voorspelde en gemeten druk-debietrelaties van de gehele kunstlong voor de drie kunstlongen met bloed als fluïdum op basis van de gelijkvormigheidsnalayse (N_{Eu}-N_{Re} relatie). **Boven:** Sarns Turbo; **Midden:** Cobe Optima; **Onder:** Dideco Compactflo.

schikking van de vezels vereenvoudigt sterk de geometrie.

- de vezels zijn gerangschikt volgens een regelmatig patroon en staan op regelmatige afstand van elkaar. De afstand in de longitudinale en dwarsrichting in elke eenheidscel is identiek zodat de radiale effecten op de bloedstroming worden verwaarloosd.

De beschrijving van stromingsfenomenen in het microscopisch model is gebaseerd op een combinatie van de continuïteitsvergelijking en de Navier-Stokes vergelijkingen (§3.5.1).

Door het gebruik van eindige elementenmethoden (SEPRAN) kan de geometrie naar willekeur uitgetest en aangepast worden. Vanwege het complexe karakter van de configuratie is het eindige elementenrooster niet gestructureerd. Door slechts één parameter tegelijkertijd te variëren, verkrijgt men inzicht in het aandeel en de invloed van deze parameter op de membraanstroming. Voor elk van deze gevallen worden dan druk en snelheid berekend. Het lokale Reynoldsgetal kan gebruikt worden om het bloeddebiet te karakteriseren:

$$N_{Re} = \frac{4 \cdot R_h \cdot U_s \cdot \rho}{\mu_\infty} \qquad [39]$$

Omwille van de specifieke stroming tussen de vezels, moet ook rekening gehouden worden met

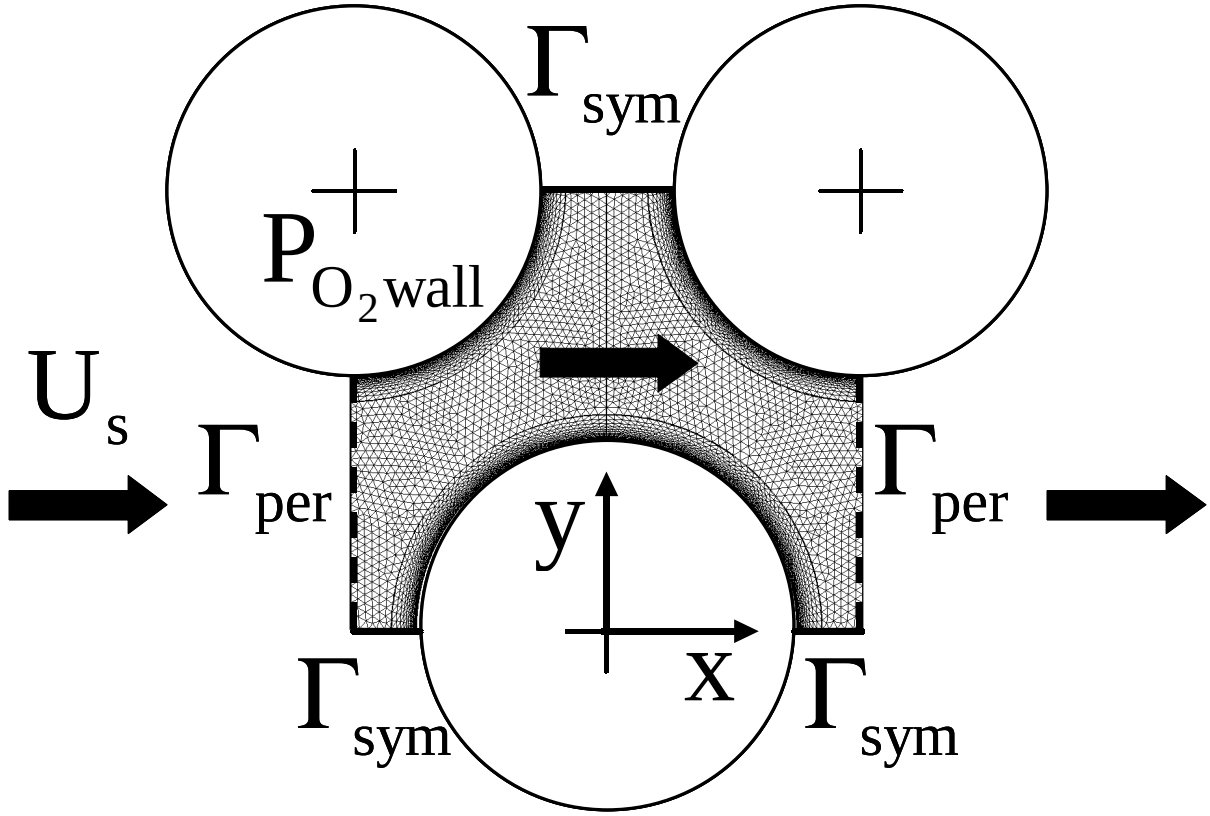

Figuur 15: Schematische voorstelling van een eenheidscel met bijhorend eindige elementenrooster. Γ_{sym} stelt de symmetrie-randvoorwaarde voor en Γ_{per} de periodieke randvoorwaarde. x duidt de stromingsrichting aan en y de afstand vanaf het centrum van de vezel loodrecht op de stroming.

de vormweerstand tegen stroming van de vezelbank en de resulterende weerstandskrachten. Hiertoe wordt een dimensieloze wrijvingsfactor, f, gedefinieerd:

$$f = \frac{\Delta p}{\rho \cdot U_s^2} \cdot \frac{4 \cdot R_h}{S_L} \qquad [40]$$

In het numeriek stromingsmodel is rekening gehouden met de rheologische kenmerken van bloed: het pseudoplastisch karakter en de verhoogde dynamische viscositeit zijn door middel van een Casson viscositeitsmodel in de berekeningen ingebracht. Simulaties zijn uitgevoerd met zowel een newtoniaanse als niet-newtoniaanse Casson bloedviscositeit om de invloed van het niet-newtoniaans karakter te bestuderen.

Vertrekkende van een tweedimensionale eenheidscel kan na een integratie in de stromingsrichting (x-richting) en na transversale extrapolatie een membraancompartiment worden geconstrueerd dat het membraancompartiment van de kunstlong benadert, rekening houdend met de geometrische kenmerken van de betreffende kunstlong (bloedpadlengte, vezellengte, dikte van het membraancompartiment, …) (§3.6.2). Aangezien in dit proefschrift drie verschillende vezelconfiguraties zijn bestudeerd, wordt het gemiddelde van het resultaat van de extrapolatie voor elk van de drie vezelconfiguraties genomen als benadering van de vezelmat van een commerciële kunstlong.

4.1.2.2 Resultaten

De invloed en het gedrag van lokale secundaire stromingen op de stroming en het zuurstoftransport onder verschillende fysiologische stromings- en randvoorwaarden die kunnen voorkomen in de klinische praktijk zijn bestudeerd. Deze lokale secundaire stromingen hebben een invloed op de ladingsverliezen en de globale efficiëntie en kunnen tegelijkertijd de hemocompatibiliteit negatief beïnvloeden.

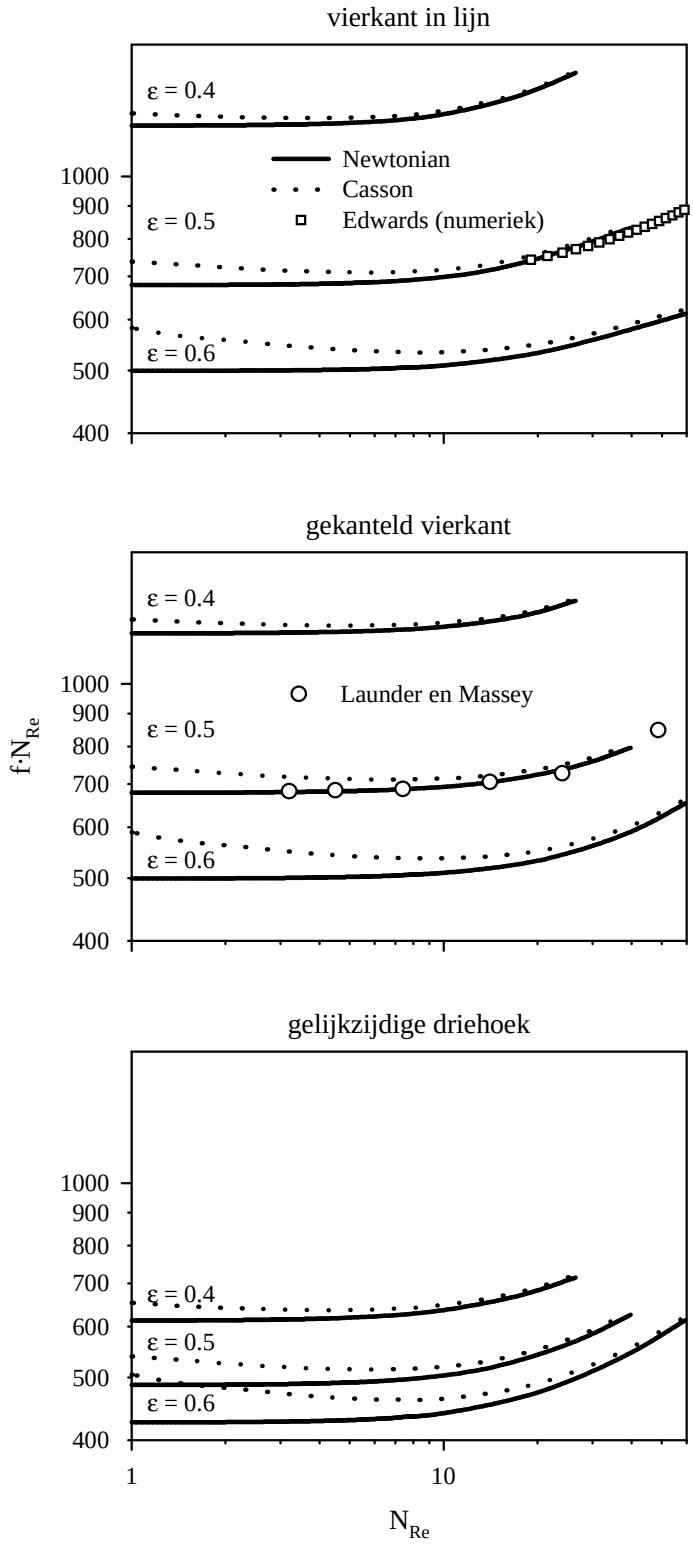

Figuur 16: De wrijvingsfactor, f, vermenigvuldigd met N_{Re}, versus N_{Re} in een bilogaritmische figuur voor zowel newtoniaanse als niet-newtoniaanse bloedstroming in de drie vezelconfiguraties. **Boven:** vierkant in lijn; **Midden:** gekanteld vierkant; **Onder:** gelijkzijdige driehoek. De resultaten zijn vergeleken met gepubliceerde numerieke en experimentele resultaten [42,43].

Het lokale Reynoldsgetal wordt gebruikt om het bloeddebiet te karakteriseren. Bij een hoger Reynoldsgetal zullen de inertiekrachten steeds meer aan invloed winnen ten opzichte van de wrijvingskrachten. Het lokale stromingsprofiel rond een holle vezel wijzigt dan ook (Figuur 17). Meer concreet laat de randlaag vroeger los van de vezel, wat gepaard gaat met een recirculatiezone of secundaire stromingen. Omwille van de specifieke stroming tussen de vezels, kan rekening gehouden worden met de vormweerstand van de vezelbank (Figuur 16). Figuur 16 toont aan dat er een goede overeenkomst is met gepubliceerde numerieke resultaten <42,43>. Voor een gegeven Reynoldsgetal en porositeit, vertoont de configuratie van de gelijkzijdige driehoek duidelijk een kleinere weerstand dan de twee andere configuraties. Een daling van de porositeit houdt ook een meer dan proportionele toename van de weerstand in vanaf $\varepsilon < 0.5$.

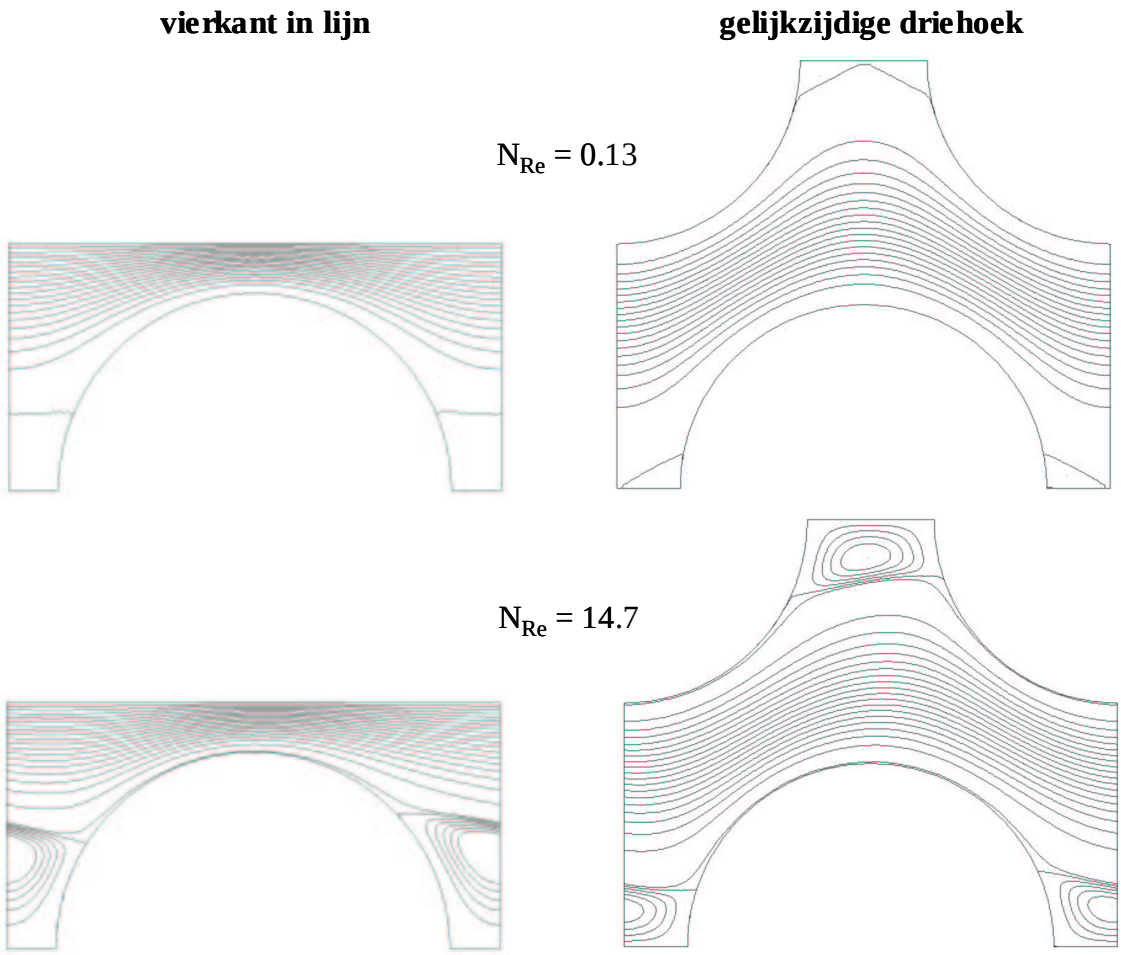

Figuur 17: Stroomlijnenpatroon voor een newtonianse bloedstroming (temperatuur 30 °C en hematocriet 30 %) voor twee vezelconfiguraties bij twee Reynoldsgetallen. **Links:** vierkant in lijn; **Rechts:** gelijkzijdige driehoek; **Boven:** N_{Re} = 0.13; **Onder:** N_{Re} = 14.7. De invloed van N_{Re} op secundaire stromingen is duidelijk.

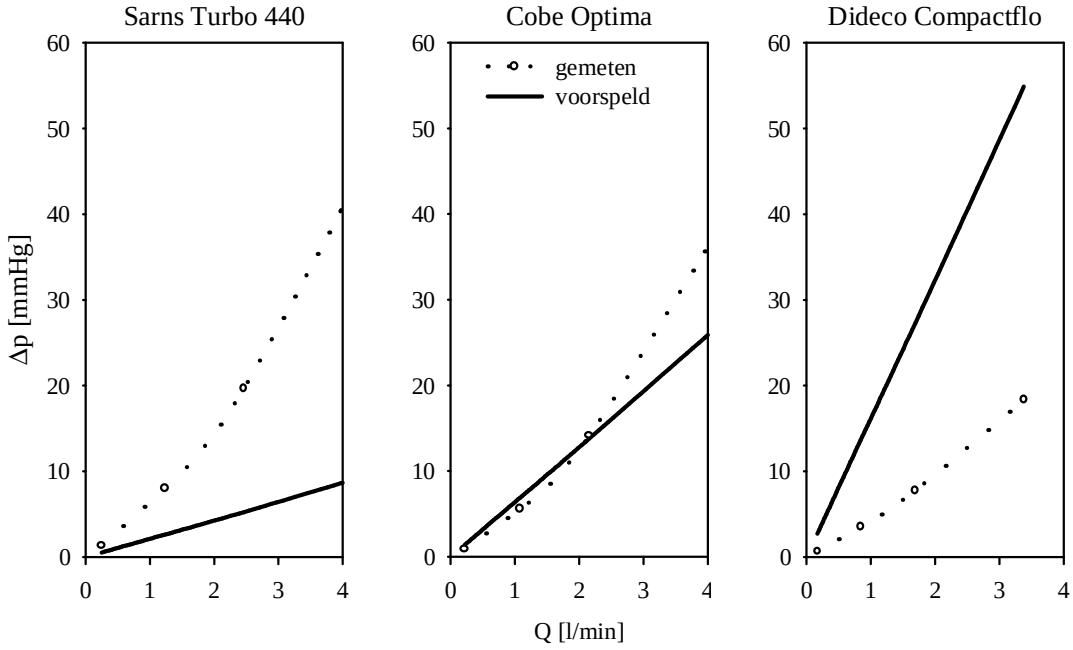

Figuur 18: Deze figuur toont voor de drie kunstlongen de gemeten druk-debietrelatie versus de druk-debietrelatie die is berekend door extrapolatie van de drukval in een eenheidscel tot de drukval in een gelijkvormig membraancompartiment. **Boven:** Sarns Turbo 440; **Midden:** Cobe Optima; **Onder:** Dideco Compactflo.

De kennis verkregen uit het berekende stromingsveld is van belang om het lokale massatransport te kunnen bestuderen.

De invloed van het niet-newtoniaanse karakter op de stromingsweerstand laat zich voelen bij lage Reynoldsgetallen ($N_{Re} < 10$) (Figuur 16). Bij hogere Reynoldsgetallen is het verschil tussen bloed gemodelleerd met een newtoniaanse en een niet-newtoniaanse Casson viscositeit nagenoeg nihil door de hoge afschuifsnelheden die bij hoge Reynoldsgetallen optreden.

Bij de vergelijking van de extrapolatie van de resultaten van het numerieke model met experimentele metingen in de drie kunstlongen is er een discrepantie in het ladingsverlies (Figuur 18). Enerzijds komt in de gemeten druk-debietrelatie duidelijk de invloed van speciale ladingsverliezen in het membraancompartiment (ingang, uitgang, niet uniforme stroomverdeling, cilindervormig membraancompartiment, randeffecten, …) naar voor. Deze ladingsverliezen zijn niet in het tweedimensionale numerieke stromingsmodel geïmplementeerd. Anderzijds houdt een afname van de porositeit een meer dan proportionele toename van de weerstand in vanaf $\varepsilon < 0.5$. Dit kan de sterke overschatting van de druk-debietrelatie in Dideco Compactflo ($\varepsilon = 0.44$) verklaren.

Figuren met representatieve *in numero* resultaten van de hemodynamica in verschillende vezelconfiguraties zijn samengebracht in de appendix.

4.1.3 Besluit

Een numeriek tweedimensionaal model is opgesteld dat toelaat de stroming rond één enkele vezel in het membraancompartiment van een kunstlong te modelleren voor verschillende vezelconfiguraties. Zowel de stroming als de weerstand zijn bestudeerd. Bij de vergelijking van de resultaten van het numerieke model met experimentele metingen in de kunstlong is er een discrepantie in het gemeten en berekende ladingsverlies. In de gemeten druk-debietrelatie komt de invloed van speciale ladingsverliezen in het membraancompartiment (ingang, uitgang, niet uniforme stroomverdeling, cilindervormig membraancompartiment, randeffecten, …) tot uiting die niet in het tweedimensionale numerieke stromingsmodel zijn geïmplementeerd.
De experimentele analyse van de stromingsweerstand in het membraancompartiment van de kunstlong leidt tot het opstellen van unieke relaties voor de stromingsweerstand in een kunstlong. Eveneens is aangetoond dat toepassing van gelijkvormigheidsanalyse toelaat de resultaten bekomen met water om te rekenen naar stroming met bloed. Deze resulaten kunnen aangewend worden voor een optimaal hydrodynamisch ontwerp van nieuwe kunstlongen.

4.2 Massatransportkarakteristieken

Eén van de doelstellingen van het proefschrift is het zuurstoftransport in het membraancompartiment van een kunstlong enerzijds numeriek (“*in numero*”) te modelleren en anderzijds experimenteel (“*in vitro*”) te bepalen. De efficiëntie van het zuurstoftransport is begroot met behulp van een eendimensionaal semi-empirisch model voor permanente stroming. De experimentele resultaten voor het zuurstoftransport bekomen met water worden dan omgerekend naar bloed en vergeleken met gemeten data. In analogie met de hydrodynamica van de kunstlong is een unieke relatie voor het zuurstoftransport in functie van de geometrische kenmerken van de kunstlong opgesteld. Het zuurstoftransport is eveneens gemodelleerd in het numerieke model en de simulaties voor water zijn vergeleken met de *in vitro* metingen. Simulaties met bloed stellen ons in staat de bloedpadlengte te bepalen die nodig is om het bloed voldoende te satureren.

4.2.1 Experimentele bepaling van het zuurstoftransport

4.2.1.1 Meetopstelling

Om de efficiëntie van het zuurstoftransport in de kunstlong te begroten, is het nodig het debiet en het zuurstofmassadebiet doorheen de kunstlong te kennen. Het zuurstoftransport is functie van de diffusiecoëfficiënt, de permeabiliteit (porositeit) van het membraan en de drijvende kracht (de aangewende partieeldrukken) <44>.

Een experimentele testopstelling is gerealiseerd om het zuurstofmassadebiet in de kunstlong te begroten. De metingen zijn uitgevoerd bij verschillende debieten en inlaatsaturaties. De uitvoering van de efficiëntiemetingen bestaat uit twee fazen. In een eerste fase dient het testfluïdum tot de gewenste zuurstofconcentratie te worden gebracht alvorens de eigenlijke test (tweede fase) uit te voeren. Hierbij is het testcircuit aanvankelijk afgesloten. Nadat de nodige ingangsvoorwaarden zijn bereikt, wordt het conditioneringscircuit afgesloten en het testcircuit aangesloten. Het testcircuit is gelijkaardig aan het circuit dat gebruikt wordt voor de meting van de stroomtechnische parameters (Figuur 9), met dit verschil dat aan de in- en uitlaat van de kunstlong voorzieningen zijn getroffen om de nodige gas- en temperatuurmetingen te realiseren. Daarnaast wordt ook gebruik gemaakt van een rollerpomp om het fluïdum doorheen het circuit te laten stromen (Figuur 19). Het niet-permanente karakter van deze stroming kan in de verdere analyse worden verwaarloosd. Het debiet van de rollerpomp is onafhankelijk van de nabelasting en kan typisch bepaald worden door het aantal omwentelingen te vermenigvuldigen met het slagvolume dat zich tussen de rollers bevindt. Ook de barometerdruk, het gasdebiet, het bloeddebiet en de drukken aan de in- en uitlaat van de kunstlong worden gemeten.

Met water als testfluïdum wordt het gedistilleerd water in het conditioneringscircuit zuurstofarm gemaakt door twee conditioneringskunstlongen met zuiver stikstof, N_2 (100 % N_2) te doorblazen. Stikstof is een inert gas met betrekking tot de oplosbaarheid in water en bloed <4,32>. Eenmaal de gewenste ingangsvoorwaarden zijn bereikt, wordt het zuurstofarme water doorheen het testcircuit gepompt waarbij de testlong wordt doorblazen met perslucht (21 % O_2). Aldus wordt het water beademd en eventueel verzadigd met zuurstof.

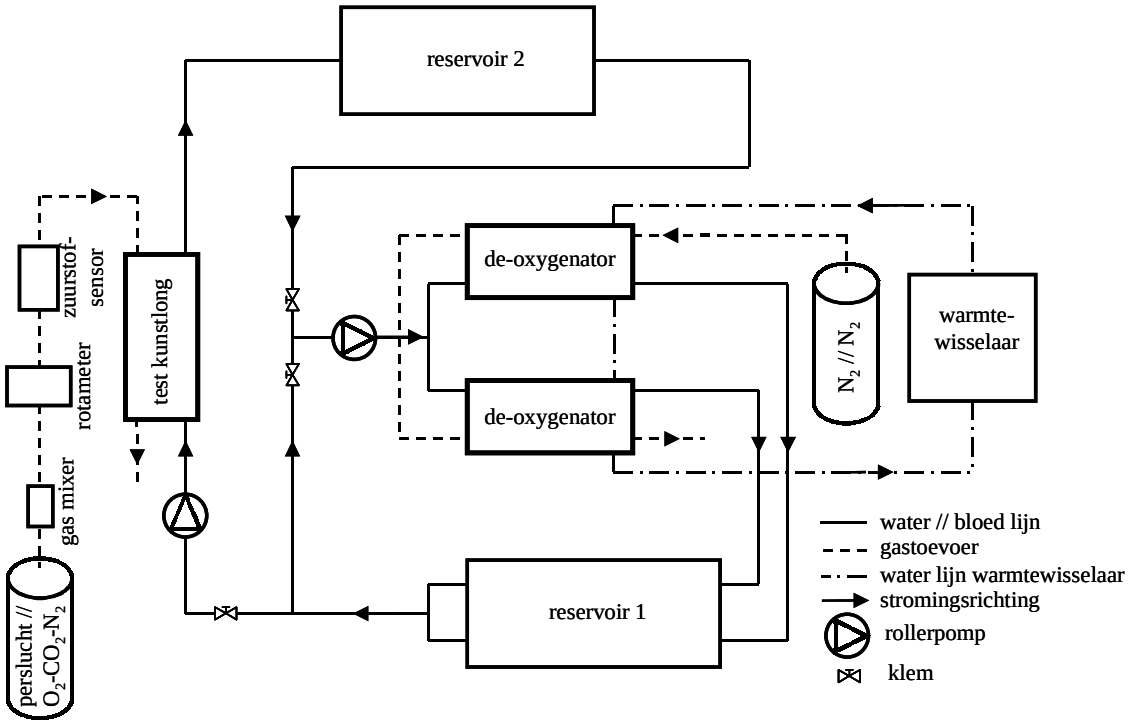

Figuur 19: Schematische voorstelling van de *in vitro*-opstelling voor het bepalen van het zuurstofmassadebiet in de kunstlong. Stikstof (N_2) wordt gebruikt om het fluïdum te deoxygeneren. Een warmtewisselaar houdt het fluïdum op de nodige temperatuur. Twee klemmen zorgen voor de omschakeling tussen het conditioneringscircuit (met twee kunstlongen) en het testcircuit (met de te testen kunstlong). De rollerpompen zorgen voor de nodige doorstroming van beide circuits. Pijlen duiden de stromingsrichting aan.

Bloed wordt in het conditioneringscircuit zuurstofarm (P_{O_2} = 25 ± 2 mmHg) gemaakt met perslucht en in het testcircuit beademd met zuivere zuurstof (100 % O_2). *In vitro* testen met bloed zijn uitgevoerd onder de AAMI standaard [45]. Bij bloedtesten dient men rekening te houden met de bloedparameters die een invloed uitoefenen op de saturatie van het bloed. Deze bloedparameters zijn: de zuurtegraad (pH), de zuurstofpartieeldruk, de koolstofdioxidepartieeldruk, de temperatuur en het hemoglobinegehalte. Alle zijn met een "288 blood gas analyzer" bloedgasmachine (Bayer, Brussel, België) gemeten. Aan de hand van de partieeldruk, temperatuur en zuurtegraad is het mogelijk de zuurstofsaturatie te bepalen. De AAMI standaard houdt in dat bloed wordt gebruikt met de volgende eigenschappen: bloedtemperatuur 37 °C, ingangssaturatie 65 % en hematocriet 45 %. Bloedtesten zijn ook uitgevoerd met een lagere (40 %) en hogere (80 %) ingangssaturatie bij een bloedtemperatuur van 37 °C. Tabel 4 geeft een overzicht van de inlaatvoorwaarden voor zowel de water- als de bloedexperimenten.

Tabel 4: Ingangsvoorwaarden voor de experimenten.

	waterexperimenten	***bloedexperimenten***
temperatuur [°C]	20.6 ± 0.7	36.7 ± 0.8
barometerdruk [mmHg]	[754.6; 772.4]	[754.8; 767.6]
debiet, Q [l / min]	[0.5; 6.0]	1.0 – 3.0 –5.0
pH		7.34 ± 0.05
koolstofdioxidepartieeldruk, P_{CO_2} [mmHg]		41.1 ± 3.3
ingangszuurstofpartieeldruk, $P_{O_2\,in}$ [mmHg]	25.1 ± 2.0	
		42 ± 3
ingangszuurstofsaturatie, $S_{O_2 in}$ [%]		64 ± 2
		80 ± 3
hematocriet, Hct [%]		34.9 ± 1.3

4.2.1.2 Resultaten

Figuur 20 (boven) toont het zuurstofmassadebiet, $\dot{V}_{O_2}$, in functie van het debiet, Q, met water als testvloeistof voor de drie kunstlongen. Zoals blijkt uit deze figuur lijkt Cobe Optima het minst efficiënt. De relatie, $\dot{V}_{O_2}$-Q, kan ook dimensieloos worden voorgesteld volgens een eendimensionale semi-empirische relatie voor het massatransport [3,4], gebaseerd op de Chilton-Colburn analogie tussen het massatransport en de warmtewisseling [46,47]. Deze relatie drukt het verband uit tussen het Sherwoodgetal, N_{Sh}, het Schmidtgetal, N_{Sc}, en het Reynoldsgetal, N_{Re}. Dat geeft de formule:

Tabel 5: Model parameters φ' en m' voor de drie kunstlongen met correlatiecoëfficiënt, R^2.

		Sarns Turbo 440	***Cobe Optima***	***Dideco Compactflo***
N_{Pe} < 3200	**φ'**	0.35	0.19	0.13
	R^2	0.66	0.62	0.96
N_{Pe} > 3200	**φ'**	0.60	0.38	0.27
	m'	0.69	0.60	0.63
	R^2	0.84	0.95	0.97

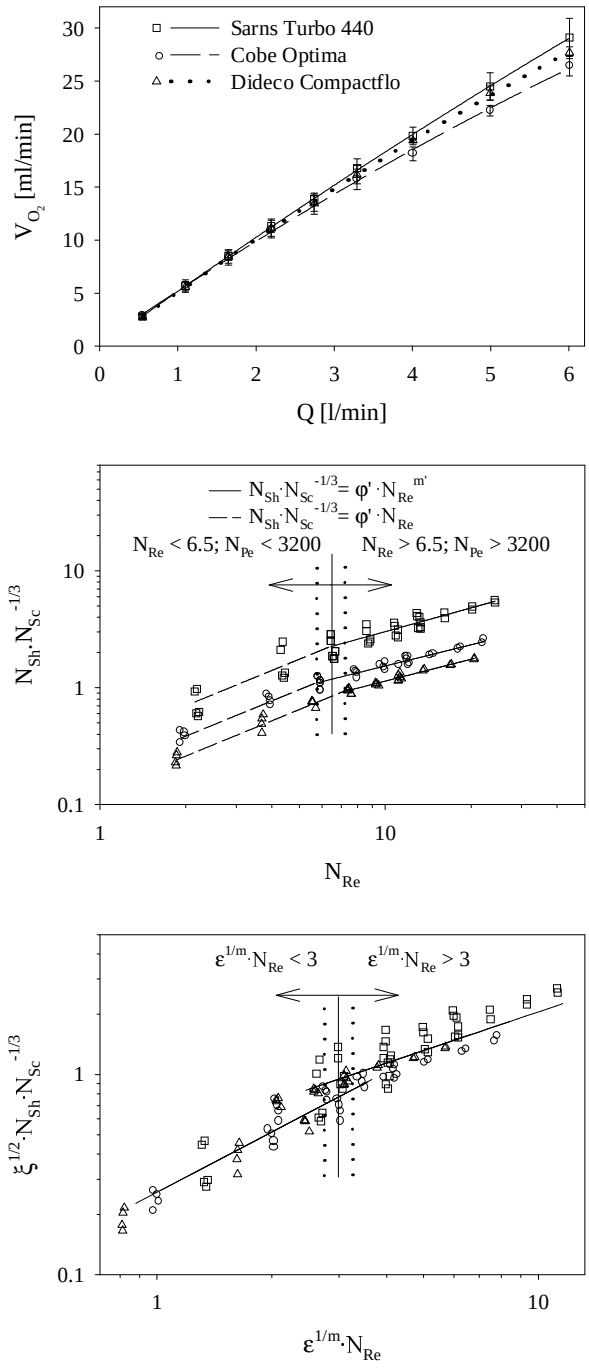

Figuur 20: Voor de drie kunstlongen Sarns Turbo 440, Cobe Optima en Dideco Compactflo zijn de volgende figuren weergegeven. **Boven:** Het zuurstofmassadebiet versus waterdebiet; **Midden:** N_{Sh}-N_{Sc}-N_{Re} op basis van voormelde zuurstofmassadebiet-waterdebiet relatie; **Onder:** Unieke N_{Sh}-N_{Sc}-N_{Re} relatie in functie van porositeit en dimensieloze karakteristieke lengte.

$$N_{Sh} \cdot N_{Sc}^{-1/3} = \varphi' \cdot N_{Re}^{m'} \qquad [41]$$

waarin φ' en m' worden bepaald door de geometrie <48>. Figuur 20 (midden) stelt vgl. [41] voor in een dubbel logaritmische grafiek. Hieruit blijkt dat enerzijds Dideco Compactflo het minst

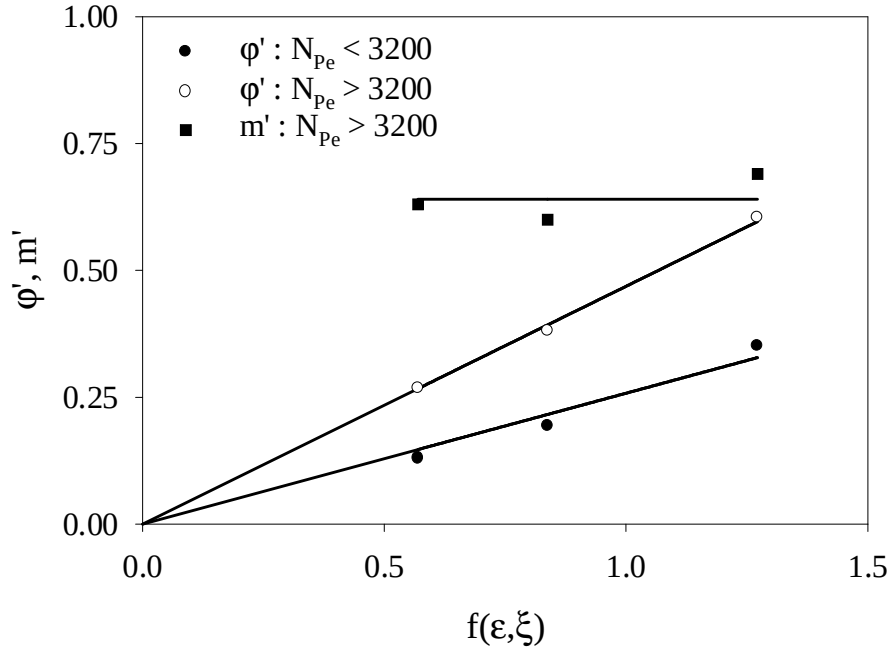

Figuur 21: Parameters φ' en m' in functie van porositeit, ε, dimensieloze karakteristieke lengte, ξ, en het Pécletgetal, N_{Pe}.

performant is voor het zuurstoftransport en dat anderzijds de parameters φ' en m' door zowel de geometrie als het Pécletgetal, N_{Pe}, worden bepaald. Tabel 5 geeft een overzicht van de modelparameters φ' en m' voor de drie kunstlongen in functie van N_{Pe}.

Rekening houdend met de geometrische kenmerken van de drie kunstlongen in Tabel 1 kan men een verband tussen de parameters (φ' en m') en de geometrische kenmerken (porositeit, ε, en dimensieloze karakteristieke lengte, ξ) van de kunstlongen opstellen (Figuur 21).

Aldus bekomt men een unieke relatie voor N_{Sh}, N_{Sc} en N_{Re} in functie van ε en ξ (Figuur 20, onder):

$$\frac{N_{Sh}}{N_{Sc}^{1/3}} \cdot \xi^{1/2} = \varphi \cdot \left(\varepsilon^{1/m} \cdot N_{Re}\right)^{m} \qquad [42]$$

met φ = 0.26 en m = 1.00 voor $N_{Pe} < 3200$ en φ = 0.47 en m = 0.64 voor $N_{Pe} > 3200$. De unieke relatie in vgl. [42] kan vervolgens worden aangewend om het zuurstofmassadebiet van de kunstlong te bepalen en te vergelijken met de bloedmetingen (Figuur 22). Figuur 22 toont het gemeten versus voorspeld zuurstofmassadebiet in bloed met verschillende ingangssaturaties en bloeddebieten voor de drie kunstlongen. Hier komt de invloed van de ingangssaturatie en het bloeddebiet op het zuurstofmassadebiet goed tot uiting. Een laag zuurstofmassadebiet correspondeert met een klein bloeddebiet waarbij de hoeveelheid zuurstofmassadebiet afhankelijk is van de ingangssaturatie. Een lagere ingangssaturatie gaat gepaard met een hoger

zuurstofmassadebiet. Merk op dat het model bij grote debieten (5 l/min) en bij lage ingangssaturaties ($S_{O_2} \approx 40$ %) het zuurstofmassadebiet overschat.

4.2.2 Modellering van het massatransport in het membraancompartiment van een kunstlong

4.2.2.1 Tweedimensionaal model

Het microscopisch *in numero* model voor de simulatie van de stroming doorheen een vezelbank is aangepast voor de modellering van het zuurstoftransport rond een holle vezel. Met behulp van de eindige elementenmethode (SEPRAN <30,31>) zijn numerieke modellen voor de drie vezelconfiguraties opgesteld en een berekeningsprogramma voor de stromingsparameters (druk en snelheden) en het daarbij horende massatransport (ruimtelijke verdeling van de zuurstofpartieeldruk) onder permanente stromingscondities.

De kennis verkregen uit het berekende stromingsveld is van belang om het lokale massatransport te kunnen bestuderen. Opnieuw zijn dezelfde symmetrische voorwaarden opgelegd (Figuur 15).

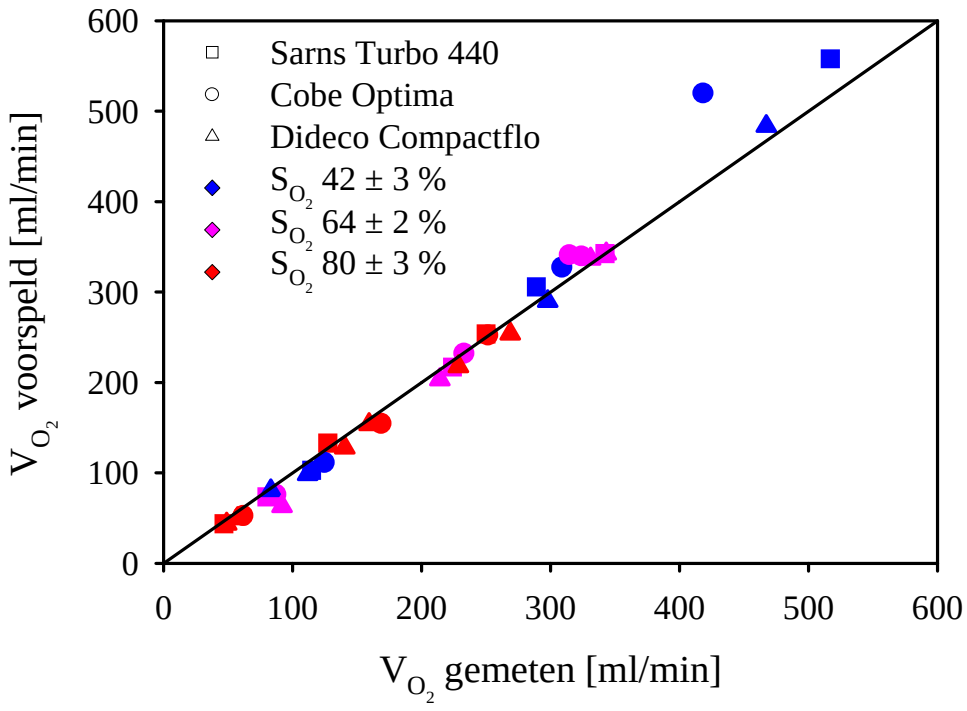

Figuur 22: Gemeten versus voorspeld zuurstofmassadebiet in bloed met verschillende ingangssaturaties (42 ± 3 %, 64 ± 2% en 80 ± 3%) en bloeddebieten voor de drie kunstlongen.

Aan de wand van de vezel heerst een constante zuurstofpartieeldruk. Deze veronderstelling wordt gerechtvaardigd door het gebruik van een zuurstofrijk gasmengsel met een relatief hoog debiet waardoor de zuurstofconcentratie aan gaszijde nagenoeg constant is over de lengte van de vezel. Immers, door het gebruik van microporeuze polypropyleenmembranen kan de weerstand voor het zuurstoftransport door het membraan en aan de gaszijde worden verwaarloosd. Men veronderstelt eveneens dat er geen interactie optreedt tussen de vezels onderling voor wat betreft het zuurstoftransport.

Als ingangsvoorwaarde wordt initieel een uniforme zuurstofpartieeldruk opgelegd. Het verloop van de zuurstofpartieeldruk aan de uitgang van de eenheidscel wordt als ingangsvoorwaarde aan de volgende eenheidscel opgelegd. Aldus kan men het zuurstofmassadebiet langsheen een bloedpad berekenen waarbij men telkens het zuurstofmassadebiet per eenheidscel berekent uitgaande van de resultaten bekomen in de voorgaande eenheidscel.

Aan de uitgang wordt verondersteld dat het concentratieverloop het snelheidsverloop in de stromingsrichting volgt <49>:

$$\bar{\mathbf{u}} \bullet \bar{\nabla} C_{O_2} = 0 \qquad [43]$$

Verscheidene numerieke experimenten zijn uitgevoerd met een groot bereik van randvoorwaarden, zowel wat betreft de stroomsnelheid als de zuurstofpartieeldruk van het instromende fluïdum. Uit de resultaten kunnen globale parameters afgeleid worden zoals de gemiddelde (“cup-mixed”) zuurstofpartieeldruk (en de zuurstofsaturatie in het geval van bloed) aan de in- en uitgang van de eenheidscel en het zuurstofmassadebiet, $\dot{V}_{O_2}$, tijdens de doorstroming van de eenheidscel. De gemiddelde zuurstofpartieeldruk aan de in- en uitlaat wordt berekend als een gewogen gemiddelde met de lokale snelheid als wegingsfactor (“cup-mixed”):

$$\overline{P_{O_2}} = \frac{1}{q} \cdot \int_{\Gamma_{per}} P_{O_2} \cdot \bar{\mathbf{u}} \bullet \overline{\mathbf{dn}} \qquad [44]$$

waarin q het volumedebiet per eenheidslengte doorheen de eenheidscel is (vgl. [38]). Integratie van de resultaten bekomen over een eenheidscel langsheen het bloedpad laat toe het zuurstoftransport in een membraancompartiment met welbepaalde geometrische kenmerken binnen nauwkeurige grenzen te voorspellen. Deze integratie maakt het ook mogelijk om het dimensieloos, semi-empirisch zuurstoftransportmodel voor holle vezel membraankunstlongen met kruisstroming <3> (vgl. [41]) toe te passen op een matrix van eenheidscellen. Bij de integratie worden de vezellengte en het aantal eenheidscellen per eenheidslengte (longitudinaal en transversaal) mee in rekening gebracht.

Voor bloed is de niet-lineaire chemische binding van zuurstof in de convectie-diffusievergelijking gebracht. Dit kan door de convectie-diffusievergelijking te herschrijven in functie van de zuurstofpartieeldruk (§3.5.2). Vgl. [14] en vgl. [15] kunnen dan herschreven worden tot:

$$\bar{\mathbf{u}} \bullet \bar{\nabla}\left(P_{O_2}\right)_i = \frac{D_{O_2}}{1+\lambda\left[\left(P_{O_2}\right)_i\right]} \cdot \Delta\left(P_{O_2}\right)_i \qquad [45]$$

waarin $\left(P_{O_2}\right)_i$ de zuurstofpartieeldruk in eenheidscel i voorstelt. Linearisatie van de partiële differentiaalvergelijking in vgl. ([45]) is dan mogelijk door de afgeleide van de saturatie naar de partieeldruk in $\lambda\left(P_{O_2}\right)$ te benaderen als een vooraf te berekenen waarde <26>. Een oplossing wordt bekomen met volgend iteratief proces:

$$\bar{\mathbf{u}} \bullet \bar{\nabla}\left(P_{O_2}{}^{k+1}\right)_i = \frac{D_{O_2}}{1+\lambda\left[\left(P_{O_2}{}^{k}\right)_i\right]} \cdot \Delta\left(P_{O_2}{}^{k+1}\right)_i \qquad [46]$$

waarin $\left(P_{O_2}{}^{k}\right)_i$ de oplossing uit de vorige iteratiestap voorstelt in eenheidscel i. Voor de eerste iteratie (k = 0) in de eerste eenheidscel (i = 1) wordt een homogene verdeling van de ingangspartieeldruk in de eenheidscel verondersteld. Voor de eerste iteratie (k = 0) in de volgende eenheidscellen (i > 1) wordt telkens de oplossing van de vorige eenheidscel (i-1) gebruikt om de niet-lineaire convectie-diffusie vergelijking te lineariseren. Voor water is de convectie-diffusievergelijking lineair door de afwezigheid van een reactieterm voor het zuurstoftransport $\lambda\left(P_{O_2}\right)$.

Het totaal aantal eenheidscellen in de stromingsrichting, N_L, wordt berekend uitgaande van de longitudinale afstand, S_L, en de bloedpadlengte, L_b:

$$N_L = \frac{L_b}{S_L} \qquad [47]$$

Het eindige elementenrooster nodig voor de modellering van het zuurstoftransport is voorgesteld in Figuur 15. Om een nauwkeurige numerieke oplossing te bekomen dient het rooster-Pécletgetal voldoende klein te zijn. Hiertoe dringt een lokale verfijning van het eindige elementenrooster aan de wand van de vezel zich op.

4.2.2.2 Resultaten

Figuur 23 geeft voor de drie vezelconfiguraties de dimensieloze, semi-empirische N_{Sh}-N_{Sc}-N_{Re} relatie (vgl.[41]) voor water weer in één enkele eenheidscel. De zuurstofpartieeldruk, $\overline{P_{O_2\ in}}$, aan de inlaat van de eenheidscel is voor alle eenheidscellen 40 mmHg. De integratie van de

resultaten in een eenheidscel over een volledige membraanmat met vaste lengte, L', vezellengte, W', en constante uitwisselingsoppervlakte, A, maar verschillende porositeit, ε, (ε = 0.5 en ε = 0.6) (Tabel 6) worden voorgesteld in Figuur 24 voor de drie vezelconfiguraties met water als fluïdum en met eenzelfde ingangszuurstofpartieeldruk. In Tabel 6 vindt men de bijhorende zuurstofpartieeldrukken aan de uitlaat van het membraancompartiment terug. Deze resultaten kunnen aan de hand van het semi-empirisch model, N_{Sh}-N_{Sc}-N_{Re}, dimensieloos worden voorgesteld (Figuur 25). Figuur 26 toont voor de drie kunstlongen het gemeten zuurstofmassadebiet versus het berekende zuurstofmassadebiet, bekomen door integratie over een volledige membraanmat en rekening houdend met bloedpadlengte, porositeit en uitwisselingsoppervlakte van de betreffende kunstlong (Tabel 1). De resultaten voor een enkele kunstlong zijn bekomen door het gemiddelde van de resultaten van de drie vezelconfiguraties te nemen.

Uit Figuur 23 blijkt dat het gekanteld vierkant het meest performant is voor wat betreft het zuurstoftransport. Tevens blijkt dat een hogere porositeit gepaard gaat met een verhoogde transportefficiëntie.

Daarentegen, uit Tabel 6 en Figuur 24 zou men kunnen opmaken dat een lagere porositeit een grotere efficiëntie met zich meebrengt. De uitlaatpartieeldruk is hoger en voor een gegeven debiet is het zuurstofmassadebiet hoger. Men dient echter rekening te houden met enerzijds de hydraulische straal van het membraancompartiment (0.10 voor ε = 0.5 versus 0.14 voor ε = 0.6) en anderzijds met het vloeistofvolume (leeg volume) in het membraancompartiment (185 ml voor ε = 0.5 versus 265 ml voor ε = 0.6). Voor een hoge porositeit heeft het vloeistofvolume dat niet volledig geoxygeneerd is, een belangrijke negatieve invloed op het zuurstofmassadebiet, $\dot{V}_{O_2}$ (Figuur 24). De hydraulische straal, R_h, heeft een proportioneel belangrijkere invloed op het Sherwoodgetal, N_{Sh} (vgl. [34]), dan dat de massatransportcoëffiënt, K, een invloed heeft op N_{Sh} (Figuur 25). Dit betekent dat een hogere porositeit efficiënter massa transporteert, maar dit resulteert in een kleiner zuurstofmassadebiet.

De resultaten in Figuur 24 kunnen worden geanalyseerd door het eendimensionaal, semi-empirisch model uit vgl. [41] toe te passen op het membraancompartiment. Figuur 25 geeft de N_{Sh}-N_{Sc}-N_{Re} relatie weer voor een membraancompartiment met een porositeit van 0.5. Merk hierbij de gelijkenis met Figuur 20 (midden) op.

De knik bij een debiet van 2 l/min kan worden toegeschreven aan het overwegend diffusief massatransport bij lage debieten (Q < 2 l/min). De vloeistof heeft voldoende tijd om de zuurstof via het diffusief proces tot zich te nemen. Bij hogere debieten (Q > 2 l/min) komt het convectief massatransport op de voorgrond. De snelheid in de kunstlong neemt toe waardoor de stromings- en massatransportgrenslaag afnemen in dikte. Dit brengt een verhoogde zuurstofconcentratiegradiënt met zich mee. De tijd nodig om zuurstof uit te wisselen is echter beperkt. Er zal een grotere hoeveelheid vloeistof aanwezig zijn die niet volledig geoxygeneerd is. Dit laatste heeft een negatieve invloed op het zuurstofmassadebiet.

De voorspelling voor het zuurstofmassadebiet is vrij nauwkeurig (< 6 % procentuele afwijking, Figuur 26) en toont de waarde van het model aan. Het verschil in zuurstofmassadebiet bij hoge debieten in de Sarns Turbo 440 kan worden geminimaliseerd door enkel de resultaten van het gekantelde vierkant te gebruiken. Voor een waterdebiet van 4 l/min is het zuurstofmassadebiet 19.1 l/min *in numero* versus 20.0 ml/min *in vitro* (< 5% verschil).

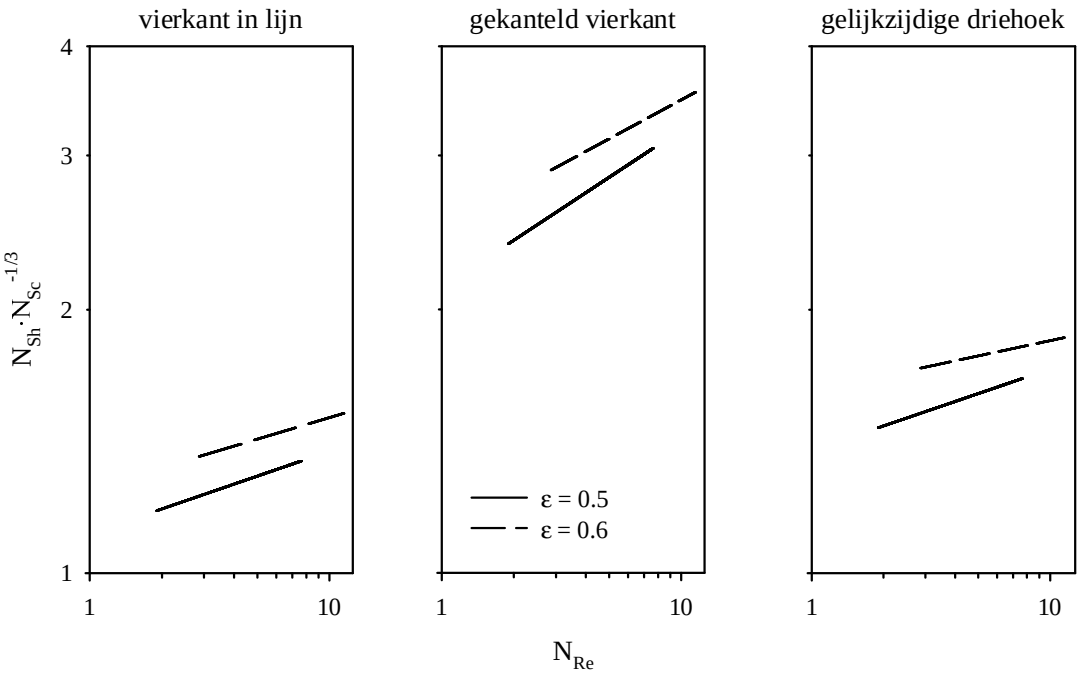

Figuur 23: Voor de drie vezelconfiguraties is N_{Sh}-N_{Sc}-N_{Re} in een bilogaritmische figuur voor het zuurstoftransport in water weergegeven.

Tabel 6: Geometrie van het membraancompartiment met vaste lengte, L', diepte, W', en uitwisselingsoppervlakte, A, voor verschillende porositeiten. IL: vierkant in lijn; SS: gekanteld vierkant; ET: gelijkzijdige driehoek.

	porositeit, ε					
	0.5			***0.6***		
lengte, L' [mm]	100			100		
breedte, W' [mm]	120			120		
uitwisselingsoppervlakte, A [m²]	1.7			1.7		
hoogte, H' [mm]	27			34		
hydraulische straal, R_h [mm]	0.10			0.14		
leeg volume, V_{void} [ml]	185			265		
aantal vezels	11867			11867		
inlaat zuurstofpartieeldruk [mmHg]	20			20		
	IL	*SS*	*ET*	*IL*	*SS*	*ET*
uitlaat zuurstofpartieeldruk [mmHg]	121	150	131	95.5	134	105

Simulaties met bloed (Hct = 30 %, T = 37 °C en $S_{O_2 in}$ = 40 %) als vloeistof en met 100 % zuurstof aan de gaszijde, tonen aan dat een uitgangssaturatie van 99.5% (corresponderend met een uitgangszuurstofpartieeldruk, $P_{O_2 uit}$, van 170 mmHg) kan worden bekomen met een bloedpadlengte van enkele tientallen millimeter voor Reynoldsgetallen variërend tussen 2.5 en 4.0. De bloedpadlengte van de commercieel beschikbare kunstlongen is ongeveer 95 mm. Dit grote verschil in bloedpadlengtes zorgt voor een grote veiligheidsmarge die toelaat om bij acuut zuurstoftekort toch nog aan de nodige zuurstoftoevoer te voldoen.

Figuren met *in numero* resultaten van het zuurstoftransport in bloed voor verschillende vezelconfiguraties zijn samengebracht in de appendix.

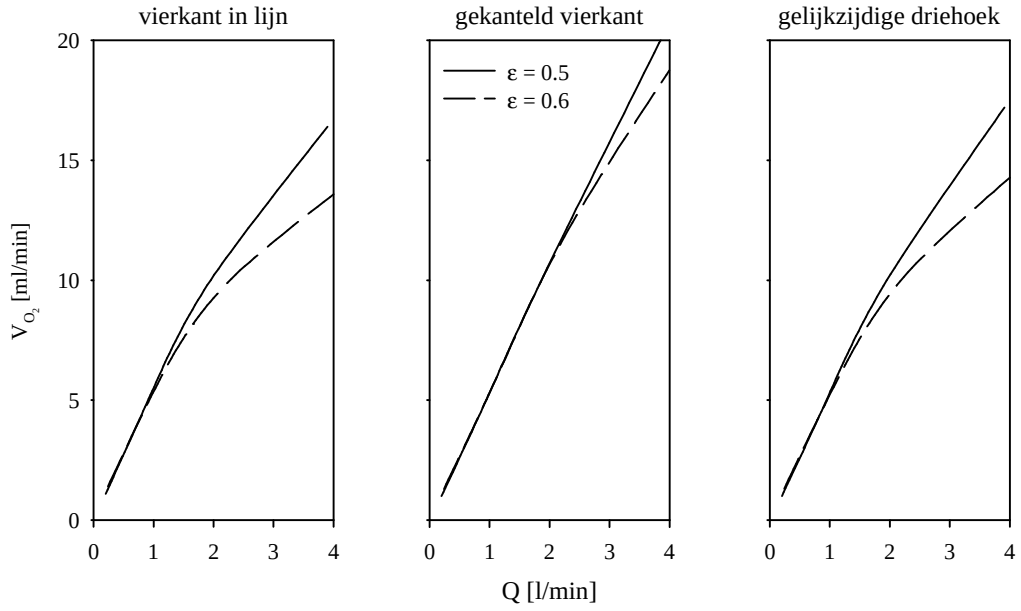

Figuur 24: Zuurstofmassadebiet in functie van debiet voor de drie vezelconfiguraties met een porositeit van 0.5 en 0.6, geëxtrapoleerd naar een membraancompartiment met dezelfde lengte, L', diepte, W', en uitwisselingsoppervlakte, A.

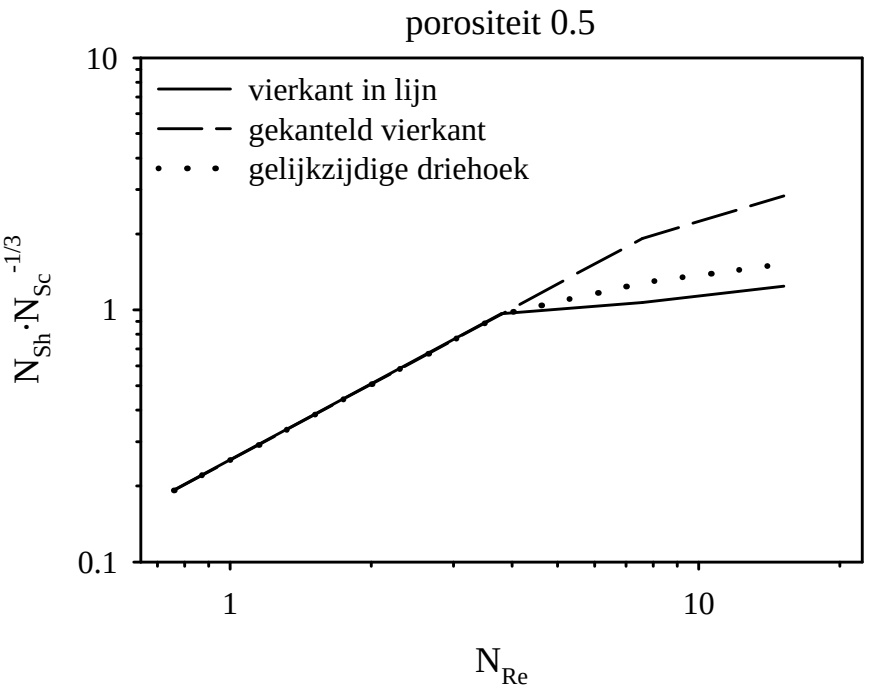

Figuur 25: N_{Sh}-N_{Sc}-N_{Re} relatie voor de drie vezelconfiguraties met een porositeit van 0.5, geïntegreerd voor een membraancompartiment met dezelfde lengte, L', diepte, W', en uitwisselingsoppervlakte, A. In dit geval is voor de karakteristieke snelheid voor N_{Re} de gemiddelde snelheid, U_m, genomen.

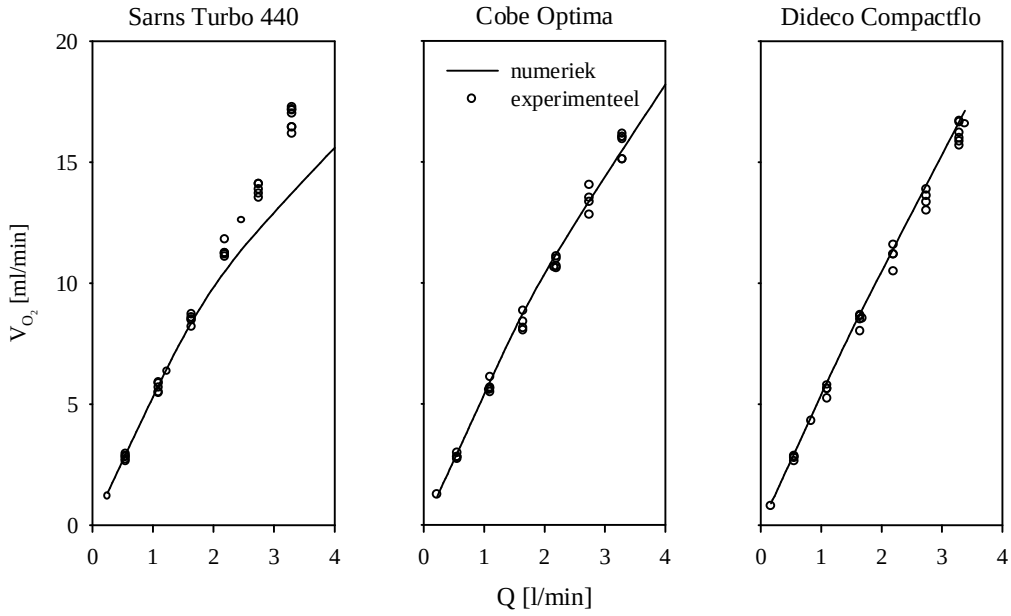

Figuur 26: Voor de drie kunstlongen wordt het gemeten zuurstofmassadebiet versus het zuurstofmassadebiet berekend door integratie van de resultaten over een volledige membraanmat weergegeven, rekening houdend met bloedpadlengte, porositeit en uitwisselingsoppervlakte van de betreffende kunstlong (Tabel 1). **Boven:** Sarns Turbo 440; **Midden:** Cobe Optima; **Onder:** Dideco Compactflo.

4.2.3 Besluit

Een numeriek tweedimensionaal model is opgesteld en maakt het mogelijk de stroming rond één enkele vezel in het membraancompartiment van een kunstlong te modelleren. Door de integratie van deze resultaten over een volledige membraanmat kan men tevens de resultaten valideren met experimentele metingen van zowel stroming als transport van water en bloed doorheen drie commercieel beschikbare kunstlongen.

Een combinatie van het eendimensionaal semi-empirisch zuurstoftransportmodel met het tweedimensionaal numeriek model modelleert het massatransport doorheen de kunstlong op microscopisch en macroscopisch niveau. Deze resulaten kunnen aangewend worden voor een optimaal ontwerp van nieuwe kunstlongen.

4.3 Ontluchtingskarakteristieken van een kunstlong

Om voldoende inzicht te krijgen in het probleemgebied, werden de ontluchtingskarakteristieken van pediatrische <38> kunstlongen *in vitro* bestudeerd. Tijdens openhartchirurgie staat de kunstlong in voor de nodige gasuitwisseling en temperatuurregeling. Dit proces dient echter gerealiseerd te worden met een minimum aan bloedbeschadiging en embolie <50>. Bij het

ontwerp van een kunstlong streeft men naar een aangepaste drukval, een efficiënte gasuitwisseling en warmtewisseling samen met een goede hemocompatibiliteit en ontluchtingskarakteristieken <7,51>.

Gasvormige microemboli (GME) (E: “gaseous microemboli”) of kleine gasbellen kunnen naar de patiënt worden geleid door verschillende vormen van gasintrede in het extracorporeel circuit (ECC). Een goed inzicht in enerzijds de risico’s die tot GME leiden en anderzijds het verwijderen van GME, is noodzakelijk om een minimale luchtintrede in het ECC te bekomen.

Een experimentele studie met betrekking tot GME in neonatale kunstlongen laat toe het belang van de invloed van de stromingskarakteristieken en het ontwerp van de kunstlong toe te lichten. Meer bepaald hebben de schikking van de vezels en de stromingsweerstand <52> geen onbelangrijke invloed op de ontluchting van membraankunstlongen.

Een gasembool bestaat voornamelijk uit zuurstof, koolstofdioxide, stikstof en eventueel stikstofoxide en is afhankelijk van o.a. het ventilatiegas en de gebruikte anesthesie <53>. De grootte van een gasembool varieert voornamelijk tussen 10 en 1000 µm <50,54,55>. Enkele oorzaken die kunnen leiden tot gasembolie zijn chirurgische handelingen, werkingskarakteristieken van de kunstlong en het ECC, koeling en opwarming van het bloed, cavitatie, aanzuigen van het bloed, ...<52,53,56-58>.

In de systeemcirculatie van de patiënt kunnen GME aanleiding geven tot een verhoogde morbiditeit en mortaliteit tijdens en na CPB <52,56,59>. De vernauwing of verstopping van capillairen door GME verhindert de levensnoodzakelijke doorbloeding van vitale organen <60-62> waardoor orgaandysfunctie en beschadiging kan optreden.

Gasvormige microemboli kunnen met behulp van een arteriële filter worden verwijderd uit het ECC.

Men kan de vraag stellen of het ontwerp van de membraankunstlong een rol speelt in het verwijderen van GME aan de bloedzijde. Is het mogelijk dat het stromingspatroon, de schikking van de vezels, de ontluchtingscapaciteit en de gasoverdracht van bloed- naar gaszijde de betrouwbaarheid en veiligheid van de kunstlong verhogen met betrekking tot de ontluchting en eliminatie van GME ?

4.3.1 Meetmethode

De efficiëntie van de ontluchting van een kunstlong wordt meestal begroot met behulp van een bellendetector <63>. Nochtans is deze techniek niet quantitatief en is de reproduceerbaarheid eerder beperkt door het werkingsprincipe <64-66>. Hierdoor is geen objectieve vergelijking van kunstlongen mogelijk. Deze studie bestaat erin dat men de hoeveelheid lucht begroot, die

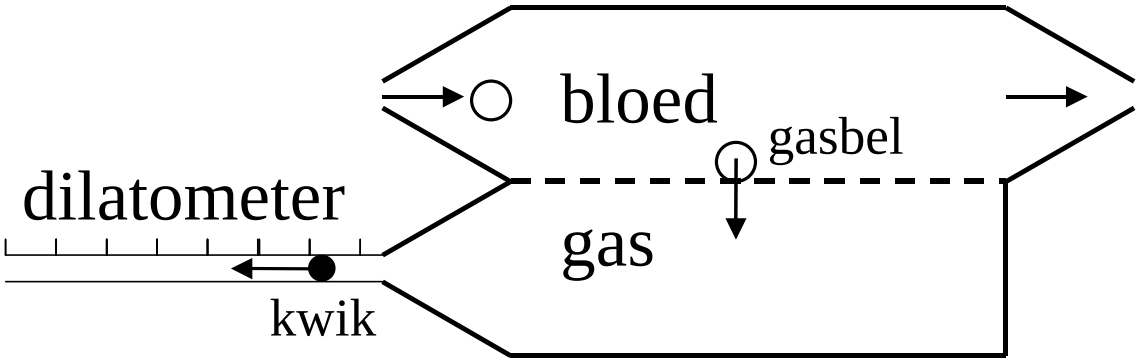

Figuur 27: Schematische voorstelling van de dilatometer.

enerzijds door het membraan naar de gaszijde wordt getransporteerd, en anderzijds via de arteriële lijn naar de patiënt wordt gevoerd. Bijgevolg kan men eveneens de hoeveelheid lucht begroten die in de kunstlong achterblijft.

Een dilatometer (Figuur 27) begroot de hoeveelheid lucht die door het membraan naar de gaszijde wordt getransporteerd. De dilatometer is opgebouwd uit een glazen buisje waarin kwik is aangebracht. Nadat alle uitlaten aan de gaszijde in de kunstlong zijn afgesloten met silicone wordt de dilatometer aan de gasinlaat bevestigd. Indien er zich lucht opstapelt aan de gaszijde zal het kwik in de dilatometer zich onder invloed van de drukopbouw verplaatsen tot er een evenwicht is bereikt met de omgevingsdruk. De verplaatsing van het kwik is dan een maat voor de hoeveelheid lucht die in de gaszijde komt.

Twee neonatale kunstlongen, Dideco Lilliput (Sorin) en Polystan Microsafe (Polystan A/S, Denmark) zijn getest op hun ontluchtingskarakteristieken. Ondanks het feit dat de efficiëntie met betrekking tot de gasuitwisseling en warmtewisseling zeer vergelijkbaar is, is het ontwerp van deze kunstlongen sterk verschillend. De testen zijn uitgevoerd met runderbloed. Een bepaalde hoeveelheid lucht wordt voor de inlaat in de bloedlijn geïnjecteerd in bolusvorm of continu.

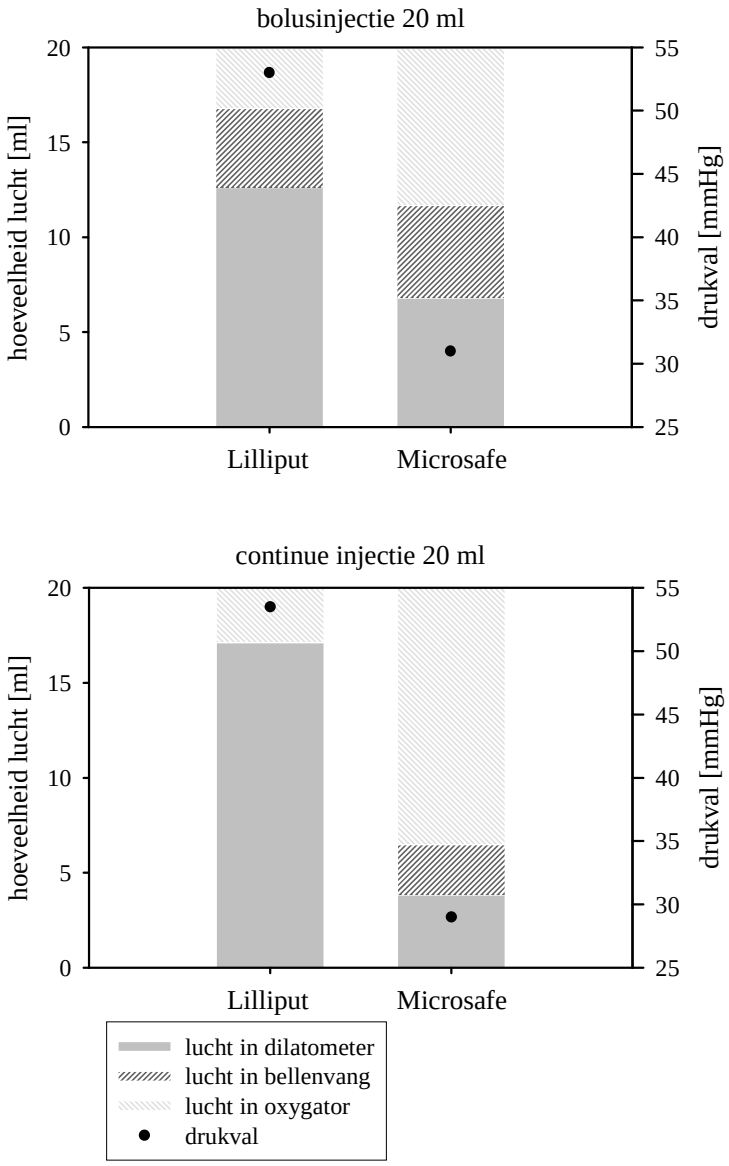

Figuur 28: De hoeveelheid lucht, gemeten in de dilatometer, de bellenvang en de kunstlong voor de twee pediatrische kunstlongen, Lilliput en Microsafe. **Boven:** bolusinjectie van 20 ml; **Onder:** continue injectie van 20 ml.

4.3.2 Resultaten

Twee resultaten zijn voorgesteld in Figuur 28 samen met de drukval bij een debiet van 600 ml/min. Uit de verschillende testen blijkt duidelijk dat het ontwerp en de constructie van de kunstlong een invloed hebben op de ontluchtingscapaciteit <38>. Met name een combinatie van een relatief hoge drukval, een direct contact met het membraan, het vermijden van hoge

snelheden en een vezelstructuur (mattechnologie) verbeteren de ontluchting van kunstlongen. Een hogere drukval blijkt voordelig te zijn bij ontwerpen waar geen onmiddellijk contact tussen het bloed en het membraan is.

Algemeen kan men stellen dat men de klinische gevolgen van GME tijdens CPB kan reduceren door de duur van CPB te verminderen, een arteriële filter te plaatsen, een membraankunstlong te gebruiken en bloedverlies in het operatieveld tot een minimum te beperken. Een holle vezel membraankunstlong met kruisstroming biedt het bijkomend voordeel dat hij de werking van een dieptefilter benadert.

5 Originele bijdragen

In dit proefschrift is de hydrodynamica en het massatransport in de kunstlong zowel *in numero* als *in vitro* bestudeerd.

De stromingsweerstand in het membraancompartiment van drie holle vezel membraankunstlongen met kruisstroming is begroot *in vitro*. Een analyse van deze stromingsweerstand in functie van de geometrische kenmerken van de kunstlong heeft geleid tot het opstellen van een unieke, dimensieloze, semi-empirische relatie voor de stromingsweerstand in het membraancompartiment van een kunstlong tussen het Eulergetal, N_{Eu}, en het Reynoldsgetal, N_{Re}, met de geometrische parameters: membraanporositeit, ε, en karakteristieke lengte, ξ. Deze semi-empirische relatie laat toe de drukval in het membraancompartiment van de kunstlong te voorspellen <34>.

$$N_{Eu} \cdot \frac{\xi}{\varepsilon^2} = \alpha + \frac{\beta}{N_{Re} \cdot \varepsilon \cdot (1-\varepsilon)}$$

Op analoge wijze is het zuurstoftransport in de kunstlong experimenteel bepaald zowel met water als bloed. Het zuurstoftransport is op basis van een bestaand eendimensionaal, dimensieloos, semi-empirische model voor het zuurstoftransport in de holle vezel membraankunstlong met kruisstroming <3> geanalyseerd in functie van de geometrische kenmerken van de kunstlong. Deze analyse heeft geleid tot het opstellen van een unieke, dimensieloze, semi-empirische relatie voor het zuurstoftransport in het membraancompartiment van een kunstlong tussen enerzijds het Sherwoodgetal, N_{Sh}, en het Schmidtgetal, N_{Sc}, en anderzijds het Reynoldsgetal. Deze semi-empirische relatie laat toe het zuurstoftransport in het membraancompartiment te voorspellen <37>.

$$\frac{N_{Sh}}{N_{Sc}^{1/3}} \cdot \xi^{1/2} = \varphi \cdot \left(\varepsilon^{1/m} \cdot N_{Re}\right)^m$$

Hierin zijn φ en m de constanten van het eendimensionaal model die afhankelijk zijn van het Péclet-getal.

Een numeriek tweedimensionaal model is ontwikkeld dat toelaat de stroming en het zuurstoftransport rond een enkele vezel in het membraancompartiment in detail te modelleren, en dit voor de eerste maal gebaseerd op eindige elementen technieken. Men veronderstelt hierbij dat:

- het membraancompartiment is opgebouwd uit parallelle, identieke, rechte vezels.
- de stroomverdeling uniform is.
- de stroming isotherm, laminair, tijdsonafhankelijk, volledig ontwikkeld en tweedimensionaal is.

Deze veronderstellingen laten toe de numerieke studie van het membraancompartiment te reduceren tot de studie in een enkele eenheidscel (met slechts één vezel) door symmetrische en periodieke randvoorwaarden in te voegen. De periodieke randvoorwaarden zijn enkel van toepassing op de snelheden in het model. Drie verschillende vezelstructuren (“vierkant in lijn”, “gekanteld vierkant” en “gelijkzijdige driehoek”) zijn gemodelleerd om de invloed van de geometrie te kunnen onderzoeken. Door de resultaten verkregen op een eenheidscel uit te breiden tot het totaal aantal cellen in de membraanmat, kunnen de resultaten vergeleken worden met eigen experimentele metingen en met gegevens van de fabrikant.

Uit de resultaten kunnen lokale parameters afgeleid worden, zoals de drukval over een eenheidscel bij een bepaald kunstlongdebiet, de zuurstofsaturatie aan de uitgang van de eenheidscel en het zuurstofmassadebiet tijdens de doorstroming van de eenheidscel.

De invloed van een niet-newtoniaanse bloedviscositeit <36>, alsook de invloed van secundaire stromingen op de stroming, is in een eenheidscel bestudeerd. Het verschil tussen een niet-newtoniaans en newtoniaans vloeistofgedrag blijkt nogal beperkt voor wat betreft het snelheidspatroon doorheen de eenheidscel.

De samenstelling van eenheidscellen tot een volledige membraanmatrix laat toe om met inbreng van de vezellengte de stromingsweerstand over en het zuurstoftransport in een membraancompartiment te voorspellen. De voorspelling van de stromingsweerstand is vrij beperkt daar we met de invloed van de stroomverdeler en de vorm van het stroompad geen rekening houden. De voorspelling voor het zuurstoftransport is vrij nauwkeurig en toont de waarde van het model aan. Dit model wordt vervolgens toegepast voor het zuurstoftransport onder verschillende fysiologische stromings- en bloedgas randvoorwaarden uit de klinische praktijk. Men kan voorspellen dat de minimale bloedpadlengte om een uitgangssaturatie van 99.5 % te bereiken maximum 40 mm bedraagt met bloed bij een temperatuur van 30 °C, een

hematocriet van 30 % en een ingangssaturatie van 40 %. De bloedpadlengte in een kunstlong is echter groter, ongeveer 95 mm. Dit grote verschil biedt echter een grote veiligheidsmarge om bij acuut zuurstoftekort toch nog aan de nodige zuurstoftoevoer te kunnen voldoen.

Tenslotte is een nieuwe techniek ontwikkeld waardoor we de ontluchtingskarakteristieken in kunstlongen kunnen begroten. De techniek laat toe de hoeveelheid lucht te begroten, die enerzijds door het membraan naar de gaszijde van de kunstlong wordt getransporteerd, en anderzijds via de arteriële lijn naar de patiënt gevoerd. Uit de verschillende testen blijkt duidelijk dat het ontwerp en de constructie van de kunstlong een invloed hebben op de ontluchtingscapaciteit <38>. Met name een combinatie van een relatief hoge drukval, een direct contact met het membraan, het vermijden van hoge snelheden en een vezelstructuur (mattechnologie) verbeteren de ontluchting van kunstlongen.

Voor zowel de hydrodynamica als het massatransport zijn unieke semi-empirische relaties en een tweedimensionaal model ontwikkeld die bij het ontwerp van nieuwe kunstlongen kunnen worden aangewend.

6 Toekomstig onderzoek

Het onderzoek dat uitgevoerd is binnen dit proefschrift heeft een aantal beperkingen. Algemeen is verondersteld dat de stroomverdeling in het membraancompartiment uniform is. Daarnaast gaat men er van uit dat het membraancompartiment een constante porositeit heeft. De stroming in het numeriek model is tweedimensionaal en isothermisch. Dit is echter niet aan de orde voor wat betreft de stroming in een kunstlong. Enerzijds is de stroming driedimensionaal en anderzijds treedt er een temperatuurverschil op bij de doorstroming van de kunstlong waardoor de fysische constanten van het fluïdum niet constant zijn. Verder onderzoek kan hierover meer duidelijkheid bieden.

De kunstlong wordt in de praktijk met bloed doorstroomd. Daarom is het belangrijk om de invloed van de bloedviscositeit op de resultaten verder te onderzoeken, meer bepaald de invloed van het gebruikte viscositeitmodel bij verschillende hematocrieten en temperaturen.

Een kunstlong dient niet alleen om zuurstof naar het bloed te transporteren, maar ook om koolstofdioxide af te voeren. De hier voorgestelde analysen kunnen opnieuw uitgevoerd worden in dit perspectief. Dit vraagt wel dat in het numerieke model rekening wordt gehouden met de partieeldrukstijging van koolstofdioxide over de lengte van de vezels.

Met het model van het gehele membraancompartiment kunnen dan simulaties onder AAMI condities uitgevoerd worden en vergeleken met metingen op werkelijke kunstlongen.

Een evaluatie van de dimensieloze relaties op basis van de doorstromingsoppervlakte in plaats van de stroomverdelerlengte kan, naast nieuwe experimenten op andere dan de drie bestudeerde kunstlongen, de algemene toepasbaarheid valideren van de ontwikkelde dimensieloze relaties.
Tenslotte is een parameterstudie op het tweedimensionale model aangewezen om de ideale vezelconfiguratie, zowel voor drukval als voor gastransport, te definiëren. Daarnaast zal een gedetailleerde studie van de invloed van de schuifspanningen op bloedbeschadiging enerzijds en op het gastransport anderzijds een nieuw licht kunnen werpen op het optimaal ontwerp van de kunstlong.

ABSTRACT

An artificial lung is used during cardiopulmonary bypass to oxygenate blood and to control blood temperature. This thesis aims at studying the hydrodynamics and the oxygen transfer in a cross-flow hollow-fiber membrane artificial lung *in numero* as well as *in vitro*. The fluids used in the numerical model and during experiments are water ("hydro") and blood ("hemo"). Comparison of the results confirms the ability to transform water results to blood data.

The figure below presents a schematic overview of the aims and the structure of the thesis. A two-dimensional numerical model is developed to study the hydrodynamics and the oxygen transfer in a unit fiber cell of a membrane compartment of a cross-flow hollow fiber membrane artificial lung. Subsequent unit fiber cells are then assembled to predict oxygen mass transfer-flow rate relationship in a membrane compartment. The model is compared to water experimental data from three commercial artificial lungs.

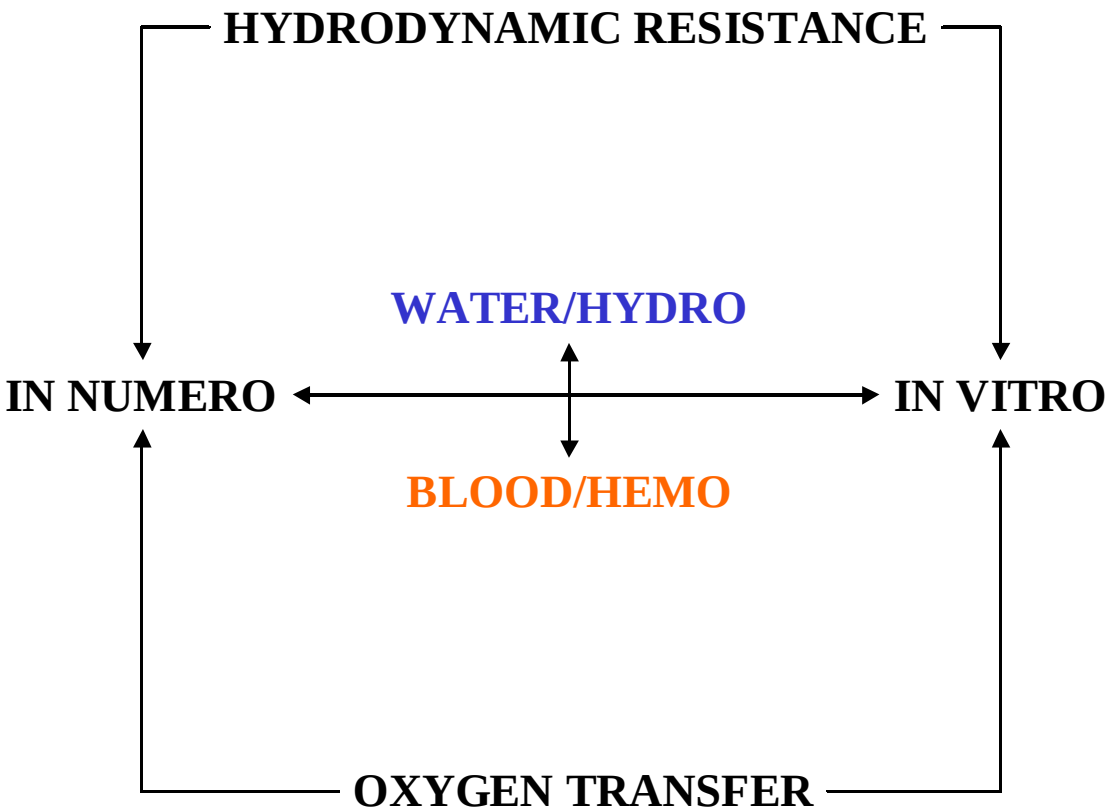

Schematic representation of the thesis, "Blood flow and gas transport in artificial lungs: *in numero* and *in vitro* analysis"

The analyses present unique, dimensionless, semi-empirical relationships for both the hydrodynamics and the oxygen transfer in the membrane of an artificial lung. These results can be applied to obtain an optimal hydrodynamic design of hollow fiber blood-gas exchange devices.

The thesis comprehends a Dutch synthesis, an elaborate English survey and one appendix. The Dutch synthesis presents a summary of the published and unpublished *in numero* and *in vitro* results for both the hydrodynamics and the oxygen transfer in an artificial lung. The English survey is composed of eight chapters providing the reader with an extended historical background, an introduction to the modelling of oxygen transfer in an artificial lung and a collection of published and submitted peer-reviewed manuscripts detailing the scientific work and results. In the conclusion, the original contributions to scientific knowledge are summarized. In the appendix, a brief survey of representative results on the hemodynamics and the oxygen mass transfer in blood for different unit fiber cells is given.

In this manner, the thesis is composed as follows:

- Dutch synthesis
- English abstract
- Eight English chapters:

I Introduction to and History of Cardiopulmonary Bypass and Artificial Lungs

II Introduction to and Modeling of Oxygen Transfer in Artificial Lungs

III Hydrodynamic Characteristics of Artificial Lungs

IV Blood Flow around Hollow Fibers

V Mass Transfer Characteristics of Artificial Lungs

VI Two-dimensional finite element model for oxygen transfer in cross-flow hollow fiber membrane artificial lungs

VII Air-Handling Characteristics of Pediatric Artificial Lungs

VIII Conclusion

- Appendix

I INTRODUCTION TO AND HISTORY OF CARDIOPULMONARY BYPASS AND ARTIFICIAL LUNGS

I.1 Introduction

The natural lung is the organ in which blood exchanges oxygen and carbon dioxide with the body environment. In turn, blood carries oxygen to all body tissues, to oxidize the nutrients needed to sustain life. The end products of the chemical reactions that take place in tissues, globally referred to as metabolism, include carbon dioxide, water and heat, all of which must be eliminated. Oxygen is obtained from the air we breathe through diffusion at the level of the pulmonary alveoli and then carried to the tissues by the hemoglobin in the red blood cells. The carbon dioxide produced by the living cells is picked up by the circulating blood and brought to the pulmonary capillaries. There it diffuses into the alveoli. Carbon dioxide is then conveyed out by ventilation through the airways. These processes can be slowed down to a speed close to resting levels by hypothermia or accelerated by hyperthermia, fever, and muscular exercise.

The challenge of replacing the functions of the natural lungs by an exchange device allowing continuous blood flow and blood arterialization, was first outlined by physiologists at the end of the 19th century, but it could not be realized until the 1950s. The large transfer areas needed for blood-gas exchange in an artificial lung were initially obtained by continuous foaming and defoaming in a circulating blood pool or by spreading a thin film of blood in an oxygen atmosphere. Because the direct blood-gas interface was found to be damaging to the blood as well as difficult to stabilize over extended periods, membrane mediated processes were introduced and are now almost universally preferred.

Between 1935 and 1954, John Gibbon, Clarence Dennis, and others pursued the development of a mechanical device to take over the function of the heart and lungs to permit surgical operations on the heart and great vessels. The entire project was stimulated by a patient with a lethal pulmonary embolism. Obviously, a machine that could be used to permit cardiopulmonary bypass for this problem could be used for cardiac surgery and a variety of other applications as

well. As a substitute for the heart, Gibbon used a roller pump that remains in general practice even today. To substitute for the lungs, he devised a system in which anticoagulated blood was directly exposed to oxygen, dripping along the wires of a vertically mounted metal screen. The approach of direct exposure of blood to oxygen was successful, and was subsequently modified by Dennis, Morrow, Cross, DeWall, Rygg, and many others, leading to the single-use, disposable, direct gas interface oxygenators which are widely used today. Lillihei was the first to use extracorporeal circulation for cardiac surgery, establishing cross circulation between a parent and a child with congenital heart disease, using the parent as the heart/lung machine. Gibbon was the first to use the prosthetic heart/lung machine for a cardiac operation, opening the door to the routine application and success of extracorporeal circulation for cardiac surgery.

Artificial lungs are designed to replace, on a temporary basis, the respiratory function of the natural lungs and are often called “blood oxygenators”. Oxygen transfer has traditionally been seen as the most important function being replaced and, in most situations, proved to be more limiting than carbon dioxide transfer. The change in blood color between inlet and outlet also encourages the term oxygenator, considering that changes in blood carbon dioxide content are not visible to the eye and are more difficult to measure than oxygen transfer. The term “pump-oxygenator” has been commonly used since the early days of cardiopulmonary bypass. It correctly describes its function: it is a pump which replaces the main function of the heart and it oxygenates blood. However, the term ignores the role of carbon dioxide elimination in maintaining acid-base balance, a critical aspect in prolonged use. Therefore, an oxygen and carbon dioxide gas exchange device is best referred to as an “artificial lung”.

Artificial lungs are primarily utilized in cardiopulmonary bypass procedures (CPB) for open-heart surgery. A second application is the treatment of acute respiratory failure (ARF), assisting the deficient gas transfer capacity of the natural organ.

As is the case for most artificial organs, artificial lungs may be called upon:

- to bypass the pulmonary circulation in order to replace the pulmonary gas exchange function entirely when the natural organ is totally disabled or, while still sound, must be taken out of commission for a limited time to allow a cardiac or cardiovascular surgical intervention.
- to assist the deficient gas transfer capacity of the natural organ temporarily in the hope that the healing process will eventually repair the diseased organ.
- to assist the deficient gas transfer capacity of the natural organ permanently when irreversible lung damage leaves the patient permanently disabled. Artificial lungs are then utilized for longterm partial or total respiratory support.

Since most artificial lungs cannot be placed in the anatomical position of the natural lung, venous blood must be diverted from its normal path through the central veins, right heart, and pulmonary vascular bed. Venous blood is then rerouted, via catheters and tubes, through an extracorporeal circuit that includes a pump and an artificial lung. Finally, the arterialized blood is returned to the arterial system.

When the pulmonary circulation is temporarily interrupted for surgical purposes and gas exchange is provided by an artificial lung, it is often referred to as extracorporeal circulation (ECC) <67> In the operating room, the gas exchange devices as well as the pumps, which circulate the blood, are located outside the body, for convenience' sake.

The vision of coupling extracorporeal blood pumping with extracorporeal gas exchange at a level of a performance sufficient to permit unhurried surgical interventions in adult patients originated with Gibbon <68>. His initial laboratory models relied on rotating cylinders which spread blood in a continuously renewed thin film, in the tradition of 19th century physiologists.

Worldwide, the annual use of disposable artificial lungs has been estimated at 1.1 million <69> with prices for each gas exchange unit ranging from € 400 to 500. More than 90 % of those procedures are performed on adult patients. This represents the major use of these devices. As a result, the focus of this thesis will be on oxygenators used for cardiac surgical procedures in adult patients.

I.2 Cardiopulmonary bypass

Cardiopulmonary bypass (CPB), also called heart-lung bypass, allows the temporary replacement of the gas exchange function of the lungs and the blood-pumping function of the heart. As a result, blood no longer flows through the heart and lungs, presenting the surgeon with an almost bloodless operative field.

The term heart-lung machine graphically describes the equipment used. The procedure is cardiopulmonary bypass by extracorporeal circulation. Strictly speaking, open-heart surgery refers to interventions inside the heart cavities, e.g. cardiac valve replacement, correction of congenital abnormality, … These provide the most frequent demand for cardiopulmonary bypass technology. By extension, the term is also applied to surgical procedures which take place primarily on the external wall of the heart, e.g. coronary artery bypass grafting (CABG) or bypass surgery. In these operations, the cardiac cavities are temporarily vented to avoid the build-up of pressure that could damage the cardiac muscle. This cardiotomy suction and venting

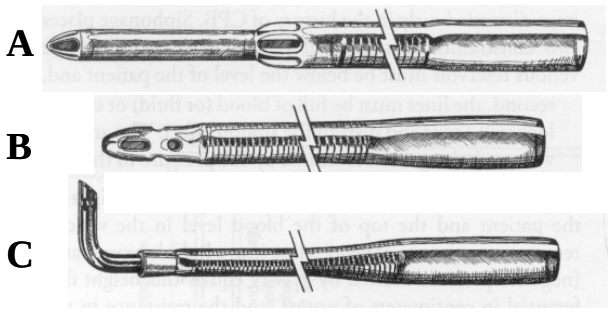

Figure I.1: Conventional venous cannulae: **A**: Standard, tapered, two-stage cannula for insertion into the right atrium or inferior vena cava; **B**: Wire-reinforced cannula for atrial or caval cannulation; **C**: Cannula with right-angled tip for insertion into the vena cava near its junction with the right atrium. <5>

are intended to prevent distension of cardiac chambers and air embolism and to provide adequate surgical exposure.

The heart-lung machine is part of a total, veno-arterial cardiopulmonary bypass circuit. This means that all the venous blood returning to the right heart cavities is collected from the vena cava in the extracorporeal circuit and is circulated through the gas exchange device. It is then pumped back into the arterial tree, thereby “bypassing” the heart cavities and the pulmonary circulation.

With respect to the blood, this procedure usually involves hemodilution, some degree of temperature control (hypothermia), (non-)pulsatile arterial perfusion at a flow rate near cardiac output at rest, and continuous recirculation of blood in an extracorporeal circuit in series with the systemic circulation of the patient. With respect to the gas, oxygen or an oxygen-enriched gas mixture (with or without a low concentration of carbon dioxide) flows from a moderately pressurized source in a continuous, nonrecycling manner and is vented to the room atmosphere.

Depending on the surgical procedure involved (e.g. CABG, cardiac valve replacement or correction of congenital abnormality), the duration of total bypass can range from 1 to 3 hours.

I.2.1 Cannula

Typically, blood is drained by enhanced gravity (vacuum assisted venous drainage (VAVD) or kinetic assisted venous drainage (KAVD)) via cannulae in the superior and inferior vena cava or inferior vena cava and right atrium to the heart-lung machine. There, the blood is pumped through an artificial lung with a roller or centrifugal pump and back into the systemic vasculature via an arterial cannula, which is placed in the ascending aorta.

Cannulae are usually made of a flexible plastic, possibly reinforced to prevent kinking. They can be straight or right-angled.

Venous cannulae (Figure I.1) are either single or two stage (cavoarterial). The latter have a wider portion with holes in the section designed to sit in the right atrium and a narrower tip designed to rest in the inferior vena cava.

The arterial cannula (Figure I.2) is usually the narrowest part of the extracorporeal circuit. Some arterial cannulae are designed for insertion into the ascending aorta and have different tip geometries.

I.2.2 Pump

The ideal pump for CPB should be able to deliver physiologic blood flows against high resistance without damaging blood, it should provide flows that are exact and easily monitored, it should create no turbulence or stagnation, and it should be manually operable in the event of a power failure. However, in reality, there is no such pump and one can only rely on two types of pumps, i.e. roller pumps and centrifugal pumps.

Roller pumps are positive displacement pumps and have the advantage of simplicity, low cost, ease of use and reliability of flow calculation. They have the ability to pump against high resistance without reducing flow. Disadvantages include the need to assess occlusiveness, the capability to pump large volumes of air, the ability to create large positive and negative pressures and spallation of the inner tubing surface which might lead to particulate arterial emboli.

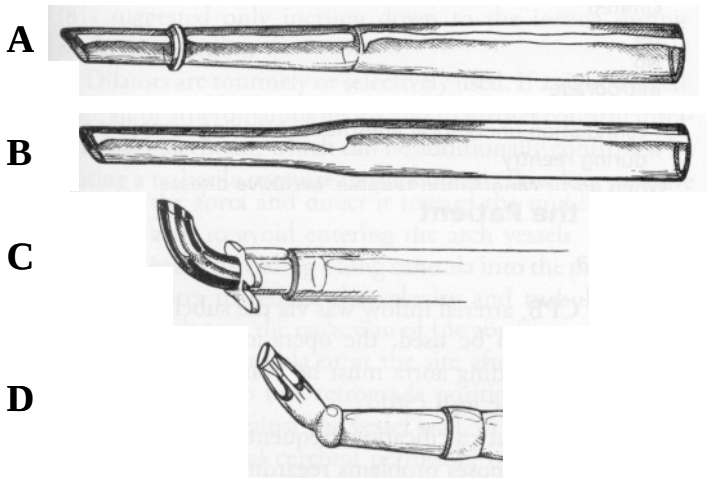

Figure I.2: Aortic cannulae. **A:** Bevel-tipped tapered THI-type cannula with molded flange near tip; **B:** Similar cannula without a flange; **C:** Metal-tipped right-angled cannula with plastic molded flange for securing cannula to aorta; **D:** Diffusion-tipped angled cannula.

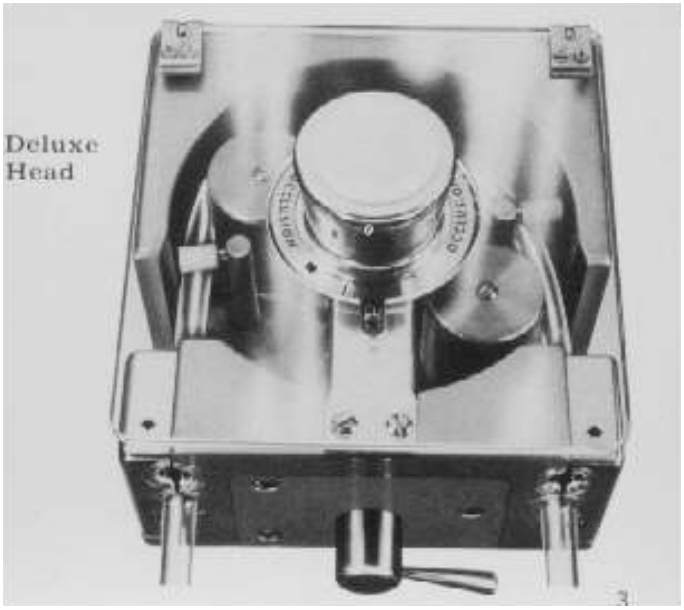

Figure I.3: Sarns developed a pump head in which the occlusion could be adjusted without any hand tools while the pump head was rotating. They eliminated a gear head drive system and transmitted power from a variable speed motor directly to the pump head using a state of the art belting system. <70>

In the 1950s and 1960s, roller pumps ("die Beckshe Mühle") (Figure I.3) prevailed over any other mechanism as the blood propulsion equipment for the clinical heart-lung machine. The roller pump was commonly used in donor-to-patient blood transfusion, and it was standard equipment for organ perfusion studies in physiology laboratories. Cardiopulmonary bypass required a much higher flow capacity (up to 8 l/min) than these earlier applications. Increased performance was achieved by resorting to large-bore flexible tubing, long circular pumping chambers in overdimensioned housings, and a fast, controllable rate of revolution of the rotor assembly. Roller pumps come as one-roller, twin-roller, and multiple-roller models. Some use elaborate stop-and-go or speed control mechanisms to achieve pulsatile rather than steady flow. Its simplicity, its longterm reliability, its occlusiveness, and its ability to use a hand crank in case of power failure positioned the twin-roller pumps as the blood-pumping system in the operating room.

Centrifugal pumps offer the advantages of lesser air pumping capabilities, lesser abilities to create large positive and negative pressures, less blood trauma, and virtually no spallation. However, centrifugal pumps are afterload-dependent requiring constant flow measurement.

I.2.3 Heat exchanger

Because of the need to offset the cooling during the extracorporeal passage of blood and the frequent desire to intentionally cool (hypothermia) and then rewarm the patient, a heat exchanger is included as part of the artificial lung, either before or contiguous with the gas exchange unit.

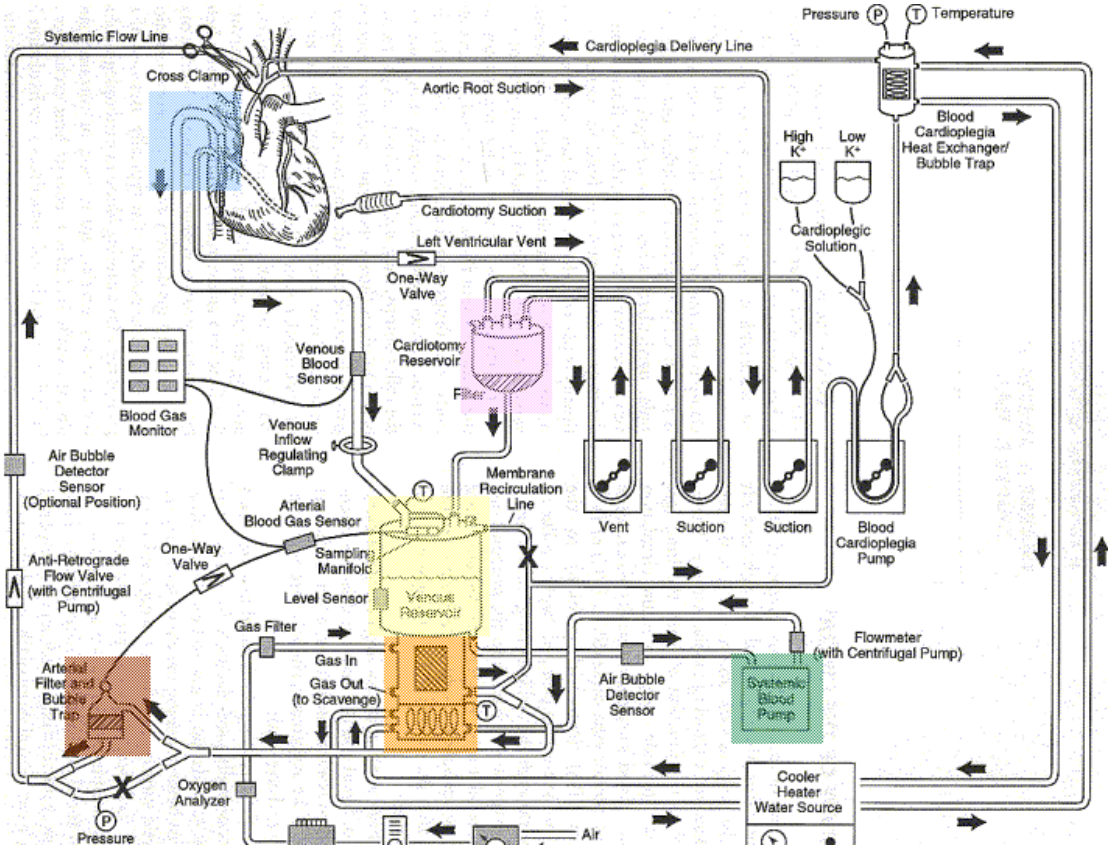

Figure I.4: Detailed schematic diagram of a typical cardiopulmonary bypass circuit using a membrane artificial lung (orange) with integral hard-shell venous reservoir (yellow) and external cardiotomy reservoir (magenta). Venous cannulation (blue) is by a cavoatrial cannula and arterial cannulation is in the ascending aorta. Some circuits do not incorporate a membrane recirculation line; in these cases the cardioplegia blood source is a separate outlet connector built-in to the artificial lung near the arterial outlet. The systemic blood pump (green) may be either a roller or a centrifugal type. The cardioplegia delivery system is a one-pass combination blood / crystalloid type. The cooler-heater water source may be operated to supply water to both the artificial lung heat exchanger and the cardioplegia delivery system. The air bubble detector may be placed on the line between the venous reservoir and systemic pump, between the pump and membrane artificial lung inlet or between the artificial lung outlet and arterial filter (neither shown) or on the line after the arterial filter (red). One-way valves prevent retrograde flow (some circuits with a centrifugal pump also incorporate a one-way valve after the pump and within the systemic flow line). Other safety devices include an oxygen analyzer placed between the anesthetic vaporizer (if used) and the artificial lung inlet and a reservoir level sensor attached to the housing of the hard-shell venous reservoir (on the left). *Arrows*, directions of flow; *X*, placement of tubing clamps; *P*, pressure sensor and *T*, temperature sensor. <5>

They are usually located proximal to the gas exchanging section of the circuit to minimize the risk of releasing microbubbles of gas from the blood, which could occur if blood is warmed after being saturated with gas. An additional risk of heat exchangers is water leakage into the blood path.

The heat transfer surface is usually made of stainless steel, aluminum, or polymers. To maximize heat efficiency of heat transfer, designers try to maximize the available surface area for heat exchange by using fins extending into the blood. Finning reduces the number of water channels, which in turn simplifies construction of the heat exchanger and decreases the potential number of places where fluid leaks might occur. Blood and water flow in counter-current or in cross-flow.

Although at times hot and cold water is supplied from wall outlets to a mixing valve to adjust the water temperature in the heat exchangers, most commonly a dedicated stand-alone water cooler and heater is used for this purpose.

In the early days of CPB, rapid cooling was commonly used at the onset of CPB, when the circulating water is cooled to temperatures approaching 0 °C by an ice bath, thus rapidly cooling the blood.

At the conclusion of CPB the rate of rewarming is not limited by physical constraints but by concerns regarding blood damage due to overheating and bubble formation because of the lower gas solubility of warmer blood. Therefore, to prevent formation of gaseous microemboli, the temperature gradient between water and blood should not exceed 10 °C.

Besides the major venous and arterial connections and the artificial lung, heat exchanger, and pump, there are many other components to the heart-lung machine (Figure I.4).

I.2.4 Venous reservoir

The venous reservoir serves as a buffer for fluctuations in venous drainage and is a source of fluid for rapid transfusion. It is placed before the membrane artificial lung. It may also serve as a gross bubble trap for air that enters the venous line, as the place where blood, fluids, or drugs may be added, and into which the cardiotomy reservoir empties. It also serves as a high-capacitance (i.e. low pressure and thus mimicking the capacitance of the venous system) receiving chamber for venous return and hence facilitating gravity drainage of venous blood. One of its most important functions, however, is to provide time for the perfusionist to act if venous drainage is sharply reduced or stopped, to avoid pumping the CPB system dry and risking massive air embolism.

To allow adequate operator reaction time, the venous reservoir should contain a minimum blood volume ranging from 0.75 to 2.00 liter, depending on the blood flow rate. It is desirable to

minimize the volume in the remainder of the CPB circuit, to avoid excessive dilution of the blood with the physiological solution.

Various fluids, such as blood and crystalloid solutions, and drugs may be added to this reservoir. Several suction devices and systems, usually using one or more of the roller pumps, may aspirate blood and gas from the open-heart chambers (hence the term “cardiotomy suction”), surgical field, aortic root (during aortic cross-clamping as a left-ventricular vent and after unclamping as an air vent), and left ventricular vent. This blood is then passed into the cardiotomy reservoir, which may be incorporated in the housing of an open (hard-shell) venous reservoir or may first flow into an external cardiotomy reservoir before being emptied into a separate venous reservoir.

Hard-shell reservoirs have the advantage of measuring volume easily, of handling venous air more effectively, of often having larger capacity and being easier to prime, and of permitting application of suction for vacuum-assisted venous return. The soft bag reservoirs eliminate the gas-blood interface and reduce the risk of massive air embolism because they will collapse when emptied and do not permit air to enter the systemic pump.

I.2.5 Cardioplegia

A cardioplegia delivery and / or coronary perfusion system is another component that typically uses one of the roller pumps for administering blood or cardioplegic solution to the coronary arteries, aortic root, or coronary sinus. This circuit usually includes a separate heat exchanger and may include a reservoir and sometimes a recirculation line from the surgical field, which is used when cardioplegic solution is not being administered into the heart, although a single pass delivery system is more commonly used.

I.2.6 Filters

A number of filters (macro or micro) is often included at various locations in the CPB circuit (e.g. cardiotomy reservoir, venous reservoir, artificial lung, and arterial line). Multiple strategies have been suggested to reduce the hazards of embolization, but the most obvious is the use of micropore filters. Two types of micropore filters are available. A depth filter consists of packed fibers or porous foam. It has no defined pore size, but presents a tortuous large wetted surface that filters by impaction and absorption. Screen filters are usually made of woven polymer thread which has a defined pore size and filters by interception. However, the smallest pore screen filters (0.2 to 5.0 μm, used for prebypass filtration) are made of membranes. They block not only particulate emboli but also gross and microscopic air emboli.

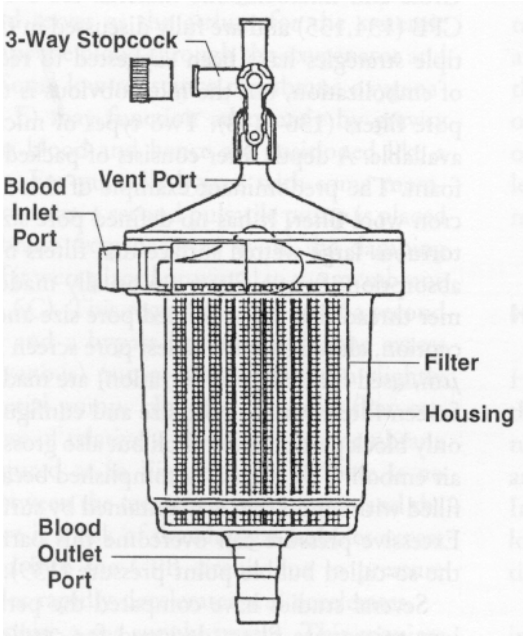

Figure I.5: A conventional adult arterial line microfilter and bubble trap. Blood enters tangentially at the top (left), which encourages any possibly entrained bubbles to rise to the top where they are vented out through a continuous purge line connecting the three-way stopcock to the cardiotomy or venous reservoir. Blood then passes through a screen microfilter (20 to 40 μm pore size). <5>

I.2.7 Miscellany

An adjustable clamp or remote venous line occluder regulates the main venous drainage line. A separate tubing clamp is used on the systemic flow line whenever the patient is not on CPB to prevent backflow out of the arterial cannula, particularly when a centrifugal pump is used.

A source of oxygen, air and sometimes carbon dioxide, with appropriate flow meters and blenders, supplies ventilating gas to the artificial lung, usually through an in-line anesthetic vaporizer.

Also included are sampling ports (pre- and post-artificial lung), pressure-monitoring sites such as the cardioplegia-coronary perfusion delivery line and the arterial line (after the systemic pump but before the arterial filter), and arterial and venous in-line blood-gas monitors. Temperature monitoring at the water inlet and outlet of the heat exchanger, of the venous and arterial blood and of the cardioplegic solution, are also present.

Whenever a centrifugal pump is used, a flow meter must be included in the systemic outflow line. Various safety devices and monitors, besides those already mentioned, are frequently incorporated into the CPB circuit. These include: a bubble trap on the arterial line with a microfilter incorporated; a purge line including a one-way valve which drains back to the venous or cardiotomy reservoir; a bypass line that goes around the arterial filter in case the latter becomes obstructed; an air bubble detector on the systemic flow line; a low-level alarm on the

Figure I.6: Charles Lindbergh and Alexis Carrel with the first pump oxygenator. <71>

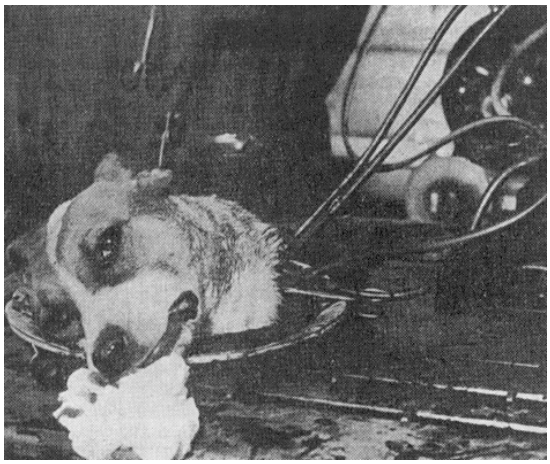

Figure I.7: Guillotined head of a dog in perfusion experiments of Brukhonenko and Tchetchuline. This preparation relied on gas exchange from a second donor dog's lungs. <72>

venous reservoir.

Minimizing blood trauma, prime volume, resistance to flow, and avoiding leaks (either outward blood flow or aspiration of air), are considerations in the selection of tubing and connectors. Keeping tubing as short as possible will reduce prime volume, pressure gradients (resistance to flow), and blood trauma.

I.3 The heart-lung machine: history and development

Cardiopulmonary bypass hinges on twin postulates:

- blood circulation can be sustained by mechanical pumps while the heart is arrested
- venous blood can be artificially arterialized in an extracorporeal gas exchange device while blood flow is excluded from the lungs.

Each of these claims was established separately through animal experimentation over the course of over 100 years. Then surgeons and engineers combined the advances made by physiologists and pharmacologists and turned them into the basic tool of cardiac surgery, beginning in 1951. A number of developments made the transition from the research laboratory to clinical open-heart surgery possible and they occurred successfully in the Department of Surgery at the University of Minnesota.

I.3.1 Historical background

The concept of blood perfusion and of a mechanical device for blood oxygenation originated in the 19th century. In 1812, César-Julian-Jean LeGallois <73> suggested that a part of the body might be preserved by some sort of external perfusion device. This suggestion was based on the observations of other investigators that some tissues and organs of apparently dead animals could temporarily be brought back to a seemingly living state by restoring the flow of blood to them.

The success of such perfusions, however, depended on the use of oxygenated blood <74>. The hardest problem in designing a mechanical CPB device was supplying an adequate amount of oxygen to the blood. Brown-Sequard recognized the need to oxygenate the blood and used syringes for perfusion. He putted oxygen into the dark venous blood by beating the blood vigorously.

In 1882, Waldemar von Schroder <76> introduced the technique of bubbling the blood. The "bubbling" method was based on the supposition that a thin layer of blood would surround the bubbles of a gas such as air or oxygen. In turn, that layer would absorb oxygen, give off carbon dioxide, and then burst and leave the blood free of gas. However, this technique was unsatisfactory because of the foaming of the blood and the gas embolism. Those difficulties could not be overcome until anti-foaming agents became available <77>.

In 1932, von Euler and Heymans <78> introduced a variant of the bubbling method, the "spraying" technique. This technique however, caused far too much damage to the blood to be useful.

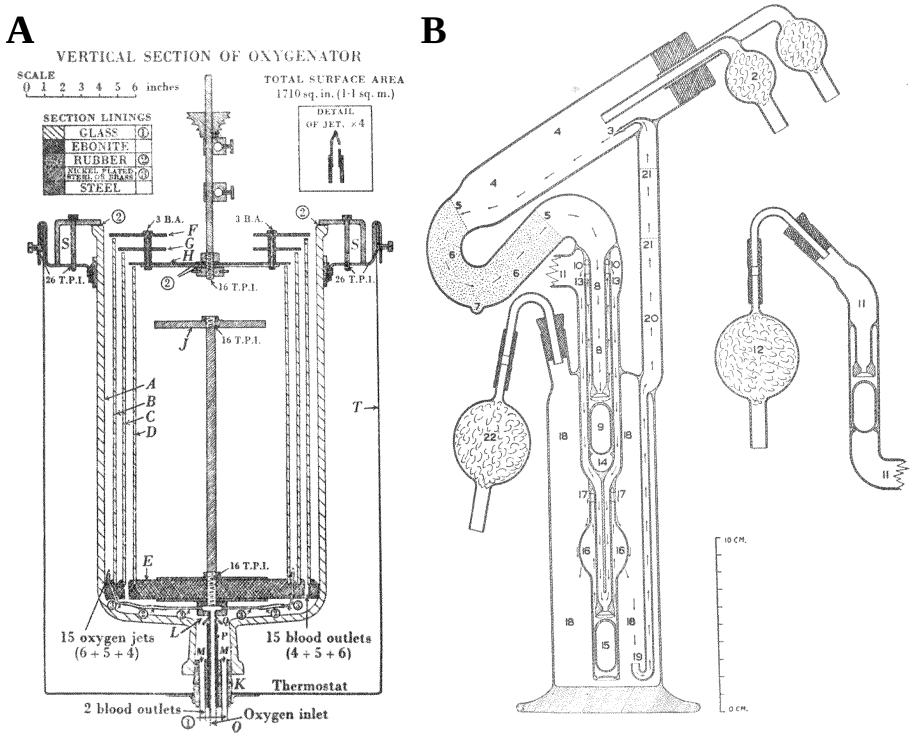

Figure I.8: A: Film oxygenator of Daly and Thorpe. This device was used for isolated dog heart preparations. Defibrinated blood was dispersed from jets onto spinning discs (*F, G, H*) where it filmed down three concentric glass cylinders (*A, B, C*). An arrangement of oxygen jets at the base provided an oxygen-rich atmosphere for gas exchange. Oxygenated blood drained through two blood outlets (*M*) to a reservoir through a filter and then into the left or right atria of the isolated heart. **B:** Perfusion system of Lindbergh and Carrel. This elaborate blown-glass device provided sterile pulsatile perfusion of various organs using regulated compressed air to vary the pressure and perfusion rate. The perfusion fluid passed from the reservoir chamber (18), which was under pulsating pressure, into the mouth of the feed tube (19) and through the feed tube (20) where it was filtered by two platinum screens (21). The fluid then passed through the cannula, through a silica sand filter (6), past the upper (9) and lower (15) floating valves which prevented back flow of the fluid, and then to the starting point in the reservoir chamber (18). The organ chamber is the slanted portion (4) at the top. Cotton-filled bulb chambers (1, 2, 12, 22) prevented bacterial contamination of the organ and circulating fluid. Floating glass valves and other chambers provided regulation of internal and external pressures on the organ. The perfusate was filtered through a column of silica sand (6). Temperature of the organ and circulating fluid was maintained by placing the entire apparatus in an incubator. The perfusion fluid was oxygenated by surface contact with the oxygen rich gas mixture. <71,72,75>

The best technique for oxygenating the blood was the "filming" method, proposed in 1885 by Max von Frey and Max Gruber <79>. This method was founded on the hypothesis that a sufficiently thin film of blood exposed to oxygen would provide a good mechanism for gas exchange. Blood was dispersed as a thin film inside a rotating slanted cylinder filled with oxygen. The oxygenating capacity, however, was quite small and sufficient only for perfusion of isolated organs. The method of Richards and Drinker <80> filmed the blood by having it flow down a cloth cylinder inside an oxygen chamber. The method of Bayliss et al. <81> dispersed the blood over the surface of a series of cones. Instead of using cones, Daly and Thorpe's device <82> dispersed and filmed the blood on a glass cylinder down which it descended (Figure I.8A).

Patterson and Starling <83> and Hemingway <84> oxygenated the blood with the help of the animal's own lungs. Others used the repetitively inflated lungs of a second "donor" animal <85-87> (Figure I.7 and Figure I.9). Brukhonenko used this technique in an attempt to bypass the nonfunctioning hearts of dogs <85,88>. Although unsuccessful, Brukhonenko's vision was remarkable because it seems clear that he recognized the ultimate value of CPB and its potential use in humans. However, using the lung of a human "donor" would never be judged entirely safe and practical, despite Lillehei's short-lived controlled cross-circulation (1954-1955) <89,90>. In the 1930s, Carrel and Lindberg <91-94> (Figure I.8B) pioneered the science of surviving organ perfusion and identified many of the obstacles to function preservation during prolonged artificial blood circulation.

The discovery of heparin, in 1916 <95>, made successful extracorporeal circulation possible.

Thus the basis for CPB had now been laid in the first decades of the 20th century, but that did not suffice for a method that would be applicable when building an apparatus for human use.

I.3.2 Hypothermia

The pioneers of hypothermia, Bigelow <96>, Lewis <97,98>, and Swan <99>, demonstrated the feasibility of temporarily lowering the body temperature to decrease tissue metabolism and consequently also perfusion needs during surgery. Moderate hypothermia (28-30 °C), also referred to as surface hypothermia because the patient was immersed in ice-cold water before cardiac surgery, served to lower body temperature and metabolism and allowed a period of circulatory arrest. The world's first successful operation within the open human heart under direct vision occurred on September 2, 1952. Dr. F. John Lewis, after a period of laboratory research on dogs, successfully closed a secundum atrial septal defect (ASD) <97> in a 5-year old girl under direct vision using inflow stasis and moderate total body hypothermia. Dr. Lewis had

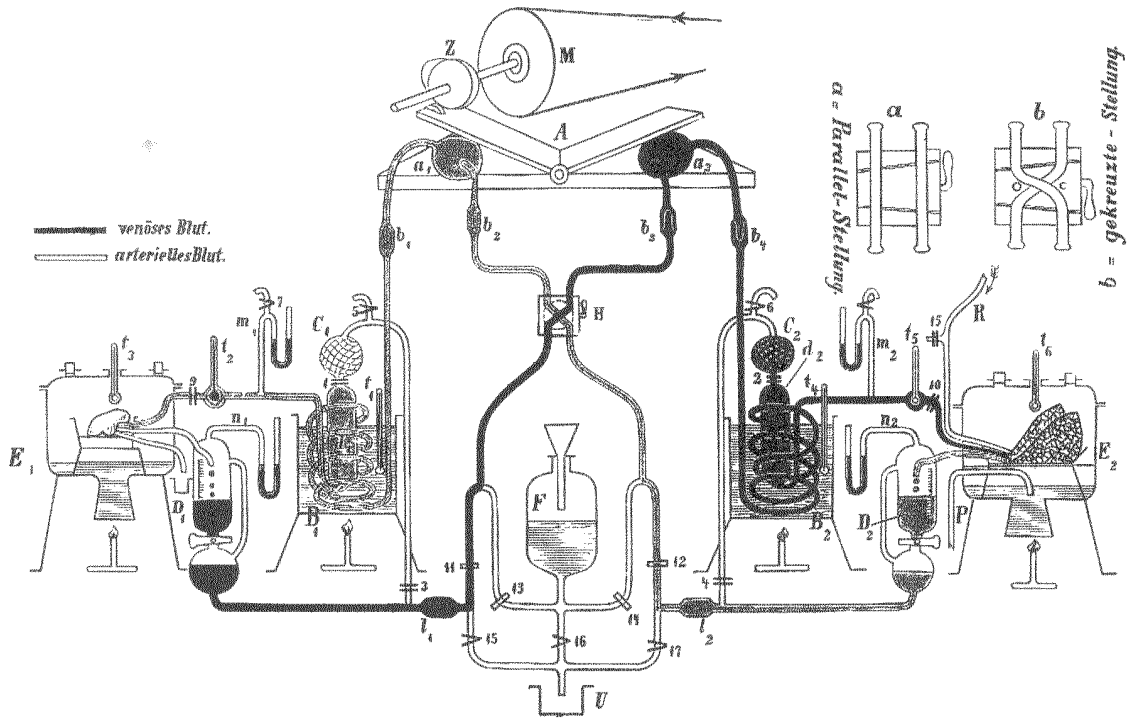

Figure I.9: Organ perfusion apparatus of Jacobi. This complex device relied on ventilated (*R*) donor longs (chamber E_2, right) to provide gas exchange. At the top center, a rotating cam (*M*) and hinged plates (*A*) arrangement alternately compressed bulbs (a_1 and a_2) to pump blood to the organ to be perfused (chamber E_1, left). <72>

been inspired by Bigelow's experimental studies <96> on general body hypothermia as a technique for open-heart repairs. Hypothermia with inflow stasis proved to be an excellent method for simple atrial defects and isolated congenital pulmonic or aortic stenoses <98,99>. However, failure was uniform when this technique was applied to more complex lesions. These experiences reconfirmed the oft-predicted need for a perfusion method for the more complex intra-cardiac lesions.

Surface hypothermia was relatively safe but time-consuming and inefficient since external cooling was slow to reach the vital organs in the major body cavities. Therefore, heat exchangers were inserted in extracorporeal blood circuits to achieve core hypothermia, that is, rapid cooling of organs and tissues. Core hypothermia combines the advantages of mechanical cardiopulmonary support with those of reduced oxygen needs. Additionally, hypothermia allows a margin of safety in the event of mechanical breakdown. Furthermore, critical organs (e.g. the brain) are protected by hypothermia for a period of 10-12 minutes if the blood flow ceases.

I.3.3 Cardiopulmonary bypass: initial efforts

The first attempts to use a heart-lung machine for total CPB to permit intra-cardiac surgery in humans were carried out by Dennis et al. on April 5, 1951 <100>. Dennis used the rotating screen

oxygenator he had developed in Minnesota. Two patients were operated on within a month's time but both died in the operating room. The failures were related to the high perfusion rates that were considered necessary. Other scientists who clinically used extracorporeal circulation in the early 1950s were Dogliotti <101> and Helmsworth <102,103>.

The next milestone was reached in May 1953 by Dr. John Gibbon <105>, who had started work on a "pump-oxygenator" in the 1930s. Inspired by the tragic death of a woman with a pulmonary embolism and faced with the apparent impossibility of shunting the blood around the obstacle, he would attempt to build an apparatus that could take over all the functions of the heart and lungs for a period of time. This heart-lung machine that would make possible operations on the heart itself and even inside its chambers, a heart-lung machine that would make CPB a reality. Gibbon's initial laboratory models of blood oxygenators relied on rotating cylinders to spread blood in a thin film in the tradition of von Frey and Gruber (Figure I.11). His clinical model, built with technical support from IBM, was a stationary oxygenator, a bulky device in which venous blood was evenly smeared over a stack of vertical wire screen meshes in an oxygen atmosphere, gently flowing downward to accumulate in a reservoir from where blood could be returned to a systemic artery. On May 6, 1953 he successfully operated on a patient with an atrial (secundum) defect <106> with the Gibbon-IBM heart-lung machine (Figure I.10). However, at the time there was little enthusiasm or interest for Gibbon's technique among cardiologists and cardiac surgeons. There were several reasons for this. Firstly, Dr. Gibbon only once repeated Dr. Lewis' successes beginning 8 months earlier and could not repeat or extend his one success

Figure I.10: Dr. Gibbon with the Gibbon-IBM heart-lung machine and the patient he saved with it. <104>

<106,107>. Secondly, Dr. Lewis was regularly closing atrial septum defects under direct vision using inflow stasis and moderate hypothermia with excellent results <97,98>. Thirdly, Dr. Gibbon himself abandoned open-heart surgery as a means to repair human heart lesions after five failures on atrial septum defects.

From 1951 until the beginning of 1954, there were many reported attempts to use CPB for intra-cardiac operations. However, there was one common scenario: good-to-acceptable survival in the experimental animals but universal failure when the same apparatuses and techniques were applied to humans. What was necessary, many thought, was a means of mechanical support for the heart during its recovery period.

I.3.4 The "azygos flow" concept

It has been observed repeatedly by Dennis et al. <100>, Gibbon <106>, and Helmsworth et al. <103> that one of the universal problems in a very large part of the early failures with ECC was the enormous and unexpected blood return out of the open hearts due to well-developed systemic-to-pulmonary collaterals, which made accurate vision almost impossible.

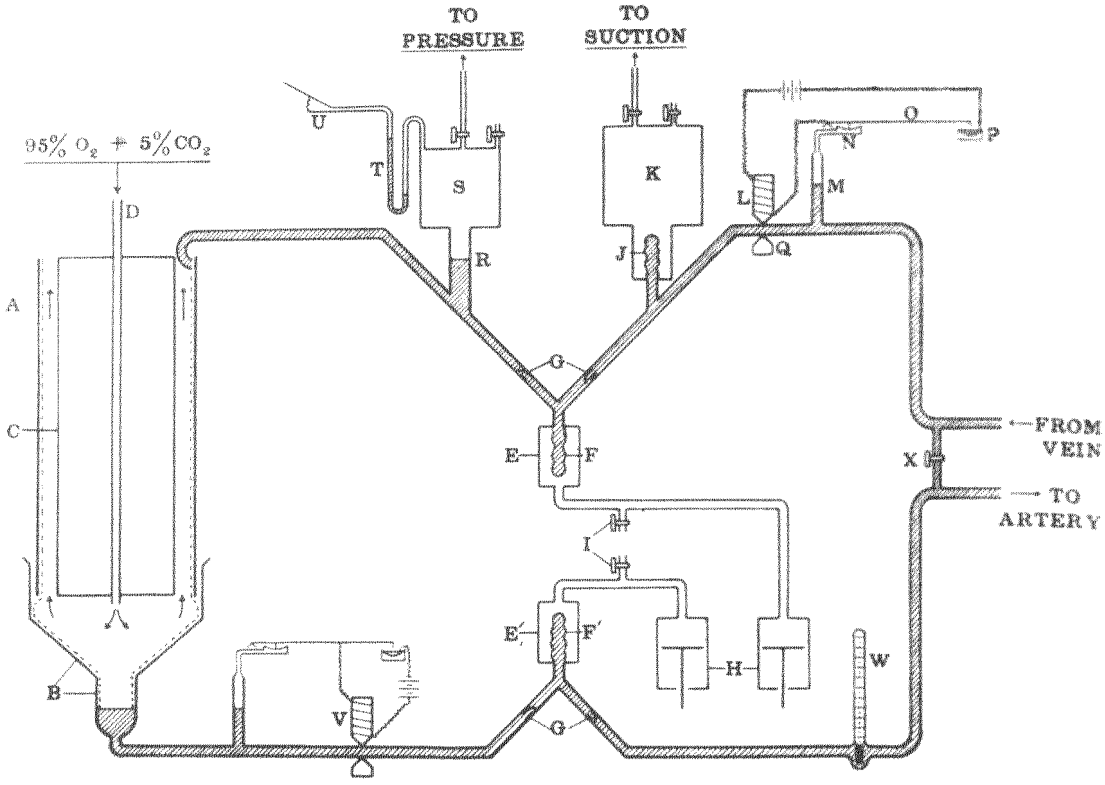

Figure I.11: Early extracorporeal circuit of Gibbon. Venous blood was withdrawn by a finger-cot pump (*E, F*) and transmitted to the inner wall of a vertical rotating cylinder (*A*, left) where it was exposed to an atmosphere of 95 % oxygen and 5 % carbon dioxide for gas exchange. Using this apparatus, Gibbon and his wife were able to support the cardio-respiratory needs of cats for up to 68 minutes during occlusion of the pulmonary artery. <72>

During some canine experiments in which the cavae were temporarily occluded to test tolerance limits of the brain and heart to ischemia <108,109>, it was discovered that if the azygos vein was not clamped (but all other inflow to the heart was), the resulting very small cardiac output (8 to 14 ml/kg/min) was sufficient to sustain the vital organs (brain, liver, heart and kidneys) safely in every animal for a minimum of 30 minutes at normothermia. The universally accepted minimum flow or basal cardiac output for CPB at normothermia was at that time considered to be 100 to 165 ml/kg/min in animals and humans <100,106,110>. Both studies however, confirmed that only about 10 % of the so-called basal cardiac output was needed to sustain animals unimpaired physiologically for a reasonable period at normothermia.

With the basal cardiac output, venous blood returned with 65 % to 75 % of its oxygen content unused. There was no physiologic harm whatsoever in fully using the oxygen contained in the blood. Thus, the "azygos flow was really not low flow, but physiologic flow" <111>. This low flow or physiologic flow quantity was only 10 % to 20 % of what others deemed necessary. Consequently, successful open-heart surgery was to be expected in the near future.

The low-flow principle made autogenous lung oxygenation much simpler and thus also more attractive. However, due to kinking problems of the extra cannulae and tubing in the operative field in animal studies, these extrapulmonary cannulae were completely removed from the operative field by using a separate donor animal for oxygenation (cross-circulation) <112>. Dodrill et al. <113>, in collaboration with the General Motors Corporation engineers in Detroit, developed a blood pump for animal and clinical use as a right, left or combined heart bypass with autogenous lung oxygenator. However, their use of high flow rates led to a significant amount of collateral flow within the bypassed heart, making it difficult to open the heart without sizable blood losses, which made therapeutic maneuvers difficult or even impossible.

I.3.5 Hemodilution

In the early days of cardiopulmonary bypass when the highest achievable perfusion flow was often much below the resting cardiac output, hemodilution implied a diminished oxygen-carrying capacity of the blood and less metabolic support of the tissues. It was therefore to be avoided. However, the blood banks could no longer supply all the blood requested for a growing number of surgical procedures and dilution was unavoidable. Hemodilution was a major technologic advance in ECC <114,115>: the "pump-oxygenator" could be primed with non-blood solutions (saline, physiologic salt solutions, plasma expanders), thereby immensely reducing the need for donor blood and at the same time improving the quality of perfusions by a reduction in viscosity and improving the safety by reducing foreign blood transfusion. Hemodilution also

improves renal blood flow and tissue perfusion and diminishes hemolysis rates. DeWall et al. <116,117> confirmed the benefits of hypothermic hemodilution in ECC.

I.3.6 Controlled cross-circulation

Lillehei et al. <89,90> used controlled cross-circulation with physiologic flow (the "azygos flow concept") on dogs to permit some open-heart experience on animals without the need for a complex conventional "pump-oxygenator". The term "controlled" refers to the use of a pump to precisely control the balance of the volume of blood flowing into and out of the donor and the patient. Cross-circulation for clinical intra-cardiac operations (mainly correction of congenital

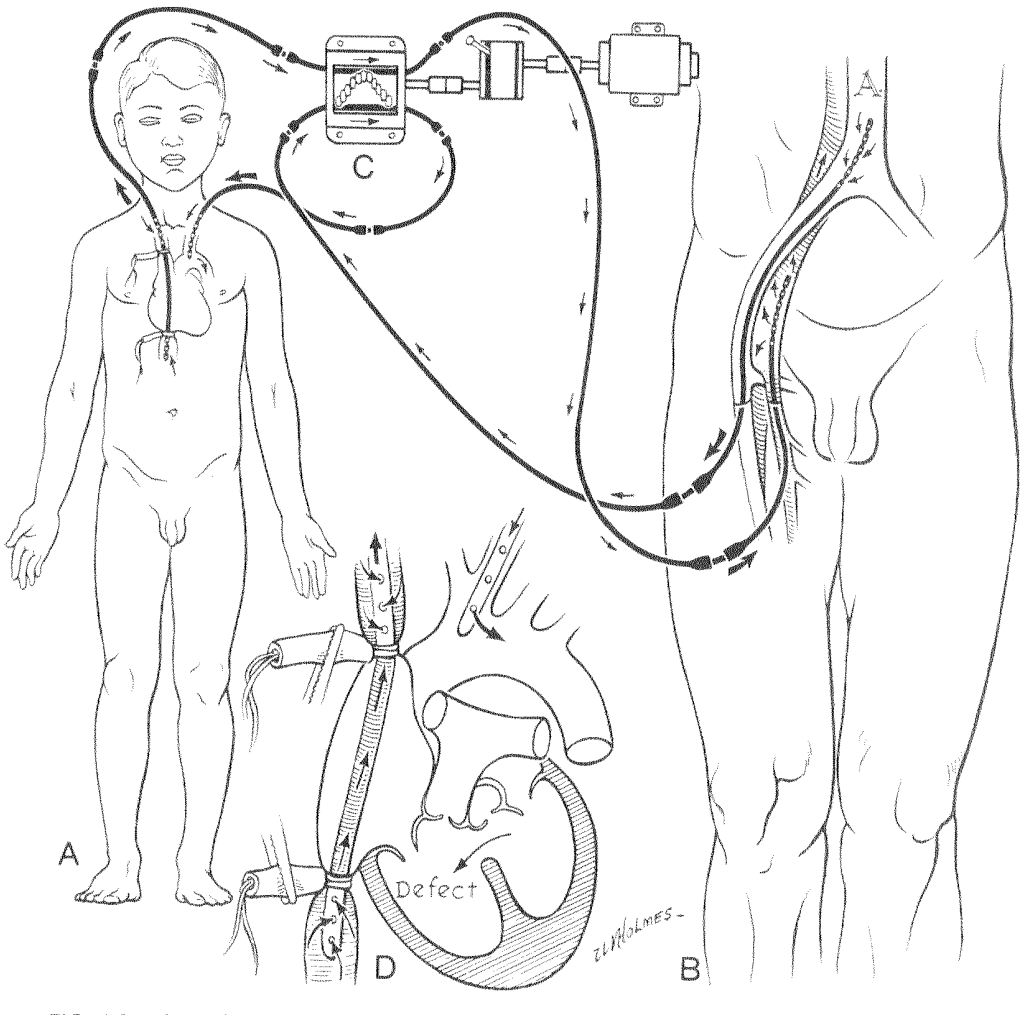

Figure I.12: Direct-vision intra-cardiac surgery using extracorporeal circulation by means of controlled cross-circulation. **A:** The patient, showing sites of arterial and venous cannulation. **B:** The donor, showing sites of arterial and venous cannulation. **C:** The single Sigmamotor pump controls the reciprocal exchange of blood between the patient and donor. **D:** Close-up of the patient's heart. The arterial blood from the donor was circulated to the patient's body through the catheter that was inserted into the left subclavian artery. <118>

heart defects) was an immense departure from established surgical practice at the time (1954) (Figure I.12).

Lillehei (1954) paired a healthy adult donor with a blood-compatible child in need of surgical

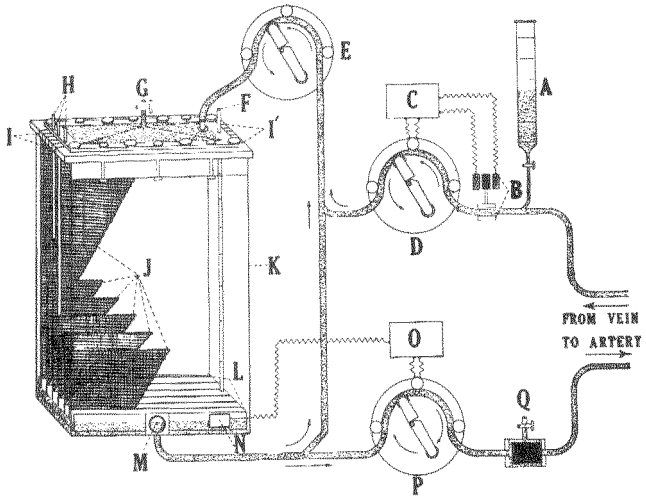

Figure I.13: Stationary screen extracorporeal circuit used by Gibbon in animal experiments just before clinical applications. Two roller pumps (D, P) are used to withdraw and reinfuse blood from the animal. A third roller pump (E) recirculates oxygenated blood by withdrawing it form the tubing line to the arterial pump (P). This maintained a constant supply of blood that was filmed down a series of screens (J) contained in an oxygen-rich atmosphere for gas exchange. A screen filter with stopcock (Q) is located in the arterial tubing line for blood filtration just before its reinfusion into the animal's artery. <72>

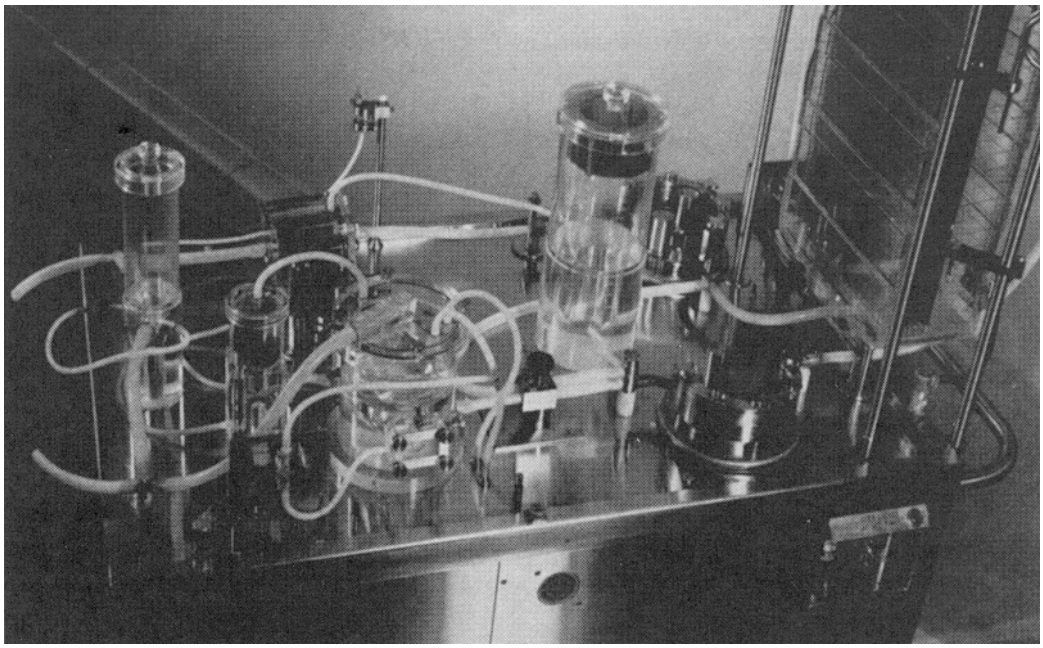

Figure I.14: The Mayo Clinic-Gibbon screen oxygenator. This model was used in 1955 during the first series of open-heart operations performed by Dr. John Kirklin and associates at the Mayo Clinic, Rochester, Minnesota. <118>

repair of a cardiac malformation <89> (Figure I.15). Cross-circulation was used exclusively from March 26, 1954 through February 1955 for 45 operations. Twenty-eight patients undergoing ECC survived their operation and were discharged from the hospital.

Cross-circulation was reserved for high-risk patients. By July 9, 1955 the bubble oxygenator had become the sole method. There was no donor mortality and no long-lasting donor sequelae <119>. Cross-circulation was so successful because the donor automatically corrected all the various hematologic and metabolic derangements. The homeostatic mechanisms of the donor automatically corrected the untold number of most, at that time, unknown physiologic aberrations evoked by total body perfusion. The spectacular success of clinical cross-circulation operations stimulated intensive laboratory work on alternative methods for CPB without the need for a living human donor.

Other bypass methods (bubble oxygenator, dog-lung and monkey-lung oxygenator <121-123> and arterial reservoir <89,124>) were used for lower risk patients.

I.3.7 Heterologous biologic oxygenators

Beginning on March 1, 1955, a series of clinical open-heart operations was started at the University of Minnesota using a pair of canine lungs as oxygenators (heterologous lung oxygenation), following an approach taken by Jacobi <87> and Brukhonenko <85,88>. Twelve

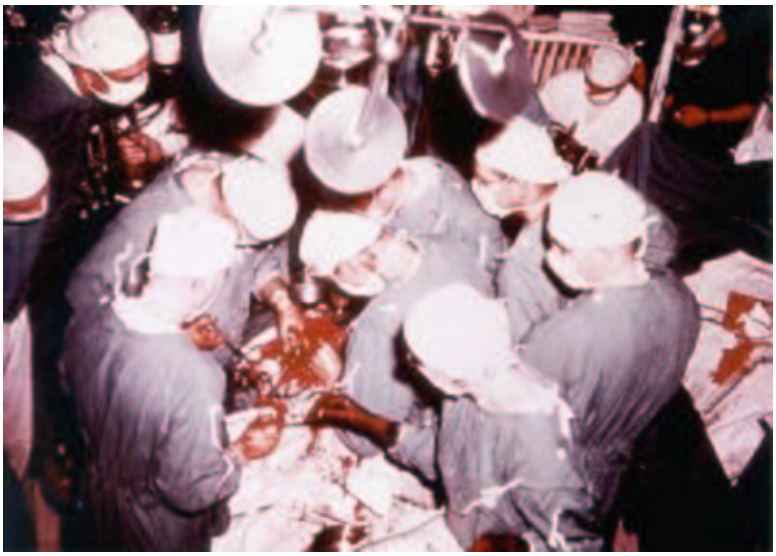

Figure I.15: The scene on March 26, 1954 in Operating Room B, University of Minnesota Medical Center, during the first controlled cross-circulation operation. At that time, a ventricular septal defect was successful visualized by ventricular cardiotomy and closed in a 12-month-old infant. Dr. Lillehei is on the patient's left with headlight; Dr. Richard Varco is the first assistant across the table. Arterial and venous cannulae from the father's groin can be seen on the right. <120>

patients were operated on, with four longterm survivors <122,123>. Mustard and associates <121> used monkey lungs, but there were only three survivors in their series of 28 patients between 1952 and 1956. The fragility of animal lungs and the risk of transmitting infections made this technique clinically precarious. This technique was abandoned once mechanical oxygenators became available.

I.3.8 Extracorporeal circulation from a reservoir of oxygenated blood

On March 3, 1955, the first of a series of five infant patients was operated on at the University of Minnesota for intra-cardiac repairs of ventricular septum defect or transposition of the great vessels by continuous perfusion from a reservoir of oxygenated blood <89,124,125>. The arterialized venous blood for perfusion was drawn in the blood bank a few hours preoperatively using an ordinary venipuncture on donors whose arms had been immersed in water heated to 45°C for 15 minutes before collection, which effectively oxygenated the venous blood.

I.3.9 The mechanical “pump-oxygenator” for cardiopulmonary bypass

The main problems with Gibbon’s clinical model, besides its cumbersome dimensions, were to avoid blood streaming and to maintain a constant blood-gas exchange area. Other investigators tried to increase the flexibility of the system by replacing the stationary film support with rotating screens or rotating discs partly immersed in a pool of blood. This allowed some control of gas transfer performance by changing the rational speed, but minimizing the blood content of the device dictated a tight fit between the discs and the horizontal glass cylinder surrounding them.

In two publications in 1955 from the Mayo Clinic, Jones et al. <126> and Donald et al. <127> described their experimental results using the design of the Gibbon-type screen film “pump-oxygenator” as originally built by IBM and modified by the Mayo Clinic (**Figure I.13** and Figure I.14). Their first clinical application was on March 22, 1955. Four out of eight patients survived <128>. By September 1958, 245 patients had been operated on at the Mayo Clinic by Kirklin et al. <129>. The Gibbon-type “pump-oxygenator”, however, was very expensive, handcrafted, and very impressive in appearance but difficult to use and maintain.

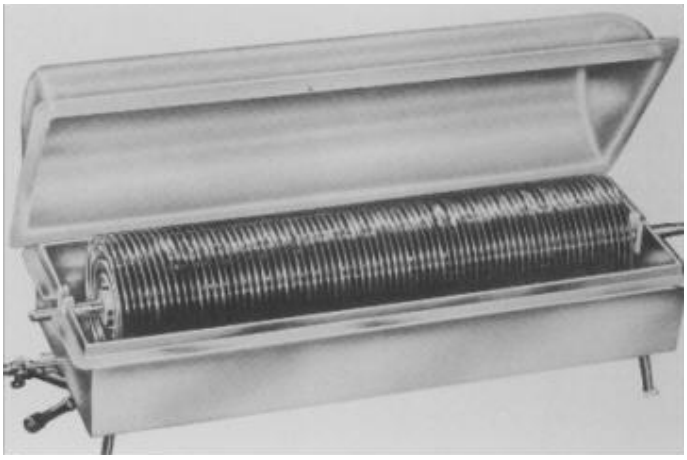

Figure I.16: The Sarns disc oxygenator took the form of a stainless steel shell with a lexan plastic cover material from General Electric. The oxygenator featured less priming volume, an anti-vortex blood outlet, and easier disassembly and cleaning. Nurses spent enormous amounts of time disassembling, cleaning and maintaining hundreds of parts used in the early open-heart surgeries. The materials of choice were stainless steel, Pyrex glass, silicon rubber, and latex tubing that was routinely autoclaved and used in surgery repeatedly. In those days the surgeons spent vast amounts of time in the laboratories perfecting their skills and running the equipment. They knew how everything worked and demanded high quality. <70>

I.3.10 The rotating disc film oxygenator (Kay-Cross)

In 1956, Dr. Frederick Cross and Earl Kay developed a rotating disc oxygenator, the Kay-Cross apparatus <130-132> , which was widely used in the later 1950s, particularly in the United States. It had multiple vertical discs placed on a horizontal axis that rotated, with the discs dipping into a pool of venous blood, creating a film on the discs in an atmosphere of oxygen. Although the device was nondisposable, difficult to sterilize and had large priming volumes and clinical limitations (rapid loss of efficiency if hemodilution was attempted), it became commercially available in contrast to the Mayo Clinic-Gibbon machine. The Kay-Cross filming unit appealed to cardiac surgeons who at that time could not or refused to believe that bubble oxygenation was more efficient, safer, ideally adapted for hemodilution, simpler to use and less expensive than the filming units. Foaming and hemolysis were encountered at high disc spinning velocity, and these designs were eventually abandoned. Nevertheless, the spinning disc oxygenator was in clinical use in Uppsala and Stockholm for almost 20 years <133>. Figure I.16 depicts a disc oxygenator designed by Richard D. Sarns <70>.

I.4 The bubble oxygenator

The very first strategy of physiologists to exchange oxygen and carbon dioxide in venous blood had been to let pure oxygen bubble through a stationary blood pool. To turn this batch process

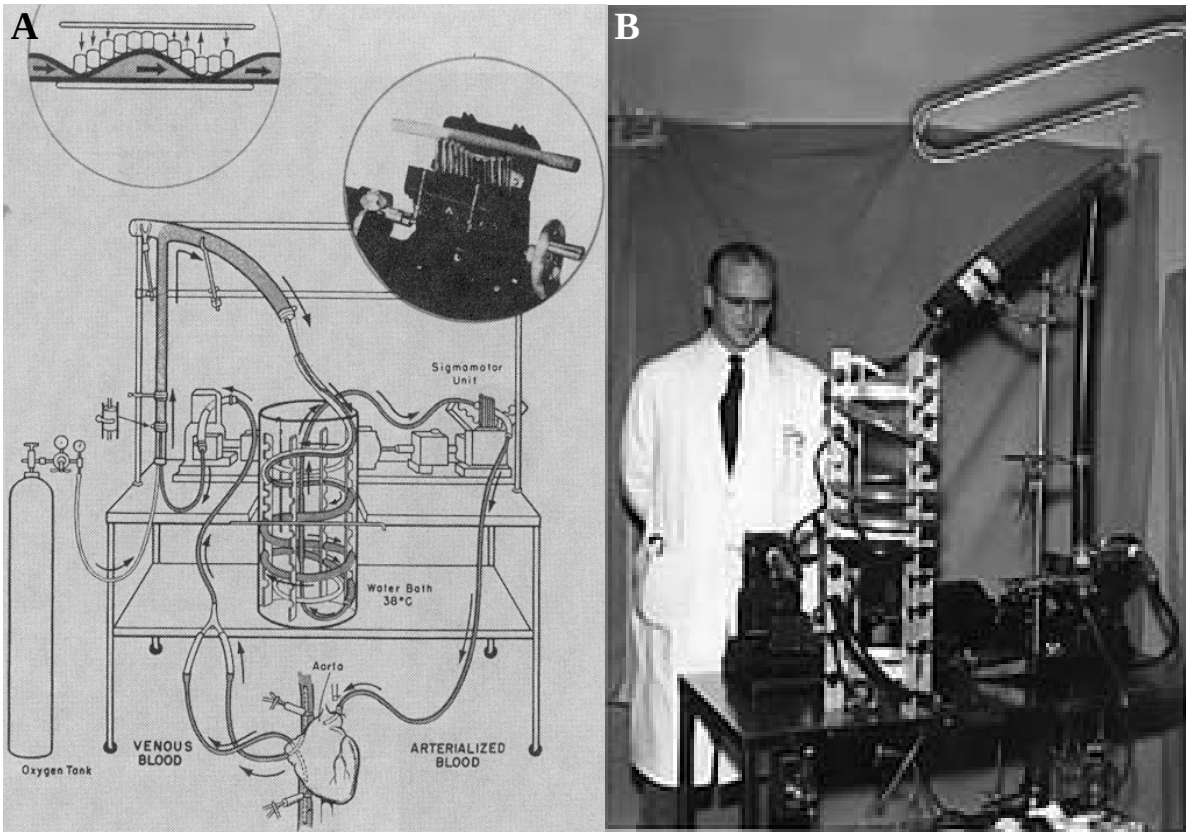

Figure I.17: A: Diagram of the 1955 DeWall-Lillehei helix reservoir, disposable bubble oxygenator for adult surgery. The upright oxygenating column with the venous blood mixing with oxygen bubbles formed at the base, transverse debubbling chamber, and the spiral (helix) debubbling reservoir immersed in a water bath are evident. The two insets show the wavelike pattern of the Sigmamotor pump's "fingers" <118> **B:** DeWall and the bubble oxygenator. <104>

into a continuous operation for total body perfusion, blood was collected through cannulae from the central veins by a siphon or a pump. It was driven upward in a vertical chimney, mixed with a stream of oxygen gas bubbles, and finally passed through filters and defoaming sponges to collect bubble-free arterialized blood, which could then be used to perfuse the arterial tree.

I.4.1 Development of the bubble oxygenator

Before 1955, there was universal agreement among the world's authorities on ECC that blood could *not* be arterialized for clinical CPB by a bubble oxygenator because of potential problems with air embolism.

However, on May 13, 1955, DeWall and Lillehei, began routine clinical use of a simple disposable helix reservoir bubble oxygenator, based on their dog laboratory research. In their first report, Lillehei et al. described surgery on seven patients, all of whom awoke postoperatively, without any evidence of neurological, hepatic, or renal impairment <134,135>. The operations took place at normothermia with perfusion rates of 25 to 30 ml/kg/min. As the

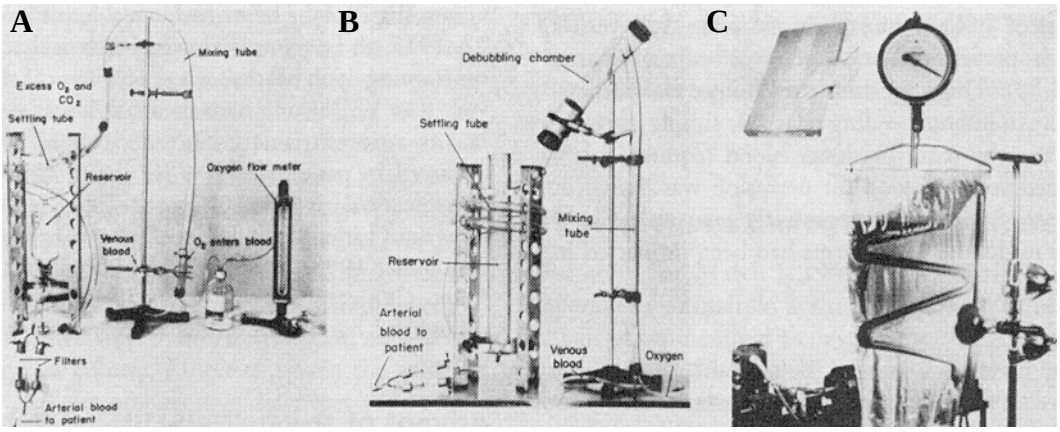

Figure I.18: Evolution of the simple disposable DeWall-Lillehei bubble oxygenator for open-heart surgery. **A:** The first 1955 clinical model, successful on infants and children. **B:** Later in 1955, the helix reservoir model with adult capacity was developed. **C:** A 1956 commercially manufactured model, shipped sterile in package, ready to hang up and use. <118>

number of patients having open-heart surgery by ECC increased rapidly, the bubble oxygenator was refined to increase capacity for adult patients (Figure I.17).

Despite concerns over the potential risk for air embolism, the DeWall-Lillehei bubble oxygenator was an instant success because it had so many practical advantages. It was efficient, inexpensive, heat sterilizable, easy to assemble and check, and it had no moving parts. Because it could be assembled from commercially available materials at a small material cost, it was also disposable. The development of the self-contained unitized plastic sheet oxygenator in 1956 by Gott et al. <136,137> (Figure I.18C and Figure I.19) further improved this system and played an important role in the tremendous expansion of open-heart surgery that occurred after 1956.

Three major advances propelled the bubble oxygenators ahead of film oxygenators in the pioneering decades of cardiac surgery. The first advance was the identification of silicone-based defoaming compounds which could be smeared on top of the bubble chimney and proved much more effective in coalescing the blood foam than previously used chemicals. The second was the quantitative process analysis by Clark <77> and Gollan <138> that showed that, since small bubbles favor oxygen transfer and large bubbles are needed for carbon dioxide removal, an optimum size could be found with the aid of a sponge in the mixing chamber. Alternatively, a mix of small and large bubbles should be used. The third and practically decisive advance was made simultaneously by Rygg <139> and DeWall <140>, who replaced the assembly of glass, steel, and ceramic parts of early bubble oxygenators with inexpensive plastic components and thereby paved the way for the industrial manufacturing of disposable bubble oxygenators (Figure I.18).

In 1966, DeWall et al. <142> introduced a hard-shell bubble oxygenator with an integrated oxygenator and omnithermic heat exchanger in a disposable, pre-sterilized, polycarbonate unit. The integrated hard-shell concept has been the basis of all subsequent refinements, both in the bubble and membrane oxygenators. As a result, reusable stationary film and disc oxygenators, which required careful cleaning and sterilization, slowly disappeared, and disposable bubble oxygenators dominated the field of extracorporeal gas exchange from 1960 until the early 1980s (Travenol Laboratories, Morton Grove, Illinois, USA; Polystan, Copenhagen, Denmark; Bentley Laboratories, Irvine, California, USA). By 1976 it was estimated that 90 % of all open-heart operations worldwide involved the use of a bubble oxygenator <143>.

I.4.2 Integrated heat exchanger

Heat exchangers were inserted in extracorporeal blood circuits to achieve core hypothermia, i.e., rapid cooling of organs and tissues. Core hypothermia combines the advantages of mechanical cardiopulmonary support with those of reduced oxygen needs.

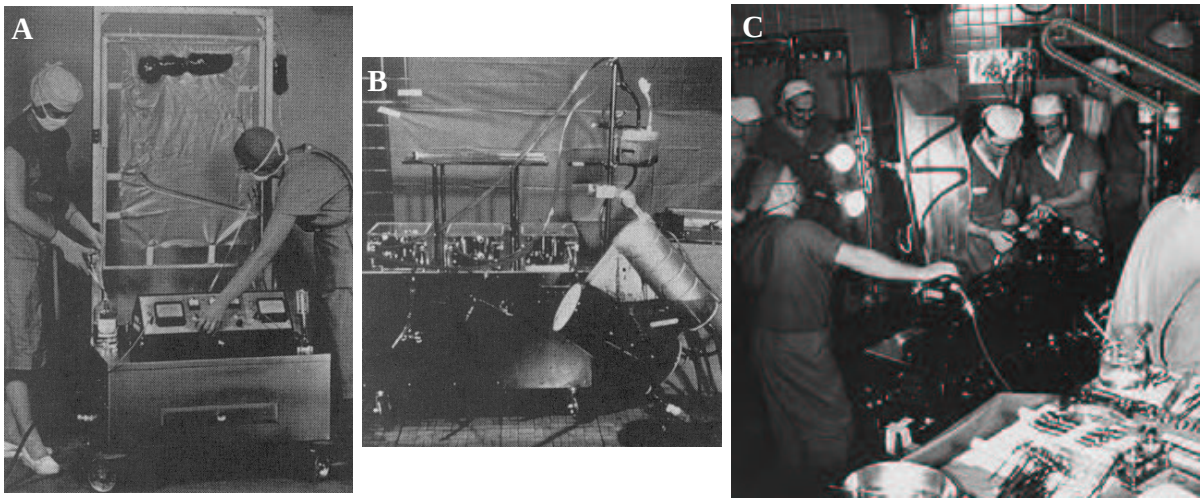

Figure I.19: A: A DeWall-Lillehei unitized plastic sheet oxygenator, commercially manufactured and shipped sterile ready to hang up, prime, and use as shown here; <118> **B:** The Temptrol disposable bubble oxygenator with self-contained heat exchanger during a perfusion. In this unit, Dr. DeWall introduced the rigid pre-sterilized plastic outer shell, which has been the basis of all subsequent oxygenator design for both bubble and membrane units. <118> It combined high gas exchange efficiency with integral heat exchange and low priming volumes. <141> **C:** Sheet oxygenator in use in the operating room. <104>

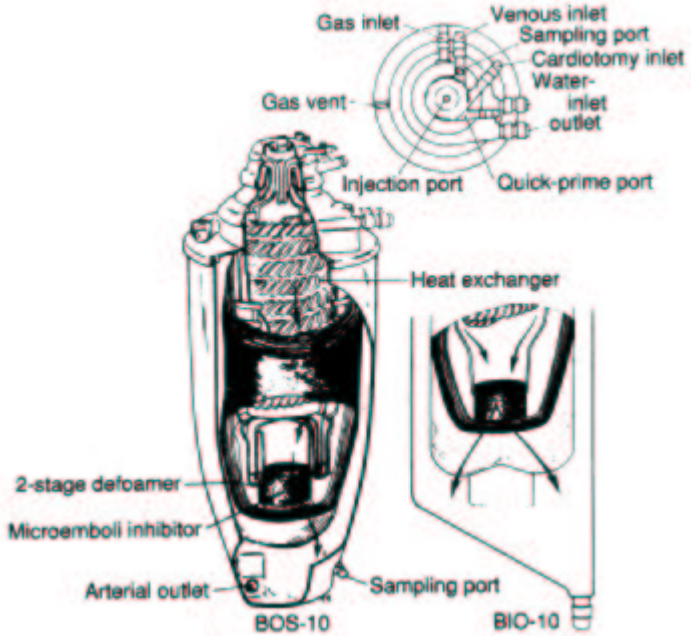

Figure I.20: Bubble oxygenator showing the mixing chamber, heat exchanger, defoamer, and arterial reservoir. <144>

In the 1970s, the bubble oxygenator was integrated with a heat exchanger (usually stainless steel coil) and placed within a clean plastic container, which also served as an arterial reservoir with a capacity of several liters of blood (Harvey H series oxygenator). The level of blood-air interface allowed direct observation of changes of blood volume in the extracorporeal circuit. This simple design feature gave the equipment operator (who eventually became known as the perfusionist) plenty of time to react to a sudden blood loss and to make compensating changes in operation. Designs were optimized to achieve adequate gas exchange with minimum gas-to-blood flow ratios, which further reduced blood damage. Examples of this group included the Bentley BOS-10, Shiley S-100, Cobe Optiflo II, and Harvey H-1500. The materials used to fabricate these devices were polycarbonate and polyurethane. A typical bubble oxygenator is shown in Figure I.20.

I.4.3 Gas transfer efficiency

The efficiency of bubble oxygenators is extremely high, because the smaller the bubbles, the larger the blood-oxygen exchange area that is developed by a steady current of gas. In the limiting case, it is even possible to saturate venous blood by introducing no more oxygen into the blood than is consumed by the tissues. This process, however, does not remove any carbon dioxide. Since the partial pressure of carbon dioxide in the excess gas vented from a bubble oxygenator, cannot exceed the carbon dioxide partial pressure in arterialized blood (and in reality

is even much lower), it follows that the carbon dioxide transfer rate of bubble oxygenators is a direct function of the volume inflow rate of oxygen. This must exceed oxygen uptake by blood and tissues several times to transfer both oxygen and carbon dioxide. Thus, the operating conditions for a bubble oxygenator are dictated to a major extent by the requirements for adequate carbon dioxide removal.

I.4.4 The advent of the membrane oxygenator

Still a number of problems occurred with bubble oxygenators because of their large blood-gas interface. If the blood foam did not coalesce completely, gaseous microemboli could be carried into the arterialized blood stream. Plasma proteins were denatured at the gas interface, leading to blood trauma associated with platelet activation and aggregation, complement activation, and hemolysis <145-147>. These problems could be ameliorated by placement of a gas-permeable membrane between the blood and gas phase.

Other oxygenators for CPB that were publicly known and worthy of mention, but which had moderate to ephemeral clinical applications were those of Rygg and Kyvsgaard <139> (bubble), Dennis <148> (film), Clark et al. <77> (bubble), Crafoord and Senning <149> (film and bubble), Clowes et al. <150> (bubble), Clowes and Neville <151> (membrane), Melrose <152> (film), and Gerbode et al. <153> (membrane).

I.5 The membrane oxygenator

Membrane oxygenators have progressively captured the largest share of the market for clinical gas exchange devices not only because their operating is less traumatic for blood but also because the blood content of the gas exchange unit is fixed. As a result volume fluctuations to calibrated reservoirs are limited and the risk of major shifts in intracorporeal blood volume during total body perfusion is minized. Membrane oxygenators were developed and used clinically in the 1950s through the 1970s, but lack of demonstrable benefit for short CPB times contributed to their infrequent use by most groups until microporous designs became predominant in the mid-1980s. Gas-permeable hollow fibers, microporous membranes, and the appreciation of secondary flows (empirically rather than analytically!) were the major advances to lead to the current generation of membrane oxygenators <10>.

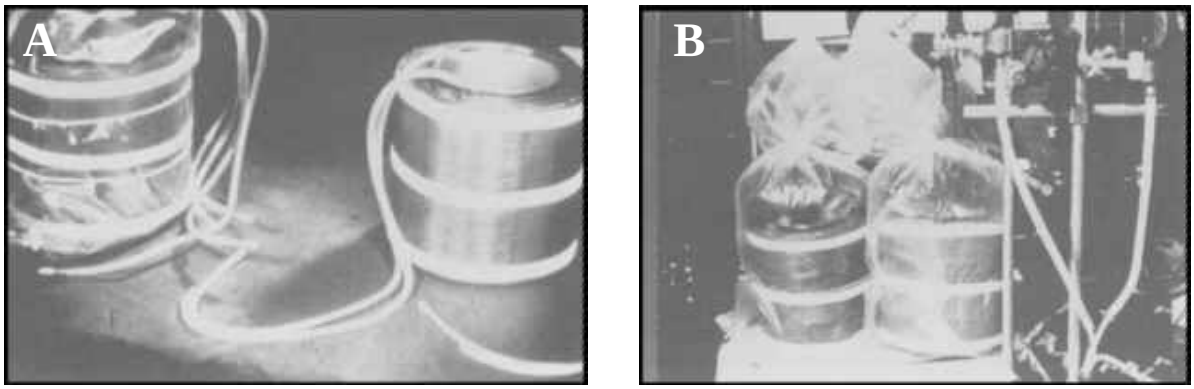

Figure I.21: A: The Kolff membrane artificial lung. The polyethylene tubing is shown compressed in a length of window screening and rolled up around a solid core in order to form the membrane lung; <155> **B:** Dr. Kolff's membrane lung ready for a clinical case. <155>

I.5.1 Development of the membrane oxygenator

In 1944, Kolff and Berk <154> observed that venous blood was oxygenated while flowing through a cellophane dialysis tube and being in contact with oxygen containing dialysate. Oxygenation was taking place across the artificial membrane. This discovery led to work on an artificial heart-lung machine. Kolff studied oxygenators which were being developed in Paris, Stockholm, and Philadelphia, but no design could yet oxygenate five liters of blood, the amount necessary to support an adult human during open-heart surgery. The idea of using membranes permeable to respiratory gases in order to separate the blood phase from the gas phase in an artificial lung, and consequently avoid the risk of foaming or the formation of thick blood rivulets inherent in bubble or film oxygenators, was stimulated after World War II by the growing availability of commercially produced thin plastic films for the packaging industry.

The two major challenges for membrane oxygenators were, and indeed remain, that no synthetic membrane could be fabricated that was as thin as the pulmonary alveolar wall, and that no manifolding and blood distribution system could match the fluid dynamic efficiency of the pulmonary circulation, where a single feed vessel, the pulmonary artery, branches over a short distance and with minimal resistance flows into millions of tiny gas exchange capillaries, the size of an erythrocyte.

The first membrane oxygenator was reported by Kolff and Balzer <156> (Figure I.21). In 1956, Kolff et al. <157> described a disposable membrane oxygenator for experimental use, a twin-coil artificial kidney design using polyethylene membranes. The membrane materials available at that time were relatively impermeable to the respiratory gases. This characteristic and the large blood channel dimensions in these units resulted in inefficient designs requiring large surface areas to

achieve adequate gas exchange. For instance, the rectangular channel or multilayer, ethylcellulose flat sheet oxygenator described by Clowes et al. <158> had a membrane surface area of 25 m². Clowes and Neville <151> described their experimental studies with membrane oxygenation and a complex apparatus they considered to be suitable for clinical perfusions in 1958.

The dialysis approach to respiratory gas exchange by Kolff <154,156,157> has retained some attractiveness for the elimination of carbon dioxide (which is highly soluble in aqueous media), either in the form of a combined artificial kidney – artificial lung (also known as klung) <159>, or a system for low blood flow hemodialysis which might allow full carbon dioxide elimination in the end-stage of a respiratory disease <10>.

The belief that membrane oxygenation renders a better perfusion than the bubble or film oxygenators has been clear only with perfusions exceeding eight hours in duration. The interest in membrane oxygenators grew from observations of reduced blood damage in these devices compared to film and bubble oxygenators. The membrane oxygenator is associated with less reduction of platelets, less complement activation, less post-operative bleeding, and fewer microemboli <160>. Because ECC times for most cardiac procedures are two to three hours or less, it has been difficult to prove that these changes, which are for the most part readily reversible, have any permanent side effects. These factors limited the clinical applications of membrane oxygenators in the 1970s and early 1980s.

Like the early direct blood-gas contact oxygenators, the early membrane oxygenators were reusable. In 1967 Landé et al. <161> described the first compact, disposable, commercially manufactured membrane oxygenator for clinical use.

I.5.2 Gas transfer efficiency

The interposition of a membrane between flowing gas and flowing blood reduces the gas transfer efficiency of the system because of the additional mass transfer resistances associated with the membrane itself and the geometry of the blood layer. The zero velocity condition at the membrane-blood interface results in oxygen diffusion perpendicular to the wall that is a part of the limiting process in most membrane lung designs. While the slowly moving blood near the membrane quickly becomes highly enriched with oxygen, the highest blood velocities are located away from the membrane and near the center of the blood stream.

The very first plastic films used, such as thin sheets of polyethylene and polytetrafluoroethylene (PTFE or Teflon), showed such a low diffusion permeability that 5-10 m² were needed to meet even the minimal oxygen needs of an anesthetized hypothermic adult <158>.

Carbon dioxide elimination, rather than oxygen uptake, was the bottleneck when using solid polyethylene, polypropylene, ethylcellulose, or Teflon membranes, since hydrophobic materials could not match the carbon dioxide solubility advantage of the water-containing alveolar membrane.

The development of dimethylpolysiloxane membranes by Kammermeyer in 1957 was a major advance and the advent of silicone elastomer films (either as solid sheets or cast over a textile support mesh) in the 1960s established the technical feasibility of membrane oxygenators <162-165>. Silicone rubber has a much higher permeability for oxygen and carbon dioxide than Teflon for equivalent thickness. Even though silicone rubber and related elastomers cannot be cast as thin as Teflon, their permeability is so high that they became the standard material for early membrane oxygenator prototypes.

The Bramson Lung <165> was the first commercially available membrane oxygenator utilizing silicone rubber membranes (Figure I.22). The Bramson Lung was followed by the flat sheet Landé-Edwards membrane oxygenator <167-169>. The improved gas exchange efficiency was evident in that only 6 m² of membrane surface area was required to support an average size adult. Reduced membrane surface areas and thinner blood film thickness in these devices meant lower

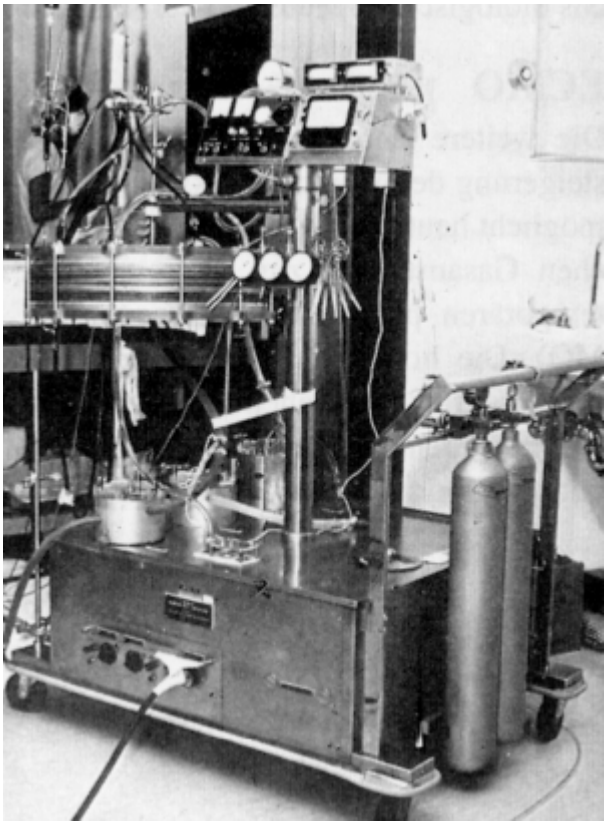

Figure I.22: The Bramson membrane oxygenator. <166>

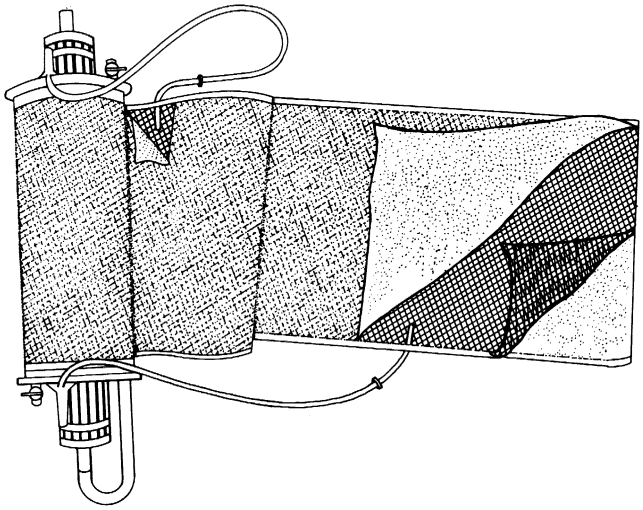

Figure I.23: An unfolded view of a Kolobow coiled membrane oxygenator showing the coiled silicone envelope with a mesh screen separating the membranes in the gas phase of the oxygenator. Fresh gas is supplied to the envelope by several silicone tubes and removed in a similar manner. <69>

priming volumes than earlier oxygenators did. However, the design and operational complexities (high priming volumes, high pressure drop and marginal mass transfer efficiency) of these oxygenators coupled with their high incidence of blood leakage limited their clinical application.

Increasing gas exchange performance by active augmentation was investigated in the 1960s and 1970s <170> as ways to reduce blood contacting surface areas in units designed primarily for longterm support. Methods such as pulsatile flow or centrifugal flow were used to break up the mass transfer boundary layer that develops in oxygenator blood channels and limits gas exchange. The clinical motivation was to provide continuous full or partial replacement of pulmonary gas exchange for several weeks to patients with advanced respiratory failure, in the hope of the natural lung recovering in the interval. Since extensive blood trauma limited the use of bubble oxygenators beyond 12-24 hours, membrane oxygenators became the key to this application. These designs, however, never achieved widespread commercial success mainly due to the need for and the lack of auxiliary equipment.

In the early 1970s, the Kolobow membrane lung became commercially available by Sci-Med, Inc. This unit was first described in 1963 <171> and utilized a silicone rubber membrane wound in a spiral coil configuration (Figure I.23). Membrane surface texture helped to augment gas transfer by mixing the blood adjacent to the membrane and only a 3.5 m^2 or 4.5 m^2 unit was needed to support adult patients. Another membrane oxygenator of this period was the Baxter-Travenol Travenol Modulung, which was of the flat sheet variety with a silicone membrane.

With the availability of more permeable membrane materials, the fluid phase convective and diffusive mass transfer of gas molecules across the blood film boundary layer were the limiting mass transfer mechanisms. Under laminar flow conditions a stationary boundary layer of blood would be formed adjacent to the membrane sheets and act as a diffusion barrier. Attempts to break up this boundary layer, through some external mechanical means, in order to improve gas exchange efficiencies were investigated in the early 1970s <170>, but the added complexity precluded prolonged acceptance.

I.5.3 Microporous membranes

In the mid-1970s, an NIH-sponsored clinical study <8> demonstrated that, with the protocols used, lung functions were not regained after one to three weeks of extracorporeal circulatory with a membrane oxygenator. Moreover, membrane devices lacked such 'marketable' features like integrated heat exchanger, blood reservoir, and filters possessed by bubble designs. Furthermore, the relatively atraumatic perfusion of blood through membrane oxygenators was masked by other sources of blood trauma, e.g. blood suction form the surgical field. The major intended application of membrane oxygenators having vanished, and the high cost of silicone rubber making these devices much more expensive than bubble oxygenators, research and development almost came to a halt, leaving bubble oxygenators in control of the remaining field of use, namely cardiopulmonary bypass <146,172>.

Three major advances have reversed this trend in the 1980s and 1990s. Firstly, the discovery that hydrophobic microporous membranes <173-175>, through which gas can freely diffuse, have a high enough surface tension to prevent significant infiltration of plasma or plasma water into the membrane pore structure (plasma filtering across the membrane causes a severe drop in oxygen transfer and a prohibitive fall in carbon dioxide removal). Secondly, the large-scale fabrication of defect-free hollow fibers of microporous polypropylene, which can be assembled in bundles, potted and manifolded at each extremity to form an artificial capillary bed of parallel blood pathways immersed in a cylindrical hard shell through which oxygen circulated. Thirdly, membrane lung surgery has a significantly lower overall cost of hospitalization than the cost of bubble oxygenator surgery <176>.

The driving force for the initial development of hydrophobic microporous capillary hollow fiber membranes was their potential in another application - membrane plasmapheresis - for the separation of plasma from the cellular components of blood. In that application hollow fibers had nominal pore sizes, around 0.5 µm, which was too large for membrane oxygenation because of plasma leakage. In the early 1980s, microporous polypropylene hollow fibers with a nominal

pore size of around 0.1 µm, which is significantly smaller than blood cells, became available. Microporous membranes are constructed of hydrophobic materials such as Teflon or polypropylene, and are, in terms of the resistance to gas exchange, not rate limiting.

The Travenol Modulung-Teflo utilized a microporous Teflon membrane and was introduced in 1974. It contained a bladder mechanism that would compress the flat sheet membrane compartment when inflated, thus reducing the blood film thickness. This oxygenator was closely followed by the Travenol TMO oxygenator, which had the same basic design but utilized microporous polypropylene. By the end of the 1970s, both the Kolobow and the Travenol TMO were used in approximately 18 % of all cardiac surgical procedures in North America. However, both devices were characterized as complex to use and potentially problematic <147>. Both devices required caution and carbon dioxide flushing in addition to vacuum ventilation to adequately prime <177,178>.

In 1982, Cobe Laboratories introduced the Cobe Membrane Lung (Cobe CML, Cobe Laboratories, Lakewood, Colorado, USA) <179>, the first integrated open system and microporous polypropylene sheet membrane oxygenator. This device combined the increased hemocompatibility of membrane technology with the operational simplicity of bubblers through the vertical integration of the venous reservoir, heat exchanger and a membrane compartment <180>. Screens placed in the blood channels of the 2.5 m² flat sheet membrane compartment maintained, on the one hand, an open and uniform blood channel with a well-mixed blood flow allowing the smaller surface area to support a complete size range of adult patients. The placement of extruded polypropylene screens in both the blood and the gas phase channels, on the other hand, improved efficiency by mixing the boundary layer passively within the membrane compartment <180>.

I.5.4 Hollow fiber membrane oxygenators

In the 1960s, the first capillary or hollow-fiber membrane oxygenators were developed <181>. They utilized silicone rubber tubing in which blood flowed outside the tube lumen and gas flowed inside the tube lumen (extraluminal blood flow). Shortly thereafter, several hollow-fiber oxygenator designs utilizing silicone rubber tubes with the blood flowing inside the tube lumen and gas flowing outside the tube lumen (intraluminal blood flow) were reported <182-185>. Dorson <184> and deFilippi <183> transferred the hollow fiber capillary configuration for low blood flow rates in hemodialyzers to blood-gas exchangers. An additional extraluminal hollow-fiber unit was reported later this decade <186>. These units were experimental and never reached the state of commercialization.

The weakest point of the intraluminal design was the configuration of the inflow face sheets: the blood stream had to change abruptly from a single feed tube to thousands of parallel channels with the result that white platelet plugs were commonly observed near loci of flow separation. Better blood inflow and outflow manifolds were designed. Better materials and techniques for potting the fiber bundles and cutting the face sheets were identified.

Intraluminal, hollow-fiber membrane oxygenators became readily available in the early 1980s <187,188>. These devices achieved limited commercial success due to the inefficient gas exchange inherent in an intraluminal design. The main resistance to oxygen transfer in a shell-and-tube hollow fiber artificial lung resides in the blood phase. This is associated with the laminar rectilinear flow within the hollow fiber lumens. If membrane resistance is small, gas transfer in artificial lungs depends on the extent to which the blood-side is convectively mixed. The lack of any augmentation, or blood side boundary layer mixing, forced the manufacturers to offer several sizes of membrane compartments, as high as 5.5 m² for adult support <188>. Eventually (in 1983), Terumo introduced the first commercial hollow fiber oxygenator on the clinical market (Terumo Capiox II, Terumo, Piscataway, New Jersey, USA). The exchange area was still in the order of four m².

To minimize mass transfer resistance, an effective but gentle transverse mixing of the blood flowing in the lungs is required. This is obtained in cross-flow hollow fiber artificial lungs by letting the blood flow over a matrix of hollow fibers with the gas flowing inside the fibers. Extraluminal hollow fiber designs not only utilize the larger outer surface area of the capillary tubes as gas transfer interface instead of the luminal surface, they also have the advantage over the flat sheet devices by breaking up the mass transfer boundary layer with the membrane material itself (i.e. effective mixing is naturally induced and enhances oxygen transfer). Therefore they have slightly reduced membrane surface areas when compared to the flat sheet devices. Laboratory and clinical experience has shown that the membrane area required for a given level of performance is reduced by 30 to 50 % in extraluminal designs compared with intraluminal designs.

Hollow fiber membrane technology was advanced by the introduction of the Extracorporeal Maxima (Johnson and Johnson) <189-191>. This device incorporated cross-wound hollow fibers with extraluminal blood flow, requiring a membrane surface area of only 2.0 m².

Toward the end of the 1980s and into the 1990s, refinements to the flat sheet designs <192> and an additional hollow-fiber technology <193> became available in the newer devices <194,195>. The demand for reduced hemodilution forced the designs to minimize priming volume without a loss of performance.

Microporous polypropylene hollow fibers occasionally lose some of their oxygen transport capacity after 12 to 24 h following protein deposition on blood-exposed surfaces or water vapor condensation in the voids of the porous wall.

Microporous hollow fiber, low prime / high gas exchange efficiency extraluminal flow membrane oxygenators have now been dominating the market for over a decade.

I.5.5 Construction of hollow fiber membrane oxygenators for extraluminal flow

Microporous polypropylene is extruded or film blown and then stretched to give a controllable pore shape and size (Figure I.24). The production process used for manufacturing the hydrophobic, microporous membrane is extremely complex. The process is a thermally induced, phase separation process in which the polymer is homogeneously mixed with two natural seed oils, then spun and cooled <197,198> (Figure I.25). When the fiber cools, a phase separation is

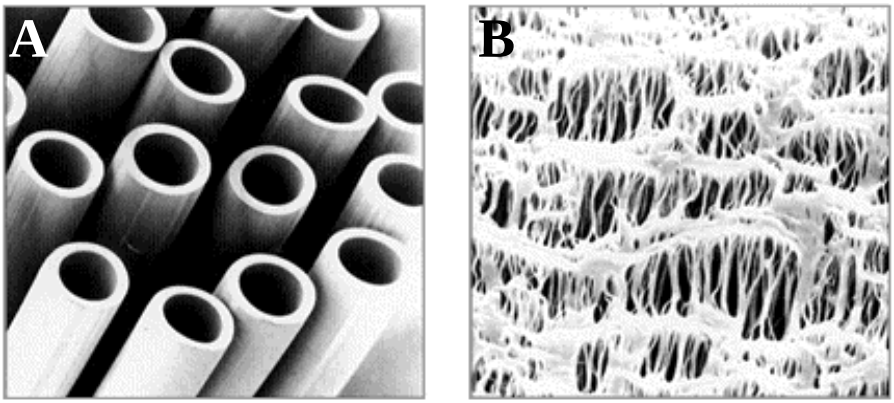

Figure I.24: A: Hollow fiber membranes; **B:** Cross-section of the membrane of an hollow fiber showing the microporous structure.<196>

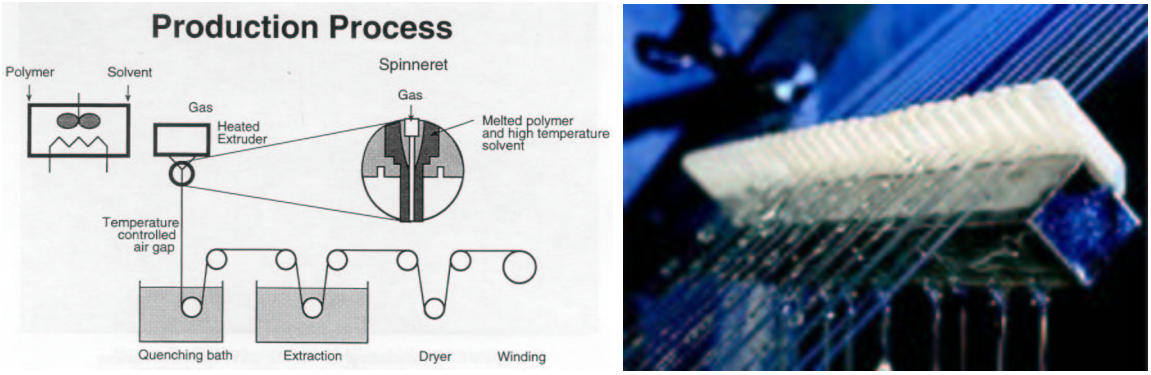

Figure I.25: Production process of a hydrophobic, microporous fiber (AKZO NOBEL Accurel production process). <197,198>

initiated, which results in a porous structure. The oils in the capillaries are removed with alcohol and the fibers are then dried. This process results in a highly porous, sponge-like structure, with consistent and uniform pore distribution throughout the entire membrane wall <197,198> (Figure I.24). High porosity is a prerequisite for high gas permeability, which yields high gas transfer efficiency.

In 1990, Akzo patented <193> a "warp thread" stabilized hollow fiber array or "mat" that consists of alternating bi-directional rows of equally spaced fibers (Figure I.26). Single-fiber (bundle or

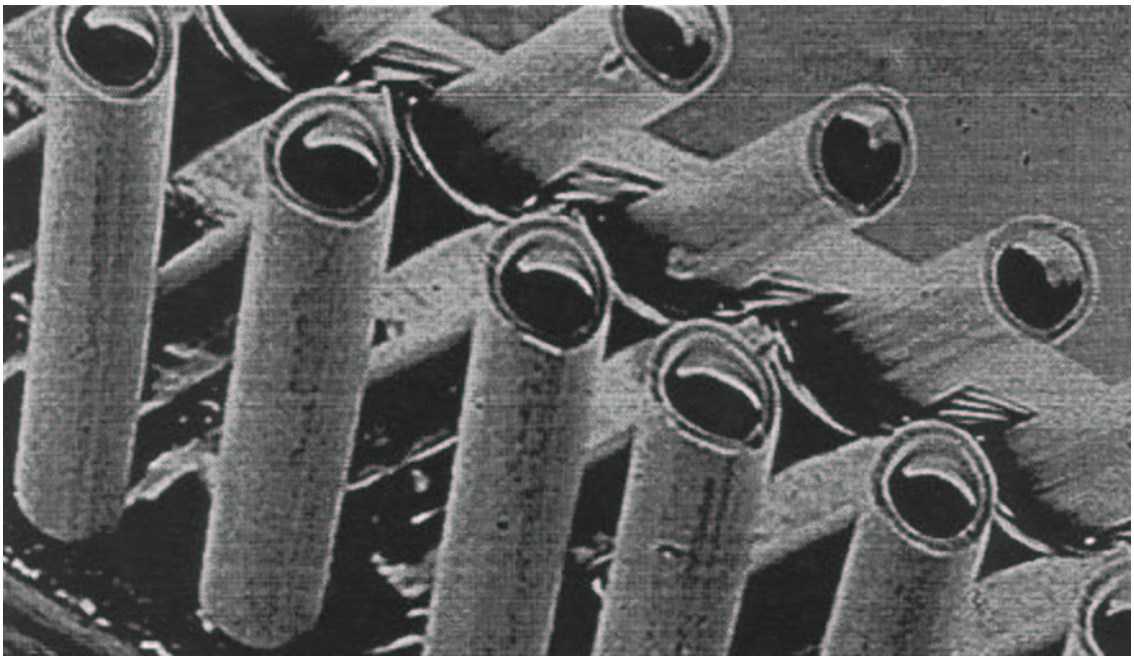

Figure I.26: Scanning electron micrograph of the Optima double-layer, cross-wound mat configuration, providing consistent bundle porosity. <198>

winding) manufacturing technology can enact exact placement of the fibers, but the fibers will shift slightly under the forces of the blood flow. This leads to preferential flow in less efficient areas (larger openings) and a generally suboptimal performance. The hollow-fiber array technology <193> minimizes this fiber movement through the stabilizing action of the warp threads. Designs incorporating this latest technology are the most efficient <199>.

The majority of hollow fiber designs on the market can be generically described as a specific orientation of fibers placed within an annular case material (polycarbonate). The membrane bundle in the Cobe Optima, e.g. utilizes a hollow fiber cross-wound mat configuration which provides consistent bundle porosity <200>. The term "cross-wound" refers to the slight angling of one layer of microporous hollow fibers relative to the adjacent layer. This angling technique eliminates nesting of the fibers between each other. Fiber to fiber spacing is controlled by weaving polypropylene warp threads perpendicular to the hollow fibers (Figure I.26).

Axial flow, defined as the flow through the bundle along the length of the annular case, is currently utilized by the Dideco Compactflo (Figure I.27, right panel). This design will typically have longer blood paths and constant cross-sectional area for flow. The angular flow path within the circumference of the annular space is accessed either from the core of the annulus (Cobe Optima, Figure I.27, bottom left panel) or from the outer radius (Sarns Turbo 440, Figure I.27, top left panel). These designs also typically have longer blood flow paths and maintain a constant cross-sectional area for flow. Radial flow is implemented by flow from the core directly to the outer diameter (Avecor Affinity). The cross-sectional area for flow can increase significantly as the flow moves outward. This design has a shorter blood path length.

The flow path choices within this configuration are simplified and illustrated in Figure I.27 for three studied artificial lungs. These choices reflect the bulk or macroscopic flow within the membrane compartment. The actual microscopic flow is stochastic in nature and can have components of all three generic types within a given device.

I.6 Respiratory assist procedures: an introduction to extracorporeal life support <201,202>

Artificial lungs have been used primarily as a component of the heart-lung machine in cardiac surgery. The natural lungs were generally healthy. The matter is quite different in respiratory assist for pulmonary insufficiency. Under these circumstances, the patient depends on the artificial lung for continuous gas exchange for days or even weeks, giving the lungs a chance to recover. The principle behind this is straightforward. When lung injury is confined to only a limited area of the lungs or to one lobe, recovery is almost taken for granted. However, when the disease process extends to several or all lobes of the lungs, such involvement is likely to lead to acute respiratory insufficiency, a life-threatening injury. In adults such a lung injury process is known as “adult respiratory distress syndrome” (ARDS).

The concept of using the membrane lung in the treatment of ARDS has occurred to many: extracorporeal veno-arterial or veno-venous membrane oxygenation (ECMO). In the mid 1960s laboratory research began on prolonged extracorporeal circulation in the laboratories of teams that were studying function and improvement of membrane lungs, particularly Kolobow, Pierce, Galletti, Bramson and Hill, Landé and Lillehei, and Drinker and Bartlett.

One of the first extracorporeal systems for use in patients with ARDS was reported by Hill et al. <203>. Unfortunately, early success was poor <9>. In a study conducted by the National Heart, Lung and Blood Institute, it was shown that a patient population with ARDS treated by extracorporeal veno-arterial membrane oxygenation respiratory arrest, while also ventilated at high airway pressures, had a 90 % mortality <204>. Patients died in spite of good arterial blood gases (sustained by the membrane lung), while the natural lungs had completely ceased to function. A control group managed with conventional mechanical pulmonary ventilation had an identical survival rate. This study concluded that under the conditions of that study, the membrane lung did not offer any benefit.

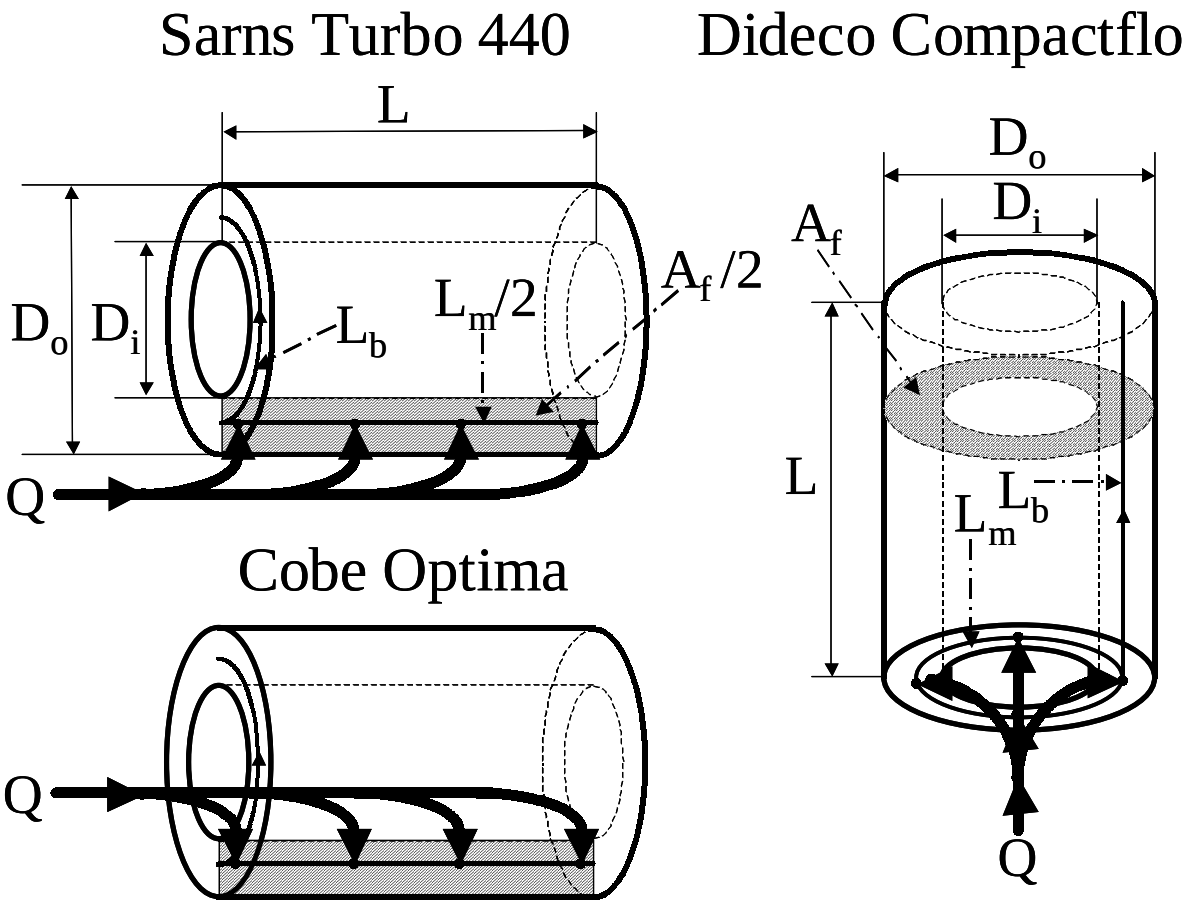

Figure I.27: Schematic representation of the flow pattern and construction of three studied commercially hollow fiber membrane artificial lungs: **Top left panel:** Sarns Turbo 440; **bottom left panel:** Cobe Optima; r**ight panel:** Dideco Compactflo. For a detailed description, please refer to §II.5.

I.6.1 Extracorporeal life support <202>

Mechanical cardiopulmonary support goes by many names, all under the general heading of extracorporeal life support. When the heart/lung machine is used in the operating room in veno-arterial mode to provide total support of heart and lung function to facilitate cardiac operations, the technique is commonly called cardiopulmonary bypass. When used with extrathoracic cannulation for respiratory support the technique can be called extracorporeal membrane oxygenation (ECMO), extracorporeal lung assist (ECLA), and extracorporeal carbon dioxide removal ($ECCO_2R$). When used with extrathoracic cannulation for emergency cardiac support the technique is called cardiopulmonary support (CPS) or extracorporeal cardiopulmonary resuscitation (ECPR). When oxygenation is the predominant aim, the term extracorporeal membrane oxygenation (ECMO) prevails.

When the membrane lung is primarily used for extracorporeal carbon dioxide removal while oxygenation is accomplished by apnoeic oxygenation using low-frequency positive-pressure ventilation, the term extracorporeal carbon dioxide removal ($ECCO_2R$) is used <205>. The respiratory quotient 'seen' by the body's own lungs can be reduced to zero by arranging an extracorporeal lung to remove the whole of the body's metabolic production of carbon dioxide from the blood, whilst performing little or no oxygen transfer via the device. In this situation the patient is, in effect, breathing in oxygen through their own lungs but has nothing to breathe out. The lungs indeed can be motionless, or apnoeic, while the uptake of oxygen occurs by steady convection from the nose or mouth down into the lungs. This method can be shown to function only in steady state when the patient breathes in a very high concentration of oxygen. Therefore, $ECCO_2R$, with apnoeic oxygenation which reduces the respiratory quotient to zero for the patient's own lungs, is a therapy for some forms of respiratory failure.

Blood pumps alone can be used as left ventricular assist devices (LVAD), right ventricular assist devices (RVAD), or both (BiVAD). The abbreviations ECLS and ECMO are used synonymously when referring to prolonged extracorporeal circulation with mechanical devices. Generally, all of these device applications include vascular access catheters, connecting tubing, servo-regulating blood pump, an artificial lung (usually incorrectly called an oxygenator), a heat exchanger, and various measuring and monitoring devices. Bleeding complications are always a potential problem, and so are problems associated with the extracorporeal circuits.

ECLS can be used for mechanical assistance during cardiac or pulmonary failure in newborn infants, older children, or adults. Depending on the application, ECLS can be used in a veno-arterial mode, a veno-venous mode, or rarely in an arterial-venous mode.

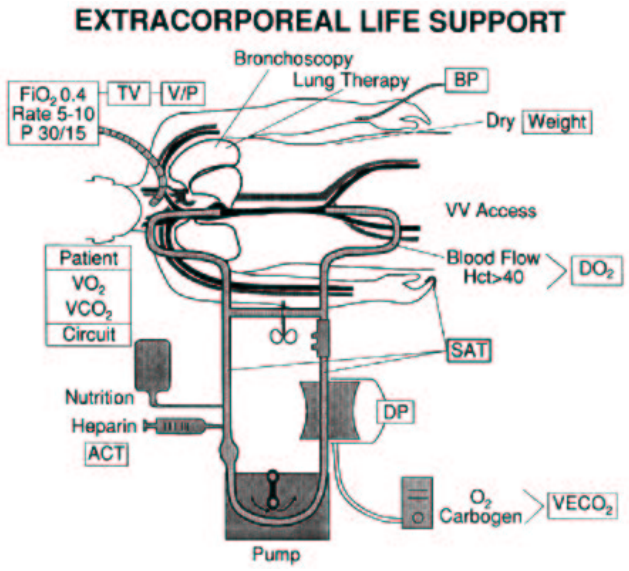

Figure I.28: A typical ECLS circuit with veno-venous cannulation is depicted. Blood drains from the right atrium to the pump, and returns to the patient. The important monitors are shown in boxes. <202>

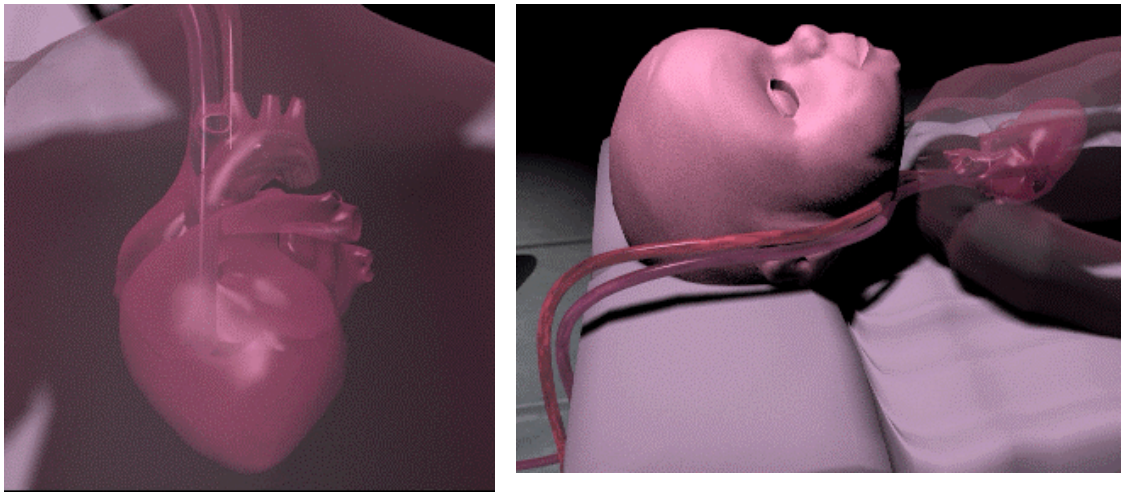

Figure I.29: A veno-arterial ECMO is shown. A small operation is performed on the right side of the neck. One cannula is positioned in the right atrium of the heart and a second cannula in the aorta. The flow of blood drains poorly oxygenated blood form the right atrium and returns oxygenated blood to the aorta. <206>

A diagram of the circuit commonly used for ECLS is shown in Figure I.28 (veno-venous) and Figure I.29 (veno-arterial). In Figure I.28, the right atrium is cannulated through a large vein, usually the right internal jugular vein. Venous blood drains out of the right atrium, usually aspirated by a simple siphon. Blood passes directly to a self-regulating pump; unlike CPB for cardiac surgery there is no venous reservoir. Blood is pumped through a membrane lung where oxygen, carbon dioxide, and water vapor are transferred. This device is commonly referred to as the "oxygenator", although for purposes of pulmonary support removal of carbon dioxide is even

more important than oxygenation. The "arterialized" blood returns to the patient. If the application is purely for respiratory support, the arterialized blood is usually returned to the venous circulation, placing the membrane lung in series with the patient's native lungs. This is the application shown in Figure I.28. Figure I.29 shows a veno-arterial ECMO. If the application requires cardiac support, blood is returned to the arterial circulation through a catheter in a large artery, usually the right common carotid. In this application the pump and membrane lung are placed in parallel with the native heart and lungs.

Once the ECLS circuit is attached and functioning, the blood flow through the circuit is regulated to provide part or all of the circulation and gas exchange. Total cardiopulmonary support is possible by extracorporeal circulation using only part of the venous blood arriving in the right atrium from the systemic circulation. Therefore ECLS is usually a "partial" bypass as opposed to a "total" bypass, which is required for cardiac operations. With circulation and gas exchange supported mechanically, the native heart and lungs are not needed for life support and are allowed to "rest". This means that ventilator settings and inotropic drugs are decreased to safe, low levels. Blood flow through the circuit continues until the heart or lung function improves. The amount of blood flow is based on the degree of support required, which in turn is based on a series of physiologic monitors in the circuit and on the patient. Many days may be required for the native heart or lungs to start functioning adequately again. Continuous anticoagulation is required. This is done with continuous heparin infusion monitored by whole blood activated clotting time (ACT). Platelet dysfunction and thrombocytopenia occur during ECLS due to complex blood/surface interactions. A variety of mechanical and physiologic complications can occur requiring emergent management.

The details of ECLS management, the indications, and the results are quite different for cardiac and respiratory support, and quite different for neonates, pediatric and adult applications. In general, ECLS is indicated in acute severe reversible cardiac or respiratory failure when the risk of dying from the primary disease despite optimal conventional treatment is high (50 to 100 %). Since ECLS is used only in patients who are most likely to die otherwise, the results are usually described in terms of simple survival. Longterm quality of life studies are ongoing. The current survival rate for neonatal respiratory failure is 80 %; for pediatric respiratory failure 60 %; adult respiratory failure 50 %; pediatric cardiac failure 45 %; and adult cardiac failure 40 %.

I.6.2 Intravenous oxygenation <10>

An interesting embodiment of the extraluminal hollow fiber concept is the intravenous oxygenator (IVOX) designed by Mortensen and Berry <207,208> for longterm respiratory support .

A long bundle of microporous polypropylene hollow fibers curled around a semi-rigid, double-lumen oxygen feed tube is introduced through a femoral vein and advanced into the inferior vena cava until it approaches the right atrium leaving only the feed tube protruding through the skin. Oxygen flows under negative pressures (i.e. aspirated by a pump) from an outside source through the lumen of the hollow fiber and back to the atmosphere. There is no need for a blood pump. Venous blood circulates around and between unfurled, buoyant, gas-filled fibers and undergoes “prepulmonary” gas exchange. Between one-third and one-half of the basal oxygen and carbon dioxide requirements can be met. The devices have been shown clinically to remain functional for several weeks. IVOX use silicone-coated polypropylene hollow fibers to avoid plasma-leakage and use heparin binding on their outer surface to render them nonthrombogenic.

I.7 Conclusion

This chapter has given the reader an introduction to cardiopulmonary bypass as well as to respiratory assist procedures. Both procedures are used worldwide nowadays and are still developing. Several aspects of the heart-lung machine and CPB are dealt with and explained extensively. The historical overview and the survey of the development of the heart-lung machine provides an insight into the very complicated but fascinating world of the cardiopulmonary bypass, in particular the artificial lung.

II INTRODUCTION TO AND MODELING OF OXYGEN TRANSFER IN ARTIFICIAL LUNGS

II.1 Introduction

This chapter covers several aspects of the numerical and semi-empirical modeling of momentum and oxygen transfer in artificial lungs. Modeling is a process which predicts, identifies or reconstructs the behavior of a system <209>. Modeling does not have to rely solely on equations, i.e. numerical modeling. In some cases, such as fluid pump design, the fluid dynamic theory is augmented by empirical data. These data may not fit known theories, but can be summarized in a semi-empirical model and are still used to aid future designs <209>.

A first paragraph introduces blood and describes its microscopic properties, its function, and mathematically its density and viscosity. In order to comprehend the modeling of oxygen transfer in an artificial lung, an overview of the physiologic oxygen transfer is given in (§II.3). In this paragraph, attention is paid to physically dissolved oxygen, chemically bound oxygen, and the oxygen diffusion coefficient. The oxyhemoglobin dissociation curve, denoting the relative amount of oxygen bound to hemoglobin, is described using several mathematical models.

§II.4 deals with the numerical modeling of momentum and mass transfer. The finite element method is described briefly. The continuity, momentum and convection-diffusion equations for blood flow and oxygen transfer in blood are given subsequently and special attention is paid to the application of the finite element method to these equations. In order to deal with the nonlinear chemical reaction of oxygen with hemoglobin in the convection-diffusion equation, the concept of an effective oxygen diffusion coefficient in blood is introduced and described in detail.

An introduction to the geometry of the three commercially available artificial lungs that are studied in this thesis, and to the geometry of the microscopic numerical model are provided in §II.5. The dimensional groups that are used in the presentation and interpretation of the results

on the one hand and in the semi-empirical modeling of momentum and oxygen transfer on the other hand are introduced in §II.6.

§II.7 provides a literature survey of the modeling of oxygen transfer in an artificial lung. Special attention is paid to several analytical and numerical models.

§II.8 gives a detailed survey of a semi-empirical model of oxygen transfer in cross-flow artificial lungs. This semi-empirical model was introduced in 1985 by Mockros and Leonard <3> and was based on the analogy between heat and mass transfer. The mass transfer coefficient is described, as well as the oxygen transfer in artificial lungs.

II.2 Blood

II.2.1 Microscopic properties and its function

Blood is a concentrated suspension of blood cells (red blood cells, white blood cells and platelets) in plasma (Table II.1). The white blood cells, or leucocytes, are roughly spherical in shape with a diameter between 7 and 22 µm. The platelets are much smaller than the leucocytes; they are oval shaped with a diameter ranging between 1 and 3 µm. Together, the leucocytes and the platelets occupy less than one percent of the volume of blood. More than 99 % of the cells are red blood cells (approximately $5 \cdot 10^{12}$ red blood cells per liter of blood), which occupy about 45 % of the volume of blood[†]. The percentage of the volume of blood occupied by red blood cells is known as the hematocrit, Hct, of blood.

The major function of red blood cells is the transport of oxygen that is achieved by the hemoglobin. The white cells are responsible for the cellular immunity and provide the body with powerful defenses against tumors and viral, bacterial, and parasitic infections. Platelets contribute to the thrombogenesis and therefore aid in the clotting of blood.

Table II.1: Blood cell properties.

type of cell	*volume fraction*	*dimension [µm]*	*number/mm³*
erythrocytes (red cells)	45 %	7 to 9	4.0 to 6.0 ($\cdot 10^6$)
leukocytes (white cells)	1 %	7 to 22	4.0 to 11.0 ($\cdot 10^3$)
platelets	1 %	1 to 3	2.5 to 5.0 ($\cdot 10^5$)

[†] Blood with a temperature of 37 °C (normothermic) and with an hematocrit of 45 % will be referred to as *normal blood*.

The primary function of the blood circulation is to provide oxygen and metabolic fuels, and to remove the metabolic final products (e.g. carbon dioxide, waste water) from every living cell of the organism. This is achieved by circulating blood through all parts of the body. The blood is responsible for:

- absorbing nutrients while circulating through the splanchic organs.
- absorbing oxygen and removing gaseous carbon dioxide and water while circulating through the lungs.
- removing non-gaseous final products of the metabolism while circulating through the liver and the kidneys.

When unstressed, the red blood cells take the form of biconcave discs having a mean diameter of approximately eight μm. However, they undergo severe deformation as they pass through small diameter capillaries.

The plasma is the fluid portion of the blood and contains about 91 % water and 9 % solids including 1.7 % proteins (albumin, globulins and fibrinogen). The primary functions of albumin and fibrinogen are, respectively, maintaining the osmotic pressure at the capillaries and preventing blood loss by clotting. The globulins carry out various functions in addition to preventing infections.

The classification of gas exchange models for membrane artificial lungs is based on how the two phases, i.e. red blood cells and plasma, are taken into consideration. Even though blood can be considered as a suspension of red blood cells in plasma, it is microscopically heterogeneous. The characteristic length of the blood channels in a membrane oxygenator (i.e. the hydraulic radii, 100 μm, (§II.5)) is generally an order of magnitude larger than the dimensions of the red blood cells (8 μm). Therefore, it is reasonable to consider blood as a homogeneous, incompressible fluid, a continuum with uniformly distributed sites of chemical reaction. This simplification is acceptable as long as the volume element in which oxygen transport occurs is large compared to the size of a single red cell but small compared to the size of the overall diffusion path.

The density of blood, ρ, is a macroscopic property and is calculated as a weighted average of the density of the red blood cells and that of the plasma:

$$\rho = 1090 \cdot \mathrm{Hct} + 1035 \cdot (1 - \mathrm{Hct}) \qquad [48]$$

e.g. a hematocrit of 45 % yields a blood density of 1060 kg/m³.

II.2.2 Blood viscosity

A strong interrelation exists between the rheology of the blood and the microscopic structure of the blood. One can assume that the red blood cell aggregation or deformability, their volume fraction, the plasma viscosity and the red cell content can affect the completely rheological behavior. It is generally accepted that the red blood cells are the only ones to be taken into account when explaining the macroscopic rheological properties of the blood. The suspension of red blood cells in blood makes blood behave as a non-Newtonian fluid even though the plasma is a Newtonian fluid. A large number of experiments with varying hematocrit, anticoagulants, temperatures, and shear rates has been performed on blood to determine its viscosity behavior. At low shear rates $\left(\dot{\gamma} < 250\,\mathrm{s}^{-1}\right)$, blood behaves as a non-Newtonian fluid. At high shear rates, $\left(\dot{\gamma} > 250\,\mathrm{s}^{-1}\right)$, however, the non-Newtonian characteristics of blood are insignificant and may therefore be ignored.

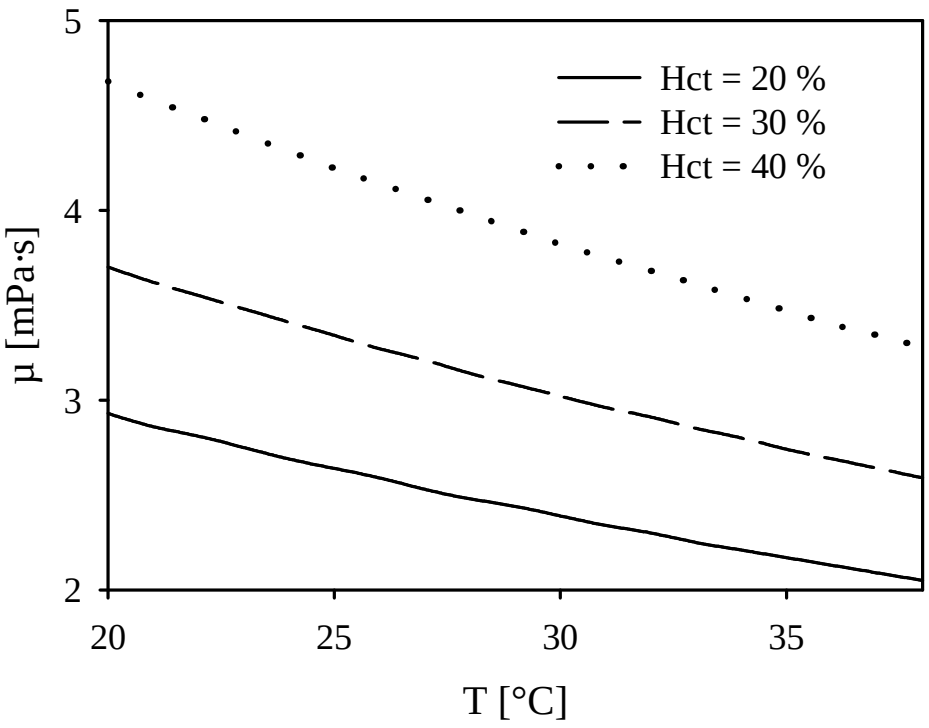

Figure II.1: Changes in viscosity, μ, of bovine blood measured *in vitro* at high shear rates $\left(\dot{\gamma} > 250\,\mathrm{s}^{-1}\right)$ with varying temperatures, T, expressed in degrees Celsius, and for a hematocrit of 20 %, 30 % and 40 %.

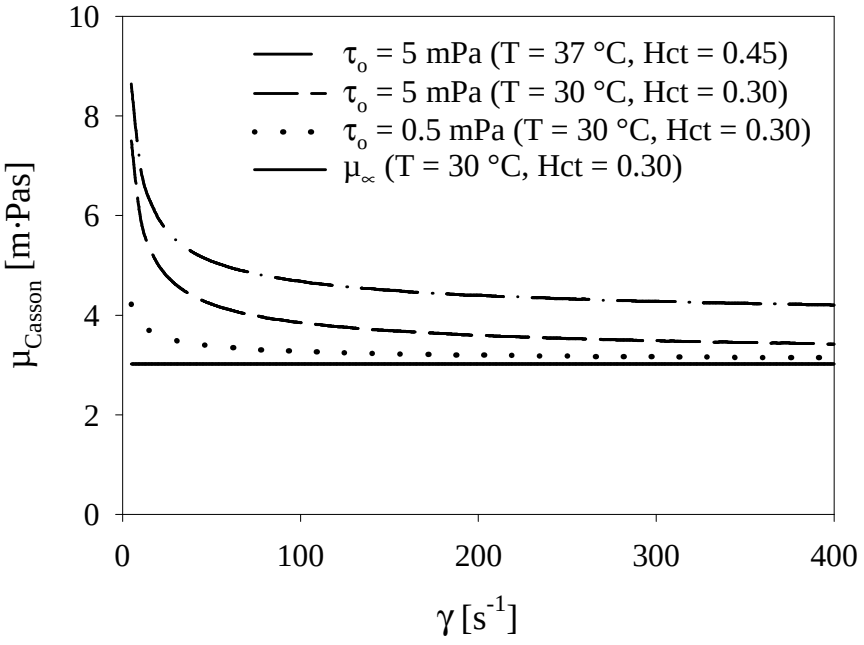

Figure II.2: A: Casson plot of the blood rheological properties at different hematocrit (1 dyne/cm² = 0.1 Pa) <210>; **B:** Both a Newtonian and non-Newtonian plastico-viscous shear-thinning Casson model (T = 30 °C, Hct = 30 % and τ_o = 5 mPa) are depicted. A significant influence on viscosity at low shear rates is observed for the Casson viscosity.

Blood viscosity primarily depends upon the temperature and the hematocrit (Figure II.1). The temperature dependence <3,13> is assumed to be due to the temperature dependence of the plasma <12>, and the hematocrit dependence is assumed to be exponential with hematocrit <12>. The absolute viscosity of the blood, μ_∞, is calculated as follows <3,14>:

$$\mu_\infty = \mu_p \cdot e^{2.34 \cdot Hct} \qquad [49]$$

in which μ_p is the absolute viscosity of the plasma <3,14>. The plasma is a Newtonian fluid and its viscosity decreases while the temperature, which is expressed in degrees Celsius, increases:

$$\mu_p = e^{-5.54+\frac{1800}{T+273}} \qquad [50]$$

Of the various models for non-Newtonian blood viscosities, the plastico-viscous shear thinning Casson model <15-17> appears to be the most suitable for the application for this thesis. This model, first proposed to describe the properties of inks <17>, is appropriate for shear thinning fluids with a yield stress and is widely used for the blood rheology. Scott-Blair used this model first to describe blood viscosity <211>. Charm et al. <212> found that the Casson equation fits the shear rates between 0 and 100000 s^{-1} satisfactory. The analytical relationship shows a linear dependence on the square root of the shear stress, τ, as a function of the square root of the shear rate, $\dot{\gamma}$ (Figure II.2):

$$\sqrt{\tau} = \sqrt{\tau_o} + \sqrt{\mu_\infty \cdot \dot{\gamma}} \qquad [51]$$

τ_o is the yield stress (stress at zero shear rate) and μ_∞ is the blood viscosity at high shear rates (Eq. [49]). Below the value of the yield stress, τ_o, the fluid is assumed to behave as a solid. Actually, the Casson model describes the rheological properties of blood in a limited range of shear rate (Figure II.2). The evidence of yield stresses in blood, however, are circumstantial and there is no consensus about the yield stress value. The yield stress, τ_o, is assumed to be 5 mPa <213,214>.

During cardiopulmonary bypass (CPB) (temperature, T = 30 °C and hematocrit, Hct = 30 %) the density, ρ, and the blood viscosity, μ_∞, are approximately 1052 kg/m³ and 3.02 mPa·s respectively <3>.

II.3 Oxygen transfer: physiology

When blood enters the venous system, the partial pressure of oxygen is low (P_{O_2} = 40 mmHg, 75 % saturated) and the partial pressure of carbon dioxide is high (P_{CO_2} = 46 mmHg) <215>. This is because blood enters the venous system after it has passed through the capillary beds where oxygen is consumed and carbon dioxide is absorbed. Venous blood then goes through the pulmonary capillaries (lung) where oxygen is absorbed and carbon dioxide is removed. Only a fraction of the oxygen in the air one breathes, is actually transferred from the pulmonary alveoli to the pulmonary capillary venous blood. Blood is almost completely saturated with oxygen (P_{O_2} = 100 mmHg, 97.5 % saturated) as it leaves the pulmonary circulation.

Because of a slight admixture with venous blood that bypasses the pulmonary capillaries (physiologic shunt), the hemoglobin in systemic arterial blood is only 97 % saturated. Only a fraction (23 %) of the oxygen carried by arterial blood is actually extracted by the tissues and only a fraction of the oxygen present in the tissues is actually replenished in a single blood pass. Similarly, only a fraction of the carbon dioxide present in the tissues is conveyed to the circulating blood, only a fraction of the mixed venous blood carbon dioxide content is actually discharged in the alveoli, and only a fraction of the carbon dioxide in the alveolar gas is eliminated into each breath. The gas exchange system is maintained in equilibrium by physiologic mechanisms that are kept in balance by chemical buffer systems.

The change in partial pressure in the circulatory system is shown in Figure II.3.

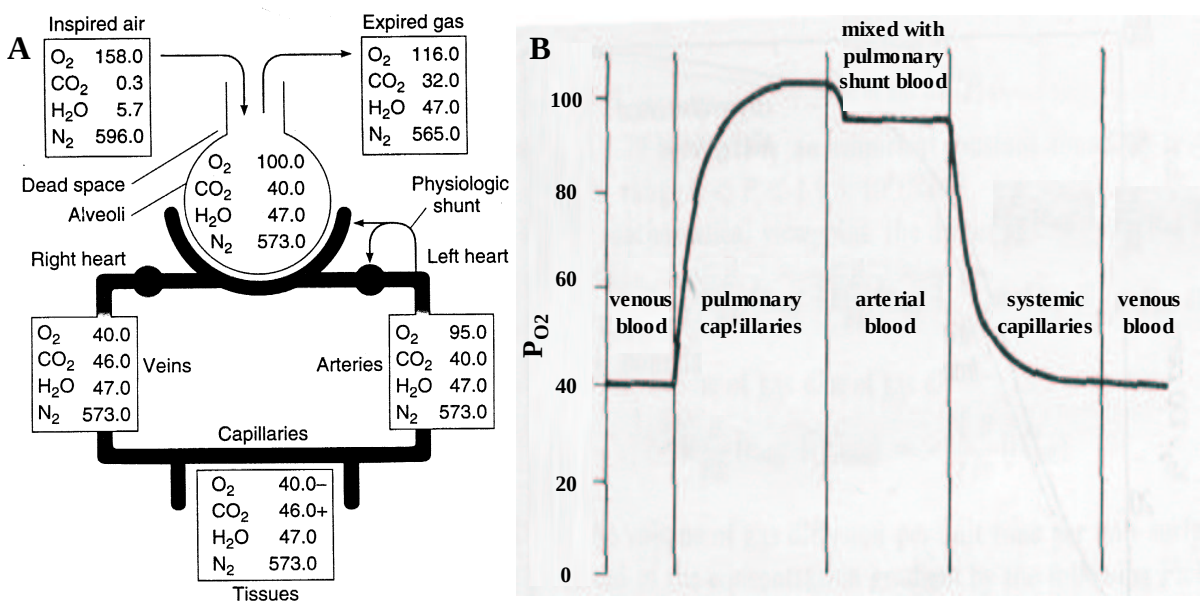

Figure II.3: A: Partial pressures (in mmHg) of gases of the human respiratory system and in the circulatory system. <215> **B:** The oxygen partial pressure in the circulatory system. <44>

II.3.1 The respiratory quotient <215,216>

The respiratory quotient, RQ, is the ratio in steady state of the volume of carbon dioxide produced, to the volume of oxygen consumed per unit of time. This means that the respiratory quotient is the ratio of the number of molecules of carbon dioxide produced to the number of molecules of oxygen consumed during combustion. This should be distinguished from the respiratory exchange ratio, R, which is the ratio of carbon dioxide, to oxygen at any given time whether or not equilibrium has been reached. The respiratory exchange ratio is affected by factors other than the metabolism. RQ and R can be calculated for reactions outside the body, for individual organs and tissues, and for the whole body. RQ for carbohydrate is 1.00, and for fat it is about 0.70 (Figure II.4). This is because hydrogen, H, and oxygen, O, are present in carbohydrate in the same proportions as in water, whereas in the various fats, extra oxygen is necessary for the formation of H_2O.

carbohydrate :

$$C_6H_{12}O_6 + 6\,O_2 \Rightarrow 6\,CO_2 + 6\,H_2O$$

glucose

$$RQ = \frac{6}{6} = 1.00$$

fat

$$2\,C_{51}H_{96}O_6 + 145\,O_2 \Rightarrow 102\,CO_2 + 98\,H_2O$$

tripalmitin

$$RQ = \frac{102}{145} = 0.70$$

Figure II.4: Calculation of the respiratory quotient, RQ, of carbohydrate (RQ = 1.00) and fat (RQ = 0.70). <215>

Determining the respiratory quotient of a protein in the body is a complex process, but an average value of 0.82 has been calculated <215>. For these circumstances, one breathes in more oxygen than one breathes out. In the case of heavy exercise, it is possible for the respiratory quotient to rise well above 1.00, to about 2.00, and under these circumstances of partial anaerobic respiration, the expiration of carbon dioxide dominates breathing.

The oxygen consumption and carbon dioxide production of an organ (e.g. the brain) can be calculated at equilibrium by multiplying its blood flow rate by the veno-arterial differences for oxygen and carbon dioxide across the organ. The respiratory quotient can then be calculated. Data on the respiratory quotient give some information about the metabolic processes occurring in the patient's organs. For example, the respiratory quotient of the brain is regularly 0.97-0.99, indicating that its main, but not its only, fuel is carbohydrate. The importance of the respiratory quotient is that it defines the relative burden of carbon dioxide exhaust on the one hand and oxygen take-up on the other hand for both the natural lung and any artificial lung.

At rest, a normal adult consumes approximately 250 ml of oxygen (STPD)[†] a minute. In these circumstances, and with a normal mixed diet, the respiratory quotient reaches values close to 0.82 and consequently the volume of carbon dioxide expiring from the lungs is approximately 205 ml/min.

Oxygen consumption (and carbon dioxide elimination) is one of the physiological variables that vary approximately with the surface area of living organisms, and consequently it is roughly related to the two-thirds power of the organism's volume (assuming similarities of shape) and mass (assuming similarities of mean density). Thus, an infant weighing 7 kg, when compared with an adult of 70 kg, has a relative mass of 0.1 and an oxygen requirement of

[†] Since gas volumes vary when temperature and pressure change and since the amount of water vapor in them varies, it is important to correct gas volume measurements to standard conditions, i.e. at standard temperature (0 °C) and barometric pressure (760 mmHg), dry (STPD). STP simply refers to standard temperature (0°C) and barometric pressure.

$$0.1^{\frac{2}{3}} \cdot 250 = 54\,\text{ml/min} \qquad [52]$$

This is more than double of what might be expected (25 ml/min) if the oxygen consumption were assumed to be proportional to mass alone, and it becomes a very important consideration when dealing with human infants.

II.3.2 Oxygen storage in blood

Part of the total amount of oxygen and carbon dioxide carried by the blood is in a dissolved state and the remaining part is chemically combined. Therefore, the total mass concentration[†] of oxygen, C_{O_2}, can be expressed as:

$$C_{O_2} = C_{O_2 d} + C_{O_2 b} \qquad [53]$$

where $C_{O_2 d}$ is the dissolved oxygen concentration (volumetric amount of oxygen per unit of blood volume) and $C_{O_2 b}$ is the chemically bound oxygen concentration.

II.3.2.1 Physically dissolved oxygen

The amount of dissolved oxygen is proportional to the oxygen partial pressure, P_{O_2}, according to Henry's law. Therefore:

$$C_{O_2 d} = \alpha_{O_2} \cdot P_{O_2} \qquad [54]$$

where α_{O_2} is the Bunsen solubility coefficient of oxygen in blood and is a function of the hematocrit, Hct, and the temperature, T (Figure II.5). The solubility coefficient can be calculated as a function of temperature using Zander <18> and Perry and Green <19>. The plasma oxygen solubility coefficient, $\alpha_{O_2 p}$, is expressed as:

$$\alpha_{O_2 p} = 2.855 \cdot 10^{-5} \cdot \left(1.01^{(37-T)}\right) \qquad [55]$$

The red blood cell oxygen solubility coefficient, $\alpha_{O_2 rbc}$, is given by:

$$\alpha_{O_2 rbc} = 4.658 \cdot 10^{-5} \cdot \left(1.01^{(37-T)}\right) \qquad [56]$$

The oxygen solubility coefficient can then be calculated as a weighted average of the solubility of the red blood cells and of the plasma:

$$\alpha_{O_2} = \alpha_{O_2 rbc} \cdot Hct + \alpha_{O_2 p} \cdot (1 - Hct) \qquad [57]$$

[†] The oxygen concentration in this thesis is expressed in [ml O_2/l] or briefly [ml/l].

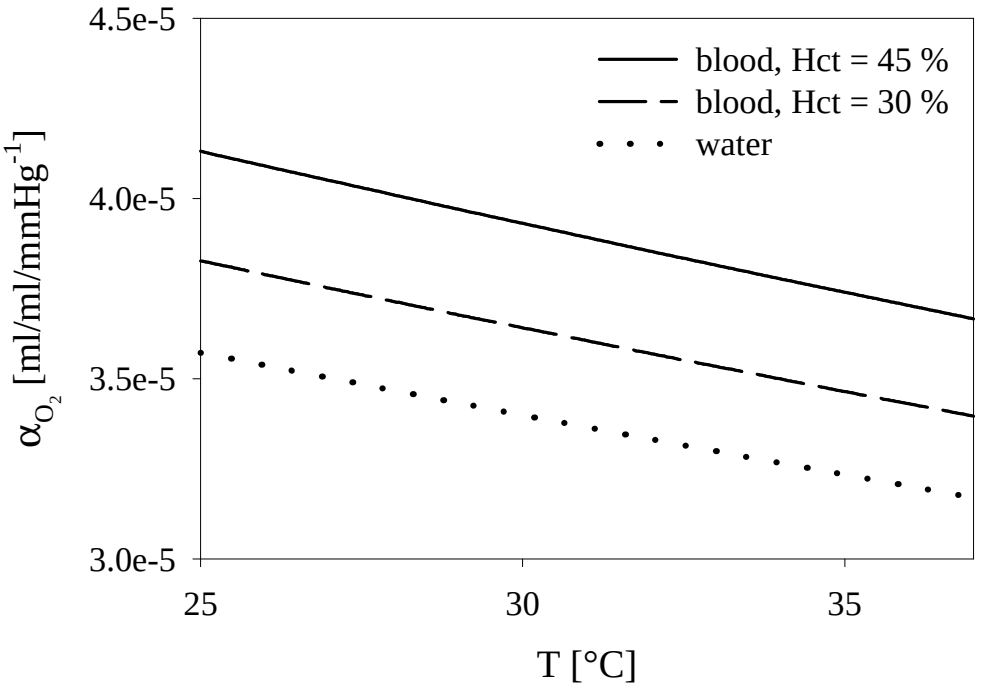

Figure II.5: The Bunsen solubility coefficient for oxygen in water and blood as a function of temperature, T, and hematocrit, Hct.

The variation of the solubility coefficient with temperature and hematocrit is shown in Figure II.5. It is clear that the solubility of oxygen in blood decreases when temperature increases, which is a general rule for gas solubility in liquids. The concentration of dissolved oxygen in arterial blood with a hematocrit of 45% and an oxygen partial pressure of 95 mmHg at a temperature of 37 °C, would be 3.5 ml/l.

The normal oxygen consumption for an adult is about 250 ml/min. With an average cardiac output of 5 l/min, one can calculate that this is inadequate to carry 250 ml of oxygen every minute. The maximum dissolved oxygen content is 17.5 ml/min, which is only 7 % of the required 250 ml/min. Therefore a far more effective means of oxygen transport is required.

The Bunsen solubility for oxygen in water is calculated as follows <19>:

$$\alpha_{O_2 water} = 3.17 \cdot 10^{-5} \cdot \left(1.01^{37-T}\right) \qquad [58]$$

or derived from tabulated data <217>.

II.3.2.2 Chemically bound oxygen - Hemoglobin

About 99 % of the oxygen which dissolves in the blood is combined with the oxygen-carrying protein hemoglobin, Hb, and about 94.5 % of the carbon dioxide which dissolves enters into a series of reversible chemical reactions converting it into other compounds. The presence of hemoglobin increases the oxygen transport capacity of the blood 70-fold. The dynamics of the

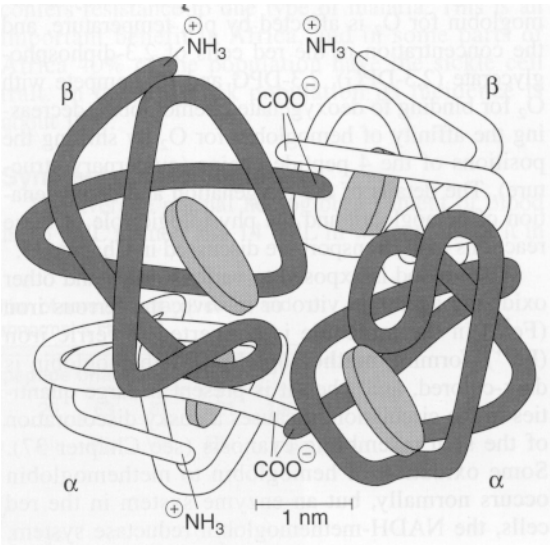

Figure II.6: Schematic representation of the hemoglobin molecule, showing the four subunits. The disks represent the heme moieties; the strings depict the polypeptide. <215>

reaction of hemoglobin with oxygen make it a particularly suitable oxygen carrier.

The red oxygen-binding pigment in the red blood cells is hemoglobin, a protein with a molecular weight of 64450 Dalton <215>. Hemoglobin is a globular molecule consisting of four subunits (Figure II.6). Each subunit contains a heme moiety conjugated to a polypeptide. Heme is an iron(Fe)-containing porphyrin derivative. The polypeptides are collectively referred to as the globin portion of the hemoglobin molecule. In other words, hemoglobin consists of the red color pigment, heme, and a protein, globin. The hemoglobin molecule can be represented as Hb_4. Since each Fe-atom can combine reversibly with an oxygen molecule, each hemoglobin molecule can combine with up to four oxygen molecules to form Hb_4O_8:

$$Hb_4 + O_2 \Leftrightarrow Hb_4O_2$$
$$Hb_4O_2 + O_2 \Leftrightarrow Hb_4O_4$$
$$Hb_4O_4 + O_2 \Leftrightarrow Hb_4O_6$$
$$Hb_4O_6 + O_2 \Leftrightarrow Hb_4O_8$$

It has been customary to write the reaction of hemoglobin with oxygen as:

$$Hb + O_2 \Leftrightarrow HbO_2$$

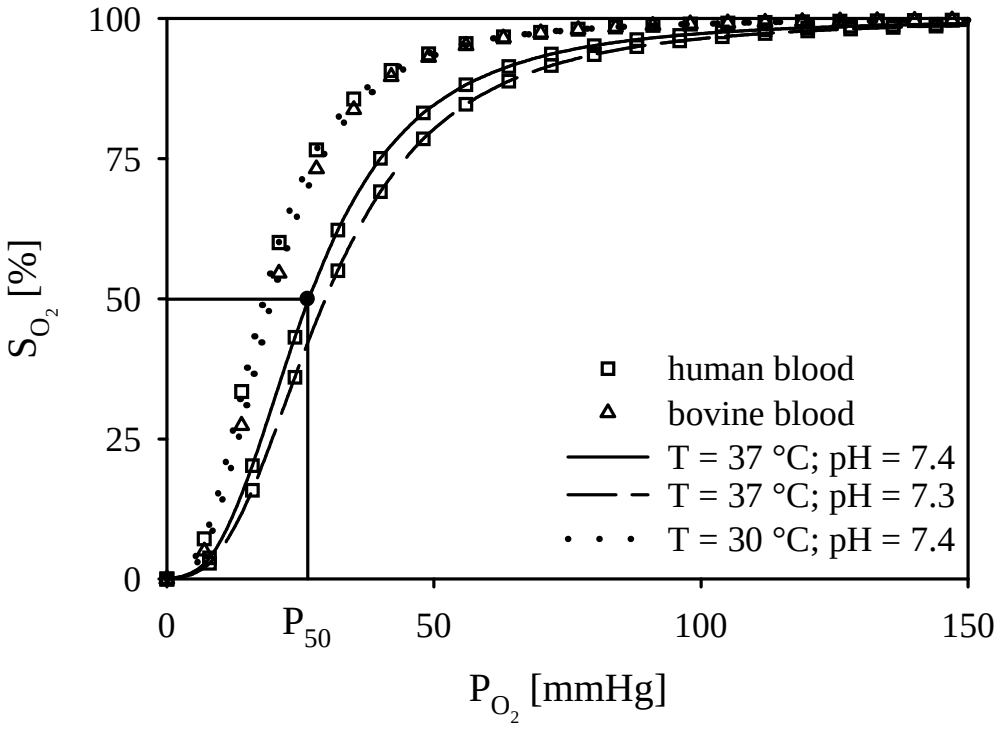

Figure II.7: Oxyhemoglobin dissociation curve for human and bovine[†] blood at different temperatures and pH reflecting the nonlinear, sigmoid relationship between hemoglobin saturation and oxygen partial pressure. The curve is shifted to the right with increasing temperature and decreasing pH. The Hill-equation <24-26> (Eq. [60]) is used to depict the oxyhemoglobin dissociation curve for human and bovine blood. In this figure, P_{50} denotes the second Hill parameter for normal human blood, i.e. the oxygen partial pressure when the oxygen saturation is 50 %.

The oxygenated form of hemoglobin is called oxyhemoglobin, HbO_2. The deoxygenated form of hemoglobin is called deoxyhemoglobin, Hb.

The concentration of hemoglobin-bound oxygen in the red blood cells is directly related to the concentration of dissolved oxygen in plasma. At equilibrium, the fraction of binding sites occupied by oxygen molecules is represented by the fractional oxygen saturation, S_{O_2}, which depends upon the partial pressure of oxygen in blood (Figure II.7). The relationship between the oxygen saturation and the oxygen partial pressure is typically a sigmoid curve, which has important physiological consequences, and is defined as the oxyhemoglobin dissociation curve. The use of this relationship implicitly assumes that the oxygen diffusion resistance of the red cell

[†] Bovine blood is used in the blood experiments and in the numerical modeling.

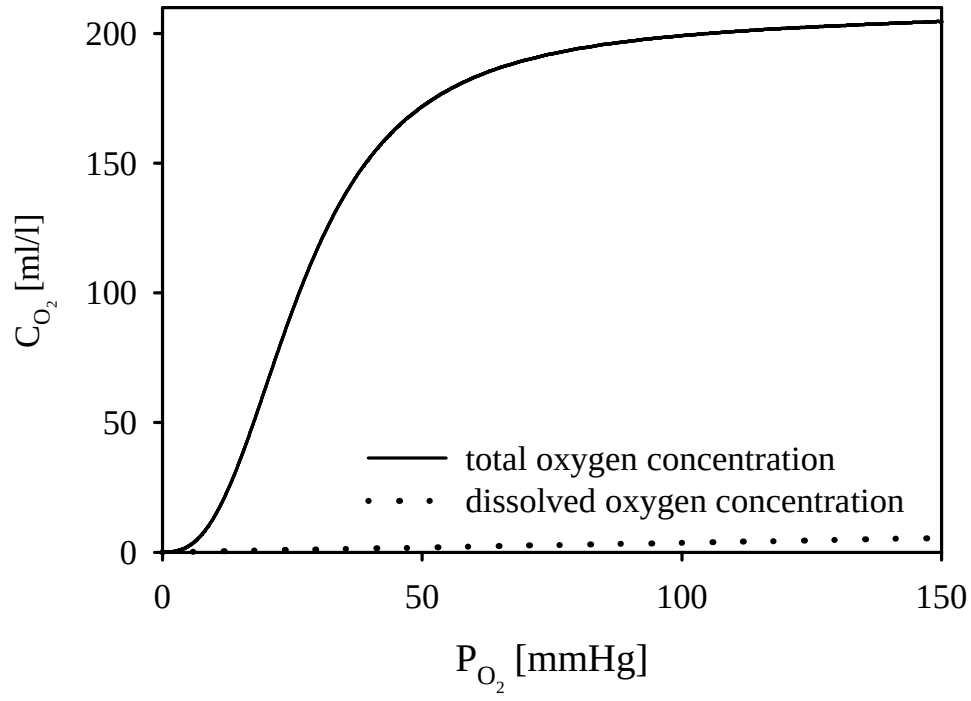

Figure II.8: Total and dissolved oxygen concentration, C_{O_2}, as a function of partial pressure, P_{O_2}, for normal human blood. The dashed line represents dissolved oxygen.

membrane is insignificant. If all the hemoglobin is combined with oxygen, it is said to be fully saturated, hence S_{O_2} = 100 %.

The affinity of hemoglobin for oxygen is usually affected by pH, temperature, hemoglobin concentration, and the concentration in the red blood cells of 2,3-diphosphoglycerate (2,3-DPG). The position of the oxyhemoglobin dissociation curve therefore depends primarily upon these factors (Figure II.7). The oxygen dissociation curve for normal physiologic conditions is shifted to the right by increased temperature or decreased pH, because of decreased hemoglobin affinity for oxygen. The oxygen dissociation curve is shifted to the right by an increase in the concentration of various organic phosphates, especially 2,3-diphosphoglycerate. 2,3-DPG and H^+ compete with oxygen to bind to deoxygenated hemoglobin, decreasing the affinity of hemoglobin for oxygen.

When blood is exposed to various drugs and other oxidizing agents *in vitro* or in vivo, the ferrous iron Fe^{+2} in the molecule is converted to ferric iron Fe^{+3}, forming the dark-colored methemoglobin. Carbon monoxide reacts with hemoglobin to form carbon mono-oxyhemoglobin

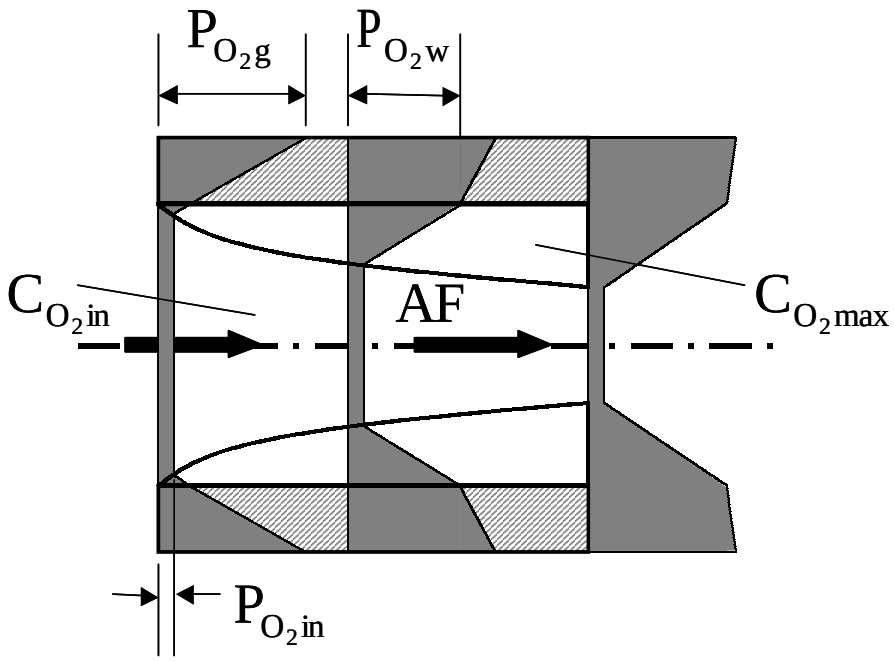

Figure II.9: Advancing Front theory for oxygenation of blood. Partial pressure profiles are superimposed on a side view of a blood channel between two parallel plates to illustrate the assumption if a linear gradient of partial pressure in the blood lying behind the advancing front (AF).

(carboxyhemoglobin). Moreover, the affinity of hemoglobin for oxygen is much lower than its affinity for carbon monoxide, which consequently displaces oxygen on hemoglobin, reducing the oxygen-carrying capacity of blood.

Based on the molecular weight of the hemoglobin molecule, the binding capacity of hemoglobin, B_{O_2}, is theoretically 1.39 ml/g <215>. However, blood contains small amounts of inactive hemoglobin derivatives, and the measured value in vivo is lower. In practice, 1 g of hemoglobin can bind with a maximum of 1.34 ml of oxygen. If C_{Hb} represents the hemoglobin mass concentration, the amount of chemically bound oxygen concentration is:

$$C_{O_2b} = B_{O_2} \cdot C_{Hb} \cdot S_{O_2} \qquad [59]$$

Under typical venous physiologic conditions (37 °C, oxygen partial pressure between 40 and 95 mmHg), the reaction between hemoglobin and oxygen reaches an equilibrium during the time of contact between the blood and the gas phase. In the lung capillaries the blood is completely oxygenated after a single passage which lasts no longer than 0.75 ± 0.25 s at rest and 0.34 ± 0.10 s during heavy exercise. Diffusion of oxygen to the red blood cells nearest to the surface takes about 0.10 s, while the chemical process of hemoglobin oxygenation takes only 0.001 s.

The total and dissolved oxygen concentration in normal human blood as a function of oxygen partial pressure is shown in Figure II.8.

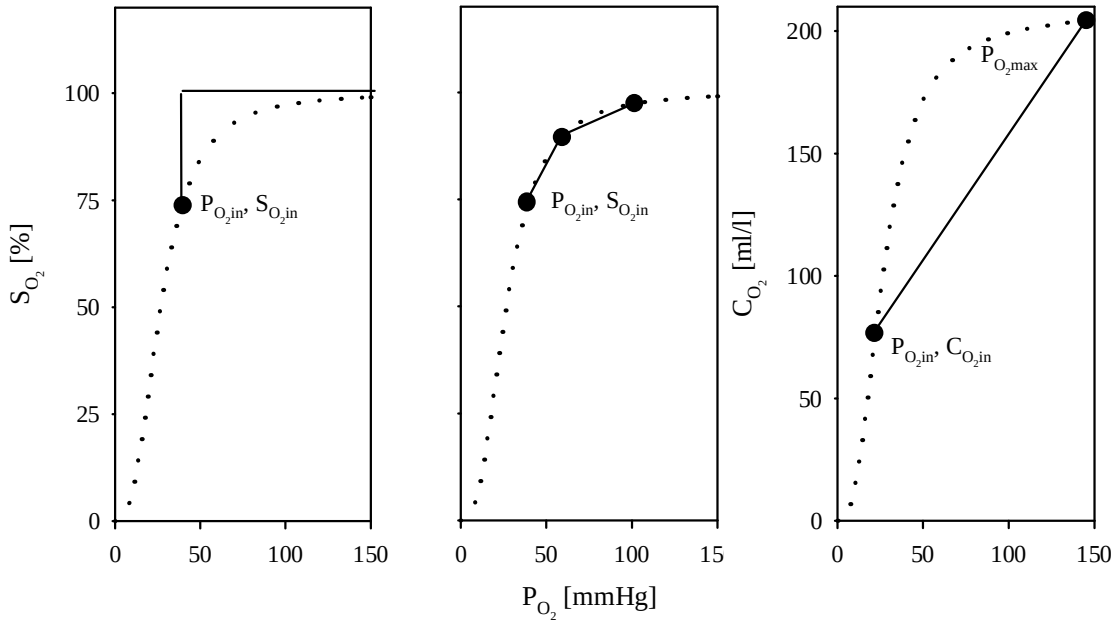

Figure II.10: Left panel: The Advancing Front theory for the oxygenation of blood with a step function located at the blood inlet condition; **middle panel:** Polygonal approximation of the oxyhemoglobin dissociation curve; **right panel:** The oxygen concentration represented by a curve with a constant slope, a linear form of the oxyhemoglobin dissociation curve.

II.3.3 The oxyhemoglobin dissociation curve

Describing the oxyhemoglobin dissociation curve is one of the most important problems in modeling oxygen exchange in blood. Many different mathematical models of the oxygen dissociation curve have been published <218-221>.

One approach is that proposed by Lightfoot <222>. Oxygenation of the blood is modeled by dividing the blood flow into two distinct regions (Figure II.9). These are separated by an advancing front at which there is an abrupt change of concentration from the inlet value, C_{O_2in}, to a maximum value, $C_{O_2 max}$. The blood is considered to be a fully saturated zone adjacent to a wall kept at a constant oxygen partial pressure, which advances into a central zone of unsaturated blood. Transport in this outer saturated level is primarily by diffusion along the gradient between the oxygen partial pressure in the gas phase and the central zone, which remains at the inlet value.

The advancing front theory is equivalent to modeling the oxyhemoglobin dissociation curve as a curve with a step (Figure II.10, left panel).

The oxyhemoglobin dissociation curve can also be approximated by a polygon or represented by a curve with a line of constant slope (Figure II.10, right panel), a linear form of the dissociation curve used in early modeling work <223>. The line is chosen to join a point which represents the inlet conditions, $\left(P_{O_2 in}, C_{O_2 in}\right)$, with a point which coincides with the maximum attainable partial pressure, $P_{O_2 max}$. This approach does not generate an analytical solution and underpredicts the achieved saturation at a given axial distance. The advancing front model overpredicts the saturation <224> (Figure II.10).

The classical Adair equation is based on four parameters, namely, the four equilibrium constants (K1, K2, K3, K4) for the successive binding of the four oxygen molecules to hemoglobin. Modified Adair equations with as many as eight parameters have been proposed. Margaria <225> has described the oxyhemoglobin dissociation curve mathematically with three empirical constants determined by the available data in the literature <226>. However, all former models was a poor fit to the Severinghaus standard oxygen dissociation curve.

Siggaard-Andersen et al. <218> described a mathematical model of the oxyhemoglobin dissociation curve of human blood, giving the oxygen saturation as a function of the oxygen partial pressure. The dependence upon temperature, pH, base excess, and concentration of 2,3-diphosphoglycerate in the erythrocytes is included in the parameters of the model. The model is a very good fit to the Severinghaus standard oxygen dissociation curve. The deviation is within 3 %, for the interval of the oxygen partial pressure between 10 and 110 mmHg.

A commonly used mathematical form of the oxyhemoglobin dissociation curve is the Hill-equation <24-26>:

$$S_{O_2} = \frac{\left(\frac{P_{O_2}}{P_{50}}\right)^n}{1+\left(\frac{P_{O_2}}{P_{50}}\right)^n} \qquad [60]$$

where n is the Hill parameter, which is constant for a particular blood species. The parameter P_{50} depends upon temperature, pH and blood species and is defined as the oxygen partial pressure in blood when the oxygen saturation is 50%:

- human blood <3>: n = 2.85

$$P_{50} = 26.6 \cdot \left(10^{0.48\cdot(7.4-pH)}\right)\cdot\left(10^{-0.024\cdot(37-T)}\right) \qquad [61]$$

- bovine† blood <3>: n = 2.70

† Bovine blood is used in the blood experiments and in the numerical modeling.

$$P_{50} = 29.0 \cdot \left(10^{0.41\cdot(7.4-pH)}\right) \cdot \left(10^{-0.024\cdot(37-T)}\right) \quad [62]$$

An example of the Hill equation for human and bovine blood is given in Figure II.7.

Both the Hill equation and the model of Siggaard-Andersen for normal human blood are depicted in a bilogarithmic plot of the oxygen saturation versus oxygen partial pressue, showing a minor difference between both mathematical models (Figure II.11). When the oxygen saturation exceeds 20 %, the Hill equation can be used <218>. In this work, the Hill equation is preferred for both its simplicity and accuracy.

II.3.4 Oxygen transfer rate

The oxygen transfer rate, $\dot{V}_{O_2}$, in artificial lungs can be measured by application of the principle of the conservation of mass to gas content measurements from blood entering and leaving the artificial lung <27>. The oxygen transfer rate may therefore be calculated as the sum of the

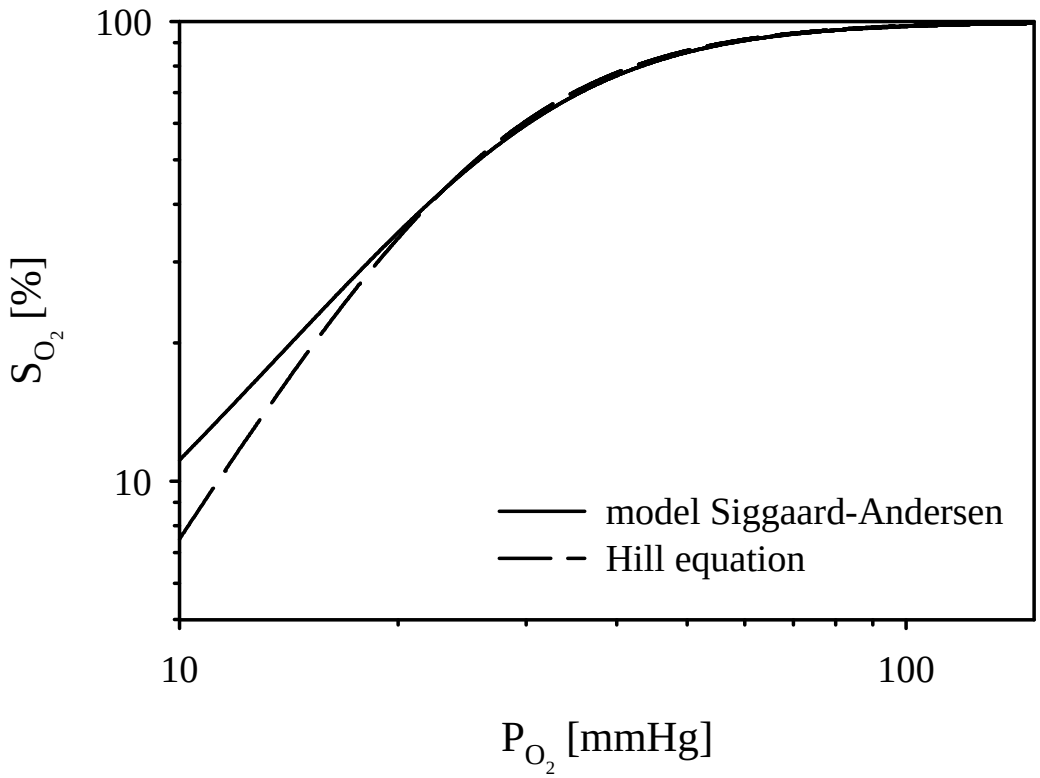

Figure II.11: Bilogarithmic plot of the oxyhemoglobin saturation showing a minor difference between the Hill equation <26> and the model of Siggaard-Anderson <218> for saturations of more than 20 %.

dissolved and the bound oxygen differences:

$$\dot{V}_{O_2} = \alpha_{O_2} \cdot Q \cdot \left(P_{O_2 out} - P_{O_2 in}\right) + B_{O_2} \cdot C_{Hb} \cdot Q \cdot \left(S_{O_2 out} - S_{O_2 in}\right) \quad [63]$$

in which the indexes “in” and “out” refer to the inlet and the outlet of the artificial lung respectively. Q is the blood flow rate.

II.3.5 Oxygen diffusion

Species of large molecular weight, e.g. oxyhemoglobin, do not diffuse significantly because they are contained within the red blood cells and because their diffusivities are two orders of magnitude lower than those of dissolved species. Therefore, it is only necessary to consider diffusion of dissolved oxygen.

The diffusion coefficient of dissolved oxygen in blood, D_{O_2}, is calculated using a modified Fricke theory <20-22>. This theory presumes that the diffusion of oxygen in blood may be expressed in terms of the diffusion of oxygen in cells, $D_{O_2 rbc}$ and the diffusion of oxygen in the suspending medium (plasma or plasma / saline mixture), $D_{O_2 p}$:

$$D_{O_2} = D_{O_2 p} \cdot \frac{\alpha_{O_2 p}}{\alpha_{O_2}} \cdot \left(\frac{1 + \chi \cdot R}{1 - R}\right) \quad [64]$$

in which

$$R = Hct \cdot \left(\frac{N \cdot \frac{D_{O_2 rbc}}{D_{O_2 p}} - 1}{N \cdot \frac{D_{O_2 rbc}}{D_{O_2 p}} + \chi}\right) \quad [65]$$

$$N = \frac{\alpha_{O_2 rbc}}{\alpha_{O_2 p}} \quad [66]$$

$$\chi = \frac{-\left(N \cdot \frac{D_{O_2 rbc}}{D_{O_2 p}} - 1\right) - \left(N \cdot \frac{D_{O_2 rbc}}{D_{O_2 p}}\right) \cdot \beta}{\left(N \cdot \frac{D_{O_2 rbc}}{D_{O_2 p}} - 1\right) - \beta} \quad [67]$$

β is a shape factor for the cells:

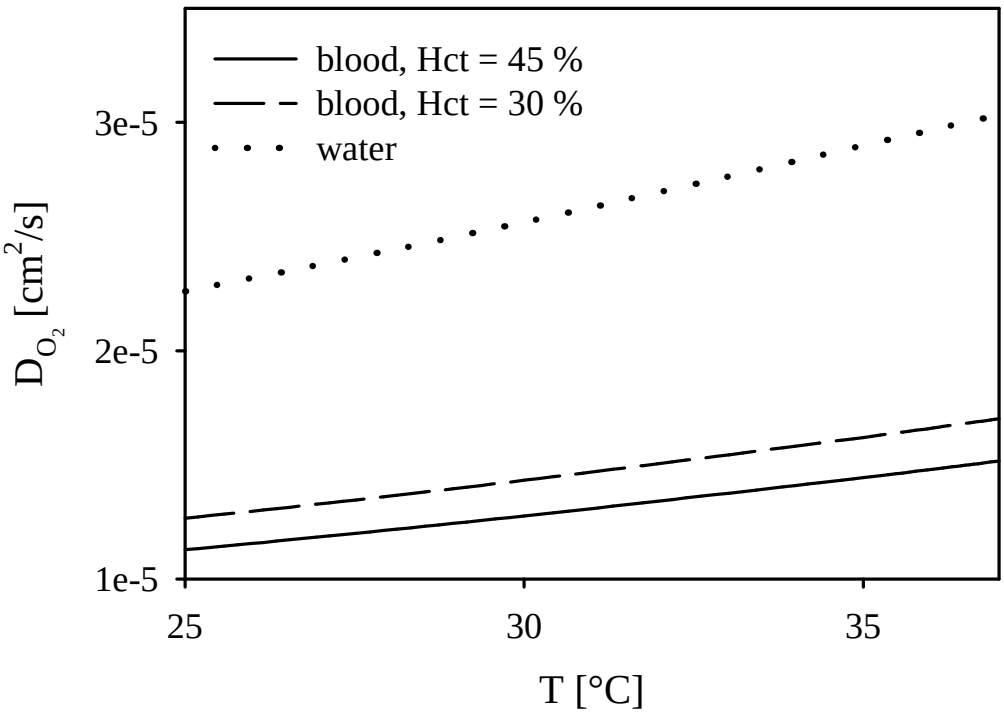

Figure II.12: Oxygen diffusion coefficient in water and blood as a function of temperature, T, and hematocrit, Hct. <20-22>

$$\beta = \frac{1}{3}\cdot\left(\frac{2}{1+\left(N\cdot\frac{D_{O_2rbc}}{D_{O_2p}}-1\right)\cdot 0.1415}+\frac{1}{1+\left(N\cdot\frac{D_{O_2rbc}}{D_{O_2p}}-1\right)\cdot 0.717}\right)\cdot\left(N\cdot\frac{D_{O_2rbc}}{D_{O_2p}}-1\right) \qquad [68]$$

Figure II.12 shows the dependence of the oxygen diffusion coefficient upon temperature and hematocrit.

At 37°C, $D_{O_2rbc} = 1.02\cdot 10^{-5}$ cm²/s and $D_{O_2p} = 2.18\cdot 10^{-5}$ cm²/s. An effective diffusion coefficient, D_{O_2eff}, for oxygen through blood is necessary to analyze gas transfer in membrane artificial lungs and will be discussed in §II.4.5.

The oxygen diffusion coefficient for water is derived from Welty et al. <227> and Bird et al. <35> (Figure II.12). It is commonly accepted that only the dissolved form of gas can diffuse through the hydrophobic microporous membranes.

II.3.6 Oxygen transfer and cardiopulmonary bypass

Venous blood in an artificial lung equilibrates with the ventilating gases by gas exchange through the microporous membrane. Normal arterial blood-gas values are obtained for all blood flow rates, venous hemoglobin-oxygen saturations, and hemoglobin concentrations.

Typical operating conditions for total CPB in an adult are summarized in Figure II.13 and Table II.2. Note the large differences in driving forces for oxygen and carbon dioxide. Under normothermia and with pure oxygen fed to the gas phase, the initial driving force is approximately 45 mmHg for carbon dioxide and 713 mmHg for oxygen yielding a ratio of carbon dioxide to oxygen driving forces of about 0.063.

In the 1970s, a silicone membrane artificial lung was utilized in CPB. The ratio of carbon dioxide to oxygen permeability for silicone rubber is roughly 5.0, and the corresponding flux ratio is 0.32, less than half of the metabolically determined respiratory quotient (0.82). Under these conditions, carbon dioxide is the limiting gas and the size of the device should be based on carbon dioxide transport rather than oxygen transport requirements. Silicone rubber was replaced by microporous polypropylene because of cost, structural stability and quality control. In that case the solubility of carbon dioxide in the membrane material, and consequently its permeability, is no longer the limiting factor. Moreover, in modern membrane artificial lungs, gas flow through the device needs to be controlled to avoid an excessive loss of carbon dioxide.

Table II.2: Typical operating parameters for cardiopulmonary bypass <10>. The oxygen partial pressure in the gas side is the barometric pressure (760 mmHg) minus the vapor pressure (47 mmHg at 37 °C).

oxygen transfer requirements		250 ml/min
carbon dioxide elimination requirement		200 ml/min
respiratory gas exchange ratio (respiratory quotient)		0.8
blood flow rate		5 l/min
gas flow rate		5 – 10 l/min
gas partial pressure [mmHg]	P_{O_2}	P_{CO_2}
blood in	40	45
blood out	100 - 300	30 – 40
gas in (humidified)	250 - 713	0 – 20
gas out	150 - 675	10 – 30

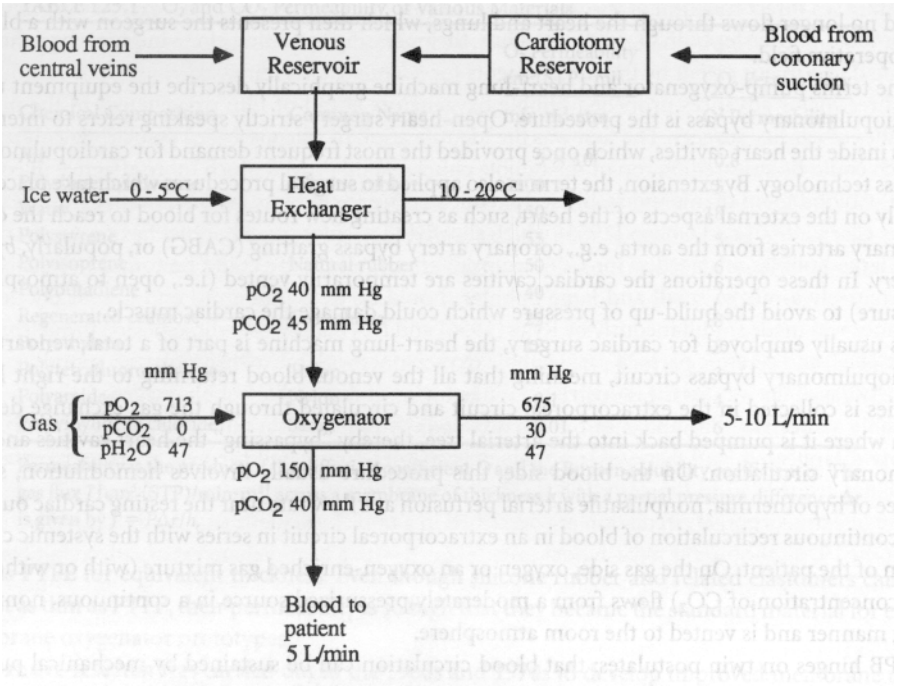

Figure II.13: Scheme of standard operating conditions during cardiopulmonary bypass. <10>

II.4 Numerical modeling

II.4.1 The finite element method <29,30>

The finite element method (FEM) is a technique to solve partial differential equations. It can be considered to be a general discretization tool for partial differential equations. In this sense, the finite element method forms an alternative for finite difference methods or finite volume methods. The finite element method can be used to solve problems that are defined on complex geometries. However, the programming of finite element methods is more complicated than that of the finite difference method, and hence in general requires standard software packages.

The first essential characteristic of FEM is that the continuum field, or domain Ω, is subdivided into cells, called elements, which form a grid. The subdivision is carried out by a mesh-generator. The elements have either a triangular or a quadrilateral form. They can be rectilinear or curved. The grid itself doesn't need to be structured. Due to this unstructured form, very complex geometries can be handled with ease. This is clearly the most important advantage of the method. This property is not shared by the finite difference method, which needs a structured grid. Therefore, in the finite difference method the domain is to be regularized by mapping a complex domain into a series of rectangular regions. The finite volume method, on the other hand, has the same geometric characteristic as the FEM.

The second essential characteristic of the FEM is that the solution of the discrete problem is assumed a priori to have a prescribed form. The solution has to belong to a function space, which is built by varying function values in a specific way, for instance linearly or quadratically, between values in nodal points. The nodal points, or nodes, are typical points of the elements such as vertices, mid-side points, mid-element points, etc. Due to this choice, the representation of the solution is strongly linked to the geometric representation of the domain. This link is, for instance, not as strong in the finite volume method.

The third essential characteristic is that the FEM does not look for a solution of the partial differential equations itself, but for a solution of some integral form of the partial differential equations. In its most general form, this integral formulation is obtained from a weighted residual formulation. Through this formulation, the method acquires the ability to naturally incorporate differential type boundary conditions. This property constitutes the second important advantage of the FEM.

The combination of the representation of the solution in a given function space, with the integral formulation treating the boundary conditions rigorously gives the method an extremely strong and rigorous mathematical formulation. Among other things, this allows a precise definition of accuracy.

A final essential characteristic of the FEM, is the modular way in which the discretization is obtained. The discrete equations are constructed from contributions on the element level, which are afterwards assembled.

In structural mechanics, the partial differential formulation of a problem can always be replaced by an equivalent variational formulation, i.e. the minimization of an energy integral (known as a functional, i.e. the mapping from a set of admissible functions into the real numbers) over the domain (extremal problems). A variational or extremal formulation is a problem such as: finding a function that minimizes, maximizes, or makes stationary a functional subject to given boundary conditions. This formulation constitutes a natural integral formulation for the FEM. Based on these extremal problems, approximate solutions can be constructed using basis functions. This method is known as the Ritz method and leads to a system of linear algebraic equations. Unfortunately, it is generally difficult or even impossible to find the correct functional corresponding to a partial differential equation, especially in fluid dynamics. Therefore, another integral (or variational) method based on the partial differential equations is used. This method is known as the Galerkin method and is applicable to partial differential equations for which no equivalent optimization formulation exists. The Galerkin method is a natural extension of the so-called weak formulation of the partial differential equations.

The numerical solution of partial differential equations always results in the solving of a number of large systems of sparse linear systems. Solution algorithms can be subdivided into direct and iterative methods. Gaussian elimination and Choleski decomposition are direct methods and can be used when the system is not too large. Iterative methods such as the conjugate gradient method for symmetric positive definite matrices and Krylov methods for general matrices, are very cheap with respect to memory requirements. However, convergence can be very slow so the computing time may be much longer than for direct methods. The Krylov subspace methods become much faster when combined with a preconditioner.

The analytical and numerical approach is to derive a model of a system using the basic mathematical equations describing the physical laws such as the conservation of mass and momentum, and to describe the causal relationships between its component parts. The Navier-Stokes equations (§II.4.2) describing the flow of a fluid, and the convection-diffusion equation (§II.4.4) describing the mass transfer in a fluid, two general types of differential equations, can be discretized by the finite element method.

One of the reasons why finite elements have been less popular than finite differences in the past, is the lack of upwind techniques. However, accurate upwind methods have now been constructed. The most popular one is the so-called streamline upwind Petrov-Galerkin method (SUPG). It shows that upwinding may increase the quality of the solution considerably and it makes the systems of linear equations more appropriate for the iterative methods for solving these systems.

In this thesis, SEPRAN <31> is employed to generate the mesh and to build and solve the system of equations. SEPRAN is an open software packet of subroutines for solving partial differential equations with the help of the finite element technique. SEPRAN is written in FORTRAN. It provides the main programs for the preprocessing, the computing part and the postprocessing of the finite element technique. Function subroutines and user element subroutines, adapted to the problem, may be attached to these programs. Besides the standard possibilities, SEPRAN allows the user also to construct his own main program using the standard subroutines SEPRAN provides.

II.4.2 The Navier-Stokes equations

The steady state, isothermal flow of a homogeneous viscous, incompressible liquid is governed by the continuity and Navier-Stokes equations. These equations express the classical principles of conservation of mass:

$$\overline{\nabla} \bullet \bar{\mathbf{u}} = 0 \qquad [69]$$

and conservation of momentum:

$$\rho \bar{\mathbf{u}} \bullet \overline{\nabla} \bar{\mathbf{u}} + \overline{\nabla} p = \overline{\nabla} \bar{\mathbf{t}} \qquad [70]$$

where $\bar{\mathbf{u}}$ is the local mass average fluid velocity vector, ρ is the local density, p is the local hydrostatic pressure, and $\bar{\mathbf{t}}$ is the deviatoric stress tensor. $\overline{\nabla}$ is the gradient operator in rectilinear cartesian coordinates (two-dimensional):

$$\overline{\nabla} = \left(\frac{\partial}{\partial x}, \frac{\partial}{\partial y} \right) \qquad [71]$$

The stress tensor, $\bar{\boldsymbol{\sigma}}$, consists of two parts, the pressure part and the deviatoric stress tensor, according to:

$$\bar{\boldsymbol{\sigma}} = -p \cdot \bar{\mathbf{I}} + \bar{\mathbf{t}} \qquad [72]$$

with $\bar{\mathbf{I}}$ being the unity tensor.

To model the deviatoric stress tensor, it is necessary to add the constitutive equation (expressing rheological properties of the fluid), which has the following form <30>:

$$\bar{\mathbf{t}} = \mu\left(\overline{\nabla} \bar{\mathbf{u}}\right)\left(\overline{\nabla} \bar{\mathbf{u}} + \overline{\nabla} \bar{\mathbf{u}}^{T}\right) \qquad [73]$$

in which μ denotes the dynamic viscosity and superscript T is the transpose of the tensor. The choice of $\mu\left(\overline{\nabla} \bar{\mathbf{u}}\right)$ defines the model. Many fluids obey Newton's law, stating that stress in the fluid is proportional to the rate of deformation. Newton's law states that $\mu\left(\overline{\nabla} \bar{\mathbf{u}}\right)$ is constant for a Newtonian fluid, μ_{∞}.

In order to solve the equations Eq. [69] and Eq. [70] it is necessary to prescribe boundary conditions. Since Eq. [70] is a system of second order differential equations in space, it is necessary to prescribe boundary conditions for each velocity component at the complete boundary of the domain. For incompressible flows, no explicit boundary conditions for the pressure must be given. At fixed walls, no-slip conditions at the wall are applied resulting in Dirichlet or essential boundary conditions for the velocity:

$$\bar{\mathbf{u}} = 0 \qquad [74]$$

At symmetry planes, Neumann or natural boundary conditions are given. There are no velocity components perpendicular to the symmetry plane and the tangential stress, σ_t, is zero.

$$\begin{aligned} u_n &= \bar{\mathbf{u}} \bullet \bar{\mathbf{n}} = 0 \\ \sigma_t &= \bar{\boldsymbol{\sigma}} \bullet \bar{\mathbf{n}} - \sigma_n \cdot \bar{\mathbf{n}} = \bar{\mathbf{0}} \end{aligned} \qquad [75]$$

with $\bar{\mathbf{n}}$ being the normal vector and σ_n the normal component of the stress:

$$\sigma_n = \bar{\mathbf{n}} \bullet \bar{\boldsymbol{\sigma}} \bullet \bar{\mathbf{n}} \qquad [76]$$

When periodicity in the flow pattern is considered, periodical boundary conditions are applied to opposite boundaries.

II.4.3 The Navier-Stokes equations for blood flow

Eq. [73] denotes the constitutive equation. Generalized Newtonian fluid models are time independent constitutive models and can be used to model the viscous properties of blood. The non-Newtonian plastico-viscous shear-thinning Casson model <214> (§II.2.2) is used to model the viscous properties of blood. The Casson model is appropriate for shear thinning fluids with a yield stress and is characterized by the following viscosity model:

$$\mu = \mu_\infty \left(1 + \left[\frac{\tau_o}{\mu_\infty} \Pi^{-\frac{1}{2}} \right]^{\frac{1}{2}} \right)^2 \qquad [77]$$

in which τ_o is the yield stress, stress at zero shear rate, and Π denotes the second invariant of the velocity deformation tensor:

$$\Pi = \frac{1}{2} \cdot \bar{\mathbf{A}} : \bar{\mathbf{A}} \qquad [78]$$

with $\bar{\mathbf{A}}$ representing the velocity deformation tensor:

$$\bar{\mathbf{A}} = \bar{\nabla}\bar{\mathbf{u}} + \bar{\nabla}\bar{\mathbf{u}}^T \qquad [79]$$

II.4.4 The convection-diffusion equation

The equations of continuity for two chemical species (e.g. A and B) in a binary fluid mixture can be established by making a mass balance over an arbitrary differential fluid element. Then the insertion of the expression for the mass flux results in the convection-diffusion equation <35>. The stationary convection-diffusion equation for mass transfer of species A in a binary fluid of species A and species B, with diffusion coefficient, D_{AB}, of species A into B, can be described as follows:

$$-\bar{\nabla}\left(D_{AB} \cdot \bar{\nabla} C_A\right) + \bar{\mathbf{u}} \bullet \bar{\nabla} C_A = r \qquad [80]$$

in which C_A is the concentration of species A, $\bar{\mathbf{u}}$ is the macroscopic fluid velocity vector of species B and r denotes a reaction (source / sink) term. When the diffusion coefficient is constant, Eq. [80] results in:

$$-D_{AB} \cdot \Delta C_A + \bar{\mathbf{u}} \bullet \bar{\nabla} C_A = r \qquad [81]$$

where Δ is the Laplace operator in rectilinear cartesian coordinates (two dimensional):

$$\Delta = \frac{\partial^2}{\partial x^2} + \frac{\partial^2}{\partial y^2} \qquad [82]$$

The concentration can be prescribed on some part of the boundary of the computational grid (Dirichlet or essential boundary conditions). At symmetry planes, Neumann or natural boundary conditions are given:

$$\frac{\partial C_A}{\partial n} = \bar{\nabla} C_A \bullet \bar{\mathbf{n}} = 0 \qquad [83]$$

with $\bar{\mathbf{n}}$ denoting the normal vector.

II.4.5 The convection-diffusion equation for oxygen transfer in blood

As has already been discussed in §II.2, blood can be considered statistically homogeneous over a sample volume <228>. Moreover, the reaction between oxygen and hemoglobin can be assumed to be fast enough so that an equilibrium dissociation curve can be used <229>. The stationary convection-diffusion equation for dissolved oxygen transfer in blood reads as follows:

$$\bar{\mathbf{u}} \bullet \bar{\nabla} C_{O_2 d} = D_{O_2 d} \cdot \Delta C_{O_2 d} + \dot{R}_d \qquad [84]$$

where $\bar{\mathbf{u}}$ is the blood velocity vector, $C_{O_2 d}$ represents the dissolved oxygen concentration in blood, $D_{O_2 d}$ the diffusion coefficient of dissolved oxygen through blood and $\dot{R}_d$ the reaction of dissolved oxygen and hemoglobin. The convective transport of bounded oxygen concentration is described as:

$$\bar{\mathbf{u}} \bullet \bar{\nabla} C_{O_2 b} = D_{O_2 b} \cdot \Delta C_{O_2 b} + \dot{R}_b \qquad [85]$$

where $C_{O_2 b}$ represents the bound oxygen concentration in blood, $D_{O_2 b}$ the diffusion coefficient of bound oxygen through blood and $\dot{R}_b$ the reaction of bound oxygen and hemoglobin. Since the the bounded oxygen (i.e. the oxyhemoglobin) is confined to the red blood cell, it can't diffuse into the blood plasma. Moreover, the diffusion and the Brownian motion of the red blood cells is negligible compared to the convection of the red blood cell, so that:

$$D_{O_2 b} \cdot \Delta C_{O_2 b} \approx 0 \qquad [86]$$

Since

$$\dot{R}_b = -\dot{R}_d \qquad [87]$$

and adding Eq. [84] and Eq. [85] while taking into account Eq. [86], yields:

$$\bar{\mathbf{u}} \bullet \bar{\nabla}\left(C_{O_2 d} + C_{O_2 b}\right) = D_{O_2} \cdot \Delta C_{O_2 d} \qquad [88]$$

where D_{O_2} is the diffusion coefficient of dissolved oxygen through blood:

$$D_{O_2} = D_{O_2 d} \qquad [89]$$

In §II.3.2, it was described that the total amount of oxygen concentration in blood is the sum of the dissolved, $C_{O_2 d}$, and bound, $C_{O_2 b}$, oxygen concentrations (Eq. [53]). The presence of the bound oxygen concentration in the convection-diffusion equation makes it nonlinear since the oxygen saturation, S_{O_2}, in Eq. [59] depends upon the oxygen partial pressure, P_{O_2}, in a complicated, nonlinear manner (e.g. Eq. [60]). Substitution of Henry's law (Eq. [54]) and of Eq. [59] into Eq. [88] and taking into account the dependency of the oxygen saturation upon the oxygen partial pressure, yields:

$$\left(1 + B_{O_2} \cdot \frac{C_{Hb}}{\alpha_{O_2}} \cdot \frac{dS_{O_2}}{dP_{O_2}}\right) \cdot \bar{\mathbf{u}} \bullet \bar{\nabla} P_{O_2} = D_{O_2} \cdot \Delta P_{O_2} \qquad [90]$$

An effective diffusion coefficient, $D_{O_2 eff}$, can now be introduced which takes into account the oxygen-hemoglobin reactions. Weissman et al. <230> have shown that (Figure II.14):

$$D_{O_2 eff} = \frac{D_{O_2}}{1 + \lambda(P_{O_2})} \qquad [91]$$

Where

$$\lambda\left(P_{O_2}\right) = B_{O_2} \cdot \frac{C_{Hb}}{\alpha_{O_2}} \cdot \frac{dS_{O_2}}{dP_{O_2}} \qquad [92]$$

Eq. [90] can than be rewritten as:

$$\bar{\mathbf{u}} \bullet \bar{\nabla} P_{O_2} = D_{O_2 eff} \cdot \Delta P_{O_2} \qquad [93]$$

The term $\left(1 + \lambda\left(P_{O_2}\right)\right)$ in Eq. [91] represents the reciprocal of the fraction of the total oxygen uptake contributed by dissolved oxygen. Thus, $\lambda\left(P_{O_2}\right)$ is a sink term accounting for oxygen uptake by hemoglobin Figure II.15. $\lambda\left(P_{O_2}\right)$ is proportional to the rate of saturation increase for an increase of oxygen partial pressure, i.e. it is proportional to the slope of the oxyhemoglobin dissociation curve (e.g. the Hill equation, Eq. [60])

For a non-reactive fluid, such as water,

$$\lambda\left(P_{O_2}\right) = 0 \qquad [94]$$

The total mass transfer is therefore represented by dissolved oxygen alone.

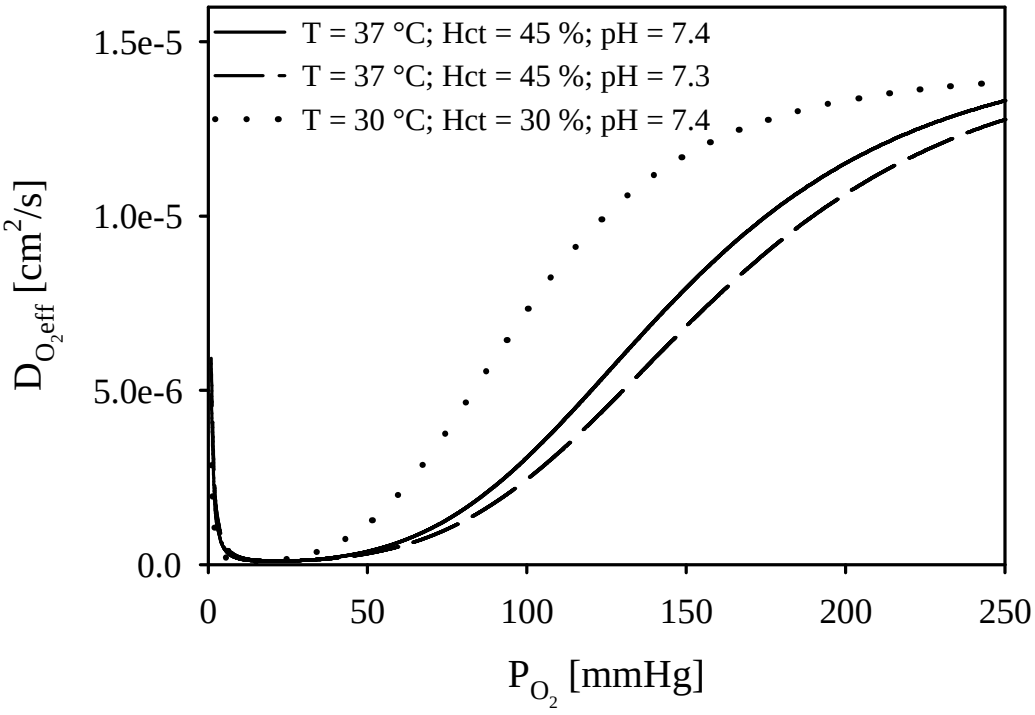

Figure II.14: Effective oxygen diffusion coefficient, D_{O_2eff}, as a function of temperature, T, hematocrit, Hct, and pH for human blood.

If the Hill equation (Eq. [60]) is used to describe the oxyhemoglobin dissociation curve, the slope of the oxyhemoglobin dissociation curve can be derived as follows:

$$\frac{dS_{O_2}}{dP_{O_2}} = \frac{n}{P_{50}} \cdot \left(\frac{P_{O_2}}{P_{50}} \right)^{n-1} \cdot \frac{1}{\left(1 + \left(\frac{P_{O_2}}{P_{50}} \right)^{n} \right)^{2}} \qquad [95]$$

Inserting Eq. [95] into Eq. [92] gives:

$$\lambda\left(P_{O_2}\right) = B_{O_2} \cdot \frac{C_{Hb}}{\alpha_{O_2}} \cdot \frac{n}{P_{50}} \cdot \left(\frac{P_{O_2}}{P_{50}} \right)^{n-1} \cdot \frac{1}{\left(1 + \left(\frac{P_{O_2}}{P_{50}} \right)^{n} \right)^{2}} \qquad [96]$$

Eq. [96] gives an expression of $\lambda\left(P_{O_2}\right)$ in terms of known quantities of human or bovine blood. Figure II.15 shows $\lambda\left(P_{O_2}\right)$ as a function of temperature, T, and hematocrit, Hct.

The convection-diffusion equation for oxygen in blood (Eq. [88]) becomes:

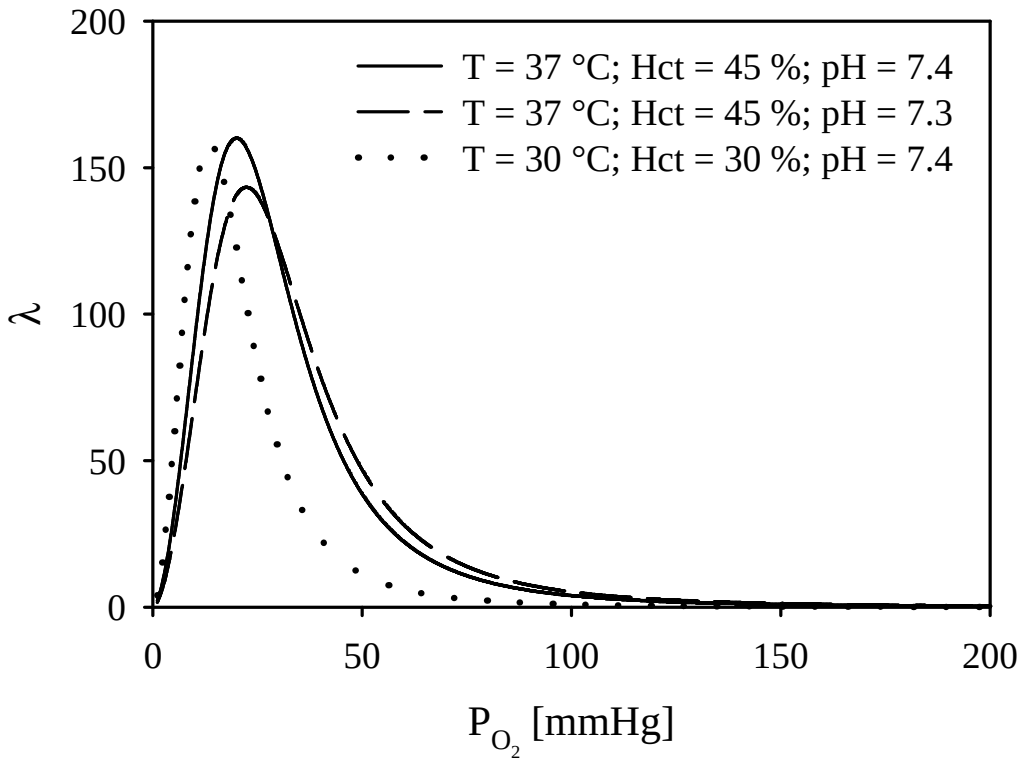

Figure II.15: The term $\lambda(P_{O_2})$ as a function of oxygen partial pressure, P_{O_2}, temperature, T, hematocrit, Hct, and pH for human blood.

$$\bar{\mathbf{u}} \bullet \bar{\nabla} P_{O_2} = D_{O_2 eff} \cdot \Delta P_{O_2} \qquad [97]$$

The resulting two-dimensional convection-diffusion equation is expressed in terms of the oxygen partial pressure. In general, the equation consists of a first-order derivative term in the direction of the flow representing the transport of species due to convection, and of a second-order derivative term representing the transport of species perpendicular to and in the direction of the flow due to molecular diffusion (governed by Fick's law and taking into account the nonlinear effective diffusion coefficient).

Assuming negligible mass transfer across the membrane compared to the mass flow along the membrane, and with no rheological blood changes due to gas transfer, blood velocity is independent of the gas transfer and is therefore solved first. The oxygen partial pressure in the blood is then solved afterwards.

II.4.6 The finite element method and the Navier-Stokes equations

When periodicity in the flow pattern is considered, periodical boundary conditions are applied on opposite boundaries (Figure II.16, left panel). SEPRAN implements periodical boundary conditions with a given volume flux, q, per unit fiber length and hence an unknown pressure difference, by a penalty function approach <41>. The volume flux is given by:

$$q = \int_{\Gamma_{per}} \bar{\mathbf{u}} \bullet \bar{\mathbf{n}} \cdot d\Gamma \qquad [98]$$

where Γ_{per} denotes the inflow periodical boundary. Hence, the Navier-Stokes equations are solved with the given volume flux as constraint. Corresponding to this constraint, an unknown pressure jump exists between the inflow and outflow boundaries. It is necessary to define a line element along the complete inflow boundary. Along this line element a special boundary element is defined that prescribes the volume flux. In order to use periodical boundary conditions, the corresponding degrees of freedom must be identified and therefore connection elements are introduced at the opposite sides. All degrees of freedom in the nodal points of the inflow boundary (I) are identified with the corresponding degrees of freedom on the outflow boundary (III) Figure II.16 (right panel). In the case of Figure II.16 (left panel), the connection elements created are depicted in Figure II.16 (right panel). The values of the flow variables at the outflow boundary are imposed upon the inlet boundary during the solution procedure.

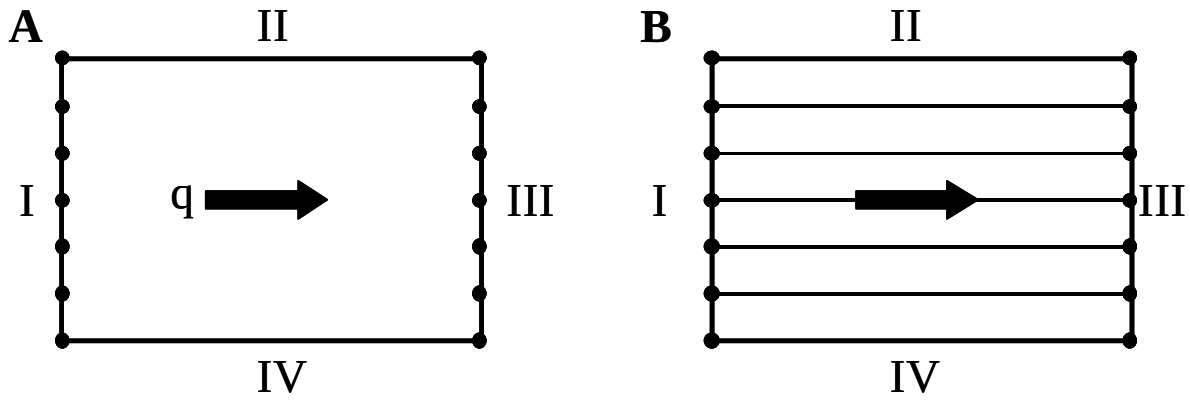

Figure II.16: A: Periodical boundary conditions at the inflow (I) and the outflow (III) boundary, volume flux q. **B:** Elements to prescribe boundary conditions on the inflow (I) and the outflow (III) boundary.

The Navier-Stokes equations, Eq. [69] and Eq. [70] are discretized using Galerkin's finite element method after substitution of Eq. [73]. This results in a system of nonlinear equations <30>. The convective term, $\bar{\mathbf{u}} \bullet \bar{\nabla}\bar{\mathbf{u}}$, renders the Navier-Stokes equations nonlinear. In order to

solve the resulting system of nonlinear equations, an iterative procedure is necessary. A standard Newton linearization can be used:

$$\bar{\mathbf{u}}^{k+1} \bullet \bar{\bar{\nabla}} \bar{\mathbf{u}}^{k+1} \approx \bar{\mathbf{u}}^{k+1} \bullet \bar{\bar{\nabla}} \bar{\mathbf{u}}^{k} + \bar{\mathbf{u}}^{k} \bullet \bar{\bar{\nabla}} \bar{\mathbf{u}}^{k+1} - \bar{\mathbf{u}}^{k} \bullet \bar{\bar{\nabla}} \bar{\mathbf{u}}^{k} \qquad [99]$$

Newton linearization converges fast (i.e. quadratically) as soon as the iteration is in the neighborhood of the final solution. An alternative linearization is constructed by the so-called Picard iteration, which has a larger convergence region but converges more slowly:

$$\bar{\mathbf{u}}^{k+1} \bullet \bar{\bar{\nabla}} \bar{\mathbf{u}}^{k+1} \approx \bar{\mathbf{u}}^{k} \bullet \bar{\bar{\nabla}} \bar{\mathbf{u}}^{k+1} \qquad [100]$$

An important question with respect to the iterative methods is how a good initial estimate can be found. One can start the iteration process with an initial guess, for example with the solution of the Stokes problem, which is formed by the Navier-Stokes equations, but where the convective terms have been neglected, $\bar{\mathbf{u}} \bullet \bar{\bar{\nabla}} \bar{\mathbf{u}} = 0$. Then the Picard iteration is performed in one step in order to approach the final solution. In the next steps, Newton iteration can be used.

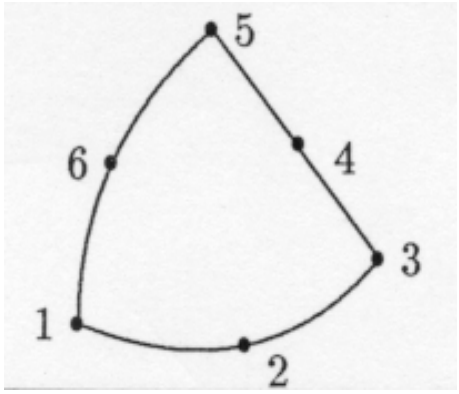

Figure II.17: Isoparametric triangle with six points. A quadratic approximation for the two velocity components in each node is applied. <31>

Since the pressure is an unknown in the momentum equations, Eq. [70], but not in the continuity equation, Eq. [69], the discretization of the Navier-Stokes equations must satisfy some special requirements. The first requirement is that the number of pressure unknowns may never exceed the number of velocity unknowns. The second one are the so-called Brezzi-Babuška conditions. These conditions create a relation between pressure and velocity approximation. In finite differences and finite volumes, the equivalent of the BB conditions is satisfied if staggered grids are applied.

The set of linear differential equations is solved on the mesh. The elements used to construct the computational grid are standard Crouzeix-Raviart bilinear triangular elements (Figure II.17). These elements contain nodes with a quadratic approximation for the two velocity components in

each node. The pressure is defined in the centroïd of each element. For post-processing purposes, it is always necessary to average the pressure to vertices.

The absence of the pressure in the continuity equation induces zeros at some of the diagonal elements of the matrix. In general, linear solvers may be influenced by such zeros; some iterative solvers do not even allow nonpositive diagonal elements. For that reason alternative solution methods have been developed which try to segregate the pressure and velocity computation, one of them being the penalty function formulation. In this approach, the continuity equation is perturbed with a small compressibility including the pressure, ε·p.

$$\varepsilon \cdot p + \overline{\nabla}\overline{\mathbf{u}} = 0 \qquad [101]$$

yielding

$$p = -\frac{\overline{\nabla}\overline{\mathbf{u}}}{\varepsilon} \qquad [102]$$

From this perturbed equation, the pressure is expressed in terms of velocity and this is substituted into the momentum equations. In this way, the velocity and the pressure are decoupled and the continuity equation is implicitly taken into account in the matrix equations. The velocity can then be computed first and the pressure afterwards.

II.4.7 The finite element method and the convection-diffusion equation

For a unique solution of partial differential equations, it is necessary to prescribe exactly one boundary condition at each part of the boundary. In many practical flow problems, however, the convection term strongly dominates the diffusive terms. Numerically this means that the character of the equations resembles that of the pure convection equation more than it does of the diffusion equation. For a pure convection equation, boundary conditions should only be given at inflow and not at outflow. Since for the convection-diffusion equation, boundary conditions must be given at outflow, it is advised to use those boundary conditions which influence the solution as little as possible. In general, this means that at outflow one usually applies natural boundary conditions.

At the outlet, the concentration profile is imposed to be remain invariable in the stream-wise direction [49]:

$$\overline{\mathbf{u}} \bullet \overline{\nabla} C_A = 0 \qquad [103]$$

The physical meaning of this outlet boundary condition is that the concentration field along the outlet contour is dominated by the stream-wise convection.

Whenever convection does not dominate diffusion, the standard Galerkin approach (SGA) can be used. However, if in equation Eq. [80] the convective part, $\bar{\mathbf{u}} \bullet \bar{\nabla} C_A$, dominates the diffusive part, $\bar{\nabla}\left(D_{AB} \cdot \bar{\nabla} C_A\right)$, the accuracy strongly decreases, especially in coarse grids. SGA is not an effective method for convection dominant flows. An improvement of the accuracy may be achieved by applying a so-called upwind scheme, in analogy with finite differences where upwind methods are applied for convection dominant flows. In finite element methods, the streamline upwind Petrov-Galerkin method (SUPG) <231> is comparable to classical finite difference upwind schemes. In a one-dimensional pure convection problem, upwinding involves that all information is transported in the direction of the velocity and therefore the discretization should be based upon information upwind. In the classical finite difference upwind scheme a backward difference scheme is applied (provided the velocity is positive). In fact, an artificial diffusion is introduced into the convection-diffusion equation.

Many of the upwind schemes in finite differences may be considered to be central difference schemes with artificial diffusion. If the SUPG method is applied in a two-dimensional problem in each of the directions, a typical cross-wind diffusion arises. This means that the solution perpendicular to the flow direction, is smoothed and becomes inaccurate. Consequently, the SUPG method must be extended in such a way that the upwinding is only applied in the direction of the flow. Brooks and Hughes have solved this problem by giving the artificial diffusion a tensor character.

Essential in the SUPG method for finite element methods, is an extra term next to the standard Galerkin equation:

$$\int_e \left(DC_A - f\right) \cdot p \cdot d\Omega \qquad [104]$$

where e denotes the element. DC_A represents the differential equation applied to C_A and f is the right-hand side. The upwind parameter, *p*, is defined by

$$p_i = \frac{h \cdot \varsigma}{2} \cdot \frac{\bar{\mathbf{u}} \bullet \bar{\nabla} \varphi_i}{\left\|\bar{\mathbf{u}}\right\|} \qquad [105]$$

with h denoting the width of the element in the direction of the flow, φ_i the i^{th} basis function, $\bar{\mathbf{u}}$ the velocity and ζ a choice parameter defining the type of upwinding. Many different schemes can be used:

- Classical upwind scheme: $\varsigma = 1$
- Il'in scheme: $\varsigma = \coth(\beta) - \frac{1}{\beta}$

- Doubly asymptotic approximation: $\varsigma = \begin{cases} \frac{\beta}{3} & -3 \le \beta \le 3 \\ \text{sign}(\beta) & |\beta| > 3 \end{cases}$
- Critical approximation: $\varsigma = \begin{cases} -1 - \frac{1}{\beta} & \beta < 1 \\ 0 & -1 \le \beta \le 1 \\ 1 - \frac{1}{\beta} & 1 \le \beta \end{cases}$

In which β is:

$$\beta = \frac{h}{2 \cdot D_{AB} \cdot \|\mathbf{u}\|} \qquad [106]$$

Mizukami has extended the upwinding scheme for triangles <232>. Many extensions of the SUPG method have been proposed, all based on different choices of the upwind parameter, *p*. These improvements have special functions, for example creating monotonous solutions <233> or discontinuity capturing <234>. Another method is the linear triangular method of Mizukami and Hughes <232> satisfying the maximum principle. This method is only applicable to linear triangles. In this method, the upwind basis functions, p_i, depends upon the flow direction as well as the solution. Hence, it is a nonlinear method. The upwind basis functions are chosen in such a way that the maximum principle is satisfied. This means that in the absence of sources or sinks, the solution can never be lower than the lowest value on the boundary and never higher than the highest value on the boundary. Since the method is nonlinear, it requires iteration. At the beginning of the iteration one might for example start with the doubly asymptotic approximation. Experiments show that sometimes the iteration displays a so-called flip-flop character. It switches between two different stages without ever converging. To suppress such behavior, a flip-flop mechanism may be triggered. In this mechanism an integer flip-flop array is used to keep track of the various stages of the upwind basis functions. If the direction of the upwind basis function is clear, it is kept.

However, it must be remarked that upwinding not always improves the accuracy and the building of the matrices in case of upwinding is more expensive than in the standard case. However, the use of upwinding makes the matrices to be solved more diagonally dominate. Consequently iterative matrix solvers will converge much faster than for SGA.

For a stable solution, the problem must be formulated with physically realistic conditions and a non-uniform grid with a sufficiently small spacing in the region close to the boundary must be used.

Linear triangular elements with three nodal points are used with one unknown in each node (Figure II.18).

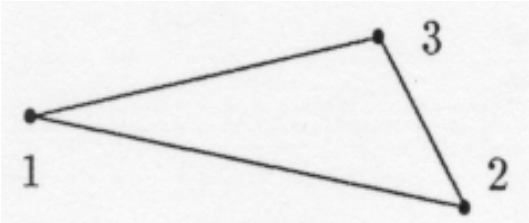

Figure II.18: Linear triangle with three points and one unknown per node.

II.5 Geometric characteristics of cross-flow hollow fiber membrane artificial lungs

Most artificial lungs consist of microporous hollow fibers (§I.5.3 & §I.5.4), the fundamental gas exchange elements, with blood flowing external to, and perpendicular to closely-spaced fibers, i.e. cross-flow. The gas flows inside the fibers. This configuration is particularly efficient in

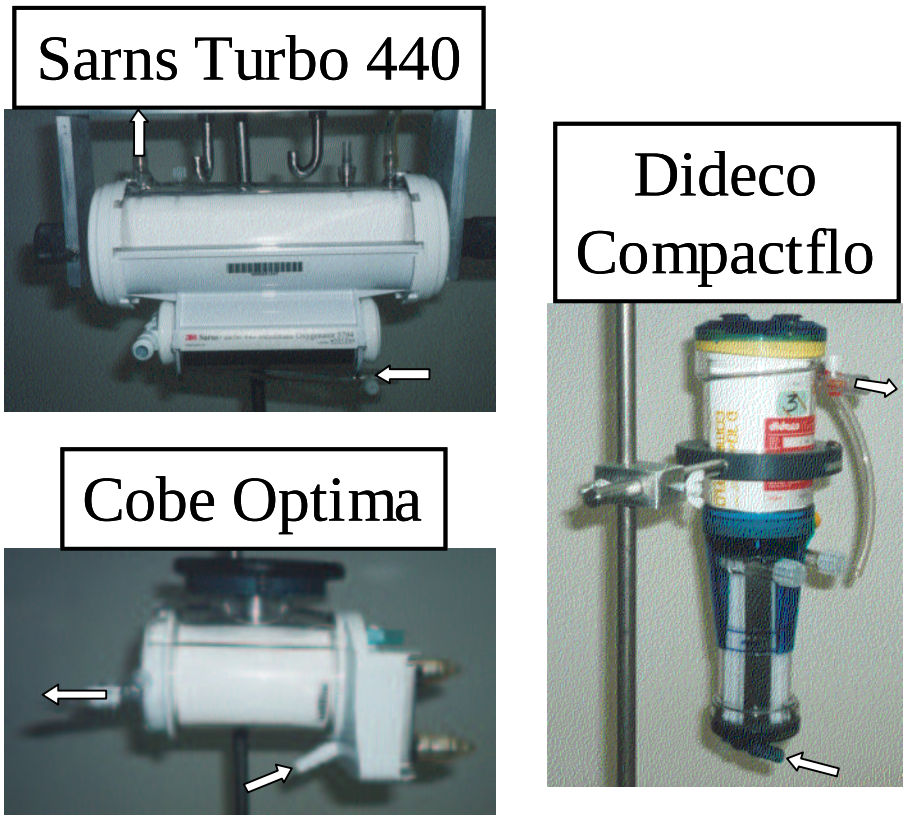

Figure II.19: In this figure, the commercially manufactured cross-flow hollow fiber membrane artificial lungs which are studied in this work, are shown. **Top left panel:** Sarns Turbo 440; **bottom left panel:** Cobe Optima; ù**right panel:** Dideco Compactflo; arrows denote the inlet and outlet blood flow.

transfer processes because of the transverse mixing on the blood side (§I.5.4). Since the fibers are densely packed, the blood flow in the void spaces is essentially that of a flow through a porous medium (macroscopic). A flow through an array of randomly oriented fibers is commonly approximated by a flow through a regular array of parallel-oriented fibers. Periodicity and symmetry are used to reduce the domain to the smallest element, i.e. a single fiber (microscopic).

Figure II.19 shows the commercially manufactured cross-flow hollow fiber membrane artificial lungs, which are studied in this work:

- Sarns Turbo 440 (Terumo)
- Cobe Optima, Cobe (Sorin Biomedica)
- Dideco Compactflo (Sorin Biomedica)

II.5.1 Macroscopic geometric characteristics

The flow in a cross-flow hollow fiber membrane artificial lung cannot be accurately characterized by tube flow, but rather by flow in a "packed column", which is approximated by flow in a tube of very complicated cross-section <35>. "Packed columns" are widely used for mass transfer operations in chemical engineering.

An artificial lung is characterized by different geometric parameters: membrane surface area, A; diameter of the fiber, d; length of the fiber compartment, L; inside housing outer diameter, D_i; outside housing inner diameter, D_o; and gross frontal area of the blood path, A_f (Figure II.20). The "void fraction" or device porosity, ε, is defined as the ratio of the volume of voids (volume in the membrane compartment occupied by blood) to the volume of the bed (total volume of the membrane compartment). A characteristic length for flow through porous beds or packed fiber bundles, is hydraulic radius, R_h, expressed in terms of ε and wetted surface area per unit of volume of bed, a <3,34,35>:

$$R_h = \frac{\left(\frac{\text{volume of voids}}{\text{volume of bed}}\right)}{\left(\frac{\text{wetted surface}}{\text{volume of bed}}\right)} = \frac{\varepsilon}{a} = \frac{\varepsilon \cdot d}{4 \cdot (1-\varepsilon)} \qquad [107]$$

Manifold length, L_m, is defined as the length by which the total artificial lung flow is divided per unit of width of fiber stack <34>. It is assumed that the length of the tortuous or microscopic path through the membrane compartment is equal to the overall bulk or macroscopic length of the packed section. Therefore, mean blood path length, L_b, is the average distance which blood has to travel through the fiber stack. Both lengths can be measured from dissected units or calculated

from technical data. A dimensionless characteristic device length, ξ, can be defined as the ratio of L_b and L_m <34>:

$$\xi = \frac{L_b}{L_m} \qquad [108]$$

It is assumed that blood is uniformly distributed over the fiber stack. In the Sarns Turbo 440 and Cobe Optima membrane artificial lungs, L_m and L_b are determined as shown in Figure II.20 (left panel). Blood enters the membrane evenly distributed over the length of the manifold, L, and the blood flow is split into two, for left and right sides. Blood flow rate per unit of width of membrane, Q´, is:

$$Q' = \frac{Q}{L_m} = \frac{Q}{2 \cdot L} \qquad [109]$$

Mean blood path length is:

$$L_b = \frac{\pi}{2} \cdot \left(\frac{D_i + D_o}{2} \right) \qquad [110]$$

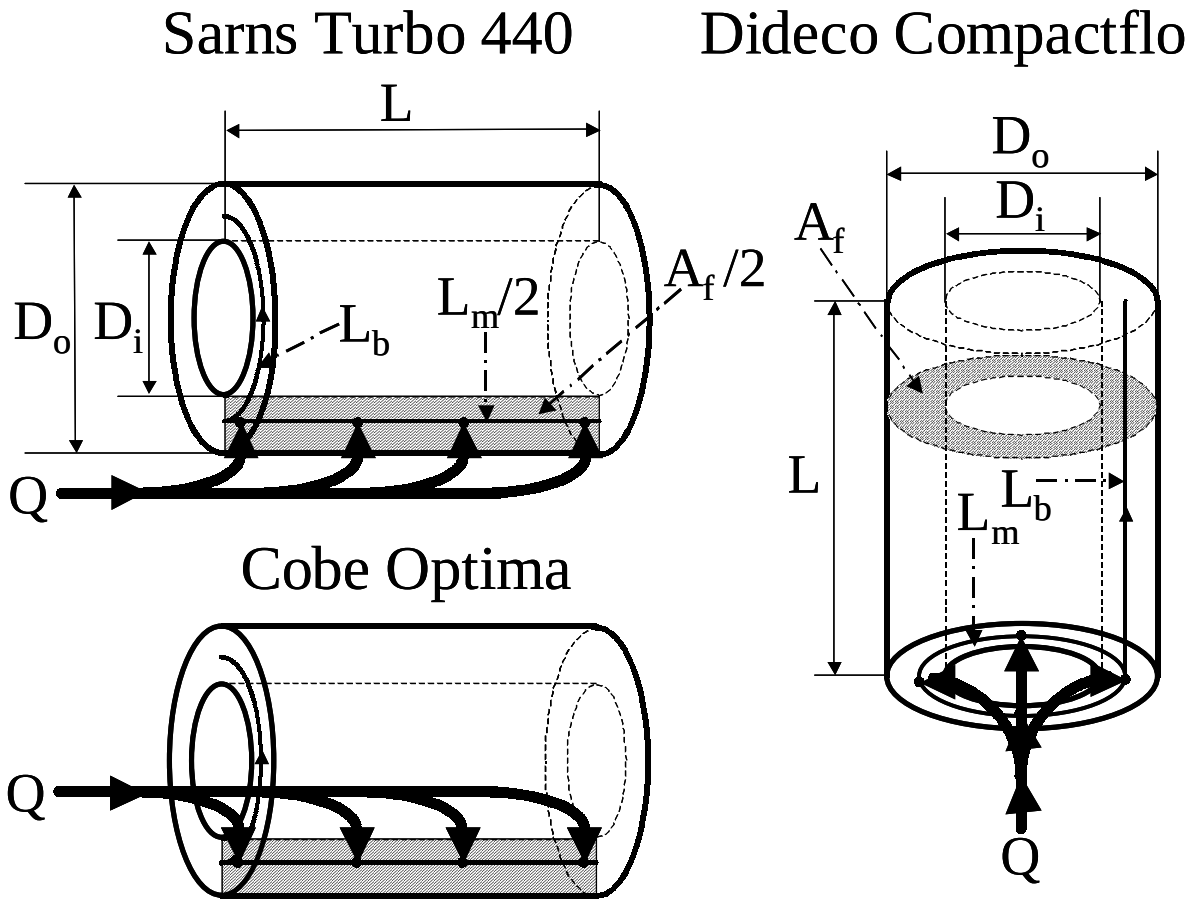

Figure II.20: Geometric characteristics of the commercially manufactured cross-flow hollow fiber membrane artificial lungs. **Top left panel:** Sarns Turbo 440; **bottom left panel:** Cobe Optima; **right panel:** Dideco Compactflo.

Table II.3: Geometric characteristics of the commercially manufactured cross-flow hollow fiber artificial lungs: Sarns Turbo 440, Cobe Optima, and Dideco Compactflo.

	Sarns Turbo 440	***Cobe Optima***	***Dideco Compactflo***
membrane surface area, A [m²]	1.6	1.7	2
fiber diameter, d [µm]	380	380	380
inside core outer diameter, D_i [cm]	5.0	4.4	5.0
outside core inner diameter, D_o [cm]	7.0	7.3	7.8
length fiber compartment, L [cm]	20.5	12.4	12
device porosity, ε	0.61	0.51	0.44
characteristic device length, ξ	0.23	0.37	0.60

In the Dideco Compactflo artificial lung, blood flow enters the fiber stack circumferentially (Figure II.20, right panel). Manifold length is:

$$L_m = \pi \cdot \left(\frac{D_i + D_o}{2} \right) \qquad [111]$$

whereas mean blood path length is determined as:

$$L_b = L \qquad [112]$$

Table II.3 lists the geometric characteristics of the three artificial lungs, which are studied in this work.

The velocity in a porous medium can be characterized by the superficial velocity, U_s, on the one hand and by the mean velocity, U_m, on the other hand. The superficial velocity or Darcy fluid velocity is defined as the average velocity in a reference direction of flow that would occur if the fibers were absent:

$$U_s = \frac{Q}{A_f} \qquad [113]$$

The mean velocity is defined as the average velocity through the pores of the porous medium:

$$U_m = \frac{Q}{\varepsilon \cdot A_f} \qquad [114]$$

so that

$$\varepsilon = \frac{U_s}{U_m} \qquad [115]$$

II.5.2 Microscopic geometric characteristics

In an artificial lung, blood can be considered to flow in a fiber bank. The fiber bank in a cross-flow hollow fiber membrane artificial lung can be considered as an assemblage of uniform, parallel, fixed circular fibers equally spaced in a plane perpendicular to the long axes of the fibers. Assuming negligible entrance, end and wall effects (which is a reasonable assumption for a fiber bank with a large number of rows) and fully developed, two-dimensional laminar steady flow through the fiber bank, periodically fully developed flow can be considered. A fiber bank can then be divided into a number of identical unit fiber cells, one fiber occupying each unit fiber cell. Fiber banks are characterized by cross-wise, S_T/d, and stream-wise, S_L/d, pitch(S)-to-diameter(d) ratios (Figure II.21). Symmetry boundary conditions ,Γ_{sym}, are imposed upon the symmetry lines (Figure II.22), no-slip wall boundary conditions upon the fiber surface. The distribution of the flow velocities (but not the local pressure, nor the concentration) is identical in all unit fiber cells, hence periodical boundary conditions, Γ_{per}, to inlet and exit planes can be

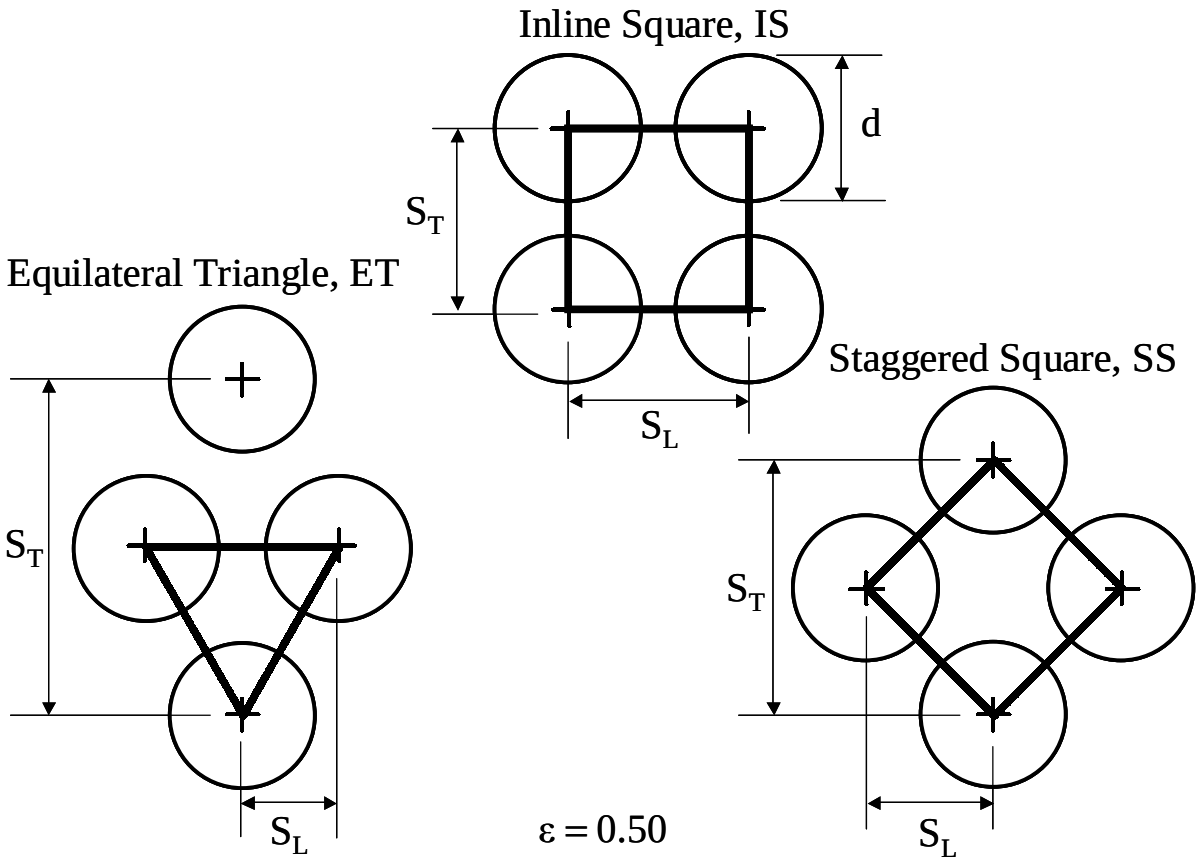

Figure II.21: Three fiber geometries with a porosity of 0.50 (horizontal flow): inline square, IS, equilateral triangle, ET, and staggered square, SS (fiber diameter, d, cross-wise pitch, S_T, and stream-wise pitch, S_L).

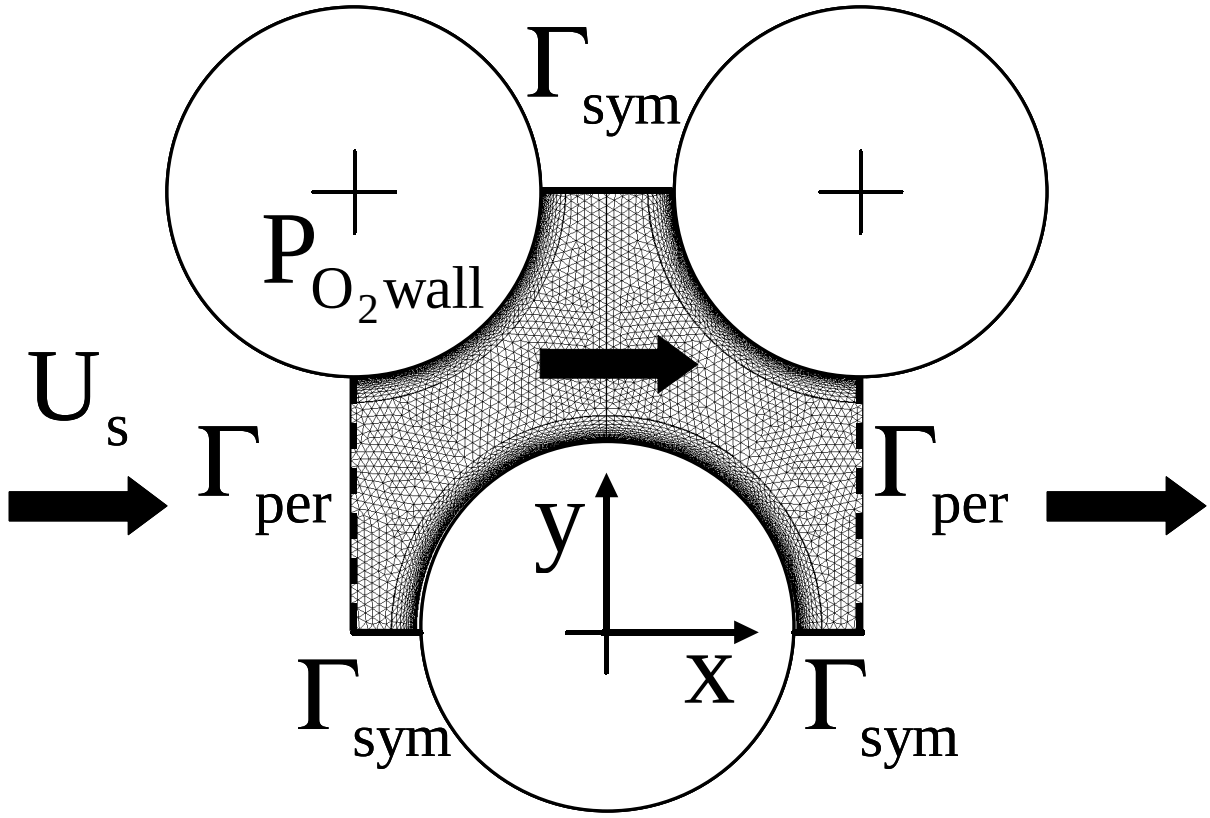

Figure II.22: Schematic representation of the unit fiber cell model. Γ_{sym} represents symmetrical boundaries and Γ_{per} periodical boundaries; x denotes the stream-wise direction and y is perpendicular to the flow direction.

applied (Figure II.22). Periodical boundary conditions (§II.4.6) are implemented with a given volume flux, q:

$$q = \int_{\Gamma_{per}} \bar{\mathbf{u}} \bullet \bar{\mathbf{n}} \cdot d\Gamma = U_s \cdot \frac{S_T}{2} \qquad [116]$$

where U_s is the superficial velocity of the porous medium (§II.5). The flow field is oriented in the x-coordinate direction (Figure II.22), i.e. the stream-wise direction. For symmetry reasons, only the meshed part of the geometry needs to be considered.

The overall dimensions of the unit fiber cell are fixed by specifying the configuration, the porosity, ε, and the fiber diameter, d. In the present study, porosity ranges from 0.4 to 0.6 for each fiber bank.

Three different fiber bank configurations are studied:

- inline square, IS: $S_T = S_L$
- equilateral triangle, ET: $S_T = 2 \cdot \sqrt{3} \cdot S_L$
- staggered square, SS: $S_T = 2 \cdot S_L$

Figure II.21 illustrates the three fiber bank unit fiber cells with a porosity, ε, of 0.50 and diameter, d, of 0.380 mm, a representative size for a polypropylene fiber used in an artificial lung.

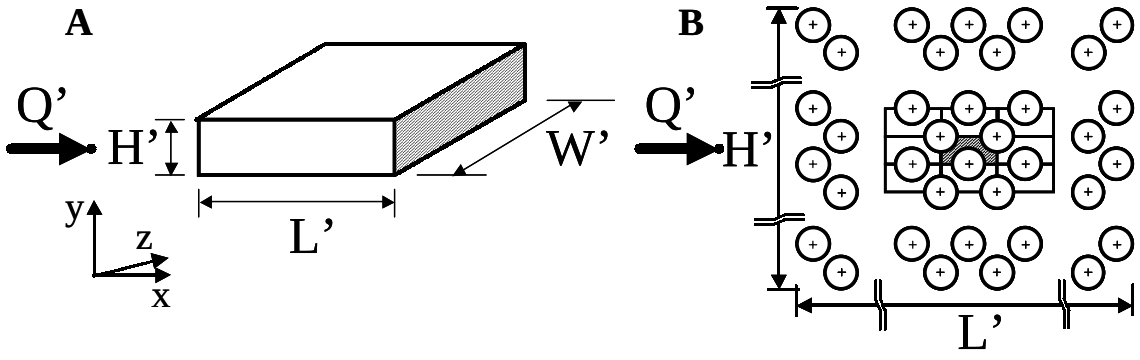

Figure II.23: **A.** Schematic presentation of a fiber bank of height, H', length, L', and width, W'. x denotes the stream-wise direction, y denotes the cross-wise direction and z the direction along the fiber axis. Q' represents the flow rate through the fiber bank. **B.** The fiber bank is presented as an idealized periodical array of cylindrical fibers perpendicular to the flow.

Figure II.23 represents a fiber bank of height, H', length, L', and width, W' (left panel) as a periodical array of cylindrical fibers perpendicular to the flow (right panel). This fiber bank is an idealized representation of the membrane compartment of the commercially manufactured cross-flow hollow fiber membrane artificial lungs in Figure II.20:

$$H' = \frac{D_o - D_i}{2}$$
$$L' = L_b \qquad [117]$$
$$W' = L_m$$

Using the geometrical data of the membrane compartment of the commercially manufactured cross-flow hollow fiber membrane artificial lungs, the two-dimensional unit fiber cell is integrated in every direction to simulate the complete membrane. The pressure drop and the oxygen transfer in a fiber bank can therefore be calculated from the results obtained in a unit fiber cell by integration into the stream-wise (x-) and cross-wise (y-) direction and by multiplication with the fiber length (z-direction).

II.6 Dimensional analysis

Because of the complex flow field in cross-flow hollow fiber artificial lungs, it is not possible to obtain a theoretical analysis of the hydrodynamic resistance or of the gas transfer efficiency beforehand. For the oxygen transfer analysis in an artificial lung, a semi-empirical approach is adopted, based on an analogy between heat and mass transfer utilizing dimensionless groups.

Dimensionless groups renders the solution to a problem more compact and the correlation of experimental data more manageable. The use of dimensionless groups allows one to use model theories to predict the behavior of a full-scale device based on the data for geometrically and dynamically similar, but scaled models.

Table II.4 lists the pertinent variables encountered in hydrodynamics and in mass transfer. From these variables, various dimensionless groups can be derived. The mass transfer coefficient, K, is defined as the mass transfer rate, per unit surface area and per unit driving force.

Table II.4: Pertinent variables encountered in hydrodynamics and in mass transfer. From these variables, various dimensionless groups can be derived. (*L* unit of length; *T* unit of time; *M* unit of mass).

variable	***symbol***	***dimension***
characteristic length: hydraulic diameter	$4 \cdot R_h$	*L*
characteristic velocity *in numero* analysis: *superficial velocity, U_s*	$U_s = \frac{Q}{A_f}$	*L/T*
characteristic velocity *in vitro* nalaysis: *mean velocity, U_m*	$U_m = \frac{Q}{\varepsilon \cdot A_f}$	*L/T*
density	ρ	M/L^3
dynamic viscosity	μ	*M/L/T*
kinematic viscosity	υ	L^2/T
pressure drop	Δp	$M/L/T^2$
diffusion coefficient	D_{O_2}	L^2/T
mass transfer coefficient	K	*L/T*

Reynolds number, N_{Re}, is defined as the ratio of inertial to viscous forces. Characteristic length in the Reynolds number for flow through a fiber stack is the hydraulic diameter, $4 \cdot R_h$. Consequently, the Reynolds number, N_{Re}, for an artificial lung is defined as:

$$N_{Re} = U \cdot \frac{4 \cdot R_h \cdot \rho}{\mu} \qquad [118]$$

with U the characteristic velocity. The superficial velocity, U_s, is used as the characteristic velocity in the *in numero* analysis:

$$N_{Re} = U_s \cdot \frac{4 \cdot R_h \cdot \rho}{\mu} \qquad [119]$$

In the *in vitro* analysis, the mean velocity, U_m, is used as the characteristic velocity:

$$N_{Re} = \frac{Q}{A_f \cdot \varepsilon} \cdot \frac{4 \cdot R_h \cdot \rho}{\mu} \qquad [120]$$

When using whole blood (Hct = 45 % and T = 37 °C yielding ρ = 1060 kg/m³ and μ_∞ = 3.76 mPa· s) with a flow rate of 5 l/min, N_{Re} with U_s as a characteristic velocity (*in numero* analysis), varies between 2.1 and 3.3 for membrane artificial lungs with a porosity between 0.4 and 0.6. When the mean velocity, U_m, is used as characteristic velocity (*in vitro* analysis), N_{Re} varies between 4.7 and 5.5. Blood with a hematocrit of 30 % and a temperature of 30 °C flowing at 5 l/min corresponds with N_{Re} of 2.6 – 4.2 (*in numero* analysis) and 5.8 – 6.8 (*in vitro* analysis). For water (T = 20 °C yielding ρ = 998 kg/m³ and μ_∞ = 1.00 mPa· s) flowing at 5 l/min corresponds with N_{Re} of 7.4 – 12.2 (*in numero* analysis) and 17.0 – 20.2 (*in vitro* analysis).

The Euler number, N_{Eu}, is defined as the ratio of pressure drop to kinetic energy:

$$N_{Eu} = \frac{\Delta p}{\rho \cdot \left(\frac{Q}{A_f \cdot \varepsilon} \right)^2} \qquad [121]$$

The Schmidt number, N_{Sc}, analogous to the Prandtl number in heat transfer, is defined as the ratio of momentum to diffusive transport and characterizes the fluid:

$$N_{Sc} = \frac{\mu}{\rho \cdot D_{O_2}} = \frac{\upsilon}{D_{O_2}} \qquad [122]$$

The Péclet number, N_{Pe}, is the product of N_{Re} and N_{Sc} and characterizes the relative importance of convective and diffusive processes with respect to the fluid flow:

$$N_{Pe} = \frac{4 \cdot R_h \cdot Q}{A_f \cdot \varepsilon \cdot D_{O_2}} \qquad [123]$$

It is the ratio of bulk mass transport by convective fluid flow to diffusive mass transport.

The Sherwood number, N_{Sh}, also known as the mass transfer Nusselt number, characterizes the relative importance of convective and diffusive transport with respect to the membrane. N_{Sh} is defined as the ratio of total mass transfer, including mixing effects by e.g. secondary flows, to diffusive mass transfer:

$$N_{Sh} = \frac{K \cdot 4 \cdot R_h}{D_{O_2}} \qquad [124]$$

The mass transfer Stanton number, N_{St}, is proportional to the ratio of actual mass flux to the mass flux capacity of the fluid flow, i.e. the amount of mass potentially transferable per unit of time and per unit of cross-sectional area. N_{St} can be written as follows:

$$N_{St} = \frac{N_{Sh}}{N_{Re} \cdot N_{Sc}} = \frac{\varepsilon \cdot A_f \cdot K}{Q} \qquad [125]$$

II.7 Modeling oxygen transfer

II.7.1 Introduction

Many of the early oxygenation systems (capillary membrane, coiled tube, membrane-lined capillary channels, spiral, cross-flow hollow fiber, etc.) have been developed (1960s – 1970s – 1980s – 1990s) on empirical grounds <44> (§I.5). Applicable theories would greatly enhance clinical progress by insuring maximum transfer efficiency and safety. Increased efficiency is very important for long-term perfusion.

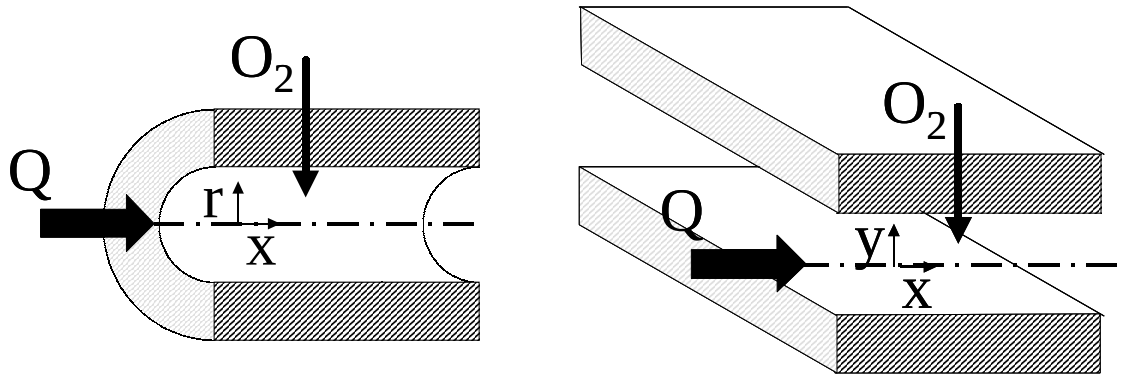

Figure II.24: Schematic detailed representation of an artificial lung: parallel tube representing the shell and tube membrane artificial lung (left panel) and parallel plate representing the flat sheet membrane artificial lung (right panel). Q denotes the blood flow and O_2 denotes the oxygen transfer through the membrane.

The design of an optimal system demands an experimental and a mathematical (analytical or numerical) approach. The experimental approach is characterized by both minimal analysis and the 'trial and error' method of making appropriate modifications for the optimal design. The cost for development and the time consumption are thus much greater than those incurred using a mathematical approach.

The analytical and the numerical approach aim to derive a model of the system using basic mathematical equations to describe the physical laws such as the conservation of mass and momentum, and to describe the causal relationships between its component parts. Prototypes designed, based on extensive analytical investigation, are frequently optimally designed and the only experimental results needed are those required to validate the model.

Once the model has been validated, additional variables can be studied analytically and / or numerically which often results in a considerable cost reduction. In general, a steady state is assumed.

II.7.2 History of the modeling of oxygen transfer <44>

Mathematical analysis of the membrane artificial lung has been attempted in the late 1960s and early 1970s on two geometries: multiple parallel permeable tubes for shell and tube membrane artificial lungs (left panel Figure II.24) and multiple parallel permeable plates with a large channel width to height ratio for flat sheet membrane artificial lungs (right panel Figure II.24).

Some theoretical developments pertinent to design-oriented analytical methods are described by Spaeth et al. <235,236> and Dorson <237>. Several reports of approximate solutions to the general convection-diffusion equation, describing the transfer of oxygen to blood, appear in the literature <222,228,237,238>. In all these attempts, the flow is considered fully developed and blood is considered to be a homogeneous fluid either with uniformly distributed chemical reactions or with uniformly distributed red blood cells as sources or as sinks. Merril et al. <239>, Jones <240>, and Dorson and Hershey <241> have only studied the pure hydrodynamic behavior of blood flow through capillary tubes. Marx et al. <242,243> investigated the oxygen transfer rate through a horizontal stagnant film of blood separated from a flowing oxygen gas stream by a silicon rubber membrane. Keller and Friedlander <244,245> studied the rate of oxygen transfer through hemoglobin solutions. Weissman and Mockros <230,246,247> solved the mass conservation equation for straight and coiled gas permeable tube flows using an empirical relation for the oxygen-hemoglobin dissociation curve, a constant effective diffusion coefficient (§II.4.5), and a Newtonian parabolic velocity profile. Buckles et al. <248> used an approach similar to that of Weissman and Mockros, but used Casson's equation describing the non-Newtonian viscosity of blood and a more general wall flux matching condition.

Spaeth and Friedlander <249> used a rotating disc membrane device to test the macroscopic model for convective diffusion of gases in blood experimentally. Martisovits and Veis <250> analyzed the statistical model of oxygen transfer in blood. Lightfoot <222> developed a low order approximation for a membrane artificial lung. Thews <251> investigated the nature of diffusion in blood. He considered blood in two concentric regions with a central saturated region separated by a moving interface through which diffusion takes place. Villaroell et al. <252,253> followed a procedure similar to that of Keller and Friedlander but solved the conservation equations for oxygen and carbon dioxide diffusion of steady and pulsatile blood flow with the help of a shell

and tube membrane artificial lung. Harris et al. <226> also solved the conservation equations for oxygen and carbon dioxide diffusion through the blood flowing in a capillary membrane using the Casson's equation and assuming a fully developed velocity profile.

The agreement between theoretical approaches and experimental data for blood oxygenation in membrane channels has resulted in a series of design-oriented articles <238,242,247,254-258>.

Some of these techniques are based on integral methods and are called advancing front models (§II.3.3). They have been proven to be useful in the design and understanding of membrane artificial lungs (multiple parallel permeable tubes and multiple parallel straight channels) <228,238>.

Other methods are currently available to predict the blood-gas transfer capabilities of membrane artificial lungs without prototype testing using blood. Shah and Leonard <259> suggest perfusing devices with a sodium sulfite solution that reacts with oxygen at a rate comparable to the reaction of hemoglobin and oxygen but is less expensive and easier to control than blood. Vaslef et al. <4> use a normalized mass transfer coefficient for cross-flow devices derived from experiments using water to characterize the gas transfer performance for a membrane oxygenator for any inlet blood conditions (§II.8). These methods approach the device as a porous medium.

II.7.3 Analytical and numerical models

Transport of oxygen through blood films has been studied extensively, and the large hemoglobin binding capacity for oxygen, coupled with the rapid hemoglobin-oxygen kinetics, led many investigators to approximate the experimental situation by using two distinct zones. These involve the transfer of oxygen through a fully saturated region leading to a front where the hemoglobin reacts with the dissolved oxygen <242,260-262>. The concept is referred to as "advancing front theory" <222> (§II.3.3). The advancing front theory idealizes the flow of blood in a tube or between plane parallel surfaces to a fully developed, laminar flow of a homogeneous Newtonian fluid. Axial diffusion is neglected with respect to radial diffusion and a steady state is assumed. The advancing front is applied in these studies assuming a large reaction rate of hemoglobin and oxygen, a high ratio of unbound to undissolved oxygen at the inlet and a large, nearly constant difference between gas and inlet oxygen partial pressure. The blood is considered a fully saturated zone adjacent to a wall kept at a constant oxygen partial pressure, which advances into a central zone of unsaturated blood. Transport in this outer saturated level is primarily by diffusion along the gradient between the oxygen partial pressure in the gas phase and the central zone, which remains at the inlet value (Figure II.9).

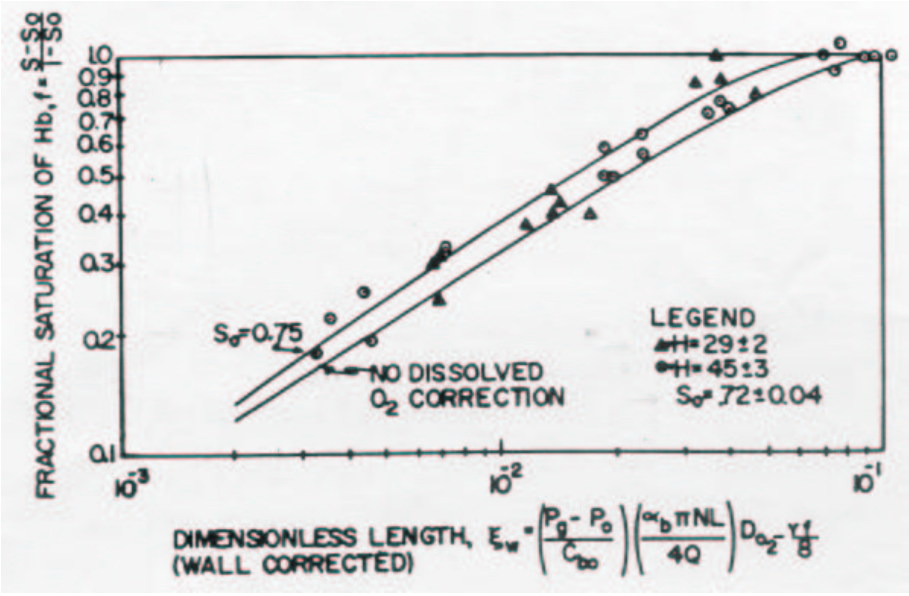

Figure II.25: Oxygen transfer to blood flowing in multiple parallel permeable tubes with generalized advancing front coordinates <263>. Comparison of theoretical predictions with experimental data. The high f-data were obtained from single tube experiments. The upper line denotes a correction for neglecting the convection of dissolved oxygen in the advancing front theory. The correction is applied at the channel inlet to mix its blood to its final saturation.

The model of Dorson <263> is a typical analysis of oxygen transfer to blood, flowing in permeable tubes. A parabolic velocity profile, an empirical oxygen dissociation curve, and a constant effective oxygen diffusion coefficient determined by comparison with experimental data, were employed. The solutions of the mass balances in Dorson's model result in the expression of the overall oxygen exchange in terms of two dimensionless numbers <222,228,237,238,264>: the fractional saturation change, f, and the dimensionless channel length for oxygen transfer, L^* (Figure II.25). The fractional saturation change or efficiency of the device expresses the ratio of the actual saturation change across the device to the total saturation change possible. the dimensionless channel length for oxygen transfer is a modified Graetz number that consists of groupings of terms relating gas and blood inlet conditions, blood physical properties and the flow and geometric properties of the ducts or tubes of any particular device. Based on these two dimensionless numbers, Curtis and Eberhart <264> present the performance of oxygen transfer by introducing the concept of a resistance of the inlet blood to complete oxygen saturation versus the fractional saturation change and the flow rate of a device. An artificial lung may be treated as a "black box" into which inlet conditions are varied and corresponding variations in outlet saturation are measured. Knowledge of the geometry, the detailed construction, or the blood oxygen solubility and diffusion should not be required for the characterization of the performance of a device as long as one assumes a constant priming

volume and blood physical properties <264>. The performance of a device could be extrapolated to any desired blood flow rate, blood inlet conditions, or barometric pressure. The model, however, is limited to fractional saturations ranging from 0.30 to 0.95 yielding it unusable for a thorough examination of the performance of artificial lungs. Overcash and Keller have shown that the advancing front model approximations break down when the ratio of dissolved to bound oxygen at the inlet is less than three. Such conditions exist at a hematocrit of 25 % and for inlet saturations higher than 65 %. Moreover, the theory can only be applied to flat sheet technologies and intraluminal blood flows.

Buckles <248> and Villaroel <252> solved Dorson's model with the Crank-Nicholson method using matching flux boundary conditions and Casson's non-Newtionian blood viscosity model. In this finite difference approach the partial differential equation is replaced by an approximating system of nonlinear difference equations whose solution is close to that of the original equation. The disadvantage of the finite difference method is that it is normally restricted to fixed order accuracy and fixed grid spacing. Clustering of grid points in the regions where the solution is known to change rapidly, i.e. at the membrane wall and at inlet, is generally very awkward to implement. These nonlinearities require iterative methods to determine the solution of each iteration step, with consequences for the stability and accuracy of the computation.

In 1985, Mayes <265> used the method of lines to solve Dorson's model. The method of lines prediction agrees closely with the prediction obtained by Colton and Drake <266> for tubular flow. Many of the disadvantages of the finite difference method, e.g. the instability of the calculation under some conditions, are avoided when using the method of lines.

Baker et al. <267> developed a two-dimensional finite-difference predictive model for gas transfer in hollow fiber membrane artificial lungs. The model is able to predict gas transfer to blood flowing outside and parallel to oxygenating fibers without experimental data. The cross-sectional fiber distribution is assumed a uniform triangular array, while the rest of the device is extrapolated by symmetry. Blood and gas flow rate are assumed to be fully developed, laminar and in steady state. Casson's blood viscosity model is used, although shear dependent viscosity did not significantly improve modeling accuracy in the range of interest. Blood is considered statistically homogeneous over a sample volume and the reaction between oxygen and hemoglobin is considered to be fast enough to use an equilibrium dissociation curve.

The model is compared to bovine and human experimental data from small test cells with microporous polypropylene fibers. They have implemented a shear-augmented oxygen diffusion bovine blood model <268>, although good accuracy is obtained with a nonaugmented diffusion

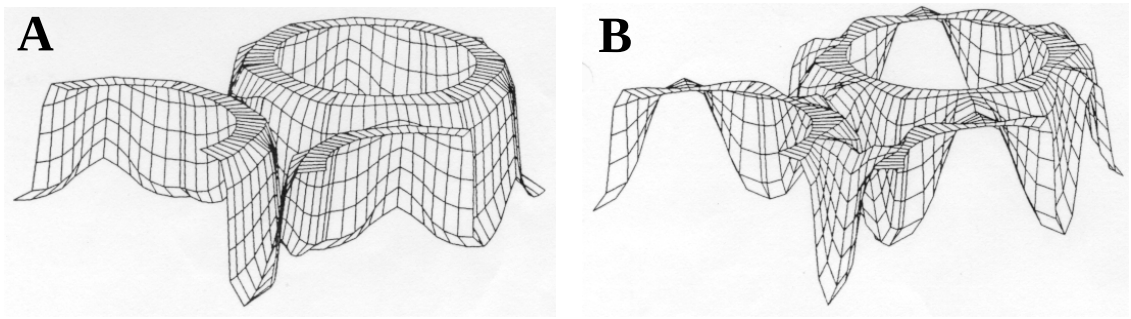

Figure II.26: Oxygen saturation profile for bovine blood. **A:** 5.8 cm from the inlet. Note the formation of appendages along the plane joining the fiber centers; **B:** 8.3 cm from the inlet. Note the formation of "bridges" of saturated blood and "pits" of unsaturated blood. <267>

model, particularly at lower flows. Comparison of the predictions with experimental results suggests that shear augmented diffusion is indeed taking place in the test cell.

Oxygen saturation profiles for bovine blood at two cross-sectional locations are shown in Figure II.26. A sharp 'front' dividing oxygenated from unoxygenated blood has been demonstrated in an axisymmetric blood path inside hollow fibers <222>. Baker's model results illustrate an "advancing cliff", the three-dimensional analogue of the advancing front with blood outside the fibers. Near the beginning of the fiber, the oxygenated blood forms a steep front along the fiber wall, and an appendage begins to form in the front along the plane connecting the fiber centers (left panel Figure II.26). This appendage eventually forms a bridge of saturated blood (right panel Figure II.26), increasing the bulk saturation. A pocket of unsaturated blood is bounded by the 'bridges'. This pocket shrinks and becomes shallower as blood advances along the fibers. Thus the dynamics of gas transfer of blood outside the fibers are richer and more complex than those of blood inside the fiber.

Niranjan et al. <269> developed a finite-difference model of the gas transfer within the IVOX intra-vascular hollow-fiber blood gas exchanger by considering fluid flow both within and outside hollow capillary fibers using the Krogh cylinder approach, previously used to model gas transport in vascular capillaries surrounded by tissue <270>. The goal of their analysis was to investigate the effects of various operating conditions on oxygen transfer rate. They validated the model using independently obtained experimental data and investigated the effects of various operating conditions on the mass transfer rates of carbon dioxide and oxygen. Blood was considered statistically homogeneous over a sample volume with a constant hematocrit, which is a common and reasonable assumption for membrane oxygenators <229>. Computed results indicated the presence of a large resistance to gas transport on the blood side of the hollow-fiber exchanger. Increasing gas flow through the device favored carbon dioxide removal from but not

oxygen addition to blood. Increasing blood flow over the device favored both carbon dioxide removal and oxygen addition.

II.8 Semi-empirical model of oxygen transfer in cross-flow artificial lungs - Mockros and Leonard theory <3>

The theory of Mockros and Leonard <3> for oxygen transfer in cross-flow hollow fiber membrane artificial lungs is examined in detail. To minimize mass transfer resistance, an effective but gentle transverse mixing of the blood flowing in the membrane artificial lungs is required. This is obtained in cross-flow hollow fiber membrane artificial lungs by letting the blood flow over a matrix of hollow fibers with the gas flowing inside the fibers. Secondary flows in the blood flow reduce the thickness of the boundary layer at the external surface of the hollow fibers. Effective mixing is thus naturally induced and oxygen transfer is enhanced.

Mockros and Leonard <3> presented a model for oxygen transfer in a compact cross-flow hollow fiber membrane artificial lung. The model was based on an analogy with heat transfer in cross-flow heat exchangers. It was assumed that the blood flowed in a direction perpendicular to the axis of the tubes. Using the Chilton-Colburn analogy, the heat exchanger equations were used to describe the oxygen transfer process in blood. A non-reactive process of oxygen exchange was assumed, with the reaction effects being incorporated in an effective oxygen diffusion coefficient, $D_{O_2 eff}$ (§II.4.5). The Hill equation was used to describe the oxyhemoglobin dissociation curve, and the Fricke theory was used to calculate the diffusion of dissolved oxygen in blood. A correlation of Sherwood number, N_{Sh}, and Reynolds number, N_{Re}, can be obtained from the analogy:

$$N_{Sh} \cdot N_{Sc}^{-1/3} = \varphi' \cdot N_{Re}^{m'} \qquad [126]$$

where φ’ and m’ are constants determined experimentally. The constants φ’ and m’ depend upon the specific artificial lung design under investigation and are influenced by tube outside diameter, porosity, and flow pattern among others. Their values must therefore be obtained experimentally. Mockros and Leonard <3> and Vaslef et al. <4> determined φ’ and m’ for oxygen transfer in water at flow rates corresponding to Reynolds numbers to be typical for clinically employed blood flow rates in cross-flow membrane artificial lungs.

II.8.1 The mass transfer coefficient <33>

The mass transfer coefficient, K, is a measure of the efficiency of gas transfer (i.e. the amount of gas transferred per unit of time, per unit of surface area and per unit of concentration difference). In a small region of an artificial lung, one can look at mass transfer from one fluid stream across a portion of the membrane to the other fluid stream. When steady-state conditions prevail the mass flux density of the transferred substance is the same at the periphery of each of the two streams as it is through the membrane itself (flux is flow per unit of time, flux density is flow per unit of time per unit of normal area). Each portion of the path taken by the transferred substance has a resistance, R, associated with it; there are separate resistances in the two fluid streams and in the membrane:

$$K = \frac{1}{R} = \frac{1}{R_b + R_w + R_g} \qquad [127]$$

where R_b denotes the resistance in blood, R_w is the membrane resistance and R_g is the resistance in the gas phase. The reciprocal of any of these resistances is by definition a mass transfer coefficient: the resistance in the fluid streams vary locally throughout the artificial lung, in general, with the fluid flow rates. The reciprocals of these resistances are often called convective mass transfer coefficients because their values depend directly upon the fluid motion. Often, one of the three individual coefficients will be much smaller than the other two, and hence dominates the overall mass transfer coefficient. The units of the mass transfer coefficient are cm/s, or, in more physical terms, ml/s/cm². By definition <35>, however,

$$\text{flux} = K \cdot \left(C_{O_2 g} - C_{O_2}\right) \qquad [128]$$

K is a transfer rate per unit of surface area per unit of driving force. The term $\left(C_{O_2 g} - C_{O_2}\right)$ represents the driving force for mass transfer; $C_{O_2 g}$ is the oxygen concentration in the gas phase and C_{O_2} is the oxygen concentration in the bulk liquid flow. Since the driving force may be different at the gas inlet than at the outlet, K may vary along the gas path length. The flux may also vary along the blood path length, L_b. The average mass transfer coefficient, $\langle K \rangle$, represents the integrated effect of the variable local mass transfer coefficient. In principle, the average value should be the blood path length-averaged value of the local mass transfer coefficient:

$$\langle K \rangle = \frac{1}{L_b} \cdot \int_0^{L_b} K \cdot dx \qquad [129]$$

The spatially averaged value of the convective mass transfer coefficients for one fluid phase is commonly referred to the average mass transfer coefficient. The value of the local mass transfer

coefficient obtained by taking the reciprocal of the overall resistance (the three component resistances in series) is known as the (local) overall mass transfer coefficient.

II.8.2 Oxygen transfer in artificial lungs <33>

Oxygen transfer occurs at the fiber interface by diffusion and/or convection. From Eq. [128], the local oxygen transfer rate, $d\dot{V}_{O_2}$, over an incremental blood path length, dx, is (Figure II.27):

$$d\dot{V}_{O_2} = K \cdot dA \cdot \left(C_{O_{2g}} - C_{O_2}\right) \qquad [130]$$

in which dA is the membrane surface area of the fibers contained in the length dx. The total transfer area may be expressed in terms of the porosity, hydraulic radius, and dimensions of the fiber bank.

The total volume for an incremental blood path length, dx, is:

$$A_f \cdot dx \qquad [131]$$

and the void volume:

$$\varepsilon \cdot A_f \cdot dx \qquad [132]$$

so that, taking into account the definition of hydraulic radius, the total transfer area in dx is:

$$dA = \frac{4 \cdot (1-\varepsilon) \cdot A_f \cdot dx}{d} \qquad [133]$$

The driving force for oxygen transfer to blood, $\left(C_{O_{2g}} - C_{O_2}\right)$, does not include the oxygen bound to hemoglobin, since the oxyhemoglobin, located inside the red blood cells, does not diffuse.

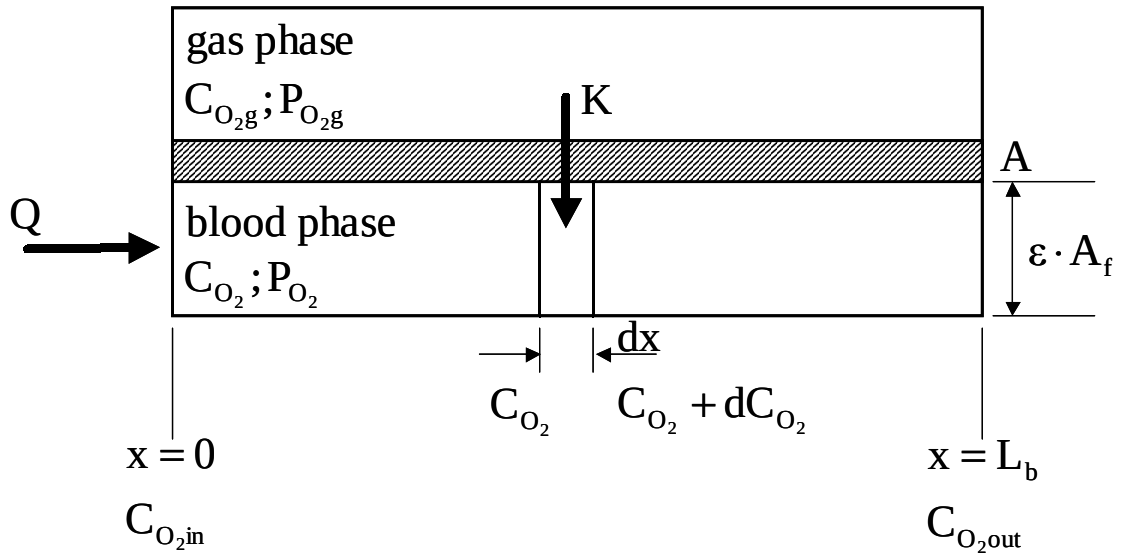

Figure II.27: Schematic representation of a simplified model for oxygen transfer in compact cross-flow hollow fiber oxygenators for the derivation of the mass balance over a differential blood path length dx.

Therefore, oxygen transfer is driven by the partial pressure difference of dissolved oxygen at the boundary and in the bulk flow. The driving force, then, becomes the difference of the partial pressure of oxygen in the gas phase, P_{O_2g}, and in the bulk flow, P_{O_2}:

$$C_{O_2g} - C_{O_2d} = \alpha_{O_2} \cdot \left(P_{O_2g} - P_{O_2}\right) \qquad [134]$$

in which α_{O_2} is the Bunsen solubility coefficient of oxygen in blood. The local oxygen transfer rate, therefore, is:

$$d\dot{V}_{O_2} = \frac{4 \cdot (1-\varepsilon) \cdot A_f}{d} \cdot K \cdot \alpha_{O_2} \cdot \left(P_{O_2g} - P_{O_2}\right) \cdot dx \qquad [135]$$

The local rate of oxygen uptake by blood must equal $d\dot{V}_{O_2}$ given in Eq. [135]. Oxygen is carried in blood as dissolved oxygen and is chemically bound with hemoglobin (§II.3.2). The rate of oxygen uptake over dx, therefore, is given by:

$$d\dot{V}_{O_2} = \alpha_{O_2} \cdot Q \cdot \frac{dP_{O_2}}{dx} \cdot dx + B_{O_2} \cdot C_{Hb} \cdot Q \cdot \frac{dS_{O_2}}{dx} \cdot dx \qquad [136]$$

$\frac{dP_{O_2}}{dx} \cdot dx$ is the incremental increase in the oxygen partial pressure over the incremental length dx and $\frac{dS_{O_2}}{dx} \cdot dx$ is the incremental increase in oxyhemoglobin saturation over incremental length dx. Eq. [136] may be rewritten as:

$$d\dot{V}_{O_2} = \left(1 + B_{O_2} \cdot \frac{C_{Hb}}{\alpha_{O_2}} \cdot \frac{dS_{O_2}}{dP_{O_2}}\right) \cdot \alpha_{O_2} \cdot Q \cdot \frac{dP_{O_2}}{dx} \cdot dx \qquad [137]$$

and equated to [135], this yields:

$$\left(1 + B_{O_2} \cdot \frac{C_{Hb}}{\alpha_{O_2}} \cdot \frac{dS_{O_2}}{dP_{O_2}}\right) \cdot \alpha_{O_2} \cdot Q \cdot \frac{dP_{O_2}}{dx} \cdot dx = \frac{4 \cdot (1-\varepsilon) \cdot A_f}{d} \cdot K \cdot \alpha_{O_2} \cdot \left(P_{O_2g} - P_{O_2}\right) \cdot dx \qquad [138]$$

which simplifies to:

$$\left(1 + B_{O_2} \cdot \frac{C_{Hb}}{\alpha_{O_2}} \cdot \frac{dS_{O_2}}{dP_{O_2}}\right) \cdot Q \cdot \frac{dP_{O_2}}{dx} = \frac{4 \cdot (1-\varepsilon) \cdot A_f}{d} \cdot K \cdot \left(P_{O_2g} - P_{O_2}\right) \qquad [139]$$

Rearranging Eq. [139] yields an expression for the local mass transfer coefficient:

$$K = \frac{Q \cdot d}{4 \cdot (1-\varepsilon) \cdot A_f} \cdot \frac{1 + \lambda\left(P_{O_2}\right)}{P_{O_2g} - P_{O_2}} \cdot \frac{dP_{O_2}}{dx} \qquad [140]$$

in which

$$\lambda\left(P_{O_2}\right) = B_{O_2} \cdot \frac{C_{Hb}}{\alpha_{O_2}} \cdot \frac{dS_{O_2}}{dP_{O_2}} \qquad [141]$$

The term $\left(1+\lambda\left(P_{O_2}\right)\right)$ in Eq. [140] represents the reciprocal of the fraction of the total oxygen uptake contributed by dissolved oxygen (§II.4.5). The mass transfer coefficient, K from Eq. [140] is therefore a function of P_{O_2}, and since P_{O_2} is a function of the blood path length, L_b, in the artificial lung, a length-averaged mass transfer coefficient, Eq. [129] may be found:

$$\langle K \rangle = \frac{1}{L_b} \cdot \int_0^{L_b} \frac{Q \cdot d}{4 \cdot (1-\varepsilon) \cdot A_f} \cdot \frac{1+\lambda\left(P_{O_2}\right)}{P_{O_2 g} - P_{O_2}} \cdot \frac{dP_{O_2}}{dx} \cdot dx \qquad [142]$$

For a fixed Q, A_f, d, and ε, eq. [142] yields:

$$\langle K \rangle = \frac{Q \cdot d}{4 \cdot (1-\varepsilon) \cdot A_f \cdot L_b} \cdot \int_0^{L_b} \frac{1+\lambda\left(P_{O_2}\right)}{P_{O_2 g} - P_{O_2}} \cdot \frac{dP_{O_2}}{dx} \cdot dx \qquad [143]$$

or

$$\langle K \rangle = \frac{Q \cdot d}{4 \cdot (1-\varepsilon) \cdot A_f \cdot L_b} \cdot \int_{P_{O_2 in}}^{P_{O_2 out}} \frac{1+\lambda\left(P_{O_2}\right)}{P_{O_2 g} - P_{O_2}} \cdot dP_{O_2} \qquad [144]$$

in which $P_{O_2 in}$ and $P_{O_2 out}$ are the measured partial pressures of oxygen at the inlet and outlet of the artificial lung, respectively.

Eq. [144] may be used to determine $\langle K \rangle$ for a particular device, assuming known geometric characteristics (ε, A_f, L_b, d).

II.8.3 Analogy between heat and mass transfer - fundamentals of Mockros' theory <3,4,33,271>

Because of the complex flow field in cross-flow artificial lungs, it is not possible to obtain a priori theoretical analysis of gas transfer. Artificial lungs can be evaluated by empirical correlations of mass transfer utilizing dimensionless groups. A semi-empirical approach is adopted, based on an analogy between heat and mass transfer utilizing dimensionless groups.

II.8.3.1 Chilton-Colburn analogy

Mockros and Leonard <3> applied the Chilton-Colburn analogy <35,46,47> to derive the oxygen mass transfer equations. The Chilton-Colburn analogy connects heat and mass transfer by introducing a j-factor (Eq. [145]), which can be expressed as a ratio of dimensionless groups, which differ depending on the type of transfer. The Chilton-Colburn relation has shown to be

satisfactory for numerous geometries, including flow of gases normal to cylinders <272>, based upon data collected in both laminar and turbulent flow regimes:

It can be written as follows:

$$j = N_{St} \cdot N_{Sc}^{2/3} = f_1(N_{Re}) \qquad [145]$$

or, since

$$N_{Sh} = N_{St} \cdot N_{Sc} \cdot N_{Re} \qquad [146]$$

one gets

$$N_{Sh} \cdot N_{Sc}^{-1/3} = \varphi' \cdot N_{Re}^{m'} \qquad [147]$$

where φ' and m' correlate with geometry <48>. The j-factor can be seen as the dimensionless local rate of mass transfers and as long as the j-factor can be determined, the local mass transfer coefficient K, can be predicted. However, the j-factor has to be obtained by experiments rather than theoretical derivation.

Eq. [147] lays the fundament of Mockros' model for oxygen transfer in compact cross-flow hollow fiber membrane artificial lungs. From this equation in conjunction with a mass balance, the basic controlling equation of Mockros' model can be derived.

The empirical relations described in Eq. [145] and Eq. [147] are applicable to non-reacting systems, but may be used for a blood / oxygen system.

The local Schmidt number, N_{Sc}, and Sherwood number, N_{Sh}, for oxygen transfer to blood may be expressed utilizing the mass transfer coefficient, K, and the concept of an effective diffusion coefficient, $D_{O_2 eff}$.

The local effective Schmidt number, N_{Sc} (Eq. [122]), taking into account the effective diffusion coefficient, $D_{O_2 eff}$, is:

$$N_{Sc} = \frac{\mu}{\rho \cdot D_{O_2 eff}} = \frac{\mu}{\rho \cdot D_{O_2}} \cdot \left(1 + \lambda\left(P_{O_2}\right)\right) \qquad [148]$$

The local effective Sherwood number, N_{Sh}, is given by:

$$N_{Sh} = \frac{K \cdot 4 \cdot R_h}{D_{O_2 eff}} = \frac{K \cdot 4 \cdot R_h}{D_{O_2}} \cdot \left(1 + \lambda\left(P_{O_2}\right)\right) \qquad [149]$$

and inserting Eq. [140] into Eq. [149] gives:

$$N_{Sh} = \frac{Q \cdot d^2 \cdot \varepsilon}{4 \cdot (1-\varepsilon) \cdot A_f \cdot D_{O_2}} \cdot \frac{\left(1 + \lambda\left(P_{O_2}\right)\right)^2}{P_{O_2 g} - P_{O_2}} \cdot \frac{dP_{O_2}}{dx} \qquad [150]$$

Combining the expression for the local Schmidt number and Sherwood number with Eq. [147] gives locally:

$$N_{Sh} \cdot N_{Sc}^{-1/3} = \frac{Q \cdot d^2 \cdot \varepsilon}{4 \cdot (1-\varepsilon)^2 \cdot A_f \cdot \upsilon^{1/3} \cdot D_{O_2}^{2/3}} \cdot \frac{\left(1+\lambda\left(P_{O_2}\right)\right)^{5/3}}{P_{O_2 g} - P_{O_2}} \cdot \frac{dP_{O_2}}{dx} = \varphi' \cdot N_{Re}^{m'} \qquad [151]$$

As with the mass transfer coefficient, a length-averaged $N_{Sh} \cdot N_{Sc}^{-1/3}$, $\left\langle N_{Sh} \cdot N_{Sc}^{-1/3} \right\rangle$, may be calculated, based on inlet and outlet oxygen partial pressures, $P_{O_2 in}$ and $P_{O_2 out}$:

$$\left\langle N_{Sh} \cdot N_{Sc}^{-1/3} \right\rangle = \frac{Q \cdot d^2 \cdot \varepsilon}{4 \cdot (1-\varepsilon)^2 \cdot A_f \cdot L_b \cdot \upsilon^{1/3} \cdot D_{O_2}^{2/3}} \cdot \int_{P_{O_2 in}}^{P_{O_2 out}} \frac{\left(1+\lambda\left(P_{O_2}\right)\right)^{5/3}}{P_{O_2 g} - P_{O_2}} \cdot dP_{O_2} = \varphi' \cdot N_{Re}^{m'} \qquad [152]$$

$\left\langle N_{Sh} \cdot N_{Sc}^{-1/3} \right\rangle$ is not normalized for the capacity of blood to take up oxygen. For instance, if one were to evaluate the performance of a given artificial lung under different inlet conditions, the total oxygen transfer rate would be greater in the case of lower venous inlet saturation or in the case of a higher hemoglobin concentration because of the greater capacity of the blood to take up oxygen. Eq. [152] should be divided by the quantity $\left(1+\lambda\left(P_{O_2}\right)\right)$ in the integral to normalize for the oxygen-carrying capacity of blood under different conditions. Thus, the normalized length-averaged parameters may be defined as:

$$\left\langle \left| N_{Sh} \cdot N_{Sc}^{-1/3} \right| \right\rangle = \frac{1}{L_b} \cdot \int_0^{L_b} \frac{N_{Sh} \cdot N_{Sc}^{-1/3}}{1+\lambda\left(P_{O_2}\right)} \cdot dx \qquad [153]$$

Therefore,

$$\left\langle \left| N_{Sh} \cdot N_{Sc}^{-1/3} \right| \right\rangle = \frac{Q \cdot d^2 \cdot \varepsilon}{4 \cdot (1-\varepsilon)^2 \cdot A_f \cdot L_b \cdot \upsilon^{1/3} \cdot D_{O_2}^{2/3}} \cdot \int_{P_{O_2 in}}^{P_{O_2 out}} \frac{\left(1+\lambda\left(P_{O_2}\right)\right)^{2/3}}{P_{O_2 g} - P_{O_2}} \cdot dP_{O_2} = \varphi' \cdot N_{Re}^{m'} \qquad [154]$$

The results obtained in Eq. [154] may be plotted against the Reynolds number on a bilogarithmic plot. On a log-log plot of Eq. [154], m' is the slope and φ' determines the vertical position of the graph. $\left\langle \left| N_{Sh} \cdot N_{Sc}^{-1/3} \right| \right\rangle$ may be interpreted as a dimensionless mass transfer coefficient, taking into account the fluid properties, and may be normalized for the oxygen carrying capacity of the blood.

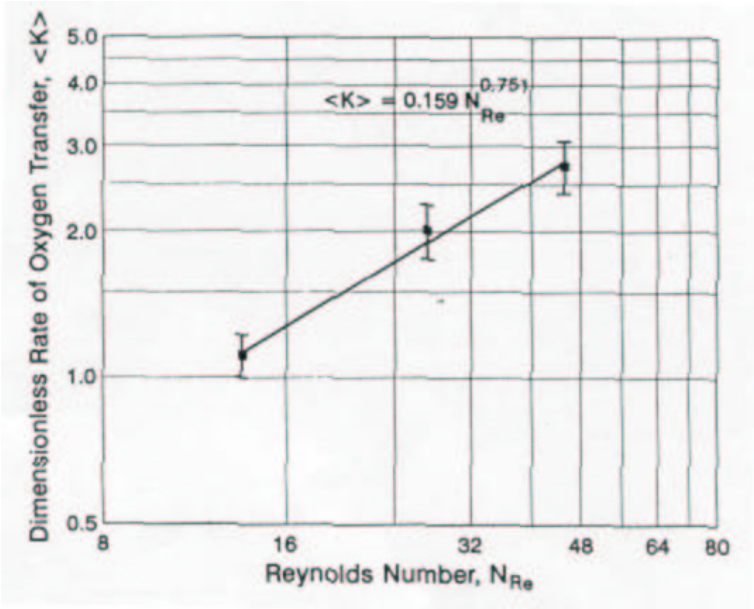

Figure II.28: Bilogarithmic plot of the length-averaged mass transfer coefficient, <K>, versus the Reynolds number, N_{Re}, for ten water tests conducted at three different flow rates for the Sarns Turbo oxygenator [4]. The slope m' = 0.751 and the vertical position φ' = 0.159.

Another goal of the dimensionless theory is to be able to predict the oxygenation performance of a device based on oxygenation of a non-reactive fluid, such as water. In order to accomplish this goal, φ' and m' may be determined from tests using water, i.e. using inlet and outlet P_{O_2} to calculate $\left\langle \left| N_{Sh} \cdot N_{Sc}^{-1/3} \right| \right\rangle$. For water, however, we use $\lambda(P_{O_2}) = 0$, making the integral somewhat simpler. Once m' and φ' are found for water, they may be used to predict the oxygen transfer rate to blood at specified inlet conditions if no other factors are involved. Normalized local parameters are defined in the same way the normalized length average parameters were defined earlier:

$$\left| N_{Sh} \cdot N_{Sc}^{-1/3} \right| = \frac{N_{Sh} \cdot N_{Sc}^{-1/3}}{1 + \lambda(P_{O_2})} \qquad [155]$$

Eq. [151] may be substituted into Eq. [155] and combined with the expression for N_{Re} (Eq. [120]), to yield:

$$\frac{Q \cdot d^2 \cdot \varepsilon}{4 \cdot (1-\varepsilon)^2 \cdot A_f \cdot \upsilon^{1/3} \cdot D_{O_2}^{2/3}} \cdot \frac{(1 + \lambda(P_{O_2}))^{2/3}}{P_{O_{2g}} - P_{O_2}} \cdot \frac{dP_{O_2}}{dx} = \varphi' \cdot \left(\frac{Q \cdot d}{\upsilon \cdot (1-\varepsilon) \cdot A_f} \right)^{m'} \qquad [156]$$

Solving for $\frac{dP_{O_2}}{dx}$ results in:

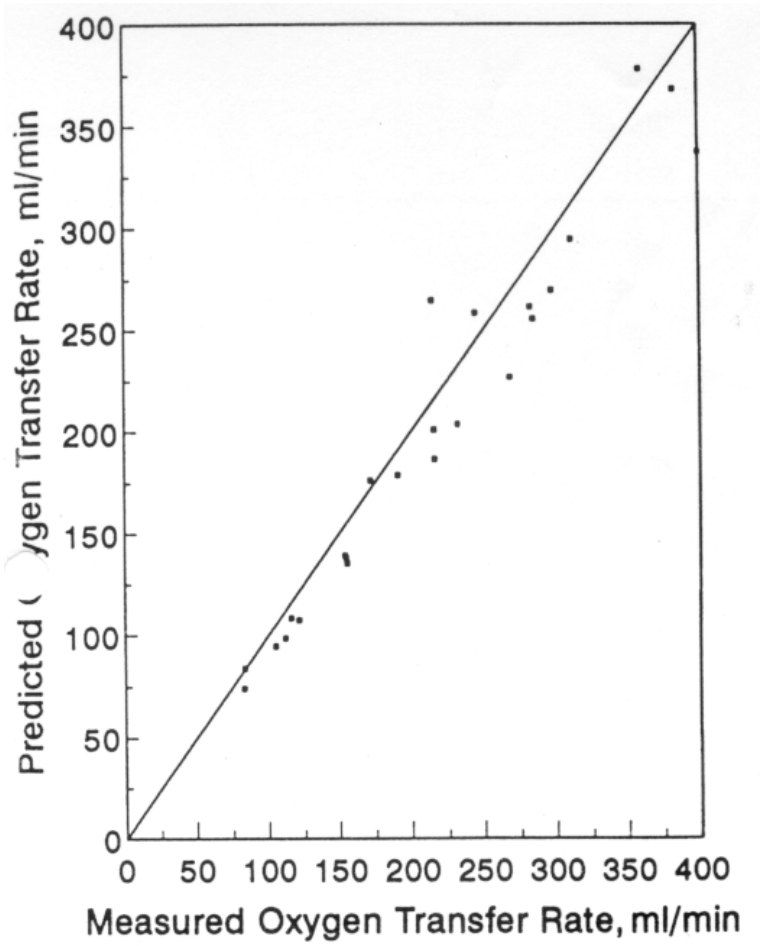

Figure II.29: Correlation of predicted and measured oxygen transfer rates compared with the line of identity for the Sarns Turbo oxygenator <4>.

$$\frac{dP_{O_2}}{dx} = \frac{4}{\varepsilon}\cdot\left(\frac{1-\varepsilon}{d}\right)^{2-m}\cdot\varphi'\cdot D_{O_2}{}^{2/3}\cdot\upsilon^{1/3-m'}\cdot\left(\frac{A_f}{Q}\right)^{1-m'}\cdot\frac{P_{O_2g}-P_{O_2}}{\left(1+\lambda\left(P_{O_2}\right)\right)^{2/3}} \qquad [157]$$

Eq. [157] is an ordinary first order differential equation that may be solved numerically to give a value of P_{O_2} at the outlet of the artificial lung, P_{O_2out}. The predicted oxygen transfer rate may be calculated from Eq. [63] and compared to the actual transfer rate (Figure II.29).

II.9 Industrial standardization of gas transfer and blood flows: criteria for gas exchange in membrane artificial lungs

The primary requirement of the artificial lung is to maintain physiological oxygen and carbon dioxide levels in the arterial blood during CPB. The associated gas transfer rates will depend upon the blood flow rate and venous input conditions, i.e. temperature, carbon dioxide partial

pressure, hemoglobin content, oxygen saturation and base excess. For adult CPB the artificial lung should be capable of processing blood flow rates up to 7.0 l/min. The gas performance of an artificial lung is usually measured according to a standard test protocol as laid down by the Association for the Advancement of Medical Instrumentation (AAMI, Arlington) <45>. This protocol defines reference blood flow rates for oxygen and carbon dioxide transfer. Specifically these are:

- *Oxygen reference flow rate* is the flow rate of normothermic whole blood that produces an increase in blood oxygen content of 45 ml/l after direct passage through the device.
- *Carbon dioxide reference flow rate* is the flow rate of normothermic whole blood which produces a decrease in blood carbon dioxide content of 38 ml/l after direct passage through the device.

The reference flow rates are determined for standardized normothermic whole blood input conditions, which relate to the physiological situation and enable inter-device comparisons to be made. These conditions are:

$T = 37 \pm 2$ °C

$S_{O_2} = 65 \pm 5$ %

$P_{CO_2} = 45 \pm 5$ mmHg

$C_{Hb} = 0.12 \pm 0.01$ g/ml

BE = 0 ± 5 mmol/l

with BE being the base excess, the excess concentration of blood base.

In respiratory assist procedures, the required gas transfer rates differ between ECMO and $ECCO_2R$ techniques. Requirements for oxygen and carbon dioxide exchange in ECMO are similar to those in CPB because extracorporeal flow rates can be as high as 80 % of the cardiac output.

Bethune <273> reviewed the development of artificial lung standards. Despite widespread reliance on AAMI standards, their clinical validity has been questioned by Fried et al. <274> and by Ueyama et al. <275>.

II.10 Conclusion

The reader is introduced to several aspects of the numerical and semi-empirical modeling of momentum and oxygen transfer in membrane artificial lungs. With this knowledge, he should be ready to comprehend the next chapters describing the *in numero* and *in vitro* analysis of the

hydrodynamics and mass transfer characteristics in cross-flow hollow fiber membrane artificial lungs.

III HYDRODYNAMIC CHARACTERISTICS OF ARTIFICIAL LUNGS

III.1 Abstract[†]

An artificial lung is used during cardiopulmonary bypass to oxygenate blood and to control blood temperature. The pressure drop-flow rate characteristics of the membrane compartment in three hollow fiber membrane artificial lungs were determined *in vitro* to characterize design features. Results are presented in a unique dimensionless relationship between Euler number, N_{Eu} (ratio of pressure drop to kinetic energy), and Reynolds number, N_{Re}, (ratio of inertial to viscous forces), and are a function of the device porosity, ε, and a characteristic device length, ξ, defined as the ratio of the mean blood path and manifold length:

$$N_{Eu} \cdot \frac{\xi}{\varepsilon^2} = \alpha + \frac{\beta}{N_{Re} \cdot \varepsilon \cdot (1-\varepsilon)}$$

This dimensionless approach allows us:

- to compare artificial lungs independently.
- to relate water tests to blood.

III.2 Introduction

An artificial lung is used during cardiopulmonary bypass to oxygenate blood and to control the blood temperature. The blood-material interaction in the artificial lung induces a complex systemic inflammatory reaction. To control this reaction, more biocompatible surfaces, in combination with blood outside the fiber geometry's (less surface for the same mass transfer) were introduced. In general, a membrane artificial lung is placed between the pump and the patient to overcome the resistance exerted by the device. Resistance can be monitored by measuring blood flow in combination with inlet and outlet pressure and is related to the

[†] The contents of this chapter are published in *ASAIO Journal* 2000; **46**:532-535:

Hydrodynamic characteristics of artificial lungs

P.W. Dierickx, F. De Somer, D.S. De Wachter, G. Van Nooten, and P.R. Verdonck

geometry of the flow pattern and to the way the fluid flows through the membrane artificial lung. Few attempts have been made to characterize hydrodynamics, including geometry and flow pattern, of an artificial lung <3,4,271>. Vaslef et al. proposed a dimensionless flow-friction relationship that only incorporated the viscous losses, eliminating nonlinear effects in the pressure drop–flow rate relationship. Our study investigated the value of a unique relationship between pressure drop in the membrane compartment and flow rate as a function of geometry and flow pattern, incorporating nonlinear effects. Such a relationship may facilitate the design of new devices.

III.3 Materials and methods

III.3.1 Dimensional analysis

An artificial lung can be characterized by different geometric parameters: membrane surface area, A; diameter of the fiber, d; length of the fiber compartment, L; inside housing outer diameter, D_i; outside housing inner diameter, D_o; and gross frontal area of the blood path, A_f. The "void fraction" or device porosity, ε, is defined as the ratio of the volume of voids (volume in the membrane compartment occupied by blood) to the volume of the bed (total volume of the membrane compartment). A characteristic length for flow through porous beds or packed fiber bundles, is hydraulic radius, R_h. Hydraulic radius is expressed in terms of device porosity, ε, and wetted surface per unit volume of bed, a <35,276>:

$$R_h = \frac{\left(\frac{\text{volume of voids}}{\text{volume of bed}}\right)}{\left(\frac{\text{wetted surface}}{\text{volume of bed}}\right)} = \frac{\varepsilon}{a} \qquad [158]$$

Manifold length, L_m, is defined as the length by which the total artificial lung flow is divided per unit width of fiber stack. Mean blood path length, L_b, is the average distance blood has to travel through the fiber stack. Consequently, a dimensionless characteristic device length, ξ, can be defined as ratio of mean blood path length, L_b, and average manifold length, L_m. We assume that blood is uniformly distributed over the fiber stack. In Sarns Turbo 440 (3M, Michigan, USA) and Optima (Cobe, Arvada, USA) membrane artificial lungs, L_m and L_b are determined as shown in Figure III.1 (left panel). Blood enters the membrane evenly distributed over the length, L, of the manifold and the blood flow is split in two, for left and right sides. Blood flow rate per unit membrane width, Q´, is:

$$Q' = \frac{Q}{L_m} = \frac{Q}{2 \cdot L} \qquad [159]$$

Mean blood path length is:

$$L_b = \frac{\pi}{2} \cdot \left(\frac{D_i + D_o}{2} \right) \qquad [160]$$

In the Dideco Compactflo (Dideco, Miranda, Italy), blood flow enters the fiber stack circumferentially (Figure III.1, right panel). Manifold length is:

$$L_m = \pi \cdot \left(\frac{D_i + D_o}{2} \right) \qquad [161]$$

whereas mean blood path length is determined as:

$$L_b = L \qquad [162]$$

The measured pressure drop, Δp and flow rate, Q, relationship is presented as a polynomial of second order:

$$\Delta p = a' \cdot Q^2 + b' \cdot Q \qquad [163]$$

The Reynolds number, N_{Re}, is defined as the ratio of inertial and viscous forces. Characteristic

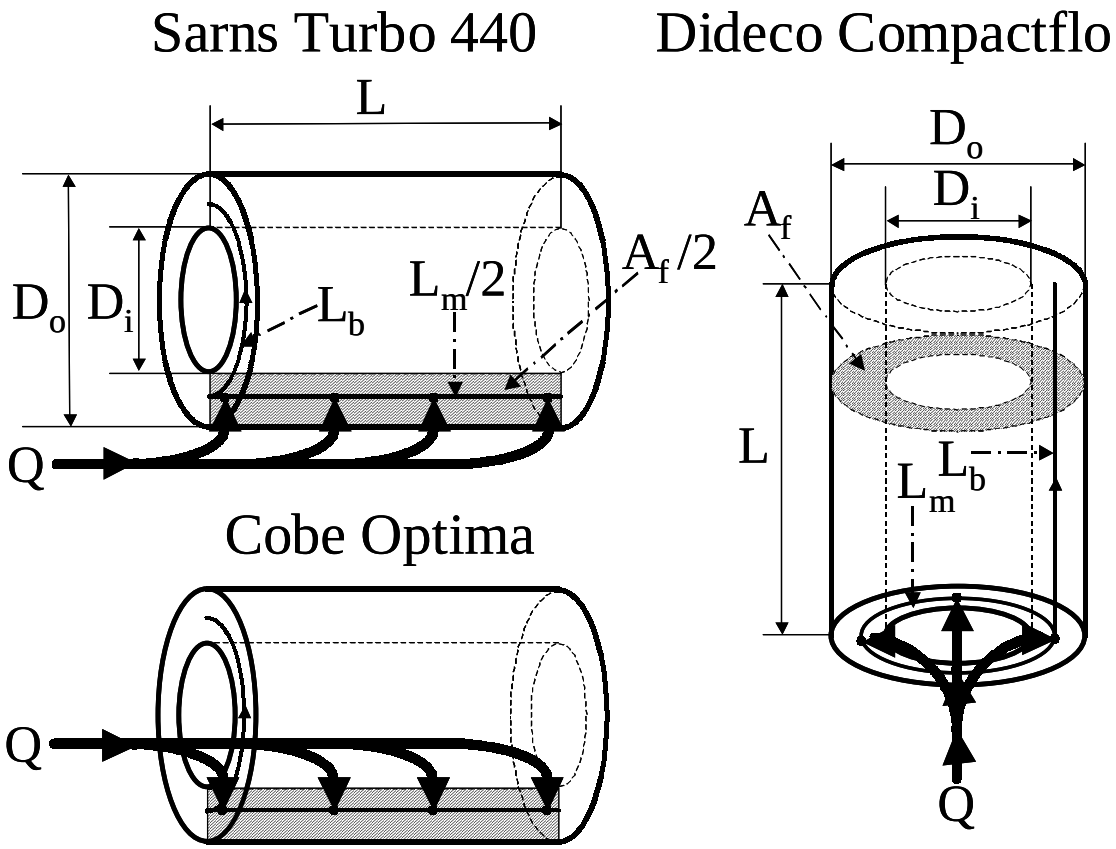

Figure III.1: Geometric characteristics of artificial lungs; **Top left panel**: Sarns Turbo 440; **bottom left panel**: Cobe Optima; **right panel**: Dideco Compactflo.

length in the Reynolds number for flow through a fiber stack, is hydraulic diameter, R_h. Consequently, the Reynolds number is defined as:

$$N_{Re} = \frac{Q}{A_f \cdot \varepsilon} \cdot \frac{4 \cdot R_h \cdot \rho}{\mu} \qquad [164]$$

in which A_f represents the gross frontal area, ρ the density, and μ the dynamic viscosity of the fluid. The Euler number, N_{Eu}, is defined as the ratio of pressure drop and kinetic energy:

$$N_{Eu} = \frac{\Delta P}{\rho \cdot \left(\frac{Q}{A_f \cdot \varepsilon} \right)^2} \qquad [165]$$

If Eq. [163] is divided by the denominator of Eq. [165], one can describe the Euler number as a dimensionless function of the reciprocal of the Reynolds number under the assumption of laminar flow conditions in the fiber stack:

$$N_{Eu} = \alpha' + \frac{\beta'}{N_{Re}} \qquad [166]$$

An analogous approach has already been successfully applied in the flow characteristics of aortic cannulae <277>. A similar, but not identical, approach is described by Ergun <276>, Bird et al. <35> and by Macdonald et al. <278> for flow through porous media. Our starting point to come to a dimensionless relationship is pressure drop–flow rate relationship, whereas Ergun <276> relates the pressure gradient to fluid velocity. α' and β' in Eq. [166] are model parameters that characterize the porous medium and, therefore, must be functions of the medium <276,278> rather than universal constants. It is assumed that the medium can be characterized by the device porosity, ε, and the dimensionless characteristic device length, ξ, and that the functional form of α' and β', in analogy with Ergun <276> and MacDonald et al. <278>, can be represented as a power function of device porosity and dimensionless characteristic length:

$$\begin{aligned} \alpha'(\varepsilon, \xi) &= \alpha \cdot \varepsilon^n \cdot \xi^m \cdot (1 - \varepsilon)^p \\ \beta'(\varepsilon, \xi) &= \beta \cdot \varepsilon^r \cdot \xi^s \cdot (1 - \varepsilon)^t \end{aligned} \qquad [167]$$

in which α, β, n, m, p, r, s, and t are constants, which may be determined by nonlinear regression analysis. Therefore, the relationship between Euler and Reynolds is solely determined by geometry of and flow pattern in the artificial lung.

III.4 Materials

Pressure drop-flow rate characteristics of the membrane compartment of three different hollow fiber membrane artificial lungs (Sarns Turbo 440 (N = 2), Cobe Optima (N = 3), Dideco Compactflo (N = 3)) are measured *in vitro* and analyzed to characterize design features.

III.4.1 Experimental setup

Experiments were performed with water, and steady flow is applied by using an upstream reservoir with constant head. Pressure was measured between the heat exchanger and the membrane compartment, and at inlet and outlet of the artificial lung, using fluid-filled pressure transducers (Ohmeda, Gent, Belgium). Flow rate was measured with an ultrasonic transit time flow meter (Transonic, Ithaca, NY, USA). Downstream the artificial lung, static pressure was kept constant at 150 mmHg.

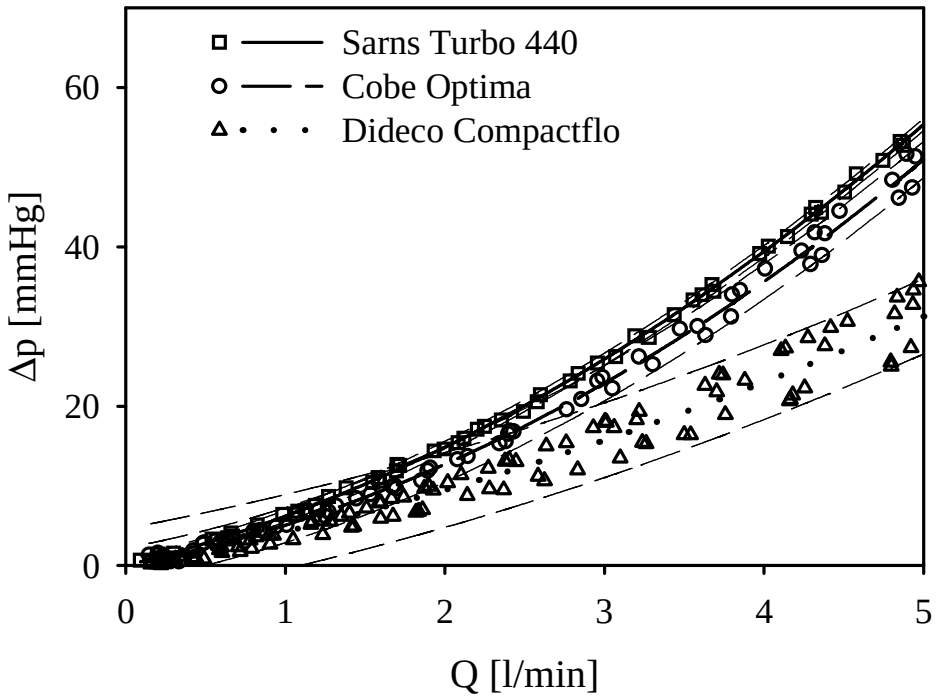

Figure III.2: Measured membrane compartment pressure drop (Δp)-flow rate (Q) relationship with confidence limits.

Table III.1: Geometric characteristics of artificial lungs, including the model parameters α' and β'.

	Sarns Turbo 440	***Cobe Optima***	***Dideco Compactflo***
membrane surface area, A [m²]	1.6	1.7	2
fiber diameter, d [µm]	380	380	380
inside core outer diameter, D_i [cm]	5.0	4.4	5.0
outside core inner diameter, D_o [cm]	7.0	7.3	7.8
length fiber compartment, L [cm]	20.5	12.4	12
device porosity, ε	0.61	0.51	0.44
characteristic device length, ξ	0.23	0.37	0.60
model parameter α'	3686	2076	514
model parameter β'	57450	22050	12930

III.4.2 Statistical analysis

Fitting of the parabolic pressure drop-flow rate relationship is performed by using the nonlinear

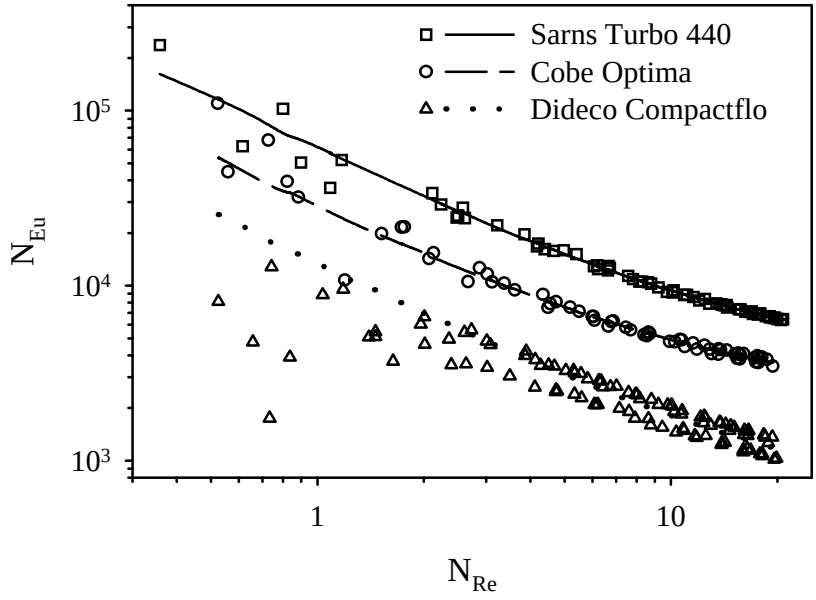

Figure III.3: Euler (N_{Eu})-Reynolds (N_{Re}) relationship for the Sarns Turbo 440, Cobe Optima, and Dideco Compactflo on a bilogarithmic plot.

Table III.2: Nonlinear regression results.

α ± SD	2365 ± 52
β ± SD	8509 ± 25
R^2	0.998

regression Marquardt-Levenberg algorithm (Sigmastat 2.0, Jandel Scientific, Germany). The same technique is used to fit geometric parameters within the Euler-Reynolds relationship. Results are presented with upper and lower confidence limits (95 %), asymptotic standard errors of fitting parameters and coefficient of determination, R^2, for nonlinear regression.

III.5 Results

Figure III.2 presents pressure drop and flow rate characteristics for the membrane compartments of three different artificial lungs, indicating a parabolic relationship between Δp and Q (Eq.

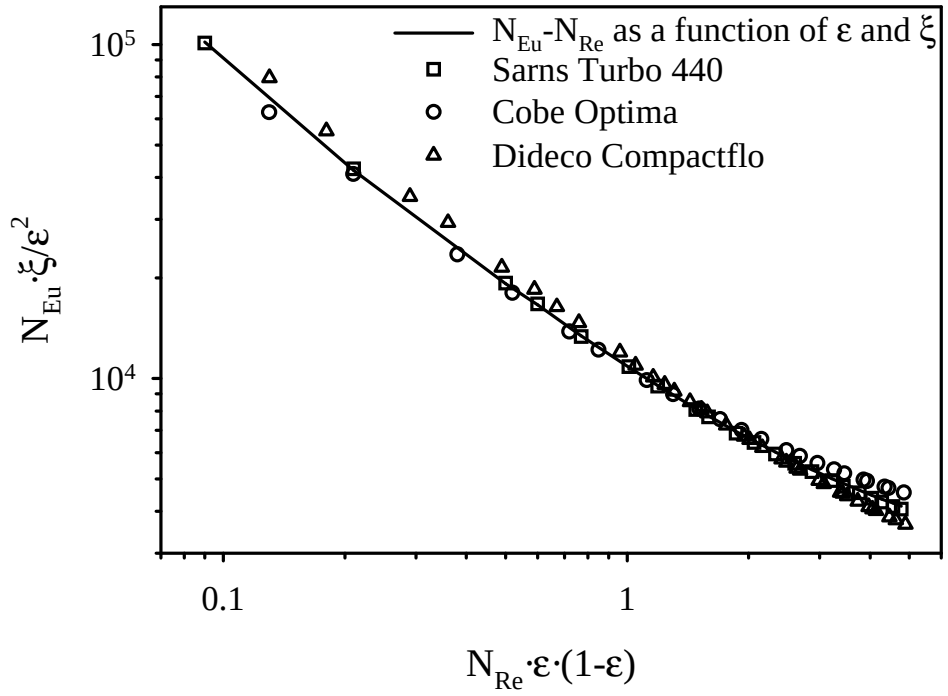

Figure III.4: Dimensionless pressure drop-flow rate relationship as a function of Euler number, N_{Eu}, Reynolds number, N_{Re}, device porosity, ε, and dimensionless characteristic device length, ξ, on a bilogarithmic plot.

[163]). The technique to measure the pressure between the heat exchanger and the membrane compartment does not influence the pressure drop-flow relationship. Hence, the variance in pressure drop–flow rate relationship in Figure III.2 for the three Dideco Compactflo artificial lungs may be attributed to a difference in construction of the membrane compartment. The corresponding Euler-Reynolds relationship for the membrane compartment (Eq. [166]) is depicted in Figure III.3. The geometric data and model parameters, α' and β', are tabulated in Table III.1, indicating a similar trend among the different artificial lungs in N_{Eu}-N_{Re} graph for device porosity, ε, and dimensionless characteristic device length, ξ. α' and β increase with ε and decrease with ξ. Based on this finding, the functions of Eq. [167] are determined and yield the following dimensionless relationship:

$$N_{Eu} \cdot \frac{\xi}{\varepsilon^2} = \alpha + \frac{\beta}{N_{Re} \cdot \varepsilon \cdot (1-\varepsilon)} \qquad [168]$$

The results of the nonlinear regression are listed in Table III.2 and depicted in Figure III.4. Figure III.5 shows the original Δp versus Q data for each artificial lung, along with the predicted Δp versus Q relationship (with 95 % regression intervals for α and β) obtained by converting the dimensionless fit from Figure III.4 back to its dimensional form.

III.6 Discussion

The importance of a given resistance and flow characteristic in an artificial lung on blood elements and the degree of inflammatory response have not yet been established. However, it is well known that shear stress plays an important role in the activation of blood platelets and white blood cells. However, from an engineering point of view, a certain pressure drop over the device is necessary for an even distribution of blood flow. In the past, few attempts have been made to characterize hydrodynamics, including geometry and flow pattern of an artificial lung. Pressure drop across a membrane compartment can be studied using a dimensionless relationship between Euler and Reynolds numbers as a function of two dimensionless characteristic geometric parameters, namely, device porosity, ε, and a dimensionless characteristic device length, ξ. This relationship indicates that the (total) pressure drop across heat exchanger and membrane compartment is directly related to:

- length of the blood path.
- length of manifold.
- flow pattern.

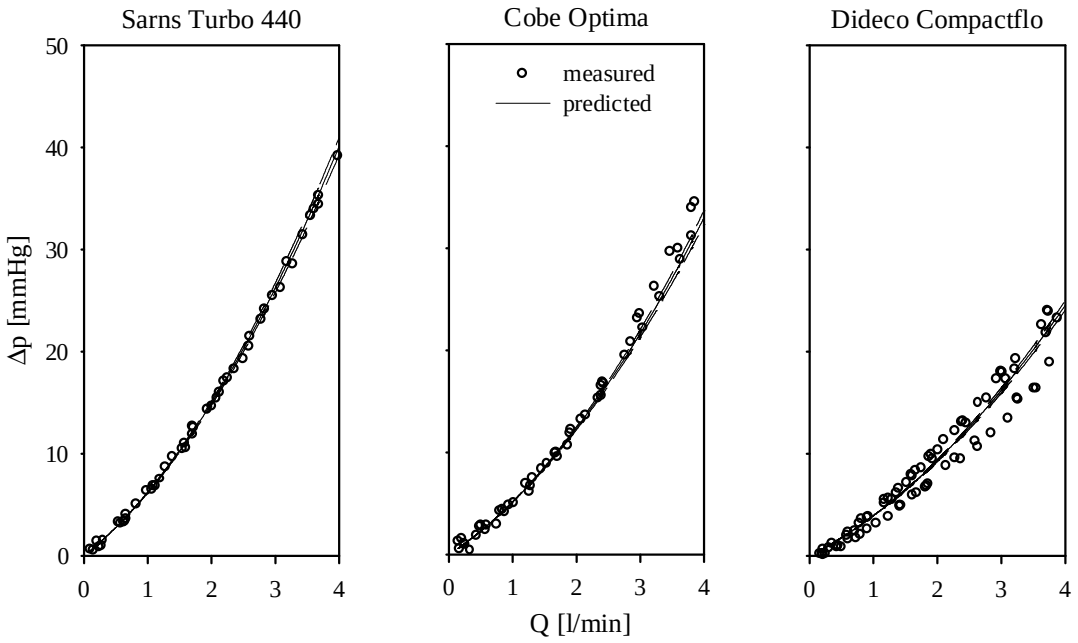

Figure III.5: Original pressure drop (Δp) -flow rate (Q) data along with the predicted pressure drop-flow rate data obtained by converting the dimensionless fit back to dimensional form. **Left panel**: Sarns Turbo 440; **Middle panel**: Cobe Optima; **Right panel**: Dideco Compactflo.

Figure III.4 can be presented as a device specific scaling of Figure III.3, resulting in one curve representing the three artificial lungs.

In Figure III.5, the dimensionless N_{Eu}-N_{Re} equation gives a good prediction of the Δp-Q relationship for water flow rates up to 3.5 l/min ($N_{Re} < 10$). However, at higher water flow rates ($N_{Re} > 10$), the predicted Δp-Q data deviate from the measured Δp-Q data, especially for the Cobe Optima.

The dimensionless approach is independent of fluid density and viscosity and enables one to relate water tests to blood, advertising the benefits of dimensionless numbers. There is no need to rescale the graphs for blood, although the measurements are performed with water. This is of great advantage when hemodilution and hypothermia are present, because they alter the dynamic viscosity and, therefore, the pressure drop-flow rate relationship. However, with the dimensionless numbers N_{Eu} and N_{Re}, the graph is normalized for a Newtonian fluid of any viscosity. Assuming a blood temperature of 30°C and a hematocrit of 30% during cardiopulmonary bypass, density and dynamic viscosity of blood can be calculated [3] $\rho = 1052$ kg/m³ and $\mu = 3.02$ mPa·s, yielding operational ranges for N_{Re} between 0 and 7. Blood pressure drop can then be calculated, using the corresponding Euler number, dimensionless geometric parameters, and kinetic energy.

With the help of the proposed dimensionless format, one can

- compare artificial lungs independently.
- relate water tests to blood tests.
- predict pressure drop of a new design of an artificial lung.

We believe that this dimensionless analysis can be an excellent tool for the study of better designs.

We demonstrate that pressure drop across a membrane compartment can be studied by using a dimensionless relationship between Euler and Reynolds numbers as a function of two dimensionless characteristic geometric parameters, namely device porosity, ε, and a newly defined dimensionless characteristic device length, ξ.

III.7 Acknowledgement

This research is funded by a grant of the Flemish Institute for the Promotion of the Scientific-Technological Research in Industry (IWT961181). The authors like to express their gratitude to Nico Vincart for doing most of the measurements.

IV BLOOD FLOW AROUND HOLLOW FIBERS

IV.1 Abstract[†]

In an artificial lung, blood is oxygenated and flows around a bundle of hollow fibers while gas flows inside the fiber. The objective of this study is to understand the hydrodynamics of three different fiber banks (inline square, IS, staggered square, SS and equilateral triangle, ET) and to investigate the influence of both a Newtonian and a non-Newtonian Casson viscosity model on the flow field. A two-dimensional finite element model for permanent, isothermal, laminar blood flow perpendicular to hollow fibers is used. All fibers are assumed identical, straight, and parallel. Porosity ranges from 0.4 to 0.6 and Reynolds number varies from 1 to 60. For a given N_{Re}, ET generates less resistance than SS, the latter being comparable with IS. A lower porosity increases resistance. Non-Newtonian viscosity affects velocity patterns only at low Reynolds numbers ($N_{Re} < 0.5$) and higher porosities ($\varepsilon > 0.5$). Resistance at low N_{Re} is significantly elevated in the fiber banks due to an overall increase in viscosity. This model makes it possible to study the influence of geometry and viscosity on hydrodynamics in fiber banks and may aid the optimization of hollow fiber artificial lung design.

IV.2 Introduction

An artificial lung in the extracorporeal circuit oxygenates blood during cardiopulmonary bypass. In most artificial lungs, blood passes a heat exchanger first and then flows through the gas exchange membrane compartment. Most artificial lungs consist of microporous hollow fibers, the fundamental gas exchange elements, with blood flowing perpendicular to the fibers (cross-flow). Mass transfer over the membrane (oxygen–carbon dioxide exchange) determines artificial lung performance. The mass transfer efficiency is determined by the resistance to gas flux of the

[†] The contents of this chapter are published in *The International Journal of Artificial Organs* 2000; **23(9)**: 610-617:

Blood flow around hollow fibers

P.W. Dierickx, D.S. De Wachter, P.R. Verdonck

hollow fiber membrane on the one hand and to the gas flux of the blood phase flowing over the exterior of the fiber surface on the other hand. It is generally accepted that cross-flow past fibers induces secondary flows, preventing the development and maintenance of the momentum and mass transfer boundary layers and resulting in a better mixing in the blood phase and improved mass transfer <279,280>. It is expected that the degree of mixing in the extraluminal flow depends upon the blood velocity and viscosity, the fiber external diameter, and the porosity and geometry of the fiber bank <199>. However, fundamental studies are lacking.

Numerical techniques are a useful tool in the study of flow in the artificial lung. They can provide local flow field properties such as surface pressure, shear stress, and mass transfer coefficient distribution that are needed to study the mechanics of fluid flow and mass transport. Mass transport over the membrane, governed by the convection-diffusion equation, is coupled to the local fluid flow in a fiber array in detail and both aspects have to be considered simultaneously. The local hydrodynamic solution of flow around fibers is complex and generally, the solution is non-trivial <42>.

Newtonian fluid flow in periodic cylinder banks has been the focus of a large number of investigations, analytical as well as numerical (finite differences) <43,267,281-283>. Flow through an array of randomly oriented fibers is commonly approximated by flow through a regular array of parallel-oriented fibers. Periodicity and symmetry are used to reduce the domain to the smallest element (a single fiber), the unit fiber cell. The classical unit fiber cell models developed by Happel <284>, Kuwabara <281>, and others further included the additional approximation that the outer boundary of the unit fiber cell is circular. The boundary conditions applied at this outer surface were estimated from periodicity and symmetry arguments. This approach was motivated in part by the limitations of computer-generated solutions at the time. These classical models, particularly those of Kuwabara, still provide good approximations to modern computer generated solutions for the average flow pattern perpendicular to square arrays of cylinders for a large range of porosities. Makarewicz <285> studied mass transfer characteristics for flow in a fiber bank based on Happel's method for a unit fiber cell <284>.

Although flow of a fluid in fiber banks resembles flow past a single cylinder, there are significant differences. These simple models do not include effects such as convective transfer of fluid from one unit fiber cell to its neighbors, for which numerical techniques which are more complex, are required. Launder and Massey <43> developed a two-dimensional finite-difference scheme for the analysis of fully developed laminar viscous flow and heat transfer in tube banks. A hybrid Cartesian grid was used to encompass the flow domain. Baker et al. <267> developed a two-dimensional finite-difference model for gas transfer to blood flowing outside and parallel to

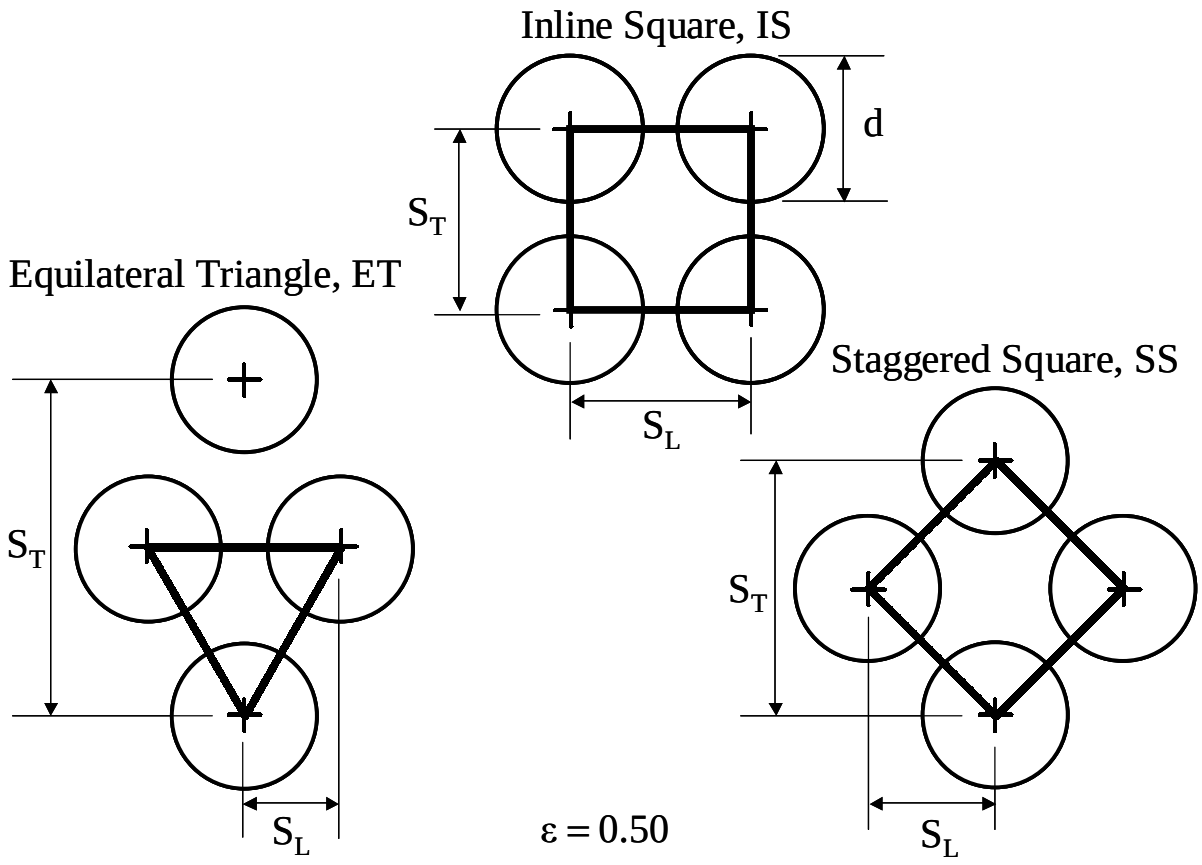

Figure IV.1: Three fiber geometries with a porosity of 0.50: inline square, IS, equilateral triangle, ET, and staggered square, SS (fiber diameter, d, cross-wise pitch, S_T, stream-wise pitch, S_L).

hollow fibers arranged in an equilateral triangle fiber bundle in a blood-gas exchange device. The reported calculations are generally limited to one or two geometries and do not consider global flow properties as expressed by Darcy's law. Edwards et al. <42> used a finite element numerical scheme to study the effect of Reynolds number on the apparent hydraulic permeability of two-dimensional arrays of cylinders. They concluded that a single apparent hydraulic permeability scalar suffices to quantify the permeable nature of the material. This scalar was found to be a function of the orientation of the applied pressure drop and of the Reynolds number.

All former studies were limited to a Newtonian fluid. In this work, we present a numerical two-dimensional model that compares both Newtonian and non-Newtonian Casson <214> blood flow across different fiber bank configurations. Three different fiber bank configurations are considered, for which we calculated the local flow fields as well as the resistance of the fiber bank. The model simulations provide insight into the impact of geometry and hydrodynamic boundary conditions on flow dynamics and convective mass transport in hollow fiber banks of the artificial lung.

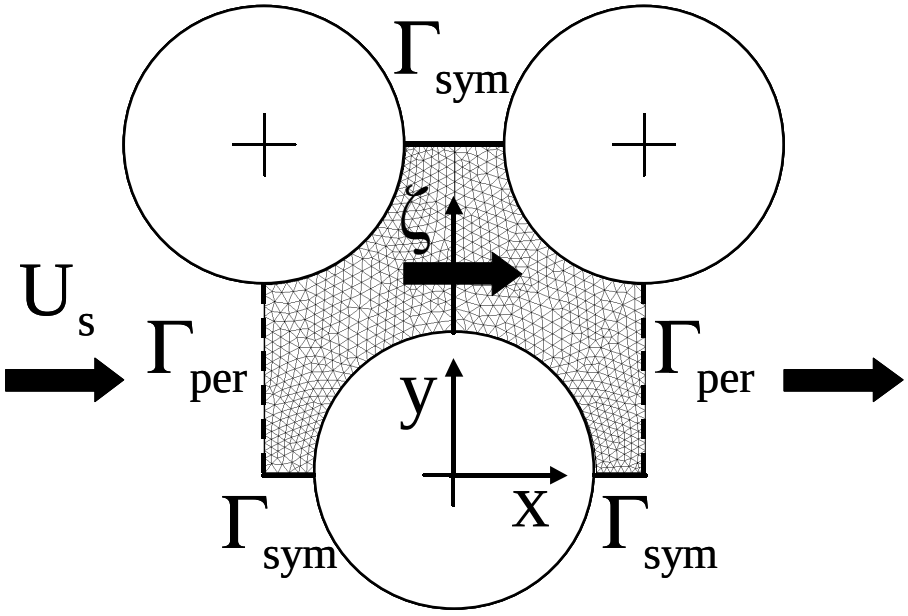

Figure IV.2: Schematic representation of the unit fiber cell model. Γ_{sym} represents the symmetrical boundaries, Γ_{per} the periodical boundaries, x the flow direction, y the distance from the fiber center perpendicular to the flow direction and ζ the dimensionless distance from the fiber surface, perpendicular to the flow direction.

IV.3 Methods

IV.3.1 Fiber bank model

The fiber bank model is an assemblage of uniform, parallel, fixed circular fibers equally spaced in a plane perpendicular to the long axes of the fibers. Assuming negligible entrance, end, and wall effects (which is a reasonable assumption for a fiber bank with a large number of rows) and fully developed, two-dimensional laminar steady flow through the fiber bank, periodically fully developed flow can be considered. A fiber bank can then be divided into a number of identical unit fiber cells, one fiber occupying each unit fiber cell. Fiber banks are characterized by cross-wise, S_T/d, and stream-wise, S_L/d, pitch (S)-to-diameter (d) ratios (Figure IV.1). Symmetry boundary conditions, Γ_{sym}, are imposed on the symmetry lines and no-slip wall boundary conditions are imposed on the fiber surface (Figure IV.2). The distribution of the flow velocities (but not the local pressure) is identical in all unit fiber cells, hence periodical boundary conditions, Γ_{per}, to inlet and exit planes can be applied (Figure IV.1). The values of flow variables at the exit plane are imposed upon the inlet plane during the solution procedure.

The overall dimensions of the unit fiber cell are fixed by specifying the configuration, the porosity, ε, and the fiber diameter, d. The porosity is defined as the ratio of the volume of voids

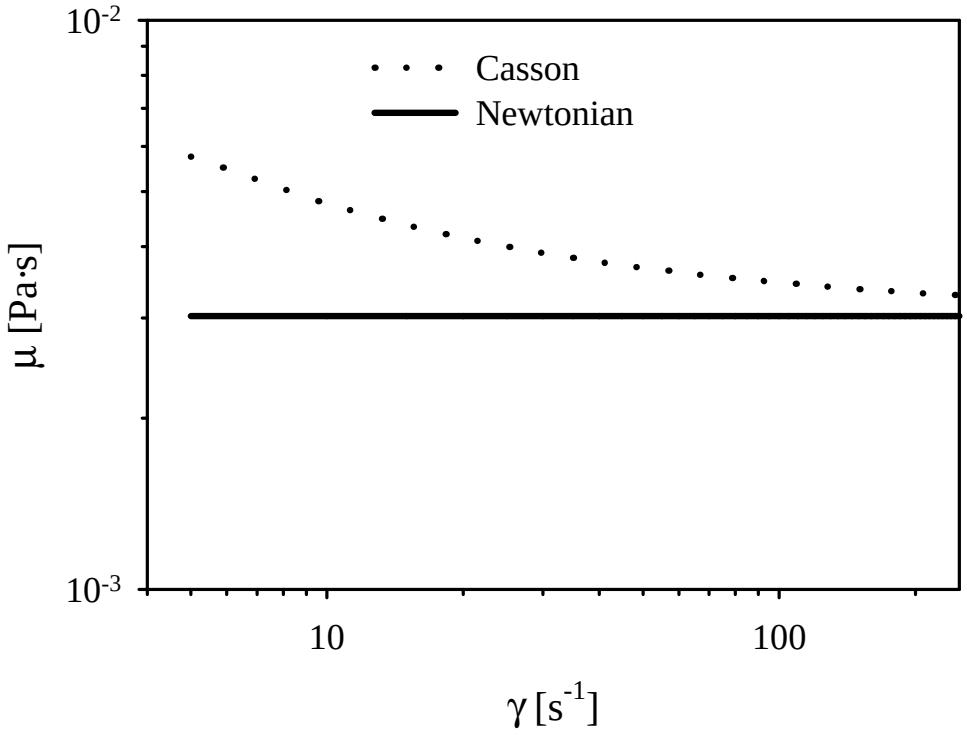

Figure IV.3: Both a Newtonian and non-Newtonian plastico-viscous shear-thinning Casson model (yield stress 5 mPa) is depicted. A significant influence on viscosity at low shear rates is observed for the Casson viscosity.

(volume in the membrane compartment occupied by blood) to the volume of the bed (total volume of the membrane compartment). In the present study, porosity ranges from 0.4 to 0.6 for each fiber bank.

We studied three different fiber bank configurations:

- inline square, IS: $S_T = S_L$
- equilateral triangle, ET: $S_T = 2 \cdot \sqrt{3} \cdot S_L$
- staggered square, SS: $S_T = 2 \cdot S_L$

Figure IV.2 illustrates the three unit fiber cells with a porosity, ε, of 0.50 and diameter, d, of 0.380 mm, a representative size for a polypropylene fiber used in an artificial lung. The flow field is oriented in the x-coordinate direction (Figure IV.1). For symmetry reasons, only the meshed part of the geometry needs to be considered.

IV.3.2 Solving the local flow field

The isothermal flow of a homogeneous viscous liquid is governed by the continuity and Navier-Stokes equations. These equations express the classical principles of conservation of mass:

$$\bar{\nabla} \bullet \bar{\mathbf{u}} = 0 \qquad [169]$$

and conservation of momentum:

$$\rho \bar{\mathbf{u}} \bullet \bar{\nabla} \bar{\mathbf{u}} + \bar{\nabla} p = \bar{\nabla} \bar{\mathbf{t}} \qquad [170]$$

where $\bar{\mathbf{u}}$ is the local mass average fluid velocity vector, ρ represents the local density, p the local pressure, and $\bar{\mathbf{t}}$ the deviatoric stress tensor. $\bar{\nabla}$ is the gradient operator (in two dimensions):

$$\bar{\nabla} = \left(\frac{\partial}{\partial x}, \frac{\partial}{\partial y} \right) \qquad [171]$$

To model the deviatoric stress tensor, it is necessary to add the constitutive equation (expressing rheological properties of the fluid), which has the following form:

$$\bar{\mathbf{t}} = \mu\left(\bar{\nabla} \bar{\mathbf{u}}\right)\left(\bar{\nabla} \bar{\mathbf{u}} + \bar{\nabla} \bar{\mathbf{u}}^{T}\right) \qquad [172]$$

in which μ denotes the dynamic viscosity and superscript T the transpose of the tensor. The choice of $\mu\left(\bar{\nabla} \bar{\mathbf{u}}\right)$ defines the model. We implemented both a Newtonian and non-Newtonian plastico-viscous shear-thinning Casson model <214>. μ is constant for a Newtonian fluid (μ_∞), whereas a Casson type fluid is characterized by the following viscosity model (Figure IV.3):

$$\mu = \mu_\infty \left(1 + \left[\frac{\tau_o}{\mu_\infty} \Pi^{-\frac{1}{2}} \right]^{\frac{1}{2}} \right)^2 \qquad [173]$$

in which τ_o is the yield stress, stress at zero shear rate, and Π denotes the second invariant of the velocity deformation tensor:

$$\Pi = \frac{1}{2} \cdot \bar{\mathbf{A}} : \bar{\mathbf{A}} \qquad [174]$$

with $\bar{\mathbf{A}}$ the velocity deformation tensor:

$$\bar{\mathbf{A}} = \bar{\nabla} \bar{\mathbf{u}} + \bar{\nabla} \bar{\mathbf{u}}^{T} \qquad [175]$$

During cardiopulmonary bypass (temperature = 30 °C and hematocrit = 30 %) density, ρ, and viscosity, μ_∞, are approximately 1052 kg/m³ and 3.02 mPa·s respectively <3>. The yield stress, τ_o, is 5 mPa <214>.

We used the Galerkin finite element methodology <30> to discretize and integrate the flow equations on the computational grid. Numerical simulations were done using the computational

fluid dynamics analysis software SEPRAN (Sepra, Leidschendam, The Netherlands). Treatment of periodic boundary conditions in the context of a finite element procedure is discussed by Segal et al. <41>. The penalty function formulation is used while the resulting system of nonlinear algebraic equations is solved by an iterative Newton linearization <30>.

IV.3.3 Resistance

The membrane compartment of an artificial lung is treated as a porous medium <34>. A modified dimensionless friction factor, f, characterizing the resistance through the fiber bank is defined by:

$$f = \frac{\Delta p}{\rho \cdot U_s^2} \cdot \frac{4 \cdot R_h}{S_L} \qquad [176]$$

in which R_h is the hydraulic radius, a length scale appropriate for internal flow. U_s is the Darcy fluid velocity (or the superficial velocity) <35>, defined as the average velocity in a reference direction of flow that would occur if the fibers were absent. $\Delta p / S_L$ is the pressure gradient in the flow direction. U_s and Δp follow from the numerical flow computation so the resistance can be computed.

The dimensionless characteristic Reynolds number, N_{Re}, determines the relative importance of inertial and viscous effects and is defined as:

$$N_{Re} = \frac{4 \cdot R_h \cdot U_s \cdot \rho}{\mu_\infty} \qquad [177]$$

The Reynolds number characterizes the flow dynamics: at low Reynolds numbers ($N_{Re} < 10$) viscous effects dominate inertia. We will study the variation of the resistance, f, with the Reynolds number. At higher Reynolds numbers, we anticipate recirculation zones distal to fibers and a significant positive influence of this recirculation on resistance. To allow a better assessment of the Reynolds number at which recirculation and consequently the relative importance of viscous effects to inertia becomes important, the relation $\log(f \cdot Re)$ versus $\log(Re)$ is plotted <35>.

IV.3.4 Recirculation

The total blood flow rate per unit fiber length, q, through the fiber bank is calculated with:

$$q = U_s \cdot S_T \qquad [178]$$

The degree of recirculation in a given geometry is quantified as the ratio of the flow rate per unit fiber length in the recirculation zone, q_{rec}, to the total flow rate per unit fiber length, q, in the

Table IV.1: $N_{Re\,c}$ values at a recirculation degree of 1 %.

$N_{Re\,c}$			
ε	**IS**	**SS**	**ET**
0.4	*6.5*	22.1	9.2
0.5	7.5	47.6	14.7
0.6	*9.5*	95.6	25.6

flow domain and can be characterized by a critical Reynolds number, $N_{Re\,c}$. The ratio, q_{rec}/q, was set at 1 % to denote a significant influence of recirculation.

The three different fiber bank configurations are compared for a given superficial velocity and porosity (this implies a constant Reynolds number but a different total flow rate per unit fiber length for each geometry) with respect to blood flow pattern, resistance, and the degree of recirculation, for Reynolds ranging from 1 to 60.

IV.4 Results

Streamline plots for Newtonian blood flow are shown in Figure IV.4 for the inline square (left panel) and for the equilateral triangle (right panel) for a porosity of 0.5 at low (0.13) and high (14.7) Reynolds number. Figure IV.5 plots the modified friction factor, f, multiplied by Reynolds number, N_{Re}, versus Reynolds number on a bilogarithmic scale for the three fiber bank geometries both for Newtonian and non-Newtonian blood flow. The results are compared to published numerical and experimental results <42,43,286-288>. Critical Reynolds numbers, $N_{Re\,c}$, are listed in Table IV.1 for the three different geometries and porosities between 0.4 and 0.6. Normalized velocity profiles, U/U_s, perpendicular to the fiber surface and the blood flow direction, are shown in Figure IV.6 as a function of the dimensionless distance from the fiber surface, ζ (Figure IV.2) at N_{Re} = 0.34 and porosities equal to 0.5 or 0.6 for both Newtonian and non-Newtonian viscosity. U is the length of the velocity vector, $\bar{\mathbf{u}}$

.

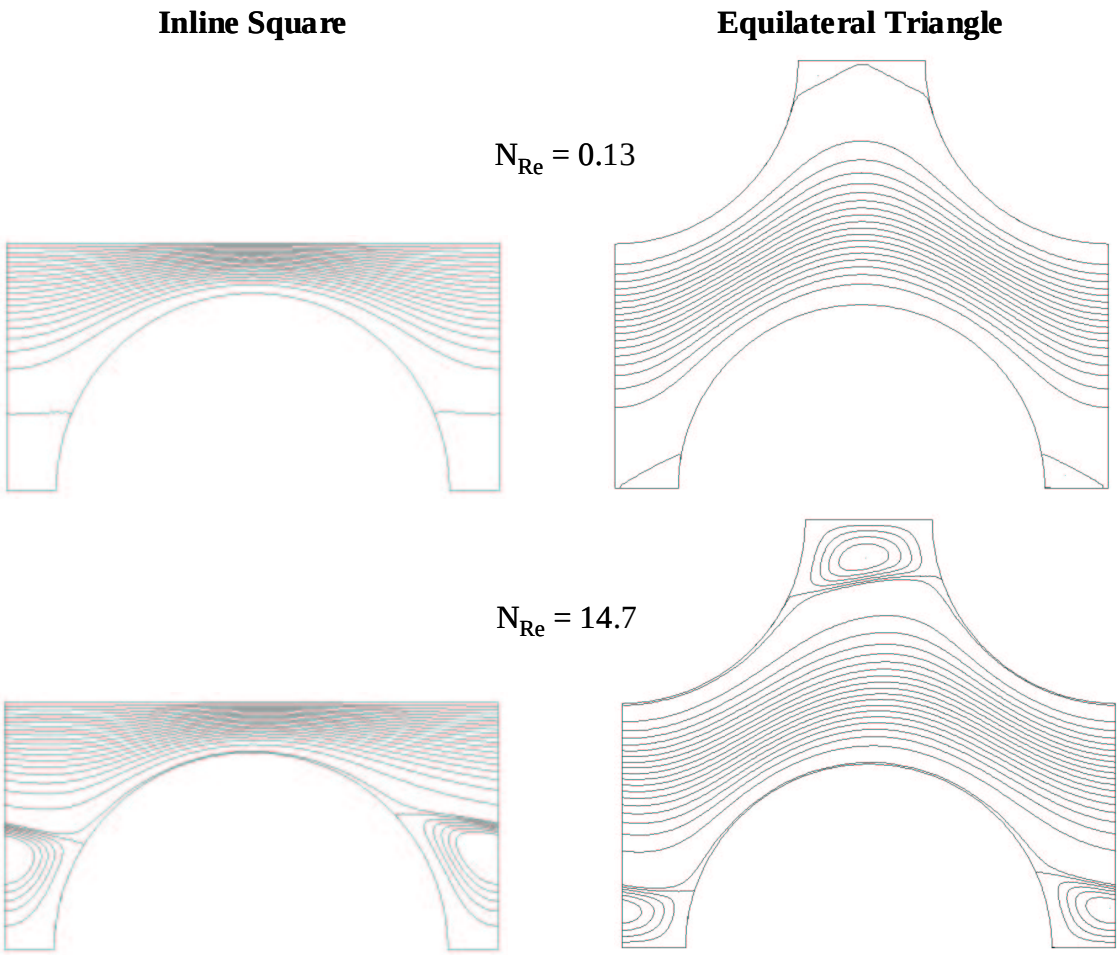

Figure IV.4: Streamline patterns for Newtonian blood flow (temperature = 30 °C and hematocrit = 30 %) at low (N_{Re} = 0.13) and high (N_{Re} = 14.7) Reynolds numbers for inline square and equilateral triangle.

IV.5 Discussion

We aimed to simulate flow conditions as they occur in most available artificial lungs.

Streamlines within a fiber array depend upon Reynolds number and upon its configuration (Figure IV.4 and Figure IV.6). For low N_{Re} (0.13) Stokes flow is obtained without vortex generation distal to the fibers (Figure IV.4, top panel). As the Reynolds number increases, a vortex develops between the fibers (Figure IV.4, lower panel).

The flow path is more tortuous and nonlinear for the equilateral triangle, while a more open, linear flow path and a region with curvilinear streamlines (of which many are closed at high Reynolds numbers) exist for the inline square. A decrease in porosity enhances the tortuosity of the flow path in a triangular array. The streamlines become closer to the front part of the cylinder before being deflected sideways, resulting in higher velocity gradients and consequently higher

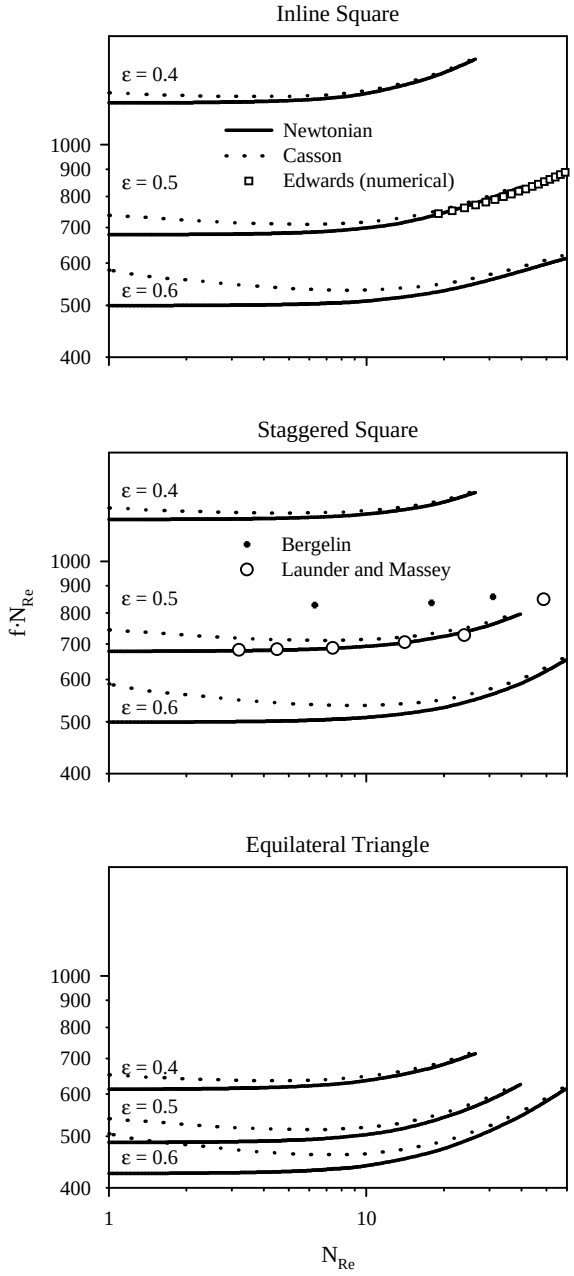

Figure IV.5: Modified friction factor, f, multiplied by Reynolds number, N_{Re}, versus N_{Re} on a bilogarithmic scale for the three fiber bank geometries both for a Newtonian and non-Newtonian blood flow. The results are compared to published numerical and experimental results <42,43,286-288>.

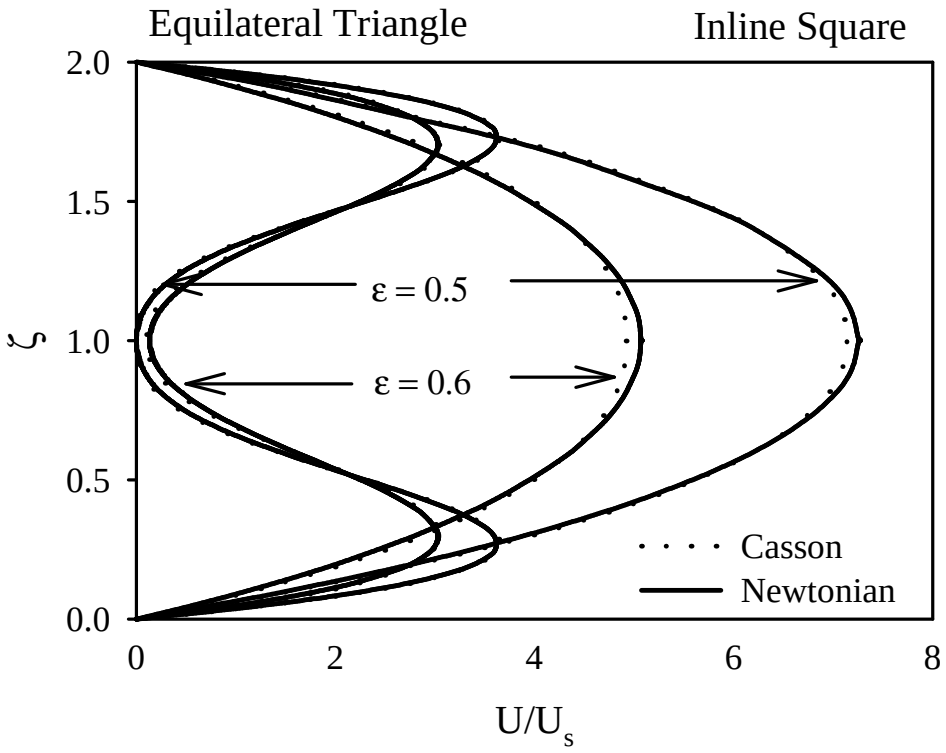

Figure IV.6: Normalized velocity profile at N_{Re} = 0.34 for inline square and equilateral triangle at porosities of 0.4 and 0.5 both for Newtonian and Casson viscosity model.

resistance (Figure IV.5). Note that the fibers are in a dead zone downstream of the preceding fiber's wake (Figure IV.4).

Figure IV.5 shows that there is a good agreement between our data and the numerical data of Edwards <42> and Launder et al. <43> The experimental data of Bergelin et al. <286-288> are approximately within 10 % of our simulations for the entire Reynolds number range studied. Our data underestimate the experimental data, due to the fact that the experimental data include the entrance and end effects since the pressure drop was estimated with static pressure taps upstream and downstream of the bank. The numerical procedure thus yields realistic data on the studied range of Reynolds numbers.

At specific Reynolds numbers and porosities, the equilateral triangle causes less resistance than the staggered square, the latter being comparable to the inline square (Figure IV.5). Friction increases with a lower porosity. The point at which the $\log(f \cdot Re)$ relation deviates from linearity at higher Reynolds numbers, is assumed to denote the end of creeping flow with no separation on the one hand (viscous effects) and a significant influence of the separation zone on

resistance on the other hand (inertia). For an equilateral triangle with a porosity of 0.50, separation is observed at $N_{Re\ c} = 9.2$ over a small area on the rear of the fiber. The vortex area increases with Reynolds number.

Resistance is a function of porosity, Reynolds number, and viscosity (Figure IV.5). The effect of viscosity is most pronounced at low Reynolds numbers. For the shear-thinning Casson viscosity model, a decrease in velocity gradients and shear rates is observed at low Reynolds numbers, resulting in a higher local fluid viscosity. This higher viscosity causes the resistance to increase. At high Reynolds numbers, no difference is observed between Newtonian and non-Newtonian blood flow due to the higher shear rates. The non-Newtonian viscosity model has only a minor influence on the velocity profile at low Reynolds numbers ($N_{Re} < 0.5$) (Figure IV.6), while the effect on resistance is maintained at higher Reynolds numbers ($N_{Re} < 10$) (Figure IV.5). The effect is somewhat elevated at higher porosities ($\varepsilon > 0.5$) for a given Reynolds number (lower shear rates).

The microporous polypropylene fibers in a hollow fiber membrane artificial lung with 200-280 µm internal diameter and 25-50 µm wall thickness are wound as a bundle with blood flow exterior to the fibers (extraluminal blood flow). In coiled construction designs, which are the most common, the blood flow path is predominantly perpendicular to the bundle <279>. These orientations are employed in many currently available hollow fiber artificial lungs (Sarns Turbo 440, Cobe Optima, Dideco Compactflo,...) <199>. For a blood flow rate of 5 l/min, the Reynolds number lies between 2.1 and 3.3 for whole blood in most hollow fiber artificial lungs ($0.4 < \varepsilon < 0.6$).

Nevertheless, we idealized inflow conditions as well as the fiber bank geometries. In practice, there may be a deviation from normal incidence of the fluid. Moreover, fiber banks seldom extend to the wall of the housing and alternate fibers are missing near the housing's surface. Near the surface, the velocity may be higher due to decreased friction. In practice, a mixture of different fiber bank geometries may be the case.

In conclusion, we have presented a computational two-dimensional model for blood flow around hollow fibers. The flow field and derived parameters (pattern, friction, and recirculation) are significantly different for the different fiber banks and porosities. Overall, a higher Reynolds number and a lower porosity increase the resistance in the fiber bank. A better mixing may be achieved by increasing the superficial blood velocity (i.e. a higher blood flow rate in a given fiber bank geometry or a smaller cross-sectional area at a given blood flow rate). Considering the non-Newtonian character of blood, we found higher resistance for a given fiber bank at lower

Reynolds numbers only. At high Reynolds numbers, no difference is observed with Newtonian fluid flow.

The model is suited for design optimization of hollow fiber blood-gas exchange devices with an extraluminal blood path. Further studies should be oriented towards blood flow and mass transfer in order to optimize fiber bank design.

IV.6 Acknowledgements

This research is funded by a specialization grant of the Flemish Institute for the Promotion of the Scientific-Technological Research in Industry (IWT-961181). The authors would like to thank P. Segers for reading the manuscript.

V MASS TRANSFER CHARACTERISTICS OF ARTIFICIAL LUNGS

V.1 Abstract[†]

An artificial lung is used during cardiopulmonary bypass to oxygenate blood and to control the blood temperature. The oxygen transfer rate-flow rate characteristics of three hollow fiber membrane artificial lungs (Sarns Turbo 440, Cobe Optima, Dideco Compactflo) are determined *in vitro* to characterize design features. Results are presented as a unique dimensionless relationship between Sherwood number, N_{Sh} (ratio of convective to diffusive mass transfer), Schmidt number, N_{Sc} (ratio of momentum to diffusive transport), and Reynolds number, N_{Re} (ratio of inertial to viscous forces). This relationship is a function of the device porosity, ε, and characteristic device length, ξ, defined as the ratio of the mean blood path and manifold length:

$$\frac{N_{Sh}}{N_{Sc}^{1/3}} \cdot \xi^{1/2} = \varphi \cdot \left(\varepsilon^{1/m} \cdot N_{Re}\right)^{m}$$

where $\varphi = 0.26$ and $m = 1.00$ for $N_{Pe} < 3200$ and $\varphi = 0.47$ and $m = 0.64$ for $N_{Pe} > 3200$ where N_{Pe} is the dimensionless Péclet number defined as $N_{Re} \cdot N_{Sc}$. We found a good correspondence between the model predictions and *in vitro* blood oxygen transfer rates. We conclude that this dimensionless approach allows us

- to compare artificial lungs independently.
- to relate water tests to blood.
- to predict the oxygen transfer rate of a new design of an artificial lung.

[†] The contents of this chapter are accepted for publication in the *ASAIO Journal*:

Mass transfer characteristics of artificial lungs

P.W. Dierickx, D.S. De Wachter, F. De Somer, G. Van Nooten, and P.R. Verdonck

V.2 Introduction

An artificial lung is used during cardiopulmonary bypass to oxygenate blood and to control the blood temperature. Oxygen transfer rate, $\dot{V}_{O_2}$, can be monitored by measuring flow rate, Q, in combination with inlet and outlet oxygen partial pressure, P_{O_2}, and is related to the geometry of and the way the fluid flows (flow pattern) through the membrane artificial lung. Nevertheless, few attempts have been done to characterize mass transfer in relation to the geometry and flow pattern of an artificial lung <3,4,48,271>. In this study, we propose a unique dimensionless relationship for oxygen mass transfer rate and flow rate in the membrane compartment of an artificial lung as a function of geometry and flow pattern that could facilitate the design of new devices. We therefore first assessed the general dimensionless relationships based on water experiments for three different types of artificial lungs (Sarns Turbo 440, Cobe Optima, and Dideco Compactflo) and derived a unique relationship based on geometry and flow pattern. Secondly, we predicted what could be the oxygen transfer rate for these artificial lungs using blood for liquid and compared these predicted values to actual experimental measurements.

V.3 Materials and methods

V.3.1 Dimensional analysis

An artificial lung can be characterized by different geometric parameters: membrane surface area, A; diameter of the fiber, d; length of the fiber compartment; L; inside housing outer diameter, D_i; outside housing inner diameter, D_o; and gross frontal area of the blood path, A_f. The "void fraction" or device porosity, ε, is defined as the ratio of the volume of voids (volume in the membrane compartment occupied by blood) to the volume of the bed (total volume of the membrane compartment). A characteristic length for flow through porous beds or packed fiber bundles, is hydraulic radius, R_h. Hydraulic radius is expressed in terms of device porosity, ε, and wetted surface per unit volume of bed, a <35,276>:

$$R_h = \frac{\left(\frac{\text{volume of voids}}{\text{volume of bed}}\right)}{\left(\frac{\text{wetted surface}}{\text{volume of bed}}\right)} = \frac{\varepsilon}{a} \qquad [179]$$

Manifold length, L_m, is defined as the length by which the total artificial lung flow is divided per unit width of fiber stack. Mean blood path length, L_b, is the average distance blood has to travel through the fiber stack. Consequently, a dimensionless characteristic device length, ξ, can be

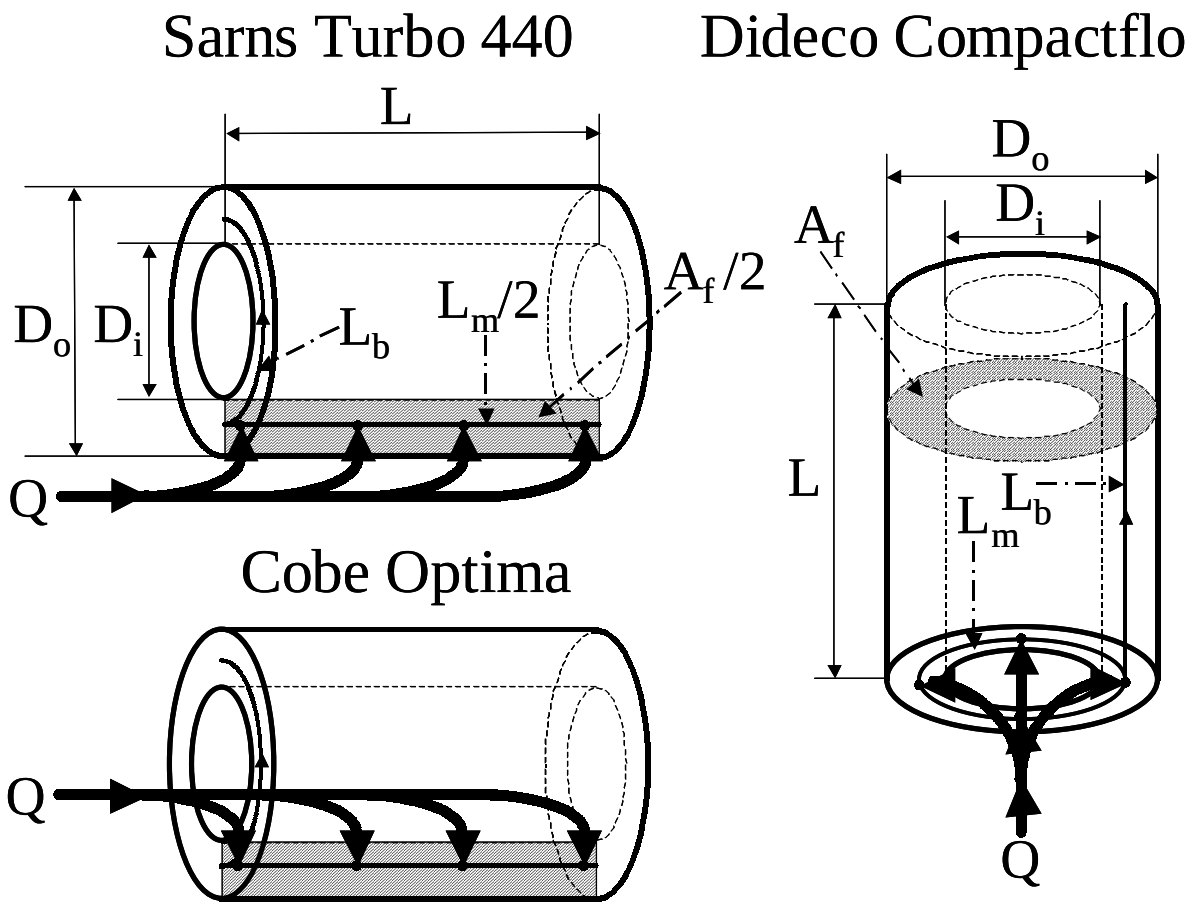

Figure V.1: Geometric characteristics of artificial lungs; **Top left panel**: Sarns Turbo 440; **Bottom left panel**: Cobe Optima; **Right panel:** Dideco Compactflo.

defined as ratio of mean blood path length, L_b, and average manifold length, L_m. We assume that blood is uniformly distributed over the fiber stack. In Sarns Turbo 440 (3M, Michigan, USA) and Optima (Cobe, Arvada, USA) membrane artificial lungs, L_m and L_b are determined as shown in Figure V.1 (left panel). Blood enters the membrane evenly distributed over the length, L, of the manifold and the blood flow is split in two, for left and right sides. Blood flow rate per unit membrane width, Q´, is:

$$Q' = \frac{Q}{L_m} = \frac{Q}{2 \cdot L} \qquad [180]$$

Mean blood path length is:

$$L_b = \frac{\pi}{2} \cdot \left(\frac{D_i + D_o}{2} \right) \qquad [181]$$

In the Dideco Compactflo (Dideco, Miranda, Italy), blood flow enters the fiber stack circumferentially (Figure V.1, right panel). Manifold length is:

$$L_m = \pi \cdot \left(\frac{D_i + D_o}{2} \right) \quad [182]$$

whereas mean blood path length is determined as:

$$L_b = L \quad [183]$$

It was earlier shown that mass transfer in hollow fiber membrane artificial lungs could be described by a semi-empirical mathematical model of convective oxygen transfer <3,4>:

$$\frac{N_{Sh}}{N_{Sc}^{1/3}} = \varphi' \cdot N_{Re}^{m'} \quad [184]$$

The Reynolds number, N_{Re}, is defined as the ratio of inertial to viscous forces. Characteristic length in N_{Re} for flow through a fiber stack is hydraulic diameter, $4 \cdot R_h$. Consequently, The Reynolds number is defined as:

$$N_{Re} = \frac{Q}{A_f \cdot \varepsilon} \cdot \frac{4 \cdot R_h \cdot \rho}{\mu} \quad [185]$$

in which ρ represents density and μ the dynamic viscosity of the fluid.

The Schmidt number, N_{Sc}, is defined as the ratio of momentum to diffusive transport and characterizes the fluid:

$$N_{Sc} = \frac{\mu}{\rho \cdot D_{O_2}} \quad [186]$$

in which D_{O_2} is the oxygen diffusivity.

The Sherwood number, N_{Sh}, characterizes the efficiency of mass transfer and is defined as the ratio of convective to diffusive mass transfer:

$$N_{Sh} = \frac{K \cdot 4 \cdot R_h}{D_{O_2}} \quad [187]$$

The overall mass transfer coefficient, K, is a measure of the efficiency of mass transfer and is defined as the oxygen transfer rate, $\dot{V}_{O_2}$, per unit surface area and per unit driving force of concentration difference for oxygen transfer $\left(\alpha_{O_2} \cdot \left(\Delta P_{O_2}\right)_{lm}\right)$ in a non-reactive fluid <35>:

$$K = \frac{\dot{V}_{O_2}}{A \cdot \alpha_{O_2} \cdot \left(\Delta P_{O_2}\right)_{lm}} \quad [188]$$

The oxygen transfer rate in a non-reactive fluid is defined as:

$$\dot{V}_{O_2} = \alpha_{O_2} \cdot \left(P_{O_2\,out} - P_{O_2\,in}\right) \cdot Q \quad [189]$$

where α_{O_2} is the oxygen solubility and $P_{O_2\,in}$ and $P_{O_2\,out}$ are inlet and outlet oxygen partial pressures, respectively.

Another dimensionless number characterizing convective mass transfer is the Péclet number, N_{Pe}:

$$N_{Pe} = N_{Re} \cdot N_{Sc} \qquad [190]$$

The parameters φ´ and m´ in Eq. [184] characterize the porous medium and therefore depend on the properties of the medium rather than on universal constants. It is assumed that the medium is mainly characterized by the device porosity, ε, and the dimensionless characteristic device length, ξ <34>. The functional form of φ´ and m´ is represented as a power function:

$$\varphi' = \varphi \cdot \varepsilon^{p'} \cdot \xi^{q'}$$
$$m' = m \cdot \varepsilon^{r'} \cdot \xi^{s'} \qquad [191]$$

in which φ, m, p', q', r' and s' are constants which may be determined by nonlinear regression analysis from experimental data. The relationship between N_{Sh}, $N_{Sc,}$ and N_{Re} is therefore solely determined by the flow pattern in the artificial lung and its geometry.

V.3.2 Methods

Oxygen transfer rate-flow rate characteristics of three different hollow fiber membrane artificial lungs (Sarns Turbo 440 (N = 2), Cobe Optima (N = 2), Dideco Compactflo (N = 2)) are measured *in vitro* and analyzed to characterize design features. Table V.1 summarizes the inlet conditions for the *in vitro* experiments.

Table V.1: Inlet conditions for the *in vitro* experiments.

	water experiments	***blood experiments***
temperature [°C]	20.6 ± 0.7	36.7 ± 0.8
barometric pressure [mmHg]	[754.6; 772.4]	[754.8; 767.6]
flow rate, Q [l / min]	[0.5; 6.0]	1.0 – 3.0 –5.0
pH		7.34 ± 0.05
carbon dioxide partial pressure, P_{CO_2} **[mmHg]**		41.1 ± 3.3
inlet oxygen partial pressure, $P_{O_2 in}$ **[mmHg]**	25.1 ± 2.0	
		42 ± 3
inlet oxygen saturation, $S_{O_2 in}$ **[%]**		64 ± 2
		80 ± 3
hematocrit, Hct [%]		34.9 ± 1.3

Oxygenation experiments were first performed with water to obtain the N_{Sh}-N_{Sc}-N_{Re} relationship and were subsequently applied for the prediction of oxygen transfer to blood. The predicted performance is then compared against that obtained from blood experiments.

V.3.3 Experimental setup: water tests

25 liter of nitrogen-equilibrated, distilled water at room temperature (T = 20.6 ± 0.7 °C) is pumped single-pass from an upstream feed reservoir (reservoir 1) through the test-artificial lung and discharged into a downstream collection reservoir (reservoir 2) (Figure V.2). Air from a compressed air supply (20.9 % O_2) is passed through a rotameter and manifolded into the gas compartment of the artificial lung. Water temperature is measured by a thermometer in the upstream and downstream reservoir. Water samples are taken at the inlet and outlet of the artificial lung and analyzed with a 288 blood gas analyzer (Bayer, Brussels, Belgium). Barometric pressure varied from 754.6 mmHg to 772.4 mmHg. The water is deoxygenated using 100 % nitrogen as the ventilating gas during the recirculation phase in a conditioning circuit containing two artificial lungs. The testing phase started once the desired inlet conditions after recirculation for deoxygenation were reached. One experiment comprehended the assessment of the oxygen transfer rate at nine different water flow rates ranging from 0.5 l/min to 6.0 l/min. Gas to water flow rate ratio was 3:1. For each artificial lung, three experiments were carried out. Before the onset of each experiment, the roller pump was calibrated volumetrically and several

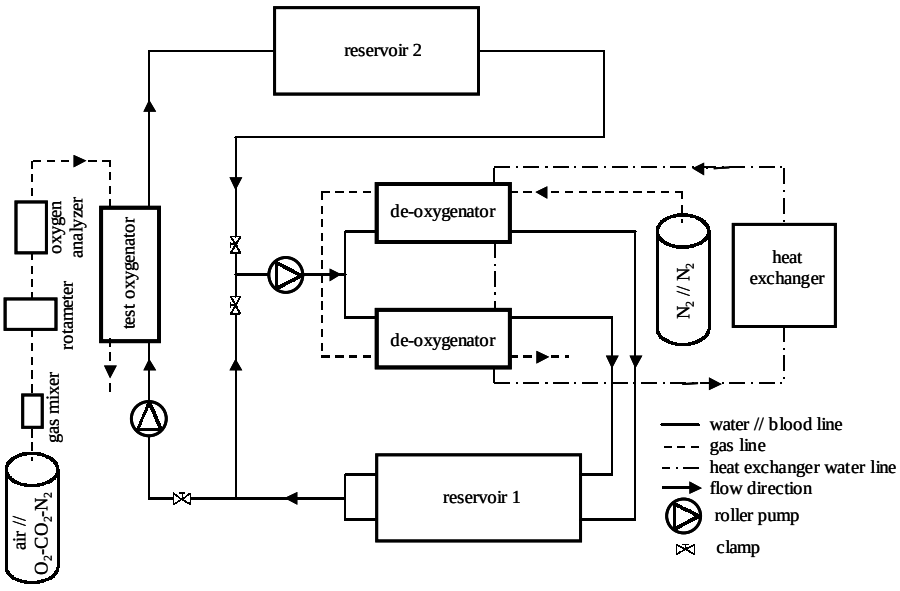

Figure V.2: Experimental circuit for the *in vitro* evaluation of the artificial lungs.

quality controls for the gas analyzer were carried out.

V.3.4 Experimental setup: blood tests

Details of the theory to calculate oxygen transfer for blood with the semi-empirical model for convective oxygen transfer have been described by others <3,4,271>. The outlet blood oxygen partial pressure, $P_{O_2\,out}$, is calculated for blood flow rates from 1.0 to 6.0 l/min. Measured and predicted oxygen transfer rates are calculated from inlet and outlet and the oxyhemoglobin dissociation relationship:

$$\dot{V}_{O_2} = \alpha_{O_2} \cdot Q \cdot \left(P_{O_2\,out} - P_{O_2\,in}\right) + 1.34 \cdot C_{Hb} \cdot Q \cdot \left(S_{O_2 out} - S_{O_2 in}\right) \qquad [192]$$

in which 1.34 denotes the binding capacity [ml/g] of oxygen to hemoglobin, Hb, and C_{Hb} the hemoglobin concentration. The oxygen saturation, S_{O_2}, is calculated from P_{O_2} using Hill's equation describing the oxyhemoglobin dissociation curve <25>. The indices in and out denote the inlet and outlet of the artificial lung, respectively.

The experimental perfusion circuit and methods for the *in vitro* blood test are the same as for the water tests. Approximately 25 liters of fresh, filtered bovine blood are anticoagulated with heparin (5000 IU/l) and citrate (100 ml/l). Before starting the experiment, blood gas values and acid base state of the blood was normalized to physiologic values. Deoxygenation of the blood was achieved by recirculation over two oxygenators fed with nitrogen. Once the desired inlet conditions were obtained, the experiment was started.

Three different inlet oxygen saturations, $S_{O_2 in}$ (42 ± 3 %, 64 ± 2 %, and 80 ± 3 %) are tested at three different blood flow rates (1.0, 3.0 and 5.0 l/min) and with a hematocrit, Hct, of 34.9 ± 1.3 %. Hemodilution is accomplished by adding 0.9 % sodium chloride to the blood.

Triplicate venous and arterial samples are taken at the artificial lung inlet and outlet, respectively, at each of the three blood flow rates. The ventilating gas through the test-artificial lung consists of pure oxygen. An in-line oxygen saturation monitor (Baxter, Brussels, Belgium) is used to measure the inlet saturation. All samples are analyzed using a 288 blood gas analyzer (Bayer, Brussels, Belgium). Experiments with $S_{O_2 in}$ = 64 ± 2 % meet the AAMI standard conditions <45>. Blood oxygen transfer rate is determined according to Eq. [192].

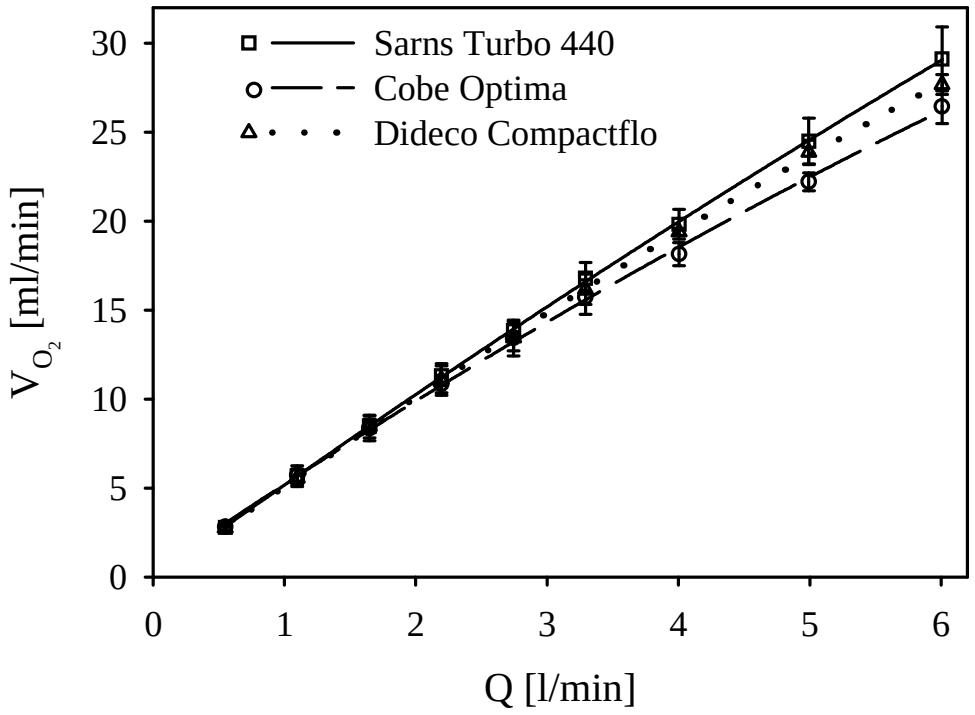

Figure V.3: Oxygen transfer rate ($\dot{V}_{O_2}$)-flow rate (Q) characteristics in water for the three artificial lungs: Sarns Turbo 440, Cobe Optima, and Dideco Compactflo.

V.3.5 Statistical analysis

Fitting of the semi-empirical dimensionless N_{Sh}-N_{Sc}-N_{Re} relationship is performed using the nonlinear regression Marquardt-Levenberg algorithm (Sigmastat 2.0, SPSS, Chicago, USA). Results are presented with twice the standard deviation and coefficient of determination R^2 for non-linear regression.

V.4 Results

Figure V.3 presents the oxygen transfer rate versus flow rate in water for the three different artificial lungs (Eq. [189]). The corresponding semi-empirical relationship for water oxygen mass transfer is depicted on a bilogarithmic plot in Figure V.4. Two distinct regions with respect to Reynolds number ($N_{Re} < 6.5$ and $N_{Re} > 6.5$) for the water experiments can be observed for the three artificial lungs. This Reynolds number, multiplied with the Schmidt number for water ($N_{Sc} = 492$), corresponds with a Péclet number of 3200, yielding a criterion for the semi-empirical model independent of fluid characteristics. The semi-empirical model (Eq. [184]) is valid in both regions. A least squares fit through the water data for each artificial lung yields values for the φ' and the slope m', both for $N_{Pe} < 3200$ and $N_{Pe} > 3200$ (Table V.2).

Included are geometrical data of the different artificial lungs for device porosity, ε, and dimensionless characteristic device length, ξ, which exhibit a similar trend as φ': φ' increases with ε and decreases with ξ, while m' is more or less constant [48,289]. Based on this finding, we can now determine the functions of Eq. [191] which gave φ' and m' as a function of ε and ξ. The results of the nonlinear regression are listed in the last column of Table V.1 and depicted in Figure V.5 leading to the following relation for φ' and m':

Table V.2: Geometric characteristics of artificial lungs, including the model parameters φ', m', φ, and m.

		Sarns Turbo 440	***Cobe Optima***	***Dideco Compactflo***	***model data***	
membrane surface area, A [m²]		1.6	1.7	2		
fiber diameter, d [µm]		380	380	380		
inside core outer diameter, D_i [cm]		5.0	4.4	5.0		
outside core inner diameter, D_o [cm]		7.0	7.3	7.8		
length fiber compartment, L [cm]		20.5	12.4	12		
device porosity, ε		0.61	0.51	0.44		
characteristic device length, ξ		0.23	0.37	0.60		
$N_{Pe} < 3200$	**φ'**	0.35	0.19	0.13	**φ**	0.26
	R^2	0.66	0.62	0.96		
$N_{Pe} > 3200$	**φ'**	0.60	0.38	0.27	**φ**	0.47
	m'	0.69	0.60	0.63	**m**	0.64
	R^2	0.84	0.95	0.97		

$$\varphi' = \varphi \cdot \frac{\varepsilon}{\xi^{1/2}} \qquad [193]$$

$$m' = m$$

with $\varphi = 0.26$ and $m = 1.00$ for $N_{Pe} < 3200$ and $\varphi = 0.47$ and $m = 0.64$ for $N_{Pe} > 3200$.

Substitution of Eq. [193] in Eq. [184] and rearranging the equation, yields the following dimensionless relationship for convective oxygen transfer as a function of geometry and flow pattern (Figure V.6):

$$\frac{N_{Sh}}{N_{Sc}^{1/3}} \cdot \xi^{1/2} = \varphi \cdot \left(\varepsilon^{1/m} \cdot N_{Re}\right)^m \qquad [194]$$

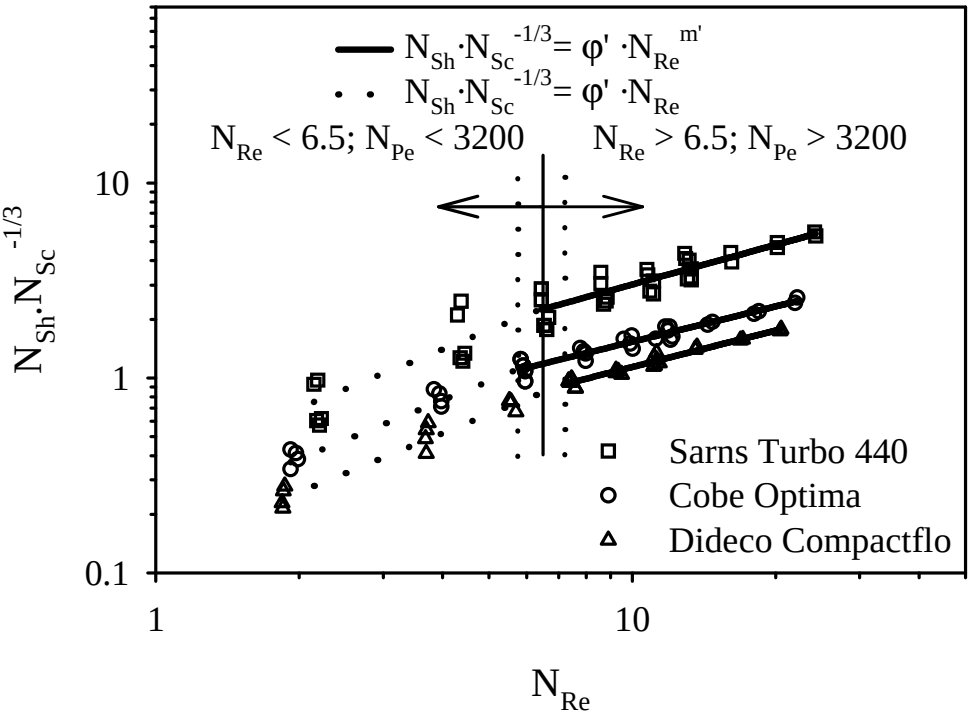

Figure V.4: The semi-empirical N_{Sh}-N_{Sc}-N_{Re} relationship for water convective oxygen mass transfer on a bilogarithmic plot. Two distinct regions with respect to the Reynolds, N_{Re}, and Péclet number, N_{Pe}, can be observed for the oxygen mass transfer in water: $N_{Re} < 6.5$ ($N_{Pe} < 3200$) and $N_{Re} > 6.5$ ($N_{Pe} > 3200$).

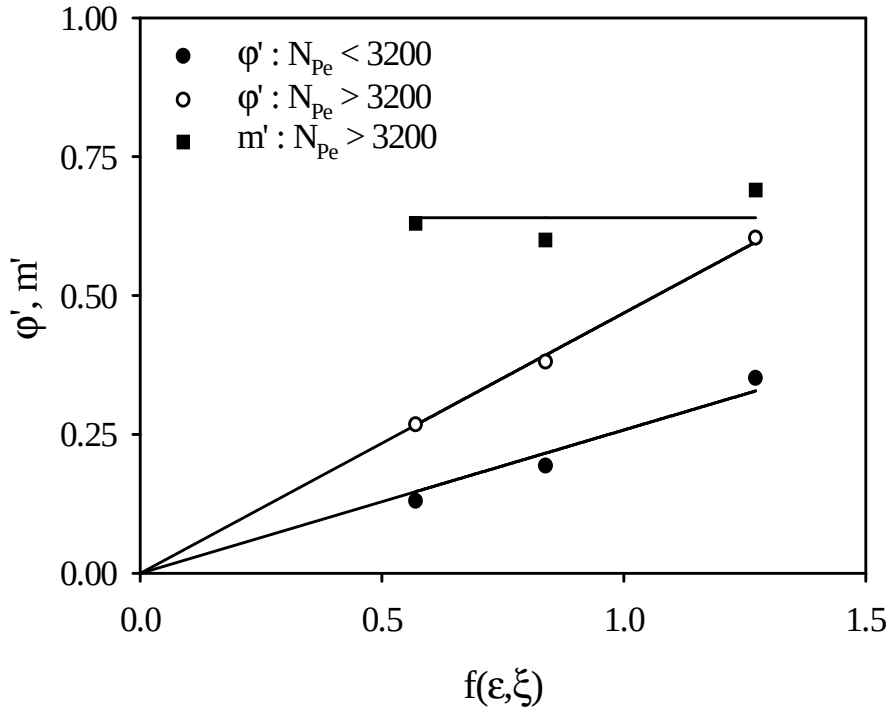

Figure V.5: Dependency of φ' and m' on ε and ξ as a function of N_{Pe}.

with φ = 0.26 and m = 1.00 for N_{Pe} < 3200 and φ = 0.47 and m = 0.64 for N_{Pe} > 3200.

The oxygen transfer rate versus flow rate in blood for three different inlet saturations (40 %, 65 %, 80 %) is presented in Figure V.7. Figure V.7 shows the original oxygen transfer rate-flow rate blood data for the three artificial lungs, along with the predicted oxygen transfer rate-flow rate relationship obtained by converting the dimensionless fit from Eq. [194] and Figure V.6 back to dimensional form for blood at the same conditions as in our experiments. Comparison of predicted values of oxygen transfer rate with blood oxygen transfer experiments for all artificial lungs is shown in Figure V.8.

V.5 Discussion

In this study, we propose a unique dimensionless relationship that allows us

- to compare artificial lungs independently.
- to relate water tests to blood.
- to predict the oxygen transfer rate of a new design of an artificial lung.

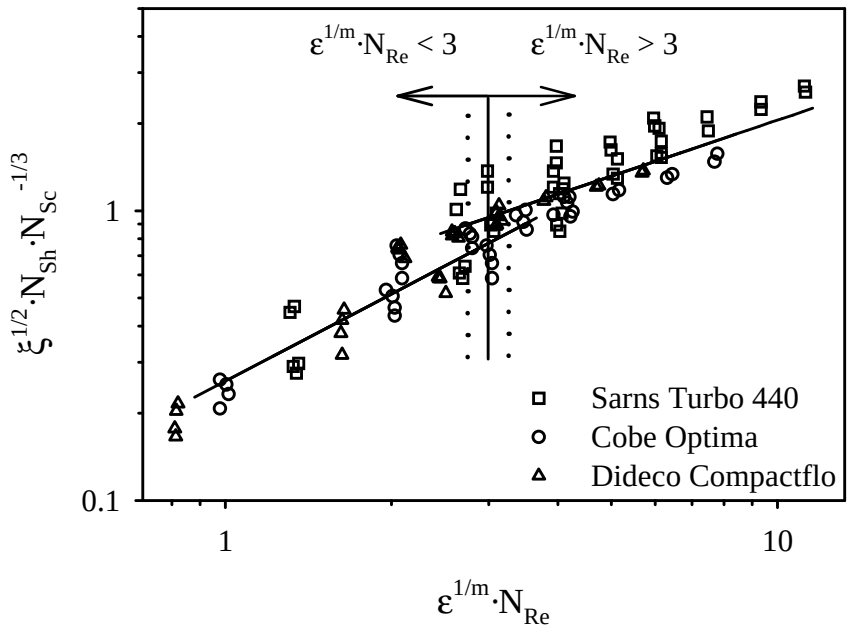

Figure V.6: A unique dimensionless relationship for convective oxygen transfer as a function of Sherwood number, N_{Sh}, Schmidt number, N_{Sc}, Reynolds number, N_{Re}, device porosity, ε, and dimensionless characteristic device length, ξ, on a bilogarithmic plot.

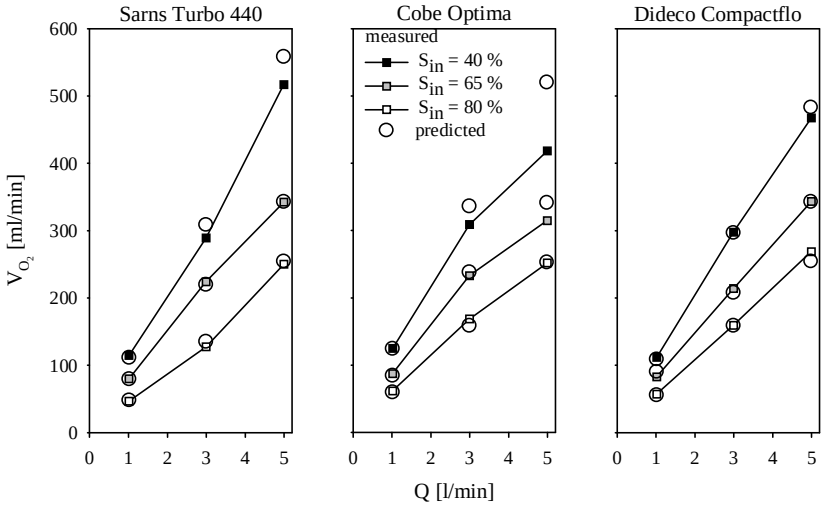

Figure V.7: Original oxygen transfer rate ($\dot{V}_{O_2}$)-flow rate (Q) blood data along with the predicted oxygen transfer rate-flow rate characteristics at three different inlet saturations (40 %, 65 %, 80 %) for the three artificial lungs (Sarns Turbo 440, Cobe Optima, Dideco Compactflo) obtained by converting the dimensionless fit (Eq. [194]) back to dimensional form.

Figure V.3 only shows a major difference in oxygen transfer rate versus flow rate for the three artificial lungs at higher flow rates (Q > 3.5 l/min). The oxygen transfer rate versus flow rate can be translated into a semi-empirical dimensionless relationship describing convective oxygen transfer (Eq. [184]).

The importance of a given mass transfer efficiency and flow characteristic in an artificial lung has already been extensively emphasized <3,37,48,271,290>. In the past, however, few attempts have been made to characterize mass transfer including geometry and flow pattern of an artificial lung. It has already been demonstrated that the pressure drop across a membrane compartment can be predicted using a dimensionless relationship between Euler (characterizing pressure drop) and Reynolds number as a function of two dimensionless characteristic geometrical parameters: device porosity, ε, and a dimensionless characteristic device length, ξ <34>.

Likewise, mass transfer can be studied by translating the oxygen transfer rate versus flow rate into a semi-empirical dimensionless relationship describing convective oxygen transfer as a

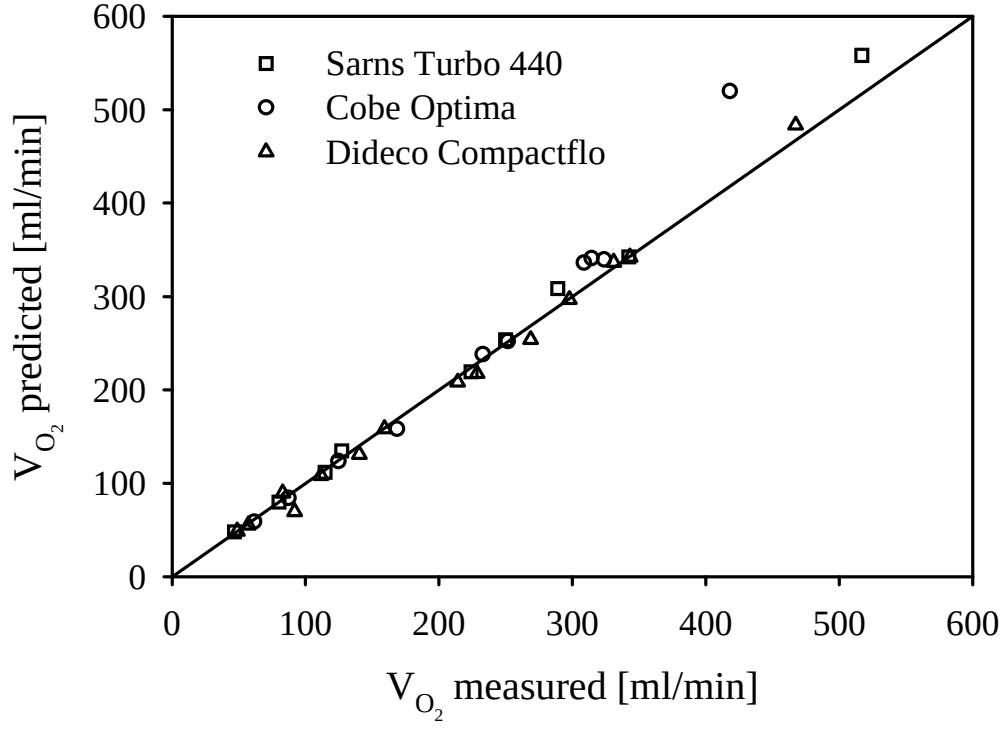

Figure V.8: Correlation of predicted and measured blood oxygen transfer rates for the three artificial lungs. Linear regression of predicted on measured values is (R^2 = 0.99): $\dot{V}_{O_2 predicted} = 1.01 \cdot \dot{V}_{O_2 measured} - 15.13$

function of Sherwood, Schmidt and Reynolds number. Vaslef et al. <4> state that this semi-empirical relationship depends on fiber orientation, porosity, and efficiency of the device.

We demonstrate a unique dimensionless relationship describing convective oxygen transfer as a function of two dimensionless characteristic geometrical parameters: device porosity, ε, and device length, ξ (Eq. [194] and Figure V.6).

Figure V.4 shows two distinct regions with respect to the Reynolds number for water experiments (and thus the Péclet number for any fluid) for the three artificial lungs indicating that φ' and m' in Eq. [184] depend on the efficiency of the device <4,289>. This discontinuity is reflected in the coefficients given in Table V.2. At low Reynolds and Péclet numbers, a near linear relationship with Reynolds number for water (Figure V.4) can be observed. The Sherwood numbers at low flow rates are below the regression line obtained using the data at high flow rates. This may be explained by the somewhat polydisperse channels between fibers, which cause uneven flows and lead to reduced mass transfer coefficients <48>. At low Reynolds and Péclet numbers, one can thus expect an increased degree of shunting and consequently a decreased influence of convection on mass transfer than is observed at higher Reynolds numbers.

Figure V.6 is a device specific scaling of Figure V.6 resulting in one curve representing the three artificial lungs. Our relationship (Eq. [194]) indicates that mass transfer is directly related to

- the blood path length.
- the manifold length.
- the flow pattern.
- the Reynolds number.

The dimensionless approach is independent of fluid physical properties: density, viscosity, oxygen solubility, and diffusivity. It enables one to relate water tests to blood, sharing the benefits of using dimensionless numbers, as discussed by Mockros et al. <3> and Vaslef et al. <4>. There is no need to rescale the graphs for blood although the measurements were performed with water. This is of great advantage when hemodilution and hypothermia are present, because they alter the physical constants and therefore the mass transfer.

In Figure V.7 a comparison is made with respect to blood oxygen transfer rate between our measurements and technical data for the Sarns Turbo 440 according to the AAMI standards <291>. It shows a good agreement (< 7 %) between our oxygen transfer rate measurements and the literature data.

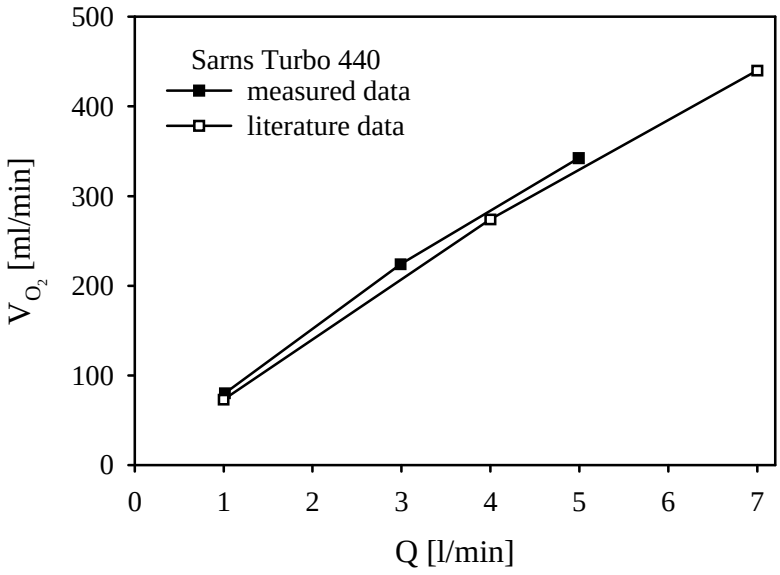

Figure V.9: Comparison between our measurements and technical data according to the AAMI standards with respect to the oxygen transfer rate ($\dot{V}_{O_2}$)-flow rate (Q) relationship in blood.

Blood oxygen mass transfer can then be calculated using the corresponding Sherwood and Schmidt number and dimensionless geometrical parameters. The good agreement between the model predictions and experimental blood oxygen transfer rate in Figure V.8 demonstrates the validity of using φ and m values derived from the *in vitro* oxygen-water experiments and the geometry of the device.

Using the proposed dimensionless format, one can

- compare artificial lungs independently
- relate water tests to blood tests
- predict the oxygen transfer rate of a new design of an artificial lung.

We believe that this dimensionless analysis is an excellent tool for the development of better designs.

V.6 Conclusion

We have demonstrated that mass transfer can be studied using a dimensionless relationship between Sherwood, Schmidt and Reynolds number as a function of two dimensionless characteristic geometrical parameters: device porosity, ε, and a newly defined dimensionless characteristic device length, ξ.

V.7 Acknowledgements

This research is funded by a grant of the Flemish Institute for the Promotion of the Scientific-Technological Research in Industry (IWT961181). The authors like to express their gratitude to Gerd De Cock and Tom Serroels for helping with the measurements and Patrick Segers for reading the manuscript.

VI TWO-DIMENSIONAL FINITE ELEMENT MODEL FOR OXYGEN TRANSFER IN CROSS-FLOW HOLLOW FIBER MEMBRANE ARTIFICIAL LUNGS

VI.1 Abstract[†]

A predictive, two-dimensional model with good absolute accuracy for flow and mass transfer in cross-flow hollow fiber membrane artificial lungs is developed. The proposed model is able to predict the gas transfer to water flowing outside and perpendicular to hollow fibers in the artificial lung. The model uses a finite element technique to solve the Navier-Stokes equations and the convection-diffusion equation on the computational domain of a unit fiber cell. Subsequent stream-wise and cross-wise unit fiber cells are then coupled/assembled to the relationship between the oxygen transfer rate and flow rate of a cross-flow hollow fiber membrane artificial lung. The model is compared to water experimental data obtained by perfusing three commercial artificial lungs with water.

VI.2 Introduction

An artificial lung is used during cardiopulmonary bypass to oxygenate blood and to control blood temperature. Many of the oxygenation systems (capillary membrane, coiled tube, membrane-lined capillary channels, spiral, cross-flow hollow fiber, etc.) have been developed (1960s – 1970s –1980s – 1990s) on empirical grounds <44>. Applicable theories would greatly

[†] The contents of this chapter is submitted to *The International Journal of Artificial Organs*:

Two-dimensional finite element model

for oxygen transfer in cross-flow hollow fiber membrane artificial lungs

P.W. Dierickx, D.S. De Wachter, and P.R. Verdonck

enhance clinical progress by insuring maximum transfer efficiency and safety which are important design factors in e.g. long-term perfusion.

The design of an optimal system demands an experimental and a mathematical (analytical or numerical) approach. The analytical and the numerical approach aim to derive a model of the system using basic mathematical equations to describe the physical laws such as the conservation of mass and momentum, and to describe the causal relationships between its component parts. Prototypes, designed based on extensive analytical investigation, are frequently optimally designed. The only experimental results needed are those required to validate the model.

Nowadays, cross-flow hollow fiber membrane artificial lungs are used during cardiopulmonary bypass. Mathematical analysis of the membrane artificial lung has been attempted in the late 1960s and early 1970s on multiple parallel permeable tubes (intraluminal blood flow) and plates. The agreement between theoretical approaches and experimental data for blood oxygenation in membrane channels has resulted in a series of design-oriented articles <238,242,247,254-258>. Semi-empirical <3> methods are developed for cross-flow hollow fiber membrane artificial lungs in the mid 1980s. In the early 1990s numerical <267> methods are developed for extraluminal membrane artificial lungs with a blood flow path parallel to the fiber axis.

This paper aims to demonstrate a predictive, two-dimensional model with good absolute accuracy for flow and mass transfer in cross-flow hollow fiber membrane artificial lungs.

VI.3 Materials and methods

VI.3.1 Fiber bank model

The fiber bank in a cross-flow hollow fiber membrane artificial lung can be considered as an assemblage of uniform, parallel, fixed circular fibers equally spaced in a plane perpendicular to the long axes of the fibers. Assuming negligible entrance, end and wall effects (which is a reasonable assumption for a fiber bank with a large number of rows) and fully developed, two-dimensional laminar steady flow through the fiber bank, periodically fully developed flow can be considered <36>. A fiber bank can then be divided into a number of identical unit fiber cells, one fiber occupying each unit fiber cell. Fiber banks are characterized by cross-wise, S_T/d, and stream-wise, S_L/d, pitch(S)-to-diameter(d) ratios (Figure VI.1).

The “void fraction” or device porosity, ε, is defined as the ratio of the volume of voids (volume in the membrane compartment occupied by blood) to the volume of the bed (total volume of the membrane compartment). A characteristic length for internal flow through fiber banks, is

hydraulic radius, R_h. Hydraulic radius is expressed in terms of device porosity, ε, and wetted surface per unit volume of bed, a [35,276]:

$$R_h = \frac{\left(\frac{\text{volume of voids}}{\text{volume of bed}}\right)}{\left(\frac{\text{wetted surface}}{\text{volume of bed}}\right)} = \frac{\varepsilon}{a} \qquad [195]$$

The overall dimensions of the unit fiber cell are fixed by specifying the configuration, the porosity, ε, and the fiber diameter, d. In the present study, porosity varies from 0.4 to 0.6 for each fiber bank.

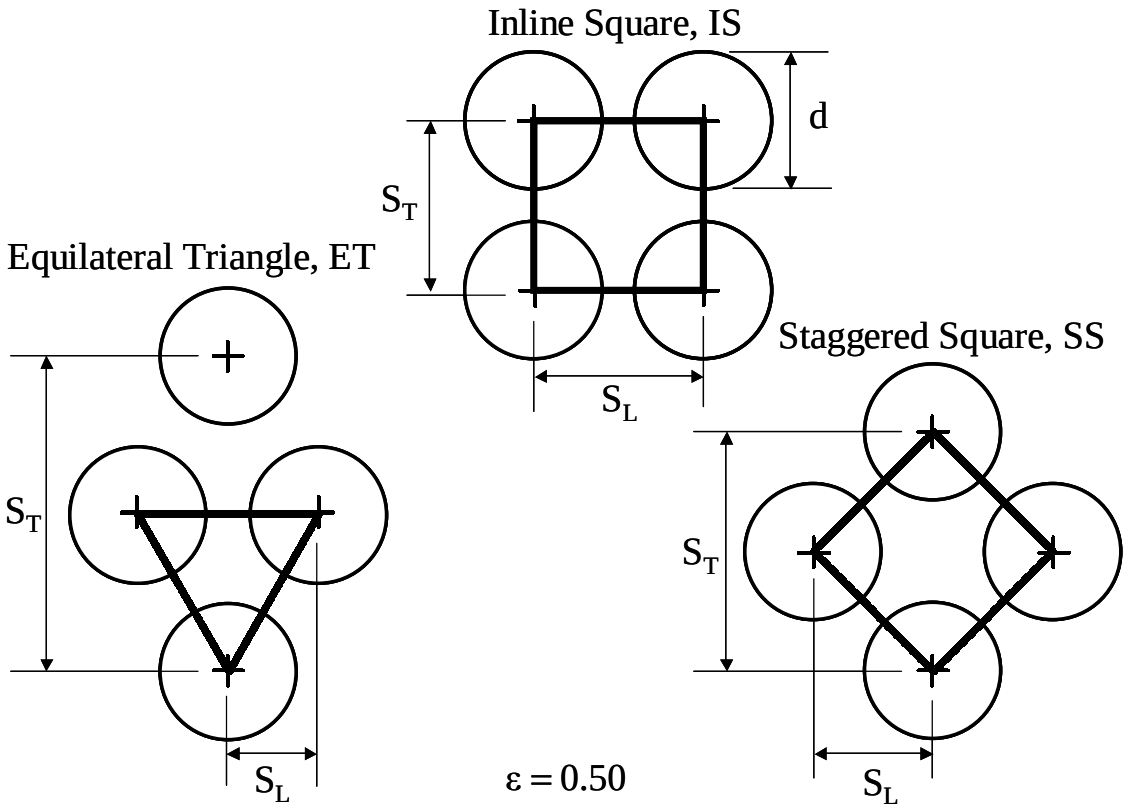

Figure VI.1: Three fiber geometries with a porosity of 0.50: inline square, IS, equilateral triangle, ET, and staggered square, SS (fiber diameter, d, cross-wise pitch, S_T, stream-wise pitch, S_L).

Three different fiber bank configurations are studied:

- inline square, IS: $S_T = S_L$
- equilateral triangle, ET: $S_T = 2 \cdot \sqrt{3} \cdot S_L$
- staggered square, SS: $S_T = 2 \cdot S_L$

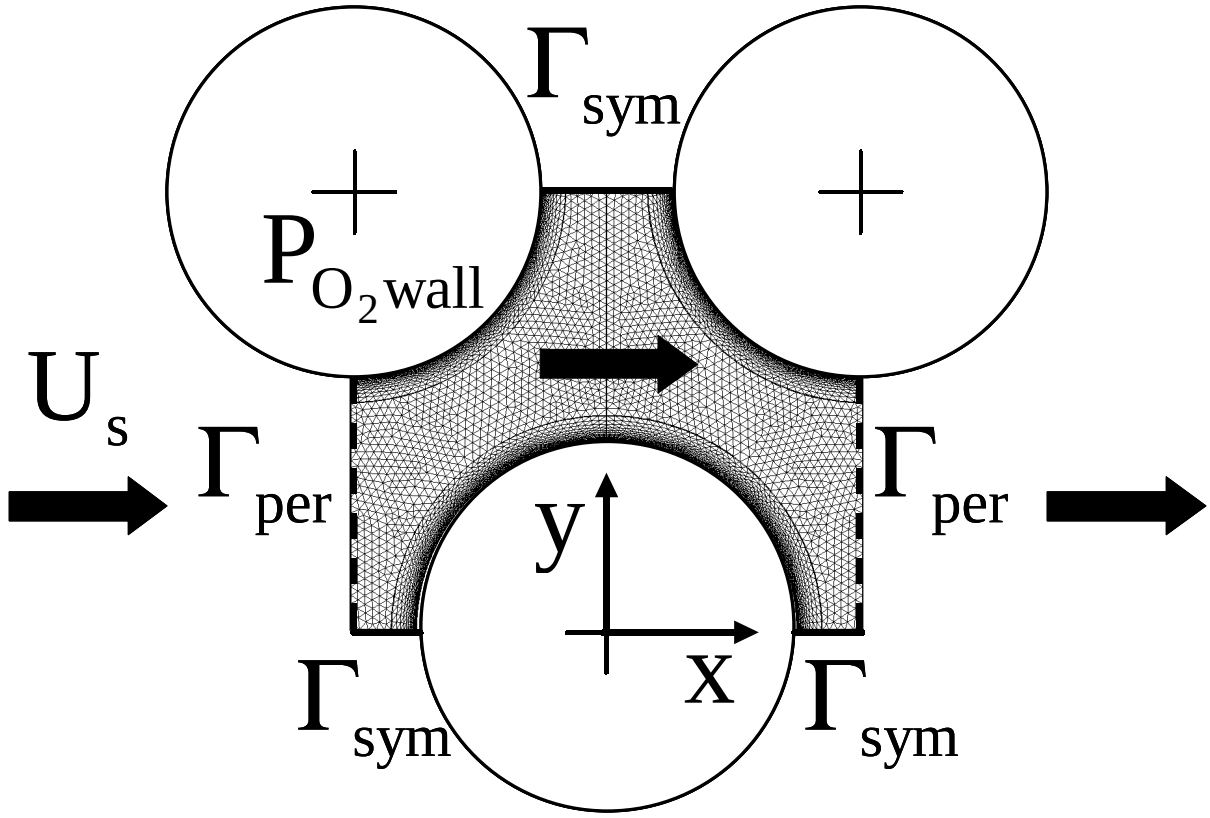

Figure VI.2: Schematic representation of the unit fiber cell model. Γ_{sym} represent symmetrical boundaries and Γ_{per} periodical boundaries; x denotes the stream-wise direction and y is perpendicular to the flow direction.

Figure VI.1 illustrates the three unit fiber cells with a porosity, ε, of 0.50 and diameter, d, of 0.380 mm, a representative size for a polypropylene fiber used in an artificial lung. The flow field is oriented in the x-coordinate direction (Figure VI.2). For symmetry reasons, only the meshed part of the geometry needs to be considered.

Figure VI.3 represents a fiber bank of height, H', length, L', and width, W' (left panel) as a

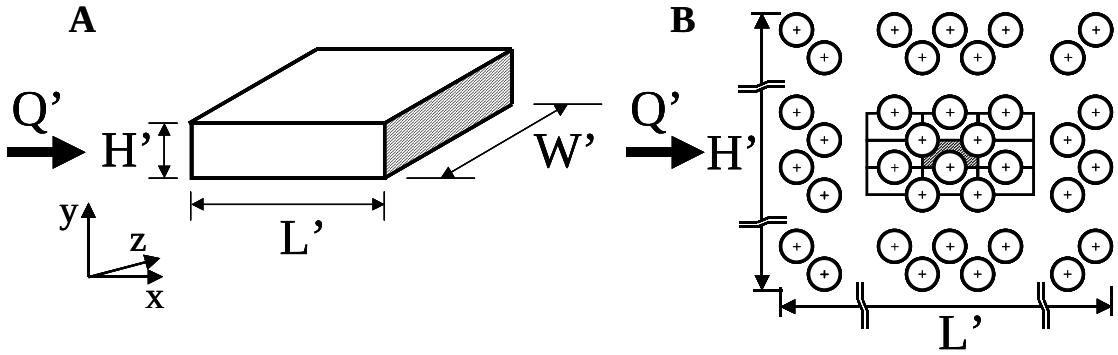

Figure VI.3: **A.** Schematic presentation of a fiber bank of height, H', length, L', and width, W'. x denotes the stream-wise direction, y denotes the cross-wise direction and z the direction along the fiber axis. Q' represents the flow rate through the fiber bank. **B.** The fiber bank is presented as an idealized periodical array of cylindrical fibers perpendicular to the flow.

periodical array of cylindrical fibers perpendicular to the flow (right panel). This fiber bank is an idealized representation of the membrane compartment of the commercially manufactured cross-flow hollow fiber membrane artificial lungs.

Using the geometrical data of the membrane compartment of the commercially manufactured cross-flow hollow fiber membrane artificial lungs, the two-dimensional unit fiber cell is integrated in every direction to simulate the complete membrane. The oxygen transfer in a whole fiber bank can therefore be calculated from the results obtained in a single unit fiber cell by integration into the stream-wise (x-) and cross-wise (y-) direction and by multiplication with the fiber length (z-direction).

VI.3.2 The fluid flow: Navier-Stokes equation

A two-dimensional, isothermal, steady state, laminar, Newtonian flow outside but perpendicular to a fiber bundle is considered. This flow is governed by the continuity and Navier-Stokes equations, expressing the classical principles of conservation of mass:

$$\overline{\nabla} \bullet \overline{\mathbf{u}} = 0 \qquad [196]$$

and conservation of momentum:

$$\rho \overline{\mathbf{u}} \bullet \overline{\nabla} \overline{\mathbf{u}} + \overline{\nabla} p = \mu \cdot \overline{\nabla} \left(\overline{\nabla} \overline{\mathbf{u}} + \overline{\nabla} \overline{\mathbf{u}}^{T} \right) \qquad [197]$$

where $\overline{\mathbf{u}}$ is the local mass average fluid velocity vector, ρ is the local density, p is the local hydrostatic pressure, and μ is the Newtonian fluid viscosity. $\overline{\nabla}$ is the gradient operator (in two dimensions):

$$\overline{\nabla} = \left(\frac{\partial}{\partial x}, \frac{\partial}{\partial y} \right) \qquad [198]$$

Symmetry boundary conditions , Γ_{sym}, are imposed upon the symmetry lines, no-slip wall boundary conditions upon the fiber surface. The distribution of the flow velocities (but not the local pressure or mass concentration) is identical in all unit fiber cells, hence periodical boundary conditions, Γ_{per}, to inlet and exit planes can be applied (Figure VI.2). Periodical boundary conditions are implemented with a prescribed volume flux, q, per unit fiber length:

$$q = \int_{\Gamma_{per}} \overline{\mathbf{u}} \bullet \overline{\mathbf{n}} \cdot d\Gamma = U_s \cdot \frac{S_T}{2} \qquad [199]$$

where U_s is the superficial velocity of the porous medium <35,36>. In this model, a uniform distribution of the flow is assumed, hence:

$$U_s = \frac{Q}{A_f} \qquad [200]$$

where Q is the flow rate through the artificial lung and A_f the gross frontal area:

$$A_f = H' \cdot W' \qquad [201]$$

VI.3.3 The oxygen transfer: convection-diffusion equation

The convection-diffusion equation describes the mass transfer in a fluid flow. The stationary convection-diffusion equation for oxygen transfer in water reads as follows:

$$\bar{\mathbf{u}} \bullet \bar{\nabla} C_{O_2} = D_{O_2} \cdot \Delta C_{O_2} \qquad [202]$$

where $\bar{\mathbf{u}}$ is the blood velocity vector, C_{O_2} represents the oxygen concentration and D_{O_2} the diffusion coefficient of oxygen in water. In Eq. [202], $\bar{\mathbf{u}} \bullet \bar{\nabla} C_{O_2}$ denotes the convective part, while $D_{O_2} \cdot \Delta C_{O_2}$ denotes the diffusive part.

The total amount of oxygen in water is in the dissolved state. Applying Henry's law <23> in Eq. [202], yields the convection-diffusion equation as a function of oxygen partial pressure:

$$\bar{\mathbf{u}} \bullet \bar{\nabla} P_{O_2} = D_{O_2} \cdot \Delta P_{O_2} \qquad [203]$$

Symmetry boundary conditions , Γ_{sym}, are imposed upon the symmetry lines between adjacent unit fiber cells, across which no net oxygen transfer occurs. Assuming a negligible gas side and membrane mass transfer resistance, a constant oxygen partial pressure, equal to the oxygen partial pressure in the gas side, is presented at the fiber surface. At the inlet, a uniform oxygen partial pressure of 20 mmHg is presented. In subsequent unit fiber cells in the flow direction (cfr. infra), the inlet oxygen partial pressure distribution equals the outlet oxygen partial pressure distribution of the former unit fiber cell.

At the outlet of the unit fiber cell, the concentration profile is imposed to remain invariable in the stream-wise direction <49>:

$$\bar{\mathbf{u}} \bullet \bar{\nabla} C_{O_2} = 0 \qquad [204]$$

The physical meaning of this outlet boundary condition is that the concentration field along the outlet contour is dominated by the stream-wise convection.

Room air (20 % O_2) is fed to the fiber bank yielding an oxygen partial pressure of 156 mmHg at the gas side. The assumption of a high oxygen concentration gas flow rate at the gas side together with negligible gas side and membrane mass transfer resistances, justify the concept of a constant oxygen partial pressure at the surface boundary.

Values for the Bunsen solubility and diffusion coefficient of oxygen in water are available from the literature <19,260>. Oxygen transfer experiments in Sarns Turbo 440, Cobe Optima and Dideco Compactflo <36> were conducted at different flow rates to evaluate the oxygen transfer to nitrogen-equilibrated water. Data obtained from these experiments are used in the validation of the model.

Mockros et al. <3,4> developed a one-dimensional semi-empirical model for the oxygen transfer in a cross-flow hollow fiber artificial lung. The model reads as follows:

$$N_{Sh} \cdot N_{Sc}^{-1/3} = \phi' \cdot N_{Re}^{m'} \qquad [205]$$

N_{Sh} represents the local Sherwood number and is defined as the ratio of the convective to diffusive mass transfer:

$$N_{Sh} = \frac{K \cdot 4 \cdot R_h}{D_{O_2}} \qquad [206]$$

where K is the local mass transfer coefficient, defined as the ratio of the local rate of mass transfer per transfer area, to the driving force. The ratio of momentum to diffusive transport is expressed by the Schmidt number, N_{Sc}:

$$N_{Sc} = \frac{\mu}{\rho \cdot D_{O_2}} \qquad [207]$$

N_{Re} represents the ratio of inertial to viscous forces:

$$N_{Re} = \frac{U_s \cdot 4 \cdot R_h \cdot \rho}{\mu} \qquad [208]$$

φ’ and and m’ are model parameters.

This model can be applied to the unit fiber cell on the one hand, and to the extrapolated membrane compartment on the other hand, yielding information about the oxygen transfer efficiency.

VI.3.4 The finite element method

We used the Galerkin finite element methodology <30> to discretize and integrate the flow equations on the computational grid. Numerical simulations were done using the computational fluid dynamics analysis software SEPRAN (Sepra, Leidschendam, The Netherlands). Treatment of periodic boundary conditions in the context of a finite element procedure is discussed by Segal et al. <41>. The penalty function formulation is used while the resulting system of nonlinear algebraic equations is solved by an iterative Newton linearization <30>. The elements used to construct the computational grid are standard Crouzeix-Raviart bilinear triangular elements.

Table VI.1: Geometry of a given membrane compartment for two different porosities but with a fixed length, L', width, W', and transfer area, A. IL: inline square; SS: staggered square; ET: equilateral triangle.

	porosity, ε					
	0.5			***0.6***		
length, L' [mm]	100			100		
width, W' [mm]	120			120		
transfer area, A [m²]	1.7			1.7		
heigth, H' [mm]	27			34		
hydraulic radius, R_h [mm]	0.10			0.14		
void volume, V_{void} [ml]	185			265		
number of fibers	11867			11867		
inlet oxygen partial pressure [mmHg]	20			20		
	IL	*SS*	*ET*	*IL*	*SS*	*ET*
outlet oxygen partial pressure [mmHg]	121	150	131	95.5	134	105

The streamline upwind Petrov-Galerkin method (SUPG) with the linear triangular method of Mizukami and Hughes <232> satisfying the maximum principle is used to solve the convection-diffusion equation.

It is assumed that the mass transferred does not influence the velocity. Hence, the Navier-Stokes equations are solved first and then the convection-diffusion equation is solved using the computed velocity vector.

In order to improve the accuracy and to eliminate numerical diffusion, the computational mesh is refined locally where high partial pressure gradients are expected.

The outlet concentration profile of the attained solution is applied to the inlet yielding the inlet boundary condition for the subsequent unit fiber cell along the flow path. This procedure is repeated until the total length of the flow path of the membrane compartment or the desired cup-mixed oxygen outlet partial pressure, is reached. The cup-mixed oxygen partial pressure at the inlet and outlet boundaries is calculated as follows:

$$\overline{P_{O_2}} = \frac{1}{q} \cdot \int_{\Gamma_{per}} P_{O_2} \cdot \bar{\mathbf{u}} \bullet \overline{\mathbf{dn}} \qquad [209]$$

where $\bar{\mathbf{u}}$ is the local velocity vector and $\bar{\mathbf{n}}$ the normal at the boundary.

The attained solution along the flow path can then be integrated cross-wise (y-direction) and along the axis of the fiber (z-direction).

VI.4 Results

Figure VI.4 presents the semi-empirical model of Eq. [205] on a bilogarithmic plot for the oxygen transfer in one unit fiber cell for the three different fiber configurations with an inlet oxygen partial pressure of 40 mmHg for two different porosities ($\varepsilon = 0.5$ and $\varepsilon = 0.6$). These results can be integrated for subsequent unit fiber cells yielding the oxygen transfer rate of a membrane compartment (Figure VI.5). The geometry of this membrane compartment with a fixed length, L', width, W' and transfer area, A is given in Table VI.1. In addition, Table VI.1 lists the outlet oxygen partial pressure. Figure VI.6 shows measured data of oxygen transfer to nitrogen equilibrated water in three commercial membrane artificial lungs versus calculated results of oxygen transfer using the numerical model taking into account the geometry of the membrane compartments. Results for a single commercial membrane artificial lung are obtained by averaging the results of the oxygen transfer simulations for the three different fiber configurations.

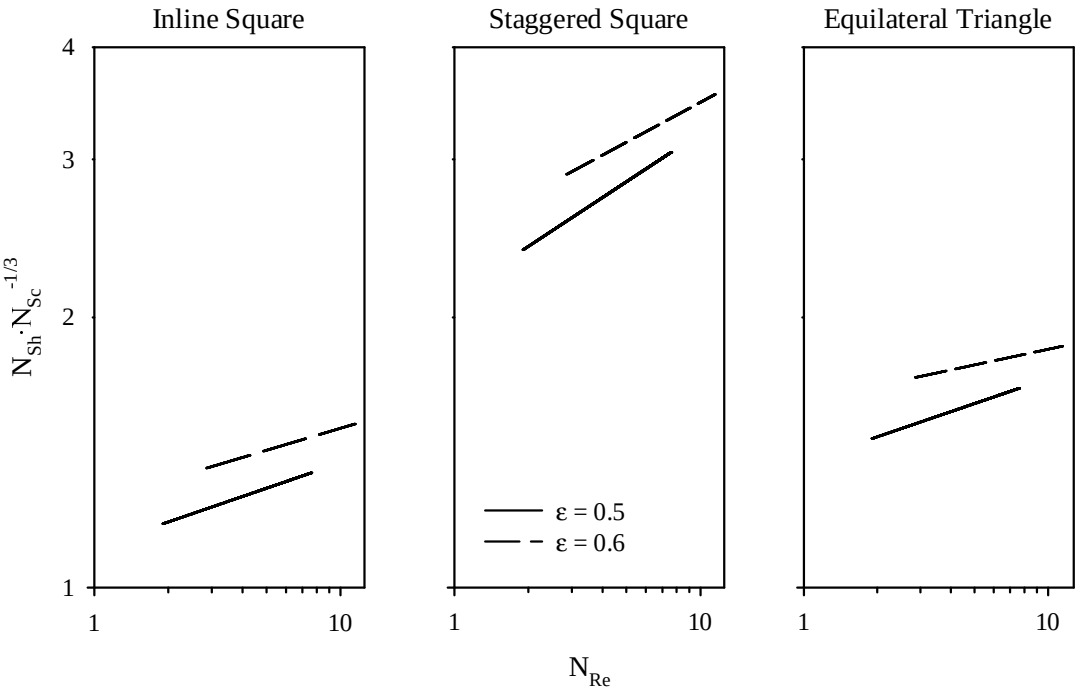

Figure VI.4: N_{Sh}-N_{Sc}-N_{Re} on a bilogarithmic plot for the oxygen transfer in one unit fiber cell (inlet oxygen partial pressure is 40 mmHg) for two porosities ($\varepsilon = 0.5$ and $\varepsilon = 0.6$). **Left panel:** inline square; **middle panel:** staggered square; **right panel:** equilateral triangle.

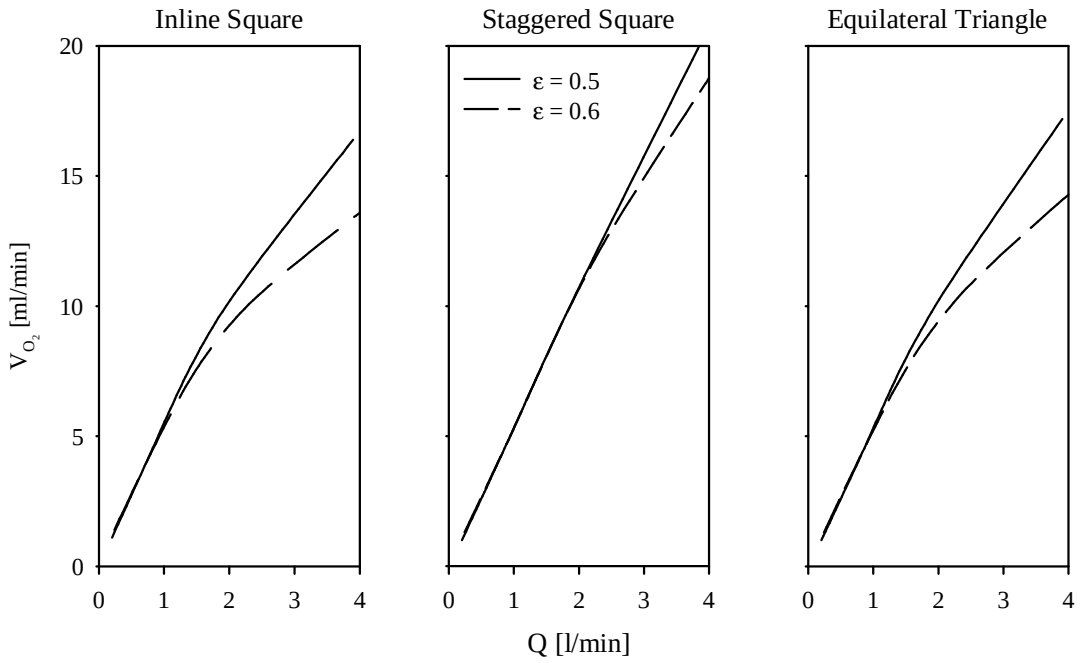

Figure VI.5: Oxygen transfer rate, V_{O_2}, versus flow rate, Q, for two porosities (ε = 0.5 and ε = 0.6) in a membrane compartment with fixed length, L', width, W' and transfer area, A. The membrane compartment is assembled by integrating unit fiber cells. **Left panel:** inline square; **middle panel:** staggered square; **right panel:** equilateral triangle.

VI.5 Discussion

Semi-empirical and numerical methods for prediction of the blood-gas transfer capabilities of membrane artificial lungs without prototype testing using blood, have been developed (and still are being developed). Vaslef et al. <4> use a normalized mass transfer coefficient for cross-flow devices derived from experiments using water to characterize the gas transfer performance of a membrane oxygenator for any inlet blood conditions. In this method, the device is approached as a porous medium. Baker et al. <267> developed a two-dimensional finite-difference predictive model for gas transfer in hollow fiber membrane artificial lungs. The model is able to predict gas transfer to blood flowing outside and parallel to oxygenating fibers without experimental data. The cross-sectional fiber distribution is assumed a uniform triangular array, while the rest of the device is extrapolated by symmetry. The model is compared to bovine and human experimental data from small test cells with microporous polypropylene fibers. Niranjan et al. <269> developed a finite-difference model of the gas transfer within the IVOX intra-vascular hollow-fiber blood gas exchanger by considering fluid flow both within and outside hollow capillary fibers using the

Krogh cylinder approach for flow parallel to the fiber axis, previously used to model gas transport in vascular capillaries surrounded by tissue <270>. The goal of their analysis was to investigate the effects of various operating conditions on oxygen transfer rate. They validated the model using independently obtained experimental data and investigated the effects of various operating conditions on the mass transfer rates of carbon dioxide and oxygen.

This paper, on the other hand, investigates the oxygen transfer to water in a cross-flow hollow fiber membrane oxygenator with a two-dimensional finite element method. Finite element modelling allows a more accurate calculation of high oxygen pressure gradients. We applied the dimensionless semi-empirical model of Vaslef et al. <4> (Eq. [205]) to the unit fiber cell of three different fiber configurations on the one hand and extrapolated the results from a single unit fiber cell to a homogeneous fiber bank on the other hand. The model is validated with experimental results obtained on three commercial artificial lungs.

Figure VI.4 shows that the staggered square configuration with a high porosity is most efficient. The mass transfer coefficient, K, in the Sherwood number, N_{Sh}, (Eq. [206]) is evaluated by dividing the local flux by the locally averaged partial pressure difference between the fluid and the gas phases.

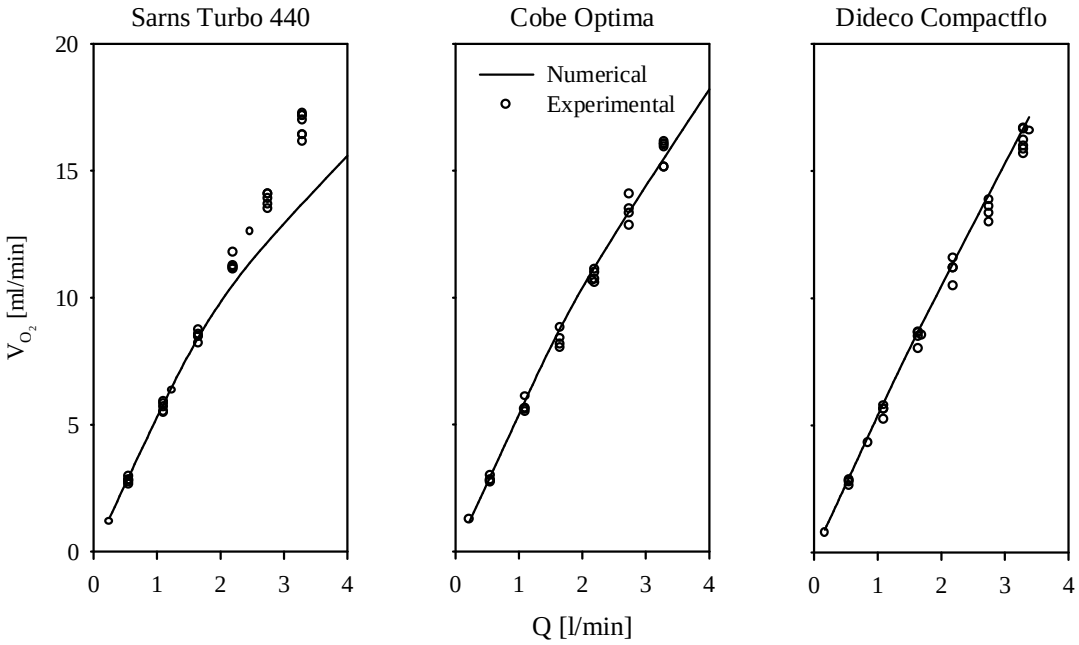

Figure VI.6: Comparison of predicted (numerical) and measured (experimental) oxygen transfer rate, V_{O_2}, as a function of flow rate, Q, for three commercial hollow fiber membrane artificial lungs. Results are obtained from an extrapolation of subsequent unit fiber cells to a membrane compartment with identical measures. **Left panel:** Sarns Turbo 440; **middle panel:** Cobe Optima; **right panel:** Dideco Compactflo.

Increasing the porosity augments the efficiency of the oxygen mass transfer.

In Figure VI.5, one observes a deviation from linearity in the oxygen transfer rate versus flow rate relationship at higher flow rates (Q > 2 l/min). At low flow rates (Q < 2 l/min), the diffusive part dominates the convective part and all water is saturated with oxygen, because the local velocity is slow enough to let the oxygen diffuse throughout the fluid. In this case the total oxygen uptake rate is flow rate limited. At higher flow rates, the convective part dominates the diffusive part (Q > 2 l/min). The velocity of the fluid becomes too high and the time to transfer and take up oxygen is decreased. Therefore some part of the water flow will leave the membrane without being fully saturated with oxygen. In this case the total oxygen uptake is limited by the boundary layer around the hollow fiber. The larger the boundary layer is, the longer it takes oxygen to diffuse through and the lower the uptake by the bulk flow. A large boundary layer will negatively influence the efficiency.

Comparison of Figure VI.5 with Figure VI.4 produces a seeming paradox. The higher efficient high porosity unit fiber cell ($\varepsilon = 0.6$) deviates earlier from the straight line at higher water flow rates than the medium porosity membrane ($\varepsilon = 0.5$). However, one should observe that although both membranes have the same effective membrane area, the former membrane has a larger void volume than the latter (Table VI.1). Though the mass transfer through the boundary layer is more efficient at higher porosities, the total mass transfer produced in the membrane is limited, because the increased oxygen transport through the membrane surface is not able to cope with the higher volume of water that needs to be saturated. The result is again that some part of the water flow rate does not become fully saturated at the outlet of the higher porosity membrane.

Figure VI.6 shows a good agreement between the *in numero* model and the *in vitro* experiments for the oxygen transfer to nitrogen-equilibrated water in commercial membrane artificial lungs. The difference at high flow rates for the Sarns Turbo 440 can be minimized by taking the staggered square fiber bank configuration instead of the average over the three fiber bank configurations. At a water flow rate of 4 l/min, the oxygen transfer rate is 19.1 ml/min *in numero* versus 20.0 ml/min *in vitro* (5% difference).

Although the excellent results correlate with experimental data of commercial artificial lungs, our model has still some limitations. Fluid flow outside and around the fibers creates a considerable complication in modelling. The overall design was considered to be a repeating pattern of a definable and reasonably small computational domain. The computational domain boundaries than become the lines of periodicity and symmetry. This level of simplification was necessary to simplify the problem and keep it two-dimensional. The model is limited by the assumption of a uniform distribution of the fibers on the one hand and a constant device porosity

on the other hand. In an idealized first approximation, the membrane compartment of a membrane artificial lung can be modelled in terms of a repeating cell unit with no net interaction between adjacent units. The behavior of the device may then be deduced from the analysis of this cell unit structure. An advantage of this type of modelling is that the blood flow around the fibers is explicitly considered.

The validity of the model is proven by its ability to predict oxygen transfer in water. The model is suited for design optimization of hollow fiber blood-gas exchange devices with an extraluminal blood path.

VI.6 Acknowledgements

This research is funded by a specialization grant of the Flemish Institute for the Promotion of the Scientific-Technological Research in Industry (IWT-961181).

VII AIR-HANDLING CHARACTERISTICS OF PEDIATRIC ARTIFICIAL LUNGS

VII.1 Abstract[†]

At present, air handling of a membrane oxygenator is generally studied by using an ultrasonic sound bubble counter. However, this is not a quantitative method and it does not give any information on where air was entrapped in the oxygenator and if it eventually was removed through the membrane for gas exchange. The study presented here gives a novel technique for the determination of the air-handling characteristics of a membrane oxygenator. The study aimed at defining not only the amount of air released by the oxygenator, but also the amount of air trapped within the oxygenator and/or removed through the gas exchange membrane. Two neonatal membrane oxygenators without the use of an arterial filter were investigated: the Polystan Microsafe and the Dideco Lilliput. Although the air trap function of both oxygenators when challenged with a bolus of air was similar, the Microsafe obtained this effect mainly by capturing the air in the heat exchanger compartment while the Lilliput did remove a large amount of air through the membrane. In conclusion, the difference in trap function was most striking during continuous infusion of air. Immediate contact with a microporous membrane, avoidance of high velocities within the oxygenator, pressure drop, transit time, and construction of the fiber mat all contribute to the air-handling characteristics of a membrane oxygenator.

VII.2 Introduction

With the introduction of neonatal oxygenators, total system priming volumes of 180 ml are feasible <292>. The use of an arterial filter in these systems is debatable. The priming volume of a pediatric arterial filter with its bypass is almost as large as the membrane or heat exchanger

[†] The contents of this chapter are published in *Perfusion* 1998; **13:**157-163:

Can an oxygenator design potentially contribute to air embolism in cardiopulmonary bypass? A novel method for the determination of the air removal capabilities of neonatal membrane oxygenators

F. De Somer, P. Dierickx, D. Dujardin, P. Verdonck, and G. Van Nooten

compartment of a neonatal oxygenator. In addition, an arterial screen filter is only effective in the removal of air emboli with an open purge line. However, especially in small babies, it is not desirable to keep this purge line open since one wants to know exactly the tissue extracorporeal blood flow for adequate tissue perfusion.

By not using an arterial screen filter, there is a risk for pumping gaseous microemboli (GME) or particles towards the patient. However, most data supporting this risk have been generated using bubble oxygenators <50,53,293>. When using membrane oxygenators, a lower incidence of GME generation is reported. However, membrane oxygenators can vary in their air-handling performance, as has been frequently reported <52,294,295>.

The assessment of air-handling capabilities of an oxygenator generally includes an ultrasonic bubble counter <63>. However, this method is not sufficiently quantitative and has low reproducibility due to the limitations of the working principle <64-66>. Therefore, an objective assessment could contribute to the air-handling improvement of a given device.

This study investigates the risk for microemboli and macroemboli when using a neonatal membrane oxygenator without an arterial screen filter. Its aims are to define not only the amount of air released by the oxygenator, but also the amount of air that is trapped within the oxygenator and/or removed through the gas exchange membrane.

VII.3 Method

VII.3.1 Circuit

To determine the amount of air released by the oxygenator, a standpipe is used as described by Miller and Johnson <198> (Figure VII.1). This standpipe (e) acts as a long cylindrical bubble trap. A dilatometer (4) measures the amount of gas evacuated through the gas exchange membrane. This meter consists of a calibrated glass capillary with a mercury bead inside. After sealing the gas outlet port and the overpressure relief with silicone, the capillary is connected to the gas inlet port. As gas goes from the blood to the gas compartment, the mercury bead will move due to the volume increase until equilibrium is established with the atmospheric pressure. The following formula converts the displacement of the mercury bead into a volume value:

$$V_{air} = \frac{\Delta L_{Hg} \cdot \pi \cdot d_c^{\,2}}{4000} \qquad [210]$$

Where V_{air} is the volume [ml], ΔL_{Hg} is the displacement of the mercury bead [mm] and d_c is the diameter of the glass capillary [mm].

Gross filtered bovine blood (hematocrit 22%, temperature 22 °C) was sequestered in a 10-liter

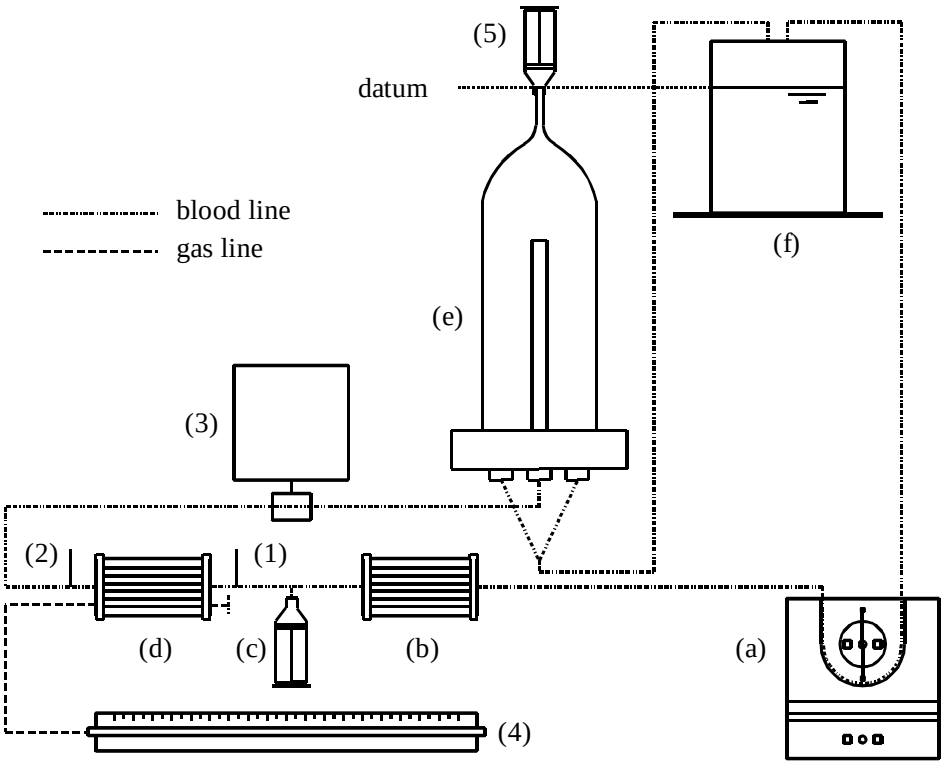

Figure VII.1: Test circuit: (a) calibrated roller pump, (b) Cobe Excel, (c) air injection port, (d) test device, (e) standpipe, (f) reservoir, (1) and (2) pressure measurements, (3) Doppler probe, (4) dilatometer, (5) syringe.

reservoir. It was pumped by a calibrated roller pump (Cobe Cardiovascular Inc., Arvada, CO, USA) through a Cobe Excel flat-sheet membrane oxygenator. Blood flow was then directed via 1/4-inch polyvinyl chloride (PVC) line through the test device into the standpipe. Blood returned to the reservoir via a 3/8-inch PVC line. Arterial line pressure was maintained at 150 mmHg. Blood flow during the experiment was set at 600 ml/min. Pressures were measured before (1) and after (2) the membrane oxygenator by fluid filled pressure transducers (Ohmeda-Spectramed, Gent, Belgium).

A connector and stopcock are added in-line to the test device inlet before the test. This gives the ability to directly inject a bolus of air (at standard temperature and pressure) 1, 5 and 20 ml) in order to simulate a gross air embolus or to attach a syringe pump and slowly inject air (20 ml at 3 ml/min) to simulate an adverse event leading to GME. After injecting a bolus, a 3-min period was allowed for equilibration after which the pump was stopped and the data recorded. During the slow injection, the pump flow was maintained for 10 min before the data were recorded.

A “Y” connector is added before the entrance of the standpipe, so that a recirculation line back to the aliquot could be used during priming and debubbling of the test device. The test device was carbon dioxide-flushed and primed according to the manufacturers’ instructions. A syringe was employed at the top of the standpipe to volumetrically quantify the amount of air passing through the membrane test device. The reservoir was positioned to minimize head pressure effects.

A Hatteland CMD-10 (Hatteland Instrumentering, Royken, Norway) pulsed Doppler microbubble counter is attached to the tubing 20 cm after the arterial outlet of the test device. The device was set at a maximum sensitivity and was used to detect microbubbles not macrobubbles. This device was connected to a computer with a COMAC computer interface supported by BUBMON (version 1.6 Hatteland Instrumentering). The addition of the bubble counter in the test circuit was to compare the bubble counts with the amount of air collected in the standpipe after the test device.

VII.3.2 Calibration

The test circuit was calibrated by initially injecting a 0.5, 1, 5, and 10 ml boluses into the circuit with no test oxygenator. The injected air was then collected at the syringe to verify that the standpipe is effectively collecting all the air injected. Injecting 0.5, 1, 5, and 10 ml before the mercury bead after which the change in distance is recorded, provides calibration of the dilatometer.

VII.3.3 Test devices

Two neonatal oxygenators were investigated, the Polystan Microsafe (Polystan A/S, Denmark) and the Dideco Lilliput (Sorin). Although their performance characteristics are comparable (Table VII.1), their design is not. The Microsafe consists of two cylinders. The first cylinder of stainless steel tubes forms the heat exchanger. The second cylinder holds the gas exchange

Table VII.1: Oxygenator characteristics

	Dideco Lilliput	***Polystan Microsafe***
Maximum blood flow [ml/min]	800	800
Priming volume in membrane and heat exchanger [ml]	60	52
Minimum volume in venous reservoir [ml]	20	25
Connector size [inch]	3/16 and 1/4	3/16 and 1/4

membrane. A rigid tube connects both cylinders. Although blood flow will be the same everywhere in the device, the velocity will not. Blood velocity will be high in the inlet connector, outlet connector, and the connecting tube between the two cylinders and much lower in the cylinders themselves. In the Lilliput, blood flows through the inner side of a spiral corrugated pipe heat exchanger after which it enters the fiber stack for gas exchange. This design gives high velocities in inlet and outlet connectors and lower velocities in the rest of the oxygenator. Both devices have a top-to-bottom flow path in order to establish a bubble trap function in the oxygenator. The fibers in the Microsafe are at an angle of approximately 15° to the longitudinal axis of the membrane module. In the Lilliput, the fibers are in parallel with the longitudinal axis of the oxygenator module and the clearly visible spacing wires are perpendicular to the longitudinal axis.

VII.4 Results

VII.4.1 Calibration

Calibration of the standpipe ($R^2 = 0.99$) and the dilatometer ($R^2 = 0.99$) show excellent correlation (Figure VII.2).

VII.4.2 Bolus injection

The results of the bolus and slow air injections are shown in Table VII.2.

Injection of 1 ml air in the Microsafe resulted in a visible air collection of 1 ml at the bottom of the heat exchanger, no air entrapping in the bubble trap and no removal of air by the membrane. In the Lilliput, no air was observed in the oxygenator module or in the bubble trap. However, the oxygenator contained 0.9 ± 0.1 ml air and 0.1 ± 0.1 ml was removed by the membrane.

The 5 ml bolus injection resulted in visible air (4.7 ± 0.1 ml) in the heat exchanger module of the Microsafe, no air in the bubble trap and an evacuation of 0.4 ± 0.2 ml by the membrane. In the Lilliput, air was found at the top of the oxygenator (1.8 ± 0.2 ml) and in the bubble trap (0.1 ± 0.2 ml). 3.1 ± 0.1 ml was evacuated by the membrane.

With an injection of 20 ml of air, air was found in both heat exchanger and membrane modules of the Microsafe (8.3 ml) as in the bubble trap (4.9 ml) while 6.8 ml was evacuated by the membrane. In the Lilliput, air was found in the oxygenator (3.2 ml) and in the bubble trap (4.2 ml). At the end of the 3-min period for stabilization, there was still some small movement of the mercury drop. At that time, the membrane evacuated 12.6 ml.

VII.4.3 Slow injection

When injecting 20 ml of air at 3 ml/min, the Microsafe entrapped air in both heat exchanger module and membrane module (12.2 ± 1.9 ml). As more air entered the oxygenator module, it was captured in the same plane as the arterial outlet connector of the oxygenator, after which it traveled along the fibers towards the arterial outlet connector (Figure VII.3). This resulted in 2.7 ± 0.1 ml of entrapped air in the bubble trap. The membrane evacuated 5.1 ± 1.7 ml.

In the Lilliput, air was observed in the membrane compartment where the membrane easily removed it. Even after the 10 min of stabilization, there was still some evacuation by the membrane as detected by the dilatometer. The oxygenator entrapped 2.9 ± 0.1 ml of air, no air was found in the bubble trap and the membrane removed 17.1 ± 0.1 ml.

Table VII.2: Air removal capabilities of the Lilliput and the Microsafe.

Bolus [ml]	*Air in dilatometer [ml]±SD*		*Air in bubble trap [ml]±SD*		*Air in oxygenator [ml]±SD*		*Bubble counter [count/min]*	
Oxygenator	***Microsafe***	***Lilliput***	***Microsafe***	***Lilliput***	***Microsafe***	***Lilliput***	***Microsafe***	***Lilliput***
1[a]	0	0.1±0.1	0	0	1	0.9±0.1	0	0
5[a]	0.4±0.2	3.1±0.1	0	0.1±0.2	4.7±0.1	1.8±0.2	101	128
20[b]	6.8	12.6	4.9	4.2	8.3	3.2	210	217
3ml/min[a]	5.1±1.7	17.1±0.1	2.7±0.1	0	12.2±1.9	2.9±0.1	49	366

[a] Two measurements.

[b] One measurement.

VII.4.4 Pressure measurements

The pressure drop over the oxygenators during the experiment was 30.1 ± 1.4 mmHg for the Microsafe and 53.1 ± 1.5 mmHg for the Lilliput.

During the bolus injections of 5 and 20 ml, there was a sudden transient increase in pre-membrane pressure with the Lilliput for a few seconds after which it returned to normal.

VII.5 Discussion

Arterial screen filtration has become a standard procedure in the USA for pediatric and adult perfusion. The rationale is to reduce the risk of gaseous and/or solid microemboli. However, the fear for these adverse effects was based mainly on the large experience with bubble oxygenators <50,53,293>. Membrane oxygenators, in contrast do have a completely different working principle. The packed fibers in the gas exchange compartment do not only provide a control of the blood path but will also work as an effective depth filter for solid particles. This was confirmed by

recent research in a pig model showing no difference in embolization of vital organs after 3 h of extracorporeal circulation using an extra-luminal hollow-fiber oxygenator with or without arterial screen filter <296>. Several papers have described a much lower, or even nonexistent, generation of GME with the introduction of membrane oxygenators <51,297>. However, there is a much controversy amongst authors about the GME generation of a given device <51,294>. This inconsistency probably has its origin in the non-quantitative nature of the data generated by bubble counters and in the severe limitations of accurately counting GME by ultrasonic techniques <66,297>. Indeed, problems can occur from the angle and coupling of the ultrasonic transducer, the frequency and pulse length of the device, the electrical circuitry employed, bubble diameter and shape, tubing diameter and curvature, amount of air and speed at which air is introduced, red cell interference, and the rate of blood flow <64,295>. Finally, the bubbles themselves may produce the most serious problems. Signal differences can result from multiple bubbles clumping, bubbles of different sizes blocking others, or the beam missing multiple bubbles, as described by Butler <297>.

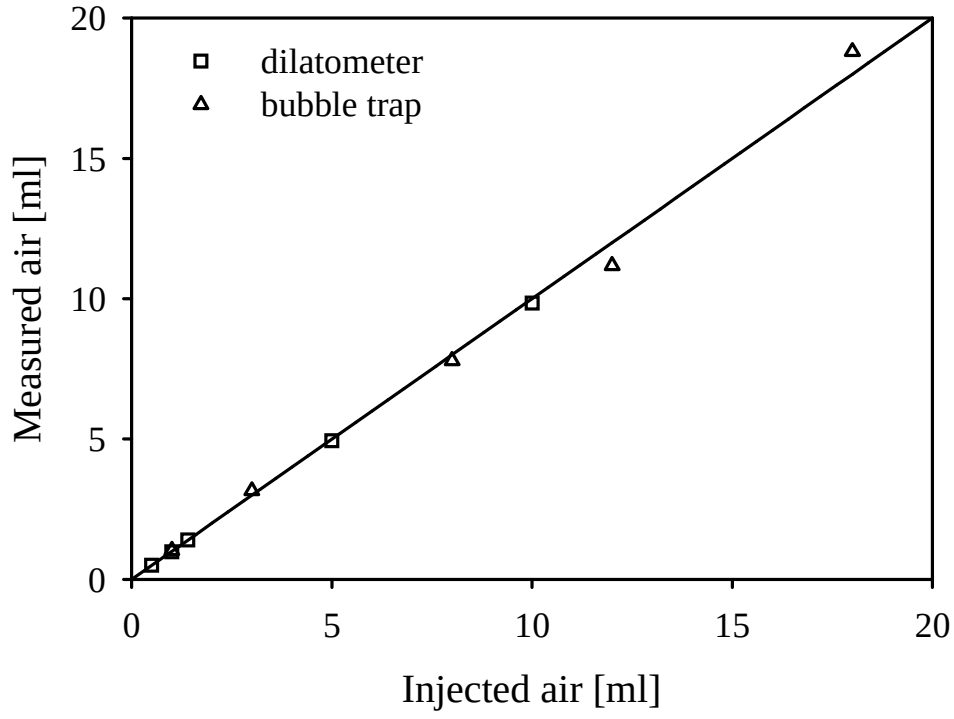

Figure VII.2: Calibration of dilatometer and bubble trap.

Our assumption was that theoretically a membrane oxygenator must be able to evacuate air because of its combination of a microporous membrane with a depth filter. The results in this study show clearly that this hypothesis is correct, but highly dependent on the oxygenator design. Both oxygenators had more or less the same bubble trap efficiency when confronted with an air challenge. However, the Microsafe obtained this effect mainly by capturing the air in the heat exchanger compartment. Since the heat exchanger is not permeable for gas, the risk for a sudden release of this air by movement of the oxygenator (taking samples, repositioning) or by changes in temperature still exists. In the Lilliput, there is almost immediately contact between the air and the gas exchange membrane and, because of this, a large portion of the air is evacuated. This difference is most obvious during the slow injection of air where the Lilliput is capable of removing almost 90% of the air via the membrane after 10 min. The Microsafe will, in the same circumstance, still release emboli; repositioning of the arterial outlet connector in another plane could probably reduce this but was not studied. Nevertheless, the design of the Microsafe will always keep an amount of gas accumulated in the heat exchanger module.

In addition, the construction of the membrane mat and the existence of high velocities within the body of the oxygenator seem to be important aspects. In the Microsafe, air is actually pushed by the high velocities generated in the connection tube between the two cylinders in the plane of the arterial outlet connector, where it is guided by the fibers towards the arterial outlet. The influence of pressure drop was also interesting in that, theoretically, a higher pressure drop should be beneficial in the removal of air, especially when there is good contact with the membrane material. The Lilliput with the higher pressure drop and the largest immediate contact with the membrane is the most effective. Because of this, one should not only open the purge line on an oxygenator when air has entered the unit, but also, at the same time, raise the pressure downstream the oxygenator. Removal of air in a neonatal oxygenator seems to be positively influenced by the following aspects: rapid and large contact with the gas exchange membrane, contact time between the fibers and the gas, avoidance of zones with high velocities within the oxygenator module, pressure drop (higher seems favorable) and the construction of the fiber mat. The dilatometer also showed an important consideration in that the evacuation of air through the membrane is most effective initially and will decrease over time. This is explained by the reduction of the contact area of the bubble against the fiber over time.

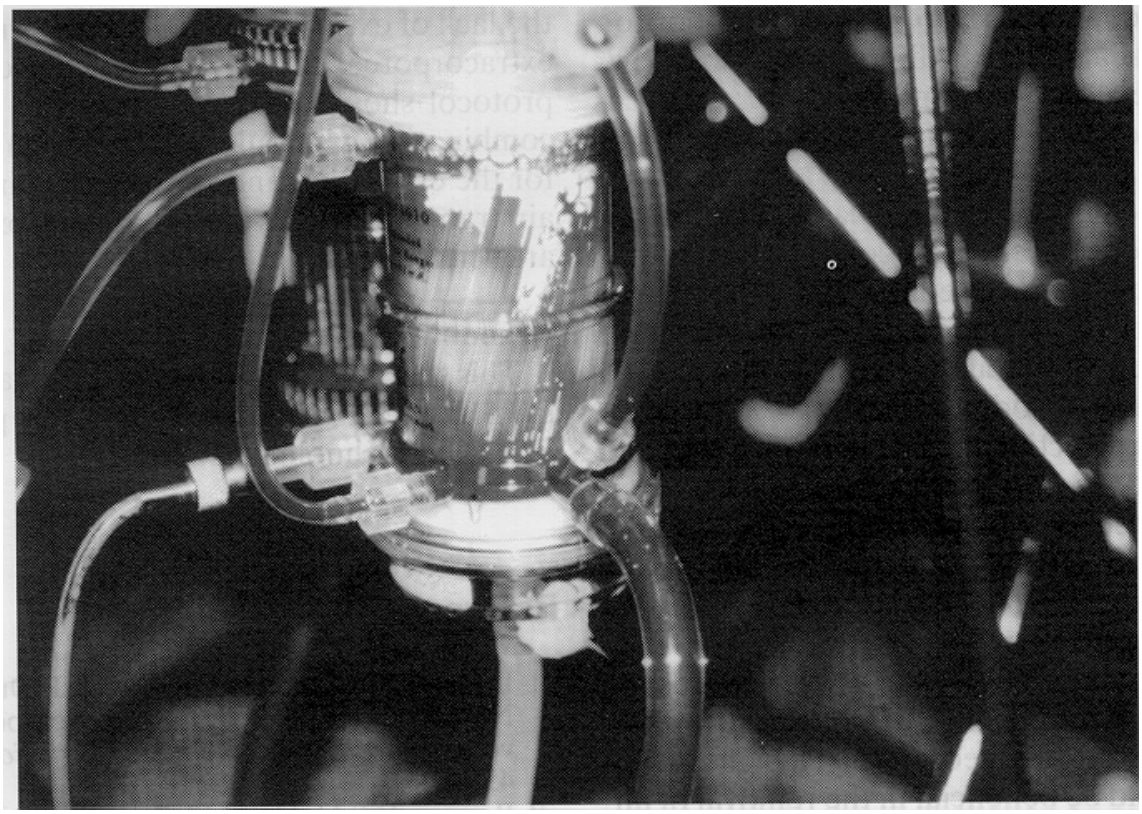

Figure VII.3: The Microsafe oxygenator

The results of this study show an important influence of oxygenator design on the air removal capability of a neonatal oxygenator. Although others have tried to speculate what was happening to gas once it had entered the oxygenator, they had no means to measure or quantify it <52>. The technique described in this paper gives the possibility to actually measure and quantify the capability of a given device to trap, release or evacuate air. Because of the lack in existing data on bubble dynamics during extracorporeal circulation, we believe this test protocol should become a standard procedure in combination with pulsed Doppler bubble counting for the evaluation and study of the air removal and air trap capabilities of membrane oxygenators or artificial lungs.

VII.6 Acknowledgements

This study was supported by a specialization grant from the Flemish Institute for the promotion of the Scientific-Technological Research in Industry (no. 961181).

VIII CONCLUSION

An artificial lung is used during cardiopulmonary bypass to oxygenate blood and to control blood temperature. In this work, the hydrodynamics and the mass transfer characteristics of cross-flow hollow fiber membrane artificial lungs are studied *in numero* and *in vitro*.

The pressure drop-flow rate characteristics of the membrane compartment in three hollow fiber membrane artificial lungs (Sarns Turbo 440, Cobe Optima, Dideco Compactflo) were determined *in vitro* to characterize design features. Results are presented in a unique dimensionless relationship between Euler number, N_{Eu} (ratio of pressure drop to kinetic energy), and Reynolds number, N_{Re}, (ratio of inertial to viscous forces), and are a function of the device porosity, ε, and a characteristic device length, ξ, defined as the ratio of the mean blood path and manifold length <34>:

$$N_{Eu} \cdot \frac{\xi}{\varepsilon^2} = \alpha + \frac{\beta}{N_{Re} \cdot \varepsilon \cdot (1-\varepsilon)}$$

In analogy with the *in vitro* hydrodynamics study, the oxygen transfer rate-flow rate characteristic of the three hollow fiber membrane artificial lungs are determined *in vitro* to characterize design features. Results are presented as a refinement of a previously published semi-empirical mathematical theory of mass transfer in artificial lungs between Sherwood number, N_{Sh} (ratio of convective to diffusive mass transfer), Schmidt number, N_{Sc} (ratio of momentum to diffusive transport), and N_{Re}. The refinement involves a unique dimensionless N_{Sh}-N_{Sc}-N_{Re} relationship a function of ε and ξ, <37>:

$$\frac{N_{Sh}}{N_{Sc}^{1/3}} \cdot \xi^{1/2} = \varphi \cdot \left(\varepsilon^{1/m} \cdot N_{Re}\right)^m$$

where φ and m depend on the Péclet number. A good correspondence is found between the model predictions and *in vitro* blood oxygen transfer rates.

A two-dimensional *in numero* finite element model for permanent, isothermal, laminar blood flow perpendicular to hollow fibers is developed to study the flow and mass transfer in cross-flow hollow fiber membrane artificial lungs. All fibers are assumed identical, straight, and parallel. The model is developed to understand the hydrodynamics in a membrane compartment. Three different fiber banks (inline square, staggered square, and equilateral triangle) are studied. The model uses a finite element technique to solve the Navier-Stokes equations and the

convection-diffusion equation on the computational domain of a unit fiber cell. The influence of both a Newtonian and a non-Newtonian Casson viscosity model on the flow field is investigated and indicates that the non-Newtonian effect becomes apparent at very low Reynolds numbers. Subsequent stream-wise and cross-wise unit fiber cells are coupled/assembled to predict mass transfer to water and blood in a cross-flow hollow fiber membrane artificial lung. The model is compared to water experimental data from three commercial artificial lungs and correlates well with the *in vitro* measurements. Blood simulations reveal that only a blood path length of no more than 40 mm is needed to attain an oxygen saturation of 99.5 %.

To study the ability of membrane artificial lungs to handle and remove air, a novel technique for the determination of the air-handling characteristics of a membrane artificial lung is developed. The study aimed at defining not only the amount of air released by the artificial lung, but also the amount of air trapped within the artificial lung and/or removed through the gas exchange membrane. Two neonatal membrane artificial lungs without the use of an arterial filter were investigated: the Polystan Microsafe and the Dideco Lilliput. This study revealed that immediate contact with a microporous membrane, avoidance of high velocities within the artificial lung, pressure drop, transit time, and construction of the fiber mat all contribute to the air-handling characteristics of a membrane artificial lung.

In conclusion, a predictive, two-dimensional model with good absolute accuracy for flow and mass transfer in cross-flow hollow fiber membrane artificial lungs is developed. This model enables one to study the influence of geometry and viscosity on hydrodynamics and mass transfer in fiber banks and may aid the optimization of hollow fiber artificial lung design. A unique, dimensionless, semi-empirical relationship for both the hydrodynamics and mass transfer is presented. This dimensionless approach enables one to compare artificial lungs independently with respect to the hydrodynamics and mass transfer charecteristics and to predict mass transfer rate to blood of a new design of an artificial lung.

The results presented in this work could be suitable for design optimization of hollow fiber blood-gas exchange devices.

SYMBOLS†

Abbreviations

AAMI	Association for the Advancement of Medical Instrumentation
ACT	Activated Clottting Time
AF	Advancing Front
ARDS	Adult Respiratory Distress Syndrome
ARF	Acute Respiratory Failure
BiVAD	BiVentricular Assist Device
CABG	Coronary Artery Bypass Grafting
CPB	CardioPulmonary Bypass
CPS	Cardiopulmonary Support
ECC	ExtraCorporeal Circulation
$ECCO_2R$	ExtraCorporeal Carbon dioxide Removal
ECLA	ExtraCorporeql Lung Assist
ECLS	ExtraCorporeal Life Support
ECMO	ExtraCorporeal Membrane Oxygenation
ECPR	Extracorporeal CardioPulmonary Resuscitation
ET	Equilateral Triangle
FEM	Finite Element Method
GME	Gaseous Microemboli
IL	Inline Square
IVOX	IntraVenous Oxygenation
KAVD	Kinetic Assisted Venous Drainage
LVAD	Left Ventricular Assist Device
PVC	PolyVinyl Chloride
R	Respiratory exchanger ratio

† In order to translate non-S.I.-units into SI-units, one can make use of the converstion factors which are listed at the end. These SI-units can than be applied in the definition / calculation of dimensionless numbers.

RBC	Red Blood Cell
RQ	Respiratory Quotient
RVAD	Right Ventricular Assist Device
SI	“Système Internationale d’Unités”
SS	Staggered Square
STPD	Standard Temperatur and Pressure, Dry
SUPG	Streamline Upwind Petrov-Galerkin
THI	Texas Heart Institute
VAVD	Vacuum Assisted Venous Drainage

Symbols

a	wetted surface per unit of volume of bed [mm^{-1}]
a’	parameter
A	membrane surface area [m^2]
A′	parameter
$\overline{\mathbf{A}}$	velocity deformation tensor
A_f	gross frontal area [cm^2]
b’	parameter
BE	base excess [mmol/l]
B_{O_2}	oxygen binding capacity of hemoglobin [ml/g]
CO_2	carbon dioxide
C_A	concentration of species A [ml/l]
C_{Hb}	hemoglobin mass concentration [g/l]
C_{O_2}	total oxygen concentration [ml/l]
$C_{O_2 b}$	bound oxygen concentration [ml/l]
$C_{O_2 d}$	dissolved oxygen concentration [ml/l]
$C_{O_2 g}$	oxygen concentration in the gas phase [ml/l]
$C_{O_2 in}$	inlet oxygen concentration [ml/l]
$C_{O_2 max}$	maximum oxygen concentration [ml/l]
$C_{O_2 out}$	outlet oxygen concentration [ml/min]
d	fiber diameter [mm]
d_c	diameter of glass capillary [mm]

D_{AB}	diffusion coefficient of species A into B [cm²/s]
D_i	inside housing outer diameter [cm]
D_o	outside housing outer diameter [cm]
D_{O_2}	oxygen diffusion coefficient [cm²/s]
D_{O_2b}	oxygen diffusion coefficient of bound oxygen in blood [cm²/s]
D_{O_2d}	oxygen diffusion coefficient of dissolved oxygen in blood [cm²/s]
D_{O_2eff}	effective oxygen diffusion coefficient in blood[cm²/s]
D_{O_2p}	oxygen diffusion coefficient in plasma [cm²/s]
D_{O_2rbc}	oxygen diffusion coefficient in the red blood cell [cm²/s]
f	fractional saturation change
f	friction factor
Fe	iron atom
h	element width in the direction of the flow [*L*]
H	hydrogen atom
H’	heigth [*L*]
Hb	hemoglobin
Hct	hematocrit
j	Chilton-Colburn j-factor
K	mass transfer coefficient [cm/s] [ml/s/cm²]
K′	parameter
L	length of fiber compartment [cm]
L	unit of length
L’	length [*L*]
L^*	dimensionless channel length for oxygen transfer
L_b	blood path length [cm]
L_m	manifold length [cm]
L_{Hg}	displacement of mercury bead [mm]
m	parameter
m′	parameter
M	unit of mass
n	model parameter
n	Hill parameter

$\bar{\mathbf{n}}$	normal vector
N	parameter
N	number
N_2	nitrogen
N_{Eu}	Euler number
N_{Pe}	Péclet number
N_{Re}	Reynolds number
N_{Sc}	Schmidt number
N_{Sh}	Sherwood number
N_{St}	Stanton number
O_2	oxygen
p	pressure [Pa]
p	upwind parameter
p’	model parameter
pH	hydronium ion concentration of a solution
P_{CO_2}	carbon dioxide partial pressure [mmHg]
P_{O_2}	oxygen partial pressure [mmHg]
$\overline{P_{O_2}}$	cup-mixed oxygen partial pressure [mmHg]
P_{O_2g}	oxygen partial pressure in the gas phase [mmHg]
P_{O_2in}	inlet oxygen partial pressure [mmHg]
P_{O_2out}	outlet oxygen partial pressure [mmHg]
P_{O_2w}	oxygen partial pressure at the membrane surface [mmHg]
P_{50}	oxygen partial pressure at S_{O_2} =50 % [mmHg
Q	blood flow rate [l/min]
q	volume flux per unit length [mm³/s/mm]
q’	model parameter
Q’	flow rate per unit width of membrane [l/cm/min]
r	reaction term [ml/l/s]
r	radial coordinate
r’	parameter
R	parameter
R	mass transfer resistance

R^2	coefficient of determination
R_b	mass transfer resistance in blood phase
$\dot{R}_b$	reaction term of (bound) oxygen with hemoglobin
$\dot{R}_d$	reaction term of (dissolved) oxygen with hemoglobin
R_g	mass transfer resistance in gas phase
R_h	hydraulic radius [mm]
R_w	membrane mass transfer resistance
s’	model parameter
S_L	stream-wise pitch [mm]
S_{O_2}	oxygen saturation
S_{O_2in}	inlet oxygen saturation
S_{O_2out}	outlet oxygen saturation
S_T	cross-wise pitch [mm]
t	model parameter
$\bar{\mathbf{t}}$	deviatoric stress tensor [$M/L/T^2$]
T	temperature [°C]
T	unit of time
$\bar{\mathbf{u}}$	velocity vector [L/T]
U_m	mean velocity [L/T]
U_s	superficial velocity [L/T]
V_{air}	volume of air [ml]
V_{bed}	volume of bed [ml]
V_{void}	void volume [ml]
$\dot{V}_{O_2}$	oxygen transfer rate [ml/min]
W’	width [L]
x	cartesian coordinate [L]
y	cartesian coordinate [L]
z	cartesian coordinate [L]

Greek symbols

α	model parameter
α’	model parameter

α_{O_2}	Bunsen solubility coefficient of oxygen in blood [ml/ml/mmHg]
α_{O_2p}	Bunsen solubility coefficient of oxygen in plasma [ml/ml/mmHg]
α_{O_2rbc}	Bunsen solubility coefficient of oxygen in the red blood cell [ml/ml/mmHg]
α_{O_2water}	Bunsen solubility coefficient of oxygen in water [ml/ml/mmHg]
β	model parameter
β'	model parameter
β	parameter (oxyhemoglobin / upwinding)
$\dot{\gamma}$	shear rate [s^{-1}]
Γ	boundary
Γ_{per}	periodical boundary condition
Γ_{sym}	symmetry boundary condition
ε	parameter penalty function method
ε	porosity
ζ	upwind choice parameter
ζ	dimensionless distance
λ	sink term accounting for oxygen uptake by hemoglobin
μ	dynamic viscosity [*M/L/T*]
μ_∞	dynamic blood viscosity [mPa·s]
μ_p	dynamic plasma viscosity [mPa·s]
Π	second invariant of the velocity deformation tensor
ρ	density [kg/m³]
$\bar{\boldsymbol{\sigma}}$	stress tensor [$M/L/T^2$]
τ	shear stress [mPa]
τ_o	yield shear stress [mPa]
υ	kinematic viscosity [cm²/s]
φ	parameter
φ'	parameter
φ_i	i^{th} basis function
ξ	dimensionless characteristic length
X	parameter
Ω	domain

Subscripts

air	air
A	species A
b	blood
b	bound
B	species B
c	capillary
d	dissolved
e	element
eff	effective
f	frontal
g	gas phase
Hg	mercury
i	internal
i	iteration number
in	inlet
L	longitudinal
m	mean
max	maximum
n	normal
o	outside
o	yield shear stress subscript
out	outlet
p	plasma
per	periodical
rbc	red blood cell
s	superficial
sym	symmetry
t	tangential
T	transversal
w	water

Superscripts

k	iteration number

T	transpose operator

Operators

d	differential
D	differential
Δ	difference
Δ	Laplace operator [L^{-2}]
$\overline{\nabla}$	gradient operator [L^{-1}]
$\|\ \|$	2-norm
$\bar{}$	weighted mean
$\langle\ \rangle$	average
$\frac{d}{dX}$	derivative with respect to variable X
$\frac{\partial}{\partial X}$	partial derivative with respect to variable X
$\int$	integral operator

Units

mm	[L]	millimeter	10^{-3} m
ml	[L]	milliliter	10^{-6} m³
cm	[L]	centimeter	10^{-2} m
l	[L³]	liter	10^{-3} m³
min	[T]	minute	60 s
s	[T]	second	1 s
mPa	[M/T²/L]	milliPascal	10^{-3} Pa
g	[M]	gram	10^{-3} kg
kg	[M]	kilogram	1 kg
K		Kelvin	
°C		degrees Celsius	
mmHg	[L]	millimeter mercury	133.3 Pa

REFERENCES

<1> Society of cardiothoracic surgeons of Great Britain and Ireland: 2000.

<2> American Heart Association: 2000.

<3> Mockros LF and Leonard R: *Compact cross-flow tubular oxygenators.* ASAIO Trans, 1985. **31**: p. 628-633.

<4> Vaslef SN, Mockros LF, et al.: *Use of a mathematical model to predict oxygen transfer rates in hollow fiber membrane oxygenators.* ASAIO Trans, 1994. **40**: p. 990-996.

<5> Hessel EA and Hill AG: *Circuitry and cannulation techniques*, in *Cardiopulmonary Bypass: Principles and Practice*, Gravlee GP, Davis RF, et al., Editors. 2000, Lippincott Williams & Wilkins: Philadelphia. p. 69-97.

<6> Gravlee GP, Davis RF, et al.: *Cardiopulmonary Bypass: Principles and Practice*. 2 ed. 2000, Philadelphia: Lippincott Williams & Wilkins. 22-34.

<7> Gallletti PM and Colton CK: *Artificial lungs and blood-gas exchange devices*, in *Biomedical Engineering*. 1995. p. 1879-1897.

<8> Zapol WM: *Membrane lung perfusion for acute respiratory failure.* Surg Clin North Am, 1975. **55**: p. 603.

<9> Zapol WM, Snider MT, and Hill JD: *Extracorporeal membrane oxygenation in severe acute respiratory failure.* JAMA, 1979. **242**: p. 2193-2196.

<10> Galletti PM: *Cardiopulmonary bypass: a historical perspective.* Artificial Organs, 1993. **17**: p. 675-686.

<11> Rodkiewicz CM, Sinha P, and Kennedy JS: *On the application of a constitutive equation for whole human blood.* J Biomech Eng, 1990. **112**: p. 198-206.

<12> Barbee JH: *The effect of temperature on the relative viscosity of human blood.* Biorheology, 1973. **10**(1).

<13> Cokelet GR: *The rheology of human blood*, in *Biomechanics: its foundations and objectives*, Fung YC, Perrone N, and Anliker M, Editors. 1972, Prentice-Hall: New Jersey.

<14> De Wachter D: *Modellering van de dialysebehandeling bij nierfalen*, in *Laboratorium voor Hydraulica,, Vakgroep civiele techniek*. 1998, Universiteit Gent: Gent; .

<15> Walawender WP, Chen TY, and Cala DF: *An approximate Casson fluid model for tube flow of blood.* Biorheology, 1975. **12**: p. 111-119.

<16> Cooney DO: *Biomedical engineering principles: an introduction to fluid, heat, and mass transport processes*. 1976: Dekker.

<17> Casson N: *A flow equation for pigment-oil suspension of the printing ink type*, in *Rheology of Disperse Systems*, Mills CC, Editor. 1959, Pergamon Press: New York. p. 84-104.

<18> Zander R: *Oxygen solubility in normal human blood*, in *Adv Physiol Sci: Oxygen Transport to Tissue*, Kovach AGB, Dora E, et al., Editors. 1981, Pergamon Press: Oxford. p. 331-332.

<19> Perry RH and Green DW: *Perry's Chemical Engineers' Handbook*. 6 ed. 1984, New York: McGaw-Hill.

<20> Fricke H: *The electric conductivity of disperse systems.* J Gen Physiol, 1924. **6**: p. 741-746.

<21> Fricke H: *A mathematical treatment of the electric conductivity and capacity of disperse systems.* Phys Rev, 1924. **24**: p. 575-587.

<22> Ciuryla VT: *Oxygen diffusion in human blood plasma*, . 1975, Northwestern University; .

<23> Mortimer C: *Chemistry, A Conceptual Approach*. 1979, New York: D. Van Nostrand Company.

<24> Severinghaus JW: *Simple accurate equations for human blood oxygen dissociation computations.* J Appl Physiol: Respir Environ Exerc Physiol, 1979. **46**: p. 599-602.

<25> Goldstick TK: *Oxygen Transport*, in *Engineering Principles in Physiology*, Brown JHV and Gann DS, Editors. 1973, Academic Press: New York.

<26> Hill AV: *The possible effects of the aggregation of the molecules of hemoglobin on its dissociation curves.* J Physiol, 1910. **40**: p. iv-vii.

<27> Staub H: *Methode fur fortlaufenden Bestimmung des Gaswechsels isoliert durchstromter Organe im geschlossenen System.* Arch Exp Pathol Pharmacol, 1929. **162**: p. 420-427.

<28> Zienkiewicz O and Morgan K: *Finite elements and approximation*. 1983: John Wiley.

<29> Dick E: *Introduction to finite element techniques in computational fluid dynamics,* in *Introduction to Computational Fluid Dynamics*, Degrez G, Anderson J, et al., Editors. 1997, von Karman Institute, Annual Lecture Series: Rhode Saint Genese, Belgium.

<30> Cuvelier C, Segal A, and van Steenhoven AA: *Finite Element Methods and Navier-Stokes Equations*. 1986, Dordrecht: D Reidel Publishing Company.

<31> Segal A: *Sepran User Manual, Programmers Guide and Standard Problems*. 1984, Leidschendam: Ingenieursbureau Sepra.

<32> Pei JM: *Carbon dioxide and oxygen exchange in cross-flow and shell-and-tube artificial lungs,* in *Bioengineering Unit*. 1993, University of Strathclyde: Glasgow. p. 245; .

<33> Vaslef SN: *Analysis and design of an intravascular lung assist device, .* 1990, Northwestern University: Evanston; .

<34> Dierickx PW, De Somer F, et al.: *Hydrodynamic characteristics of artificial lungs.* ASAIO Trans, 2000. **46**: p. 532-535.

<35> Bird RB, Stewart WE, and Lightfoot EN: *Transport Phenomena*. 1960: John Wiley & Sons.

<36> Dierickx PW, De Wachter DS, and Verdonck PR: *Blood flow around hollow fibers.* Int J Artif Organs, 2000. **23**(9): p. 610-617.

<37> Dierickx PW, De Wachter DS, et al.: *Mass transfer characteristics of artificial lungs.* ASAIO Trans, Accepted for publication in the ASAIO Journal 2001.

<38> De Somer F, Dierickx PW, et al.: *Can an oxygenator design potentially contribute to air embolism in cardiopulmonary bypass? A novel method for the determination of the air removal capabilities of neonatal membrane oxygenators.* Perfusion, 1998. **13**: p. 157-163.

<39> Lissens J: *Stromingsgedrag door arteriële kindercanules,* in *Faculteit Geneeskunde*. 1999-2000, Universiteit Gent: Gent; .

<40> Simonin D and Barcouda M: *Measurements and predictions of turbulent flow entering a staggered tube bundle, .* 1988, Laboratoire Nationale d'Hydraulique: Chatou; .

<41> Segal G, Vuik K, and Kassels K: *On the implementation of symmetric and antisymmetric periodic boundary conditions for incompressible flow*. International Journal for Numerical Methods in Fluids, 1994. **18**: p. 1153-1165.

<42> Edwards DA, Shapiro M, et al.: *The influence of Reynolds number upon the apparant permeability of spatially periodic arrays of cylinders.* Physics of Fluids A: Fluid dynamics, 1990. **2**(1): p. 45-55.

<43> Launder BE and Massey TH: *The numerical prediction of viscous flow and heat transfer in tube banks.* Transactions of the ASME: Journal of Heat Transfer, 1978. **100**: p. 565-571.

<44> Shah VL: *Blood flow*, in *Advances in Transport Processes*, Mujumdar AS, Editor. 1980, Wiley Eastern Limited: New Dehli.

<45> Association for the Advancement of Medical Instrumentation: *Cardiovascular implants and artificial organs - blood gas exchangers*, . 1997, American National Standard / International Organization for Standards: Arlington, VA; .

<46> Chilton TH and Colburn AP: *Mass transfer (absorption) coefficients: prediction from data on heat transfer and fluid friction.* Ind Eng Chem, 1934. **26**: p. 1183-1187.

<47> Colburn AP: *A method of correlating forced convection heat transfer data and a comparison with fluid friction.* Trans AIChE, 1933. **29**: p. 174-210.

<48> Wicksramasinghe SR, Semmens MJ, and Cussler EL: *Mass transfer in various hollow fiber geometries.* Journal of Membrane Science, 1992. **69**: p. 235-250.

<49> Chen CJ and Wung TS: *Finite analytic solution of convective heat transfer for tube arrays in crossflow: part II - heat transfer analysis.* Transactions of the ASME: Journal of Heat Transfer, 1989. **111**: p. 641-648.

<50> Pearson D, Holden M, et al.: *A clinical evaluation of the performance characteristics of one membrane and five bubble oxygenators: gas transfer and gaseous microemboli production.* Perfusion, 1986. **1**: p. 15-26.

<51> Gourlay T, Fleming J, et al.: *Evaluation of a range of extracorporeal membrane oxygenators.* Perfusion, 1990. **5**: p. 117-133.

<52> Beckley P, Shinko P, and Sites J: *A comparison of gaseous emboli release in five membrane oxygenators.* Perfusion, 1997. **12**: p. 133-141.

<53> Sellman M, Ivert T, et al.: *Doppler ultrasound estimation of microbubbles in the arterial line during extracorporeal circulation.* Perfusion, 1990. **5**: p. 23-32.

<54> LeClair BP and Hamielec AE: *Viscous flow through particle assemblages at intermediate Reynolds numbers.* Industrial and Engineering Chemistry Fundamentals, 1970. **9**(4): p. 608-613.

<55> Hammond G and Bowley W: *Bubble mechanics and oxygen transfer.* J Thorac Cardiovasc Surg, 1976. **71**(3): p. 422-428.

<56> Gallagher E and Pearson D: *Ultrasonic identification of sources of gaseous microemboli during open heart surgery.* Thorax, 1973. **28**: p. 295-305.

<57> Hatteland K and Semb B: *Gas bubble detection in fluid lines by means of pulsed doppler ultrasound.* Scand J Thorac Cardiovasc Surg, 1985. **19**: p. 119-123.

<58> Pedersen T, Karlsen H, et al.: *Comparison of bubbles release from various types of oxygenators.* Scand J Thorac Cardiovasc Surg, 1987. **21**: p. 73-80.

<59> Friedman I, Gelman S, et al.: *The effects of intra-arterial microbubbles on normothermic and hypothermic dogs.* J Surg Res, 1962. **2**(1): p. 19-25.

<60> Spencer M, Lawrence G, et al.: *The use of ultrasonics in the determination of arterial aeroembolism during open-heart surgery.* Ann Thorac Surg, 1969. **8**(6): p. 489-497.

<61> Lar L, Lai L, and Ren L: *Massive arterial air embolism during cardiac operation: successful treatment in a hyperbaric chamber uder 3 ATA.* J Thorac Cardiovasc Surg, 1990. **100**(6): p. 928-930.

<62> Kol S, Ammar R, et al.: *Hyperbaric oxygenation for arterial air embolism during cardiopulmonary bypass.* Ann Thorac Surg, 1993. **55**: p. 401-403.

<63> Butler B: *Gaseous microemboli: a review.* Perfusion, 1990. **5**: p. 81-89.

<64> Kurusz M and Butler B: *Embolic events and cardiopulmonary bypass,* in *Cardiopulmonary Bypass: Principles and Practice*, Gravlee G, Davis R, and Utley J, Editors. 1993, Williams & Wilkins: Baltimore. p. 267-290.

<65> Pugsley W: *The use of Doppler ultrasound in the assessment of microemboli during cardiac surgery.* Perfusion, 1989. **4**: p. 115-122.

<66> Wright G, Furness A, and Haigh S: *Integral pulse frequency modulated ultrasound for the detection and quantification of gas microbubbles in flowing blood.* Perfusion, 1987. **2**(131-138).

<67> De Wachter DS, De Somer F, and Verdonck PR: *Extracorporeal circulation,* in *Intra- and Extracorporeal Fluid Dynamics*, Verdonck P, Editor. 1999.

<68> Gibbon JH: *An oxygenator with a large surface-volume ratio.* J Lab Clin Med, 1939. **24**: p. 1192.

<69> High KM, Bashein G, and Kurusz M: *Principles of oxygenator function: gas exchange, heat transfer, and operation,* in *Cardiopulmonary Bypass: Principles and Practice*, Gravlee GP, Davis RF, et al., Editors. 2000, Lippincott Williams & Wilkins: Philadelphia. p. 49-68.

<70> Sarns RD: *History of perfusion: Richard N. Sarns: Pioneer Biomedical Engineering*, . 1999; http://members.aol.com/amaccvpe/history/history.htm.

<71> Lawrence E: *History of Pefusion 1902 - 1932: Alexis Carrel: Forgotten hero in medicine*, ; http://members.aol.com/amaccvpe/history/history.htm.

<72> Shumacker HB: *The birth of an idea and the development of cardiopulmonary bypass*, in *Cardiopulmonary Bypass: Principles and Practice*, Gravlee GP, Davis RF, et al., Editors. 2000, Lippincott Williams & Wilkins: Philadelphia. p. 22-34.

<73> Le Gallois CJ: *Experiences sur le principe de la vie, notamment sur celui des mouvements du coeur, et sur le siege de ce principe; survies du rapport fait a la premiere classe de l'Institut sur celles relatives aux mouvements du coeur*, ed. d'Hautel. 1812, Paris.

<74> Brown-Sequard CE: *Recherches experimentales sur les proprietes physiologiques et les usages du sang rouge et du sang noir et de leurs principaux elements gazeux, l'oxygene et l'acide carbonique.* J Physiol Homme, 1858. **1**: p. 729-735.

<75> Wharton TG: *Thomas G Wharton Memorial Lecture.* Proc Am Acad Cardiovasc Perf, 1985. **6**.

<76> von Schroder W: *Uber die Bildungstatte des Harnstoffs.* Arch Exp Pathol Pharmacol, 1882. **15**: p. 364-402.

<77> Clark LC, Gollan F, and Gupta V: *The oxygenation of blood by gas dispersion.* Science, 1950. **111**: p. 85-87.

<78> von Euler ES and Heymans C: *An oxygenator for perfusion experiments.* J Physiol, 1932. **74**: p. 2P-3P.

<79> von Frey M and Gruber M: *Untersuchungen uber den Stoffwechsel isolierte Organe. Ein Respiration-Apparat fur isolierte Organe.* Virchow's Arch Physiol, 1885. **9**: p. 519-532.

<80> Richards AN and Drinker CK: *An apparatus for perfusion of isolated organs.* J Pharmacol Exp Ther, 1915. **7**: p. 467-483.

<81> Bayliss CE, Fee AR, and Ogden EA: *Method of oxygenating blood.* J Physiol, 1928. **66**: p. 443-448.

<82> Daly IB and Thorpe WV: *An isolated mammalian heart preparation capapble of performing work for long periods.* J Physiol, 1933. **79**: p. 199-217.

<83> Patterson SW and Starling EH: *On the mechanical features which determine the output of the ventricles.* J Physiol, 1914. **48**: p. 357-379.

<84> Hemingway A: *Some observations on the perfusion of the isolated kidney by a pump.* J Physiol, 1913. **71**: p. 201-213.

<85> Brukhonenko S and Tchetchuline S: *Experiences avec la tête isolée du chien. 1. Technique et conditions des experiences.* J Physiol Pathol Gen, 1929. **27**: p. 31-45.

<86> Binet L and Mayer C: *Technique nouvelle de perfusion du sanguine.* Comp Rend Acad Sci, 1929. **189**: p. 1330-1331.

<87> Jacobi C: *Ein Beitrag zur Technik der kunstliechen Durchblutung ueberlebender Organe.* Arch Exp Pathol Pharmacol, 1895. **36**: p. 330-348.

<88> Brukhonenko S: *Circulation artificielle du sang dans l'organisme entier d'un chien avec coeur exclus.* J Physiol Pathol Gen, 1929. **27**: p. 257-272.

<89> Lillehei CW, Cohen M, and Warden HE: *Direct vision intracardiac surgery: by means of controlled cross circulation or continuous arterial reservoir perfusion for correction of ventricular septal defects, atrio-ventricularis communis, isolated infundibular pulmonic stenosis, and tetralogy of Fallot*. in *Proceedings of Henry Ford Hospital Symposium*. 1955. Philadelphia.

<90> Lillehei CW: *Controlled cross circulation for direct vision intracardiac surgery correction of ventricular septal defects, atrioventricularis communis and tetralogy of Fallot.* Postgrad Med, 1955. **17**: p. 388-396.

<91> Bing RJ: *Lindbergh and the biologic sciences (a personal reminiscence).* Tex Heart Inst J, 1987. **14**: p. 231-237.

<92> Carrel A and Lindbergh CA: *The culture of organs*. 1938, New York: Paul B. Hoeber.

<93> Lindbergh CA: *Autobiography of values*. 1977, New York: Harcourt Brace Jovanovich.

<94> Lindbergh CA: *An apparatus for the culture of whole organs.* J Exp Med, 1935. **62**: p. 409-432.

<95> McLean J: *The discovery of heparin.* Circulation, 1959. **19**: p. 75-78.

<96> Bigelow WG, Callaghan JC, and Hopps JA: *General hypothermia for experimental intracardiac surgery.* Ann Surg, 1950. **132**: p. 531-539.

<97> Lewis FJ and Taufic M: *Closure of atrial septal defects with the aid of hypothermia; experimental accomplishments and the report of one successful case.* Surgery, 1953. **33**: p. 52-59.

<98> Lewis FJ: *Some physiologic concepts of hypothermia and their applications to cardiac surgery.* J Thorac Surg, 1954. **28**: p. 463-480.

<99> Swan H, Zeavin I, and Blount SG: *Surgery by direct vision in the open heart during hypothermia.* JAMA, 1953. **153**: p. 1081-1085.

<100> Dennis C, Spreng DS, and Nelson GE: *Development of a pump-oxygenator to replace the heart and lungs: an apparatus applicable to human patients and application to one case.* Ann Surg, 1951. **134**: p. 709-721.

<101> Dogliotti AM: *Clinical use of the artificial circulation with a note on intra-arterial transfusion.* Bull Johns Hopkins Hosp, 1952. **90**: p. 131-133.

<102> Helmsworth JA, Clark LC, and Kaplan S: *Clinical use of extracorporeal oxygenation with oxygenator-pump.* JAMA, 1952. **150**: p. 451-453.

<103> Helmsworth JA, Clark LC, and Kaplan S: *An oxygenator pump for use in total bypass of heart and lungs.* J Thorac Surg, 1953. **26**: p. 617-631.

<104> The Providence Journal Company: *Into the heart: a medical odyssey*, . 1999; http://www.projo.com/.

<105> Gibbon JH: *Artificial maintenance of circulation during experimental occlusion of pulmonary artery.* Arch Surg, 1937. **34**(1105-1131).

<106> Gibbon JH: *Application of a mechanical heart and lung apparatus to cardiac surgery.* Minnesota Med, 1954. **37**: p. 171-180.

<107> Kirklin JW: *Open heart surgery at the Mayo Clinic - the 25th anniversary.* Proc Mayo Clin, 1980. **50**(339-341).

<108> Andreason AT and Watson F: *Experimental cardiovascular surgery.* Br J Surg, 1952. **39**: p. 548-551.

<109> Cohen M, Hammerstrom RW, and Spellman MW: *The tolerance of the canine heart to temporary complete vena caval occlusion.* Surg Forum, 1952. **3**: p. 172-177.

<110> Gibbon JH: *The maintenance of life during experimental occlusion of the pulmonary artery followed by survival.* Surg Gynecol Obstet, 1939. **69**: p. 602-614.

<111> Cohen M and Lillehei CW: *A quantitative study of the "azygos factor" during vena caval occlusion in the dog.* Surg Gynecol Obstet, 1954. **98**: p. 225-232.

<112> Cohen M and Lillehei CW: *Autogenous lung oxygenator with total cardiac bypass for intracardiac surgery.* Surg Forum, 1953. **4**: p. 34-41.

<113> Dodrill FD, Hill E, and Gerish RA: *Some physiologic aspects of the artificial heart problem.* J Thorac Surg, 1952. **24**: p. 134-150.

<114> Zuhdi N, McCollough B, and Carey J: *Double helical reservoir heart lung machine designed for hypothermic perfusion primed with five percent glucose in water inducing hemodilution.* Arch Surg, 1961. **82**: p. 320-325.

<115> Zuhdi N, McCollough B, and Carey J: *Hypothermic perfusion for open heart surgical procedures - report of the use of a heart lung machine primed with five*

percent dextrose in water inducing hemodilution. J Int Coll Surg, 1961. **35**: p. 319-326.

<116> DeWall R, Lillehei CW, and Sellers R: *Hemodilution perfusions for open heart surgery.* N Engl J Med, 1962. **266**: p. 1078-1084.

<117> DeWall R and Lillehei CW: *Simplified total body perfusion-reduced flows, moderate hypothermia, and hemodilution.* JAMA, 1962. **179**: p. 430-434.

<118> Lillehei WC: *Historical development of cardiopulmonary bypass in Minnesota,* in *Cardiopulmonary Bypass: Principles and Practice*, Gravlee GP, Davis RF, et al., Editors. 2000, Lippincott Williams & Wilkins: Philadelphia. p. 3-21.

<119> Lillehei CW, Varco RL, and Cohen M: *The first open heart repairs of ventricular septal defect, atrioventricular communis, and tetralogy of Fallot using extracorporeal circulation by cross circulation: a 30-year follow-up.* Ann Thorac Surg, 1986. **41**: p. 4-21.

<120> Gott VL: *C. Walton Lillehei, M.D., Ph.D. 1918 - 1999,* ; http://www.ctsnet.org/home/vgott.

<121> Mustard WT and Thomson JA: *Clinical experience with the artificial heart lung preparation.* J Can Med Assoc, 1957. **76**: p. 265-269.

<122> Campbell GS, Vernier R, and Varco R: *Traumatic ventricular septal defect. Report of two cases.* J Thorac Surg, 1959. **37**(496-501): p. 364-371.

<123> Campbell GS, Crisp NW, and Brown EB: *Total cardiac bypass in humans utilizing a pump and heterologous lung oxygenator (dog lungs).* Surgery, 1956. **40**: p. 364-371.

<124> Warden HE, DeWall RA, and Read RC: *Total cardiac bypass utilizing continuous perfusion from a reservoir of oxygenated blood.* Proc Soc Exp Biol Med, 1955. **90**: p. 246-250.

<125> Warden HE, Read RC, and DeWall RA: *Direct vision intracardiac surgery by means of a reservoir of "arterialized venous" blood.* J Thorac Surg, 1955. **30**: p. 649-657.

<126> Jones RA, Donald DE, and Swan HJ: *Apparatus of the Gibbon type for mechanical bypass of the heart and lungs.* Proc Mayo Clin, 1955. **30**: p. 105-113.

<127> Donald DE, Harshbarger HG, and Hetzel PS: *Experiences with a heart lung bypass (Gibbon type) in the experimental laboratory.* Proc Mayo Clin, 1955. **30**: p. 113-115.

<128> Kirklin JW, DuShane JW, and Patrick RT: *Intracardiac surgery with the aid of a mechanical pump oxygenator system (Gibbon type): report of eight cases.* Proc Mayo Clin, 1955. **30**: p. 201-206.

<129> Kirklin JW, McGoon DC, and Patrick RT: *What is adequate perfusion?*, in *Extracorporeal Circulation*, Allen JG, Editor. 1958, Thomas, C: Springfield. p. 125-138.

<130> Cross FS, Berne RM, and Hirose Y: *Description and evaluation of a rotating disc type reservoir oxygenator.* Surg Forum, 1956. **7**: p. 274-278.

<131> Cross FS, Berne RM, and Hirose Y: *Evaluation of a rotating disc-type oxygenator: in vitro and in vivo gas exchange measurement*. in *Society for Experimental Biology and Medicine*. 1956.

<132> Kay EB, Zimmerman HA, and Berne RM: *Certain clinical aspects in the use of the pump oxygenator.* JAMA, 1956. **162**: p. 639-641.

<133> Bjork VO, Sternlieb JJ, and Davenport C: *From the spinning disc to the membrane oxygenator for open-heart surgery.* Scand J Thor Cardiovasc Surg, 1985. **19**: p. 207-216.

<134> DeWall RA, Warden HE, and Read RC: *A simple, expendable, artificial oxygenator for open heart surgery.* Surg Clin North Am, 1956. **36**: p. 1025-1034.

<135> Lillehei CW, DeWall RA, and Read RC: *Direct vision intracardiac surgery in man using a simple, disposable artificial oxygenator.* Dis Chest, 1956. **29**: p. 1-8.

<136> Gott VL, Sellers RD, and DeWall RA: *A disposable unitized plastic sheet oxygenator for open heart surgery.* Dis Chest, 1957. **32**: p. 615-625.

<137> Gott VL, DeWall RA, and Paneth M: *A self-contained, disposable oxygenator of plastic sheet for intracardiac surgery.* Thorax, 1957. **12**: p. 1-9.

<138> Gollan F: *Oxygenation of circulating blood by dispersion, coalesence and surface tension separation.* J Appl Physiol, 1956. **8**: p. 571.

<139> Rygg IG and Kyvsgaard E: *A disposable polyethylene oxygenator system applied in a heart-lung machine.* Acta Chir Scand, 1956. **112**: p. 443-447.

<140> DeWall RA, Lillehei CW, and Vareo RL: *The helix reservoir pump-oxygenator.* Surg Gynecol Obstet, 1957. **104**(699).

<141> Kalke BR, Casteneda A, and Lillehei CW: *A clinical evaluation of the new Temptrol (Bentley) disposable blood oxygenator.* The Journal of Thoracic and Cardiovascular Surgery, 1969. **57**: p. 679-687.

<142> DeWall RA, Bentley DJ, and Hirose M: *A temperature controlling (omnithermic) disposable bubble oxygenator for total body perfusion.* Dis Chest, 1966. **49**: p. 207-211.

<143> Bartlett RH and Harken DE: *Instrumentation for cardiopulmonary bypass-past, present, and future.* Medical Instrumentation, 1976. **10**: p. 119-124.

<144> Hessel EA: *Cardiopulmonary bypass circuitry and cannulation techniques*, in *Cardiopulmonary Bypass: Principles and Practice*, Gravlee GP, Davis RF, and Utley JR, Editors. 1993, Lippincott Williams & Wilkins: Philadelphia. p. 55-92.

<145> Peirce EC: *The membrane versus bubble oxygenator controversy.* Ann Thorac Surg, 1980. **29**(6): p. 497-499.

<146> Massimino RJ and Maurer WG: *Membrane versus bubbler.* The Journal of Extra-Corporeal Technology, 1983. **15**: p. 156-161.

<147> Kalshoven D, Cameriengo L, and Dearing J: *Membrane oxygenators: a few observations.* The Journal of Extra-Corporeal Technology, 1983. **15**: p. 41-44.

<148> Dennis C: *Perspective in review: one group's struggle with development of a pump-oxygenator.* ASAIO Trans, 1985. **31**: p. 1-11.

<149> Crafoord CA and Senning A: *Utvecklingen av extra-corporeal cirkulation med hjart-lungmaskin.* Nordisk Med, 1956. **56**: p. 1263.

<150> Clowes GH, Neville WE, and Hopkins A: *Factors contributing to the success of failure in the use of a pump oxygenator for complete bypass of the heart and lung, experimental and clinical.* Surgery, 1954. **36**: p. 557-579.

<151> Clowes GH and Neville WE: *The membrane oxygenator*, in *Extracorporeal Circulation*, Allen JG, Editor. 1958, Thomas, C: Springfield. p. 81-100.

<152> Melrose DM: *A mechanical heart-lung machine for use in man.* Br Med J, 1953. **2**: p. 57-66.

<153> Gerbode F, Osborn JJ, and Bramson ML: *Experiences in the development of a membrane heart-lung machine.* Am J Surg, 1967. **114**: p. 16-23.

<154> Kolff WJ and Berk HT: *Artificial kidney: dialyzer with great area.* Acta Med Scand, 1944. **117**: p. 121-134.

<155> Keck PS and Meserko JJ: *History of perfusion: Willem J. Kolff, Pioneer in Artificial Organs*, , The Cleveland Clinic Foundation; http://members.aol.com/amaccvpe/history/history.htm.

<156> Kolff WJ and Balzer RR: *Artificial coil lung.* ASAIO Trans, 1955. **1**: p. 39-42.

<157> Kolff WJ, Effler DB, and Groves LJ: *Disposable membrane oxygenator (heart-lung machine) and its use in experimental surgery.* Cleve Clin Q, 1956. **23**: p. 69-97.

<158> Clowes GH, Hopkins AL, and Neville WE: *An artificial lung dependent upon diffusion of oxygen and carbon dioxide through plastic membranes.* J Thorac Surg, 1956. **32**: p. 630-637.

<159> Galletti PM and Brecher GA: *Heart Lung Bypass*. 1962, New York: Grune and Stratton.

<160> Boers M, van den Dungen JJ, and Karlicek GF: *Two membrane oxygenators and a bubbler. A clinical comparison.* Ann Thorac Surg, 1983. **35**: p. 455-462.

<161> Landé AJ, Dos SJ, et al.: *A new membrane oxygenator-dialyzer.* Surg Clin North Am, 1967. **47**: p. 1461-1470.

<162> Peirce EC: *The membrane lung, its excuse, present status, and promise.* J Mt Sinai Hosp, 1967. **34**: p. 437.

<163> Peirce EC and Dibelius NR: *The membrane lung: studies with a new high permeability co-polymer membrane.* ASAIO Trans, 1968. **14**: p. 220-226.

<164> Galletti PM, Snider MT, and Silbert-Aidan D: *Gas permeability of plastic membrane for artificial lungs.* Med Res Eng, 1966. **5**(2): p. 20-23.

<165> Bramson RH, Osborn JJ, and Main FB: *A new disposable membrane oxygenator with integral heat exchange.* The Journal of Thoracic and Cardiovascular Surgery, 1965. **50**: p. 391-400.

<166> Buchwald D and Klak K: *A short history of extracorporeal circulation*, . 1997; http://www.ruhr-uni-bochum.de/~buchwdbs/kt2/kt19e.htm#Anfang.

<167> Carlson RG, Landé AJ, et al.: *The Landé-Edwards membrane oxygenator during heart surgery.* The Journal of Thoracic and Cardiovascular Surgery, 1973. **66**(6): p. 894-905.

<168> Landé AJ, Edwards L, and Block JH: *Prolonged cardiopulmonary support with a practical membrane oxygenator.* ASAIO Trans, 1970. **16**: p. 352-356.

<169> Landé AJ, Fillmore SJ, et al.: *24 hour venous-arterial perfusion of awake dogs with a simple membrane oxygenator.* ASAIO Trans, 1969. **15**: p. 181-186.

<170> Drinker PA: *Progress in membrane oxygenator design.* Anesthesiology, 1972. **37**: p. 242-260.

<171> Kolobow T and Bowman RL: *Construction and evaluation of an alveolar membrane artificial heart-lung.* ASAIO Trans, 1963. **9**: p. 238-242.

<172> Music K, Horgan WJ, and Richards R: *Controversy concerning the use of membrane oxygenators.* Proc Am Acad Clin Perf, 1982. **3**: p. 17-19.

<173> Gille JP, Trudell L, and Snider MT: *Capability of the microporous membrane-lined, capillary oxygenator in hypercapnic dogs.* ASAIO Trans, 1970. **16**: p. 365-374.

<174> Lautier A, Rey P, and Bizot J: *Comparison of gaseous transport through synthetic membranes for oxygenators.* ASAIO Trans, 1969. **15**: p. 144-150.

<175> Dantowitz P and Borsanyi A: *Blood oxygenator with preformed, membrane lined channels*, in *Artificial Heart Program Proceedings*, Hegyeli R, Editor. 1969, Government Printing Office: Washington D.C. p. 339-346.

<176> Hill A: *Symposium on extracorporeal oxygenation. New technology. Recent Advancement in Cardiopulmonary Bypass*. in *Fifth World Congress of the ISAO*. 1985. Chicago.

<177> Ross IM and Kiernan M: *Roller pump vacuum ventilation of the Sci-Med Membrane Oxygenator.* Proc Am Acad Clin Perf, 1983. **4**: p. 41-43.

<178> Ross IM and Christman EW: *Carbon dioxide flush and vacuum priming of the Travenol Membrane Oxygenator.* Proc Am Acad Clin Perf, 1982. **3**: p. 58-59.

<179> *New product information.* The Journal of Extra-Corporeal Technology, . **14**: p. A18.

<180> Elgas RJ and Gordon TM: *Blood oxygenator*, . 1984: US. p. 562; .

<181> Bodell BR, Head JM, and Head LR: *A capillary membrane oxygenator.* The Journal of Thoracic and Cardiovascular Surgery, 1963. **46**: p. 639-650.

<182> Wilson R, Shepley DJ, and Lewellyn-Thomas E: *A membrane oxygenator with low priming volume for extracorporeal circulation.* Can J Surg, 1965. **8**: p. 309-311.

<183> deFilippi RP, Tompkins FC, and Porter JH: *The capillary membrane blood oxygenator: in vitro and in vivo gas exchange measurement.* ASAIO Trans, 1968. **14**: p. 236-241.

<184> Dorson WJ, Baker E, and Hull H: *A shell and tube oxygenator.* ASAIO Trans, 1968. **14**: p. 242-249.

<185> Dutton RC, Mather FW, and Walher SN: *Development of a new hollow-fiber membrane oxygenator.* ASAIO Trans, 1971. **17**: p. 331-336.

<186> Zingg W: *Membrane oxygenator for infants.* ASAIO Trans, 1967. **13**: p. 334-337.

<187> Sinkewich MG, Meserko JJ, et al.: *Clinical evaluation of the Terumo hollow fiber membrane oxygenator.* Proc Am Acad Clin Perf, 1982. **3**: p. 13-16.

<188> Sinkewich M, Ogella D, and Golding LR: *Early clinical experiences with the new Bentley Oxygenator System - Capillary Membrane (BOS-CM).* Proc Am Acad Clin Perf, 1984. **5**: p. 125-129.

<189> Gassmann CJ, Balbraith GD, and Smith RG: *Evaluation of three types of membrane oxygenators and their suitability for use with pulsatile flow.* The Journal of Extra-Corporeal Technology, 1987. **19**(3): p. 297-304.

<190> Iatridis A, Chan T, and Thompson R: *Experimental and clinical trials with the extracorporeal hollow fiber lung.* Proc Am Acad Clin Perf, 1985. **6**: p. 47-50.

<191> Alpha D, King E, and Bicknell DA: *Clinical evaluation of the extracorporeal Maxima hollow fiber membrane.* Proc Am Acad Cardiovasc Perf, 1986. **7**: p. 32-34.

<192> Dyga RM and Gibbs BW: *Clinical evaluation of the Cobe closed reservoir membrane system. CML Duo reference.* Proc Am Acad Clin Perf, 1992. **13**: p. 122-124.

<193> Bauermeister U: *Multilayer hollow fiber wound body*, . 1990: US. p. 617; .

<194> De Somer F, De Smet D, and Vanackere M: *Clinical evaluation of a new hollow fibre membrane oxygenator.* Perfusion, 1994. **9**: p. 57-64.

<195> Bearss MG, Bolles R, and Brennan K: *A multi-center trial with a modified design of the Sarns membrane oxygenator.* J Extra-Corp Technol, 1992. **24**: p. 49-51.

<196> Lund L: *Hollow fiber membrane permeability analysis*, ; http://info.pitt.edu/~wfedersp/Brochure/Projects2.html.

<197> Nobel A: *Technical product reference OXYPHAN: Oxyray Manual*, . 1994, Akzo Nobel; .

<198> Miller MJ: *Membrane material used in the Cobe Optima hollow fiber membrane oxygenator*, . 1996, Cobe Cardiovascular Inc: Arvada; .

<199> Gaylor JD, Hickey S, et al.: *Membrane oxygenators: influence of design on performance.* Perfusion, 1994. **9**: p. 173-180.

<200> COBE: *Compendium of scientific data for the Optima adult hollow fiber oxygenator*, . 1996, COBE Cardiovascular Inc; .

<201> Kolobow T, Borelli M, and Spatola R: *Artificial lung (oxygenators).* Artificial Organs, 1986. **10**(5): p. 370-377.

<202> Zwischenberger JB and Bartlett RH: *An introduction to extracorporeal life support*, . 1996; http://www.med.umich.edu/ecmo.

<203> Hill JD, O'Brien TG, et al.: *Prolonged extracorporeal oxygenation for acute post-traumatic respiratory failure (shock-lung syndrome): use of the Bramson membrane lung.* N Engl J Med, 1972. **286**: p. 629-634.

<204> National Heart LaBI: *Extracorporeal support for respiratory insufficiency. A collaborative study*, . 1979, National Heart, Lung and Blood Institute; .

<205> Gattinoni L, Pesenti A, et al.: *Treatment of acute respiratory failure with low-frequency positive-pressure ventilation and extracorporeal removel of carbon dioxide.* Lancet, 1980. **2**: p. 292-294.

<206> Smith L, Parr T, and Macrae D: *What is ECMO*, ; http://www.ich.bpmf.ac.uk/.

<207> Mortensen J: *Intravascular oxygenator: a new alternative method for augmenting blood gas transfer in patients with acute respiratory failure.* Artificial Organs, 1992. **16**(1): p. 75-82.

<208> Mortenson JD and Berry G: *Conceptual and design features of a practical, clinically effective intravenous mechanical blood oxygen / carbon dioxide exchange device (IVOX).* Int J Artif Organs, 1989. **12**: p. 384-389.

<209> Damm G: *An engineer in the medical world.* Artificial Organs, 1994. **18**(11): p. 783-784.

<210> Cokelet G: *The rheology of human blood*, in *MIT*. 1963: Cambridge, Mass; .

<211> Scott-Blair GW: *An equation for the flow of blood, plasma and serum through glass capillaries.* Nature, 1959. **183**: p. 613-614.

<212> Charm SE and Kurland GS: *Viscometry of human blood for shear rates 0 - 100,000 sec-1.* Nature, 1965. **206**: p. 617-618.

<213> Cho YI and Kensey KR: *Effects of the non-Newtonian viscosity of blood on flows in a diseased arterial vessel. Part 1: steady flows.* Biorheology, 1991. **28**: p. 241-262.

<214> Mujumdar AS and Mashelkar RA: *Advances in transport Processes*. Vol. 1. 1980, New Delhi: Wiley Eastern Limited.

<215> Ganong WF: *Review of Medical Physiology*. 1995, Norwalk, Connecticut: Appleton & Lange.

<216> Dorrington KL: *Anaesthetic and Extracorporeal Gas Transfer*. 1989, New York: Clarendon Press - Oxford.

<217> Lax E and Synowietz C: *Taschenbuch für Chemiker und Physiker*. 1967, Berlin: Springer-Verlag.

<218> Siggaard-Andersen O, Wimberley PD, et al.: *A mathematical model of the hemoglobin-oxygen dissociation curve of human blood and of the oxygen partial pressure as a function of temperature.* Clinical Chemistry, 1984. **30**(10): p. 1646-1651.

<219> Thomas LJ: *Algorithms for selected blood acid-base and blood gas calculations.* J Appl Physiol, 1972. **33**: p. 154-158.

<220> Nordby GL and Ellis JH: *Efficient computer subroutines for interconversion of oxygen tension and saturation.* J Appl Physiol: Respir Environ Exerc Physiol, 1981. **51**: p. 1080-1085.

<221> Gabel RA: *Algorithms for calculating and correcting blood-gas and acid-base variables.* Respir Physiol, 1980. **42**: p. 211-232.

<222> Lightfoot EM: *Low order approximations for membrane blood oxygenators.* AIChE J, 1968. **14**: p. 669-670.

<223> Weissman MH: *Analysis of oxygen and carbon dioxide diffusion into flowing blood*, . 1967, Norhtwestern University; .

<224> Mikic BB, Benn J, and Drinker PA: *Upper and lower bounds on oxygen transfer rates: a theoretical consideration.* Ann Biom Eng, 1972. **1**: p. 212-220.

<225> Margaria R: *A mathematical treatment of the blood dissociation curve for oxygen.* Clinical Chemistry, 1963. **9**: p. 745-762.

<226> Harris GW, Tompkins FC, et al.: *Development of capillary membrane blood oxygenators*, in *Blood Oxygenation*, Hershey D, Editor. 1970, Plenum Press.

<227> Welty JR, Wicks CE, and Wilson RE: *Fundamentals of Momentum, Heat and Mass Transfer*. 1984, New York: John Wiley & Sons.

<228> Lautier A, Grossin R, and Laurent I: *The use of mathematical and physical models for optimization of oxygenators.* ASAIO Trans, 1971. **17**: p. 303-308.

<229> Colton CK: *Fundamentals of gas transport in blood*, in *Artificial Lungs for Acute Respiratory Failure: Theory and Practice*, Zapol WM and Qvist J, Editors. 1976, Academic Press: New York. p. 1-42.

<230> Weissman MH and Mockros LF: *Oxygen transfer to blood flowing in round tubes.* Transactions ASCE: J Eng Mech Div, 1967. **93**: p. 225-244.

<231> Brooks AN and Hughes TJ: *Streamline upwind / Petrov Galerkin formulation for convection dominated flows with particular emphasis on the incompressible Navier-Stokes equation.* Computer Methods in Applied Mechanics and Engineering, 1982. **32**: p. 199-259.

<232> Mizukami A and Hughes TJ: *A Petrov-Galerkin finite element method for convection-dominated flows: an accurate upwinding technique for satisfying the maximum principle.* Computer Methods in Applied Mechanics and Engineering, 1985. **50**: p. 181-193.

<233> Rice JG and Schnipke RJ: *A monotone streamline upwind finite element method for convection-dominated flows.* Computer Methods in Applied Mechanics and Engineering, 1984. **48**: p. 313-327.

<234> Hughes T, Mallet M, and Mizukami M: *A new finite element formulation for computational fluid dynamics: II. Beyond SUPG.* Computer Methods in Applied Mechanics and Engineering, 1986. **54**: p. 341-355.

<235> Spaeth EE: *Blood oxygenation in extracorporeal devices: theoretical considerations.* CRC Crit Rev Bioeng, 1973. **1**: p. 383-417.

<236> Spaeth EE: *The oxygenation of blood in artificial devices*, in *Blood Oxygenation*, Hershey D, Editor. 1970, Plenum Press: New York.

<237> Dorson WJ: *Oxygenation of Blood for Clinical Applications*. Blood oxygenation, ed. Hershey. 1970, New York: Plenum Press.

<238> Dorson WJ, Larsen KG, et al.: *Oxygen transfer to blood: data and theory.* ASAIO Trans, 1971. **17**: p. 309.

<239> Merril EW, Benis AM, et al.: *Pressure-flow relations of human blood in hollow fibers at low flow rates.* J Appl Physiol, 1965. **20**: p. 954-967.

<240> Jones AL: *On the flow of blood in a tube.* Biorheology, 1966. **3**: p. 183-188.

<241> Dorson WJ and Hershey D: *Blood flow through long capillary tubes*. in *62nd National Meeting AIChE*. 1967.

<242> Marx TI, Snyder WE, et al.: *Diffusion of oxygen into a film of whole blood.* J Appl Physiol, 1960. **15**: p. 1123-1129.

<243> Marx TI, Baldwin BR, and Miller DR: *Factors influencing oxygen uptake by blood in membrane oxygenators.* Ann Surg, 1962. **156**: p. 204-213.

<244> Keller KH and Friedlander SK: *The steady state transport of oxygen through hemoglobin solutions.* J Gen Physiol, 1966. **49**(4): p. 663-687.

<245> Keller KH and Friedlander SK: *Diffusivity measurements of human methemoglobin.* J Gen Physiol, 1966. **49**(4): p. 681-687.

<246> Weissman MH and Mockros LF: *Gas transfer to blood flowing in coiled circular tubes.* Transactions ASCE: J Eng Mech Div, 1968. **94**: p. 857.

<247> Weissman MH and Mockros LF: *Oxygen and carbon dioxide transfer in membrane oxygenators.* Med Biol Eng, 1969. **7**: p. 169-184.

<248> Buckles RG, Merril EW, and Gilliland ER: *Analysis of oxygen absorption in a tubular membrane oxygenator*. AIChE J, 1968. **14**(5): p. 703-708.

<249> Spaeth EE and Friedlander SK: *The diffusion of oxygen, carbon dioxide and inert gas in flowing blood.* Biophys, 1967. **7**: p. 827-851.

<250> Martisovits V and Veis S: *Quantitative description of blood oxygenation process in oxygenator for extracorporeal circulation.* Bulletin of Mathematical Biophysics, 1967. **29**: p. 485-497.

<251> Thews G: *The theory of oxygen transport and its application to gaseous exchange in the lung*, in *Oxygen Transport in Blood and Tissues*, Wetol D, Editor. 1968, Georg Thieme Verlag: Stuttgart.

<252> Villarroel F, Lanham CE, et al.: *Gas transfer to blood flowing in semipermeable tubes under steady state and pulsatile flow conditions*. in *AIChE Meeting*. 1970. Puerto Rico: Harry Diamond Laboratories Report.

<253> Villarroel F: *Oxygen-carbon dioxide transport to and from blood flowing under pulsatile conditions in semipermeable tubes*, . 1970, Harry Diamond Laboratories Report; .

<254> Villarroel F and Lanham CE: *A design calculation method for capillary tube oxygenators.* Med Biol Eng, 1973. **11**: p. 732-742.

<255> Smeby L and Grimsrud L: *Theoretical investigation of mass transfer in membrane oxygenators.* Med Biol Eng, 1974. **12**: p. 698-705.

<256> Oomers JM and Spaan JA: *A generalized advancing front model describing the oxygen transport in flowing blood*. in *Proceedings of the 2nd International Symposium on Oxygen Transport to Tissue*. 1975. Mainz, West Germany: Plenum.

<257> Mockros LF and Gaylor JD: *Artificial lung design: tubular membrane units.* Med Biol Eng, 1975. **13**: p. 171-181.

<258> Gaylor JD and Mockros LF: *Artificial lung design: sheet membrane units.* Med Biol Eng, 1975. **13**: p. 425-435.

<259> Shah SS and Leonard EF: *Bloodless evaluation of blood oxygenators.* Ann Biom Eng, 1983. **11**: p. 67-81.

<260> Thews G: *Ein Verbahren zur Berchnung des O2-Diffusionskoeffizienten aus Messungen der Sauerstoffdiffusion in Häemoglobin und Myoglobin Lösungen.* Pflueger Arch Gesamte Physiol Menschen Tiere, 1957. **265**: p. 138-153.

<261> Roughton FJ: *Diffusion and simultaneous chemical reaction velocity in hemoglobin solutions and red cell suspensions.* Progr Biophys Chem, 1959. **9**: p. 55-104.

<262> Hill AV: *The diffusion of oxygen and lactic acid through tissues.* Proc Roy Soc Lond [Biol], 1929. **104**: p. 39-96.

<263> Dorson WJ and Voorhees ME: *Analysis of oxygen and carbon dioxide transfer in membrane lungs*, in *Artificial Lungs for Acute Respiratory Failure: Theory and Practice*, Zapol WM and Qvist J, Editors. 1976, Academic Press: New York. p. 43-68.

<264> Curtis RM and Eberhart RC: *Normalization of oxygen transfer data in membrane oxygenators.* ASAIO Trans, 1974. **20**: p. 210-218.

<265> Mayes P: *An application of the method of lines in biological mass transfer.* Biotechnology Progress, 1985. **1**(4): p. 269-272.

<266> Colton CK and Drake RF: *Effect of boundary conditions on oxygen transport to blood flowing in a tube.* Chem Eng Progress Symposium Series, 1971. **114**(67): p. 88-95.

<267> Baker DA, Holte JE, and Patankar SV: *Computationally two-dimensional finite-difference model for hollow-fibre blood-gas exchange devices.* Med Biol Eng Comp, 1991. **29**: p. 482-488.

<268> Wang NL and Keller KH: *Solute transport induced by erythrocyte motions in shear flow.* ASAIO Trans, 1979. **25**: p. 14-17.

<269> Niranjan SC, Clark JW, et al.: *Analysis of factors affecting gas exchange in intravascular blood gas exchanger.* J Appl Physiol, 1994. **77**(4): p. 1716-1730.

<270> Leonard EF and Jorgansen SB: *The analysis of convection and diffusion in capillary beds.* Annu Rev Biophys Bioeng, 1974. **3**: p. 293-339.

<271> Vaslef SN, Mockros LF, et al.: *Computer-assisted design of an implantable, intrathoracic artificial lung.* Artificial Organs, 1994. **18**(11): p. 813-817.

<272> Treybal RE: *Mass Transfer Operations*. 1980, New York: McGraw-Hill.

<273> Bethune DW: *Standards for blood gas exchange devices.* Perfusion, 1994. **9**: p. 207-209.

<274> Fried DW, DeBenedetto BN, and Leo JJ: *Rethinking the AAMI / ISO "International Standard" for oxygen transfer performance of artificial lungs.* Perfusion, 1994. **9**: p. 335-342.

<275> Ueyama K, Niimi Y, and Nosé Y: *How to test oxygenators for extracorporeal membrane oxygenation: is the Association for the Advancement of Medical Instrumentation's protocol enough?* Artificial Organs, 1996. **20**: p. 741-742.

<276> Ergun S: *Fluid flow through packed columns.* Chemical Engineering Progress, 1952. **48**(2): p. 89-94.

<277> Verdonck PR, Siller U, et al.: *Hydrodynamical comparison of aortic arch cannulae.* Int J Artif Organs, 1998. **21**(11): p. 705-713.

<278> Macdonald IF, El-Sayed MS, et al.: *Flow through porous media - the Ergun equation revisited.* Industrial and Engineering Chemistry Fundamentals, 1979. **18**(3): p. 199-208.

<279> Catapano G, Wodetzki A, and Baurmeister U: *Blood flow outside regularly spaced hollow fibers: the future concept of membrane devices?* Int J Artif Organs, 1992. **15**(6): p. 327-330.

<280> Conrad SA, Brown EG, et al.: *Arteriovenous extracorporeal carbon dioxide removal: a mathematical model and experimental evaluation.* ASAIO Trans, 1998. **44**: p. 267-277.

<281> Kuwabara S: *The forces experienced by randomly distributed parallel circular cylinders or spheres in a viscous flow at small Reynolds numbers.* Journal of the Physical Society of Japan, 1959. **14**(4): p. 527-532.

<282> Happel J and Brenner H: *Low Reynolds Number Hydrodynamics*. fourth printing ed. 1986, Dordrecht: Martinus Nijhoff Publishers. 553.

<283> Henry FS and Ariman T: *A staggered array model of a fibrous filter with electrical enhancement.* Particulate Science and Technology, 1983. **1**: p. 139-154.

<284> Happel J: *Viscous flow relative to arrays of cylinders.* AIChE, 1959. **5**(2): p. 174-177.

<285> Makarewicz AJ: *Static and dynamic artifical lungs*, . 1994, Northwestern University. p. 160; .

<286> Bergelin OP, Brown GA, et al.: *Heat transfer and fluid friction during viscous flow across banks of tubes - III.* Transactions of the ASME, 1950. **72**: p. 881-888.

<287> Bergelin OP, Brown GA, and Doberstein SC: *Heat transfer and fluid friction during viscous flow across banks of tubes - IV.* Transactions of the ASME, 1952. **74**: p. 953-960.

<288> Bergelin OP, Brown GA, and A P Colburn AP: *Heat transfer and fluid friction during flow across banks of tubes - V.* Transactions of the ASME, 1954. **76**: p. 841-850.

<289> Rajasubramanian S, Nelson KD, et al.: *Design of an oxygenator with enhanced gas transfer efficiency.* ASAIO Trans, 1997. **43**: p. M710-M714.

<290> Vaslef SN, Mockros LF, and Anderson RW: *Development of an intravascular lung assist device.* ASAIO Trans, 1989. **35**: p. 660-664.

<291> 3M Health Care: *Sarns 5794 turbo 440 membrane oxygenator*, . 1995: Michigan; .

<292> De Somer F, Foubert L, et al.: *Low extracorporeal priming volumes for infants: a benefit?* Perfusion, 1996. **11**: p. 455-460.

<293> Smith P: *Interventions to reduce cerebral injury during cardiac surgery - introduction and the effect of oxygenator type.* Perfusion, 1989. **4**: p. 139-145.

<294> Mehra A, Atkins A, et al.: *Air handling characteristics of five membrane oxygenators.* Perfusion, 1994. **1994**(9): p. 357-362.

<295> Miller MJ and Johnson R: *Comparative analysis of air handling in membrane oxygenators*, . 1996, Cobe Cardiovascular Inc: Arvada; .

<296> Dewanjee M, Wu S, and Kapadvanjwala M: *Emboli from an extraluminal blood flow hollow fiber oxygenator with and without an arterial filter during cardiopulmonary bypass in a pig model.* ASAIO Trans, 1996. **42**: p. 1010-1018.

<297> Butler B: *Biophysical aspects of gas bubbles in blood.* Biomed Instrum, 1985. **19**: p. 59-62.

APPENDIX

A Introduction

B Hemodynamics

X

X

X

X

X

C Oxygen transfer

a) Oxygen partial pressure

X

X

X

X

X

b) Oxygen saturation

APPENDIX

A Introduction

This appendix offers a brief survey of representative in numero results on the hemodynamics and the oxygen mass transfer in blood for three different unit fiber cells: inline square, IL, staggered square, SS, and equilateral triangle, ET. Results are presented as coloured contour plots of the hydrostatic pressure, p, the oxygen partial pressure, P_{O_2}, and the oxygen saturation, S_{O_2}. The streamlines are visualized as contour plots. The influence of three parameters on hemodynamics and mass transfer in three unit fiber cells is presented. These parameters are porosity, ε, superficial velocity, U_s, and inlet oxygen saturation, $\overline{S_{O_{2in}}}$. The table below gives an overview of the parameter values in the three unit fiber cells. Blood in the simulations has a temperature of 30 °C and a hematocrit of 30 %.

	ε	U_s	$\overline{S_{O_{2in}}}$	Results
IL **SS** **ET**	0.5	20	0.40	p, P_{O_2}, S_{O_2}
ET	0.6	20	0.40	p, P_{O_2}, S_{O_2}
SS	0.5	5	0.40	p, P_{O_2}, S_{O_2}
ET	0.5	20	0.85	P_{O_2}, S_{O_2}

B Hemodynamics

X

X

X

X

X

C Oxygen transfer

a) Oxygen partial pressure

X

X

X

X

X

X

b) Oxygen saturation

B Hemodynamics

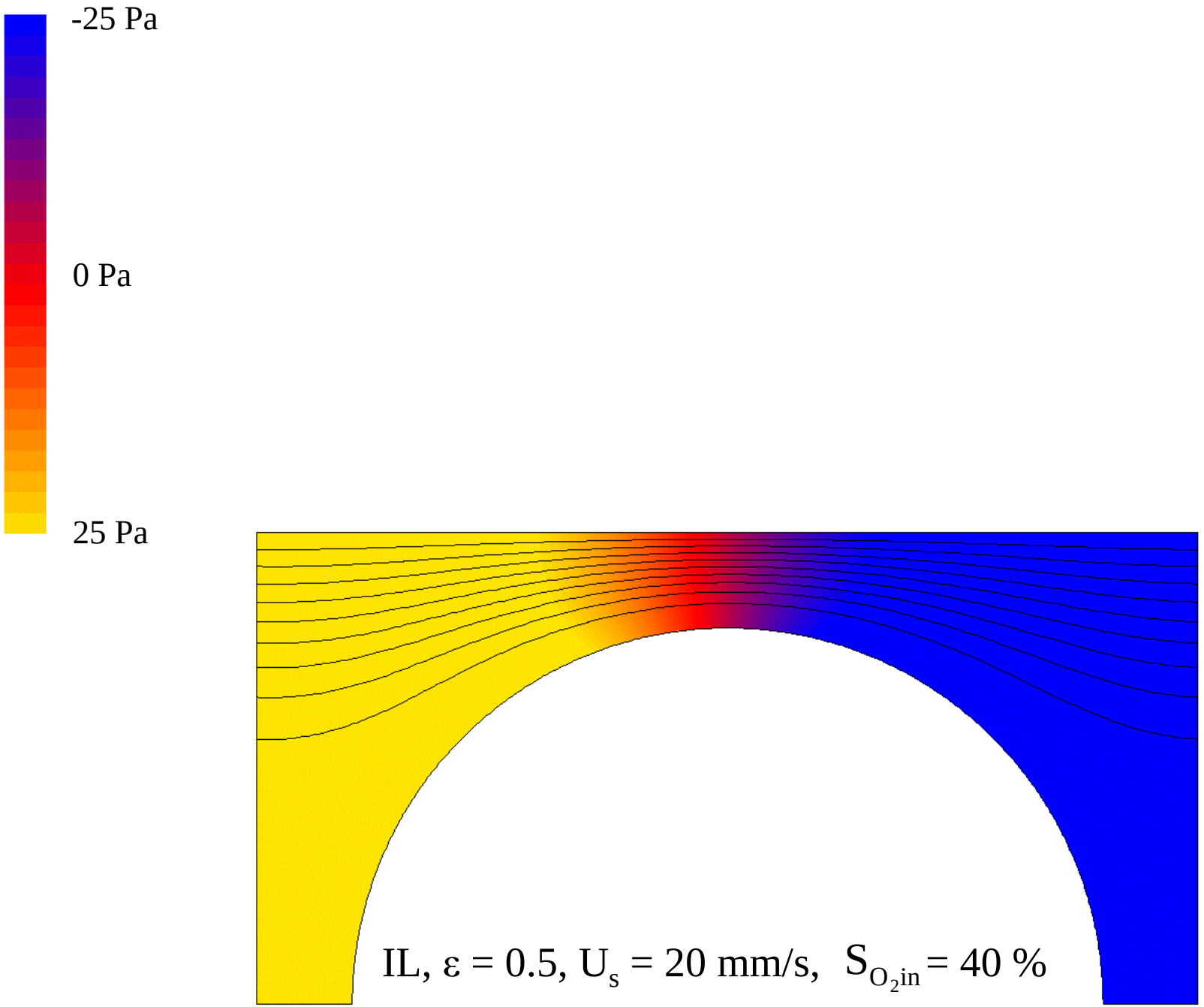
-25 Pa
0 Pa
25 Pa
IL, ε = 0.5, U_s = 20 mm/s, $S_{O_2 in}$ = 40 %

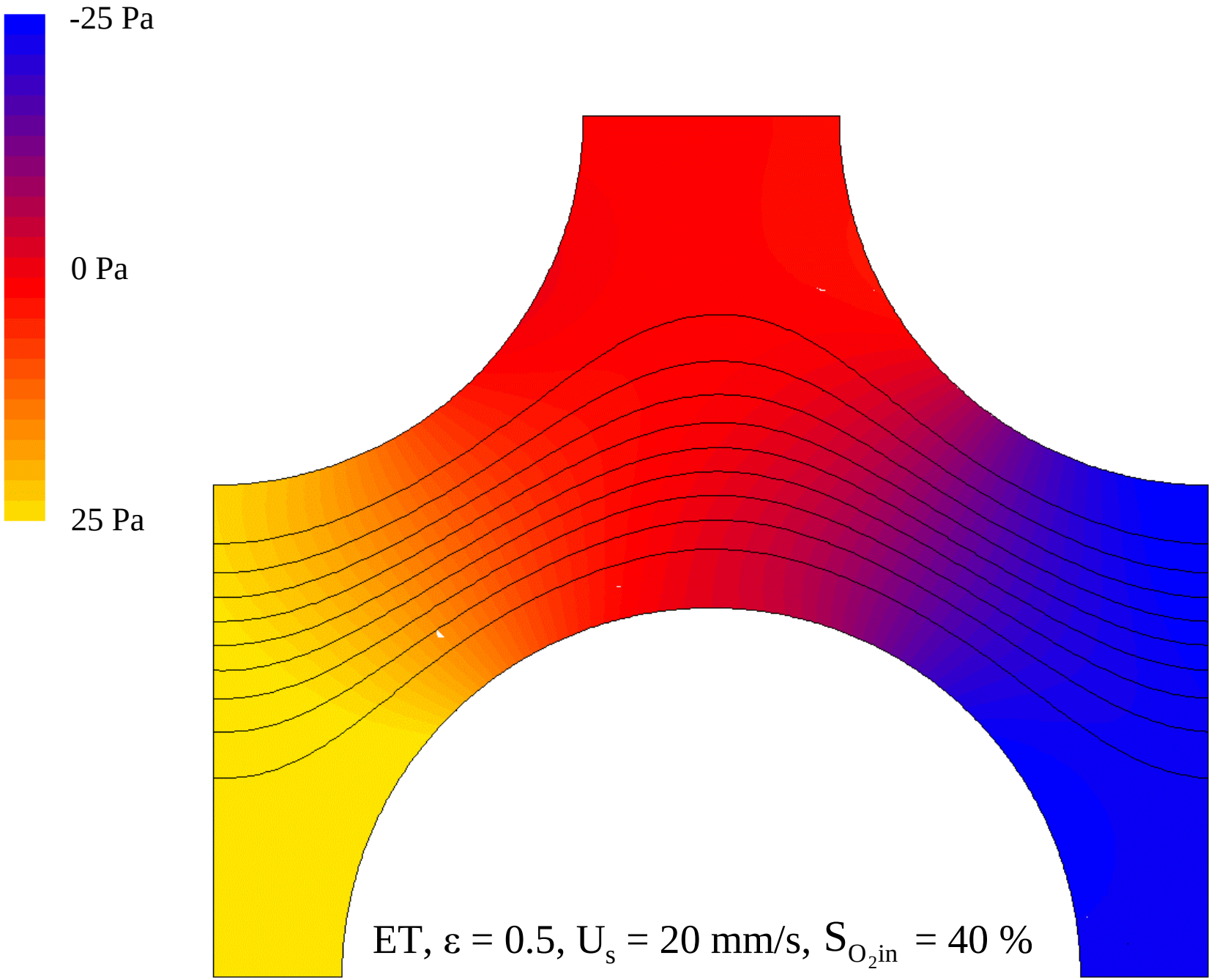
-25 Pa
0 Pa
25 Pa
ET, ε = 0.5, U_s = 20 mm/s, S_{O_2in} = 40 %

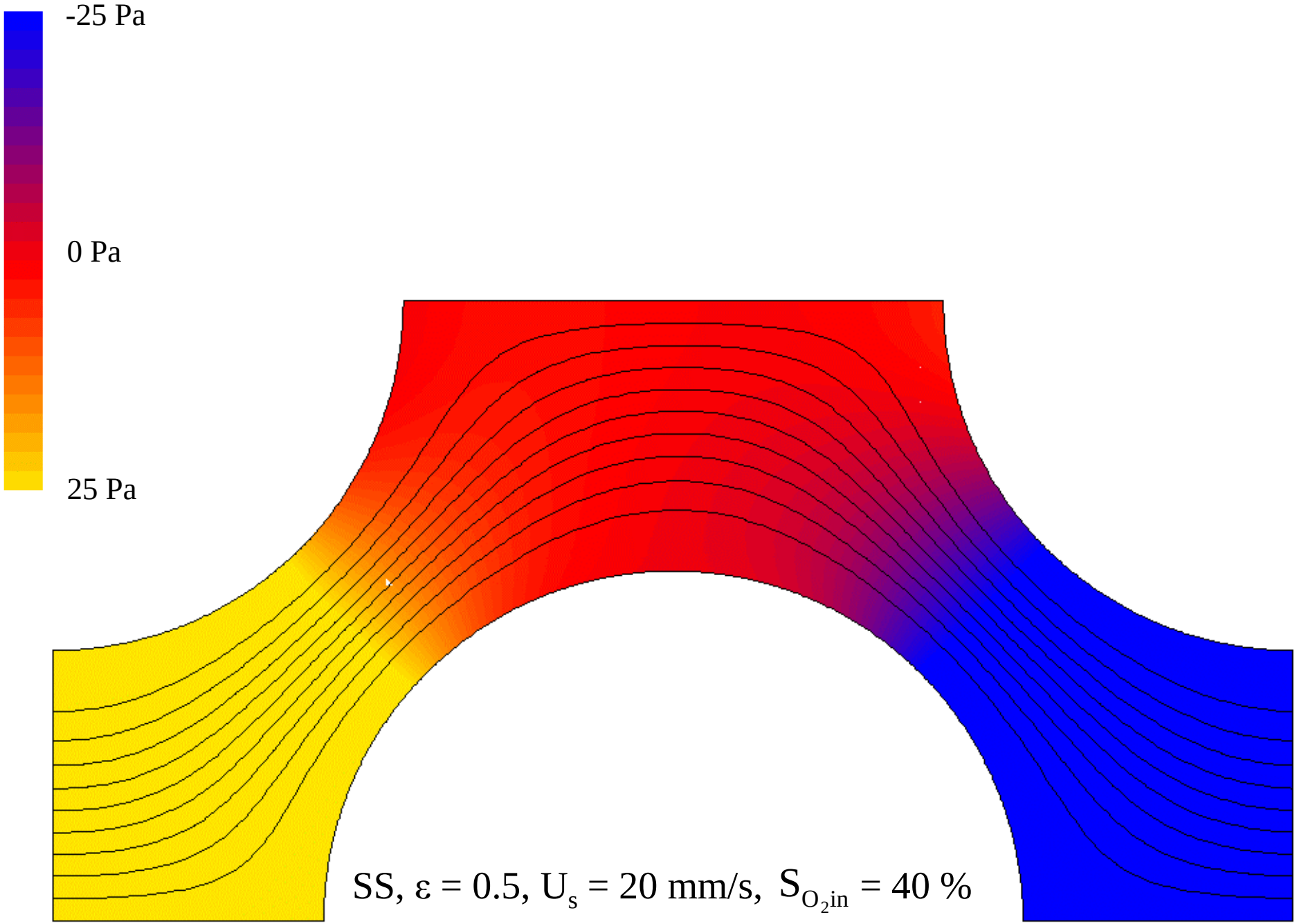
-25 Pa
0 Pa
25 Pa
SS, ε = 0.5, U_s = 20 mm/s, $S_{O_2 in}$ = 40 %

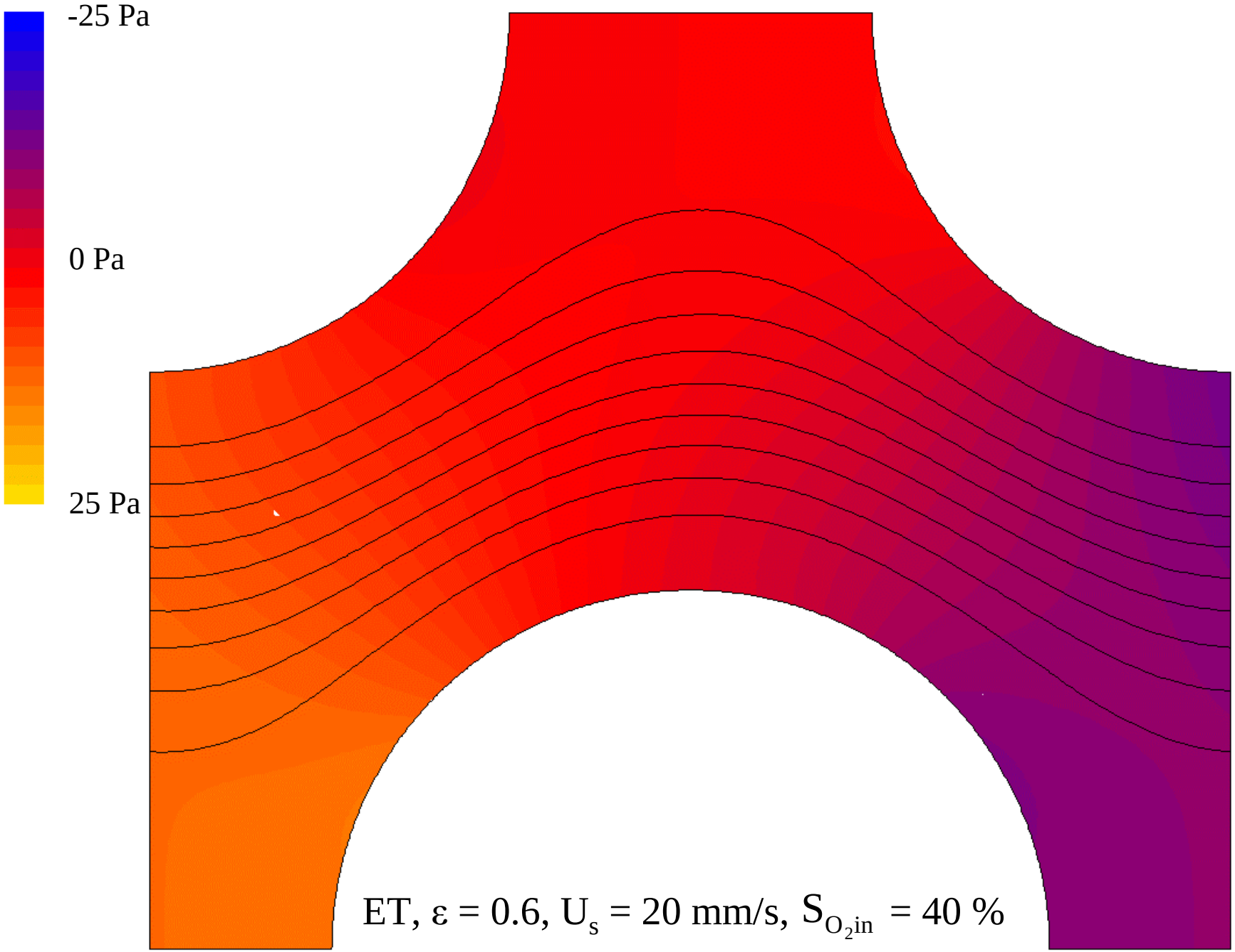
-25 Pa
0 Pa
25 Pa
ET, ε = 0.6, U_s = 20 mm/s, $S_{O_2 in}$ = 40 %

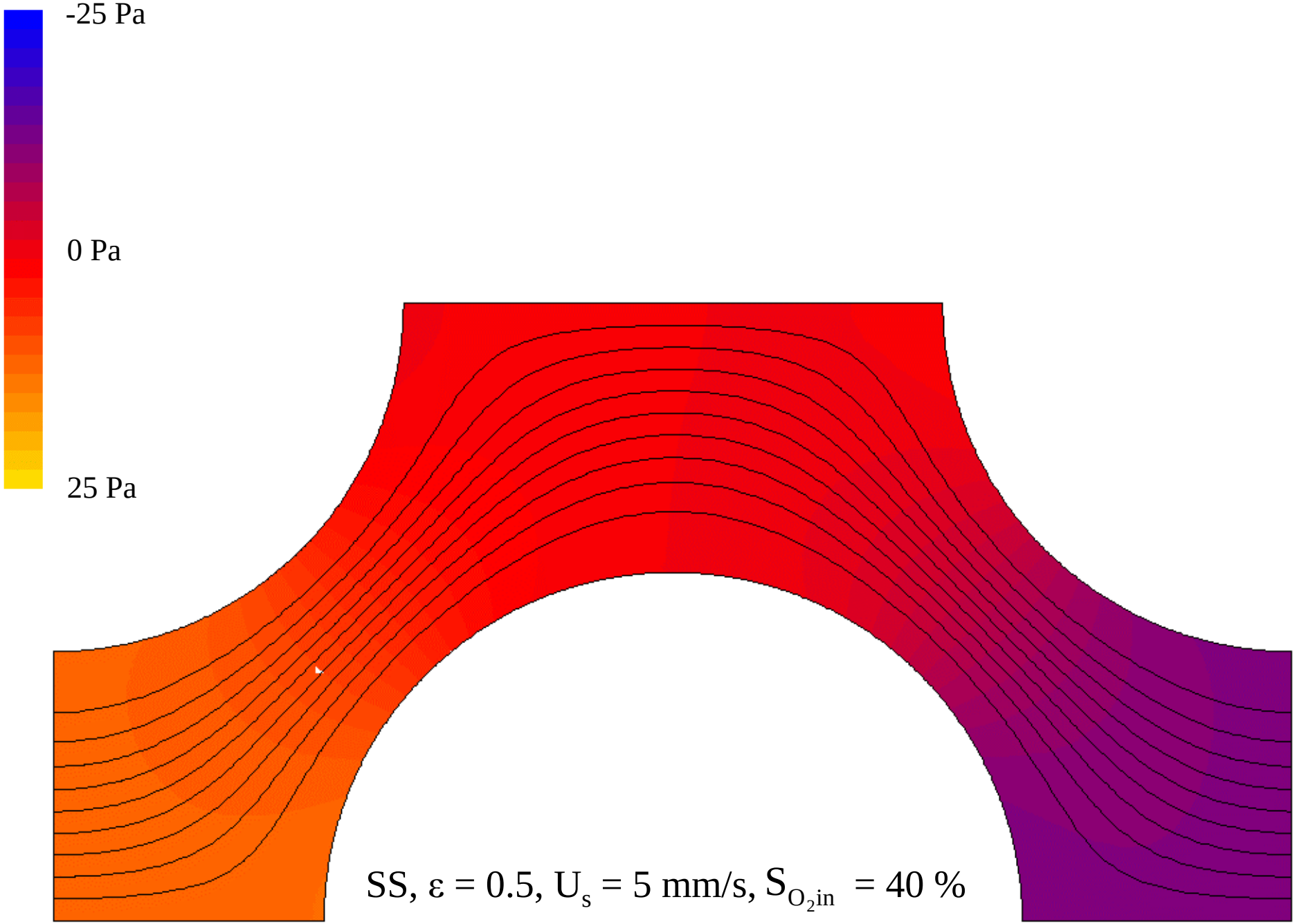
-25 Pa
0 Pa
25 Pa
SS, ε = 0.5, U_s = 5 mm/s, $S_{O_2 in}$ = 40 %

C Oxygen transfer

a) Oxygen partial pressure

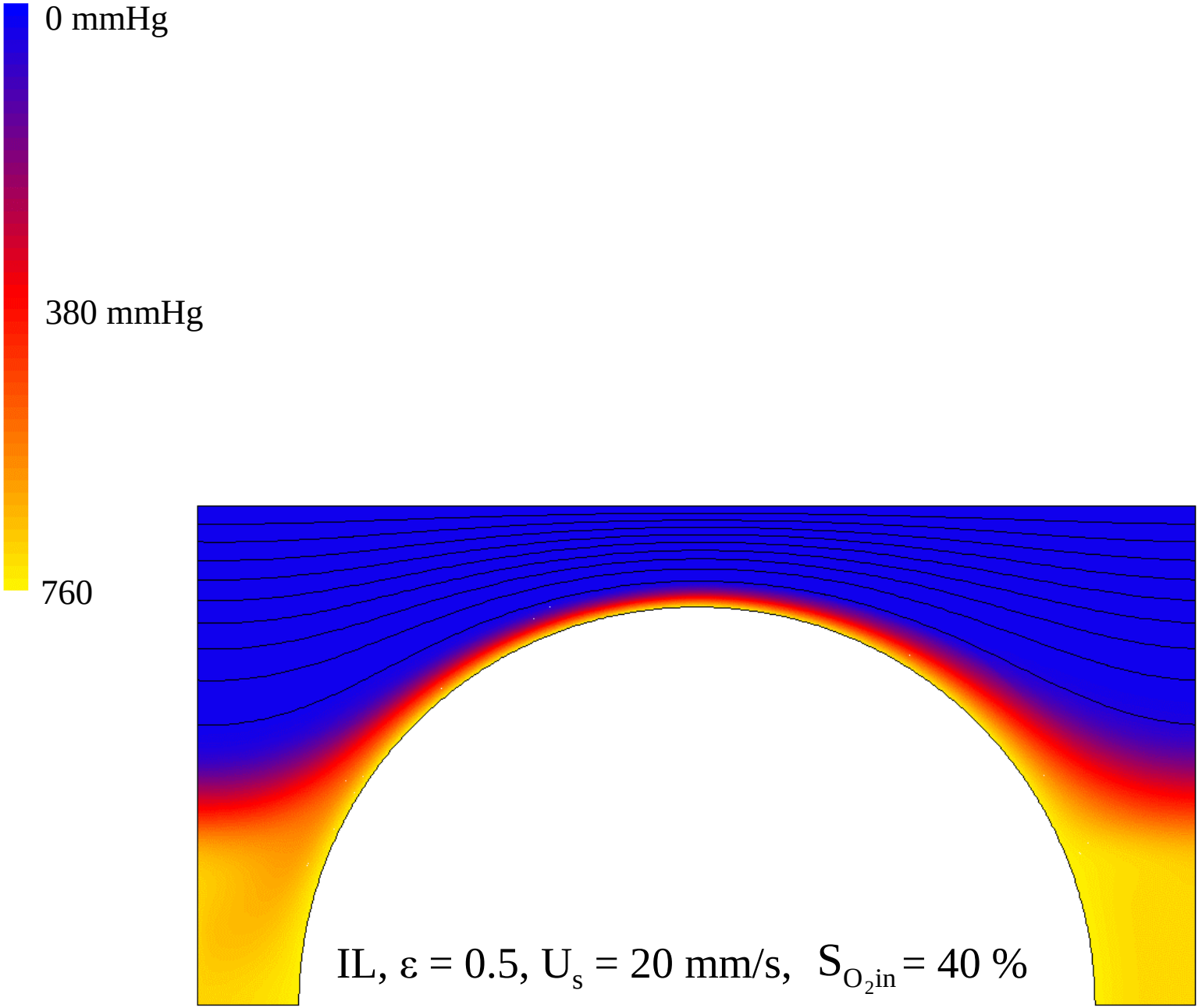

IL, $\varepsilon = 0.5$, $U_s = 20$ mm/s, $S_{O_2 in} = 40$ %

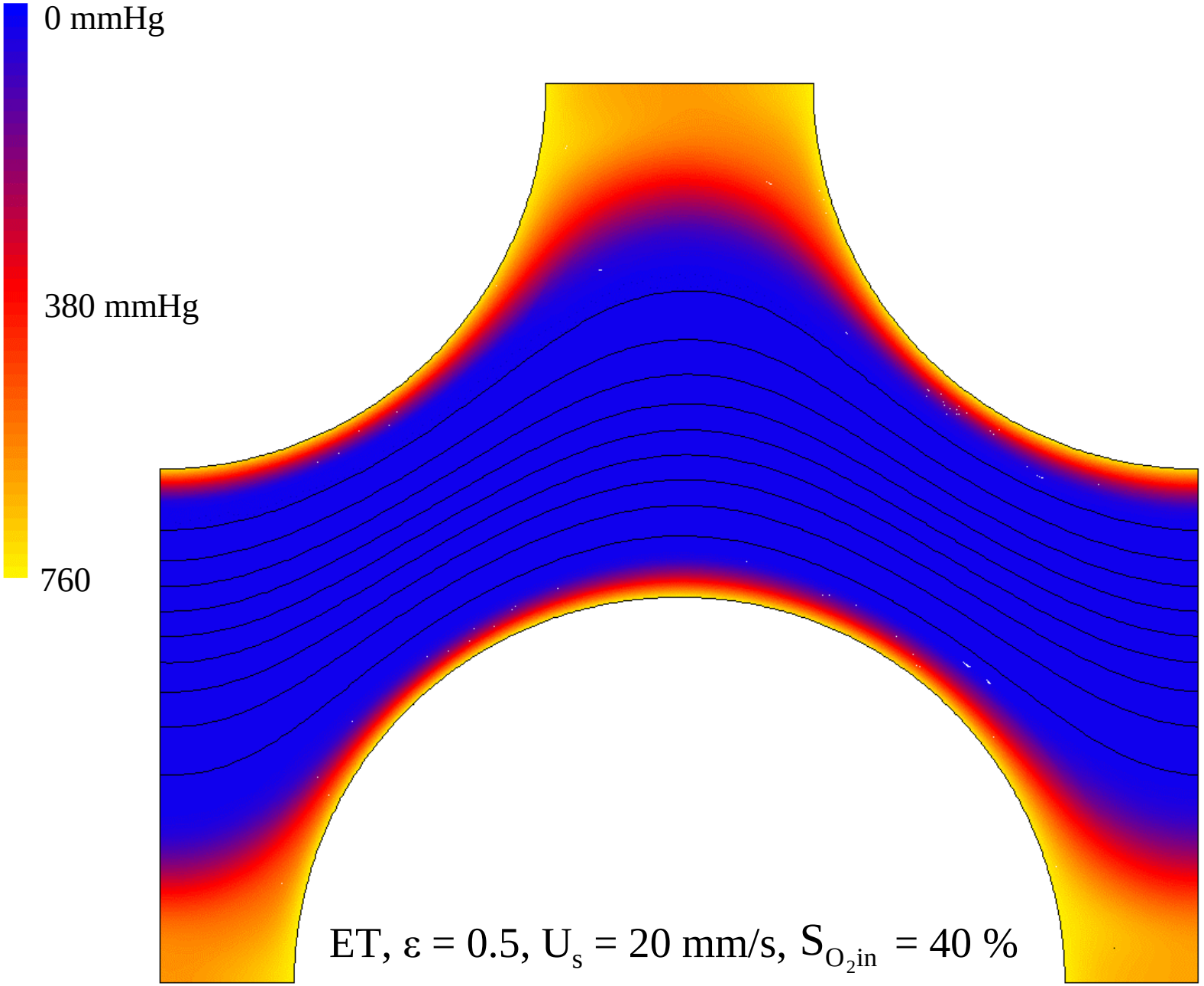

ET, $\varepsilon = 0.5$, $U_s = 20$ mm/s, $S_{O_2 in} = 40$ %

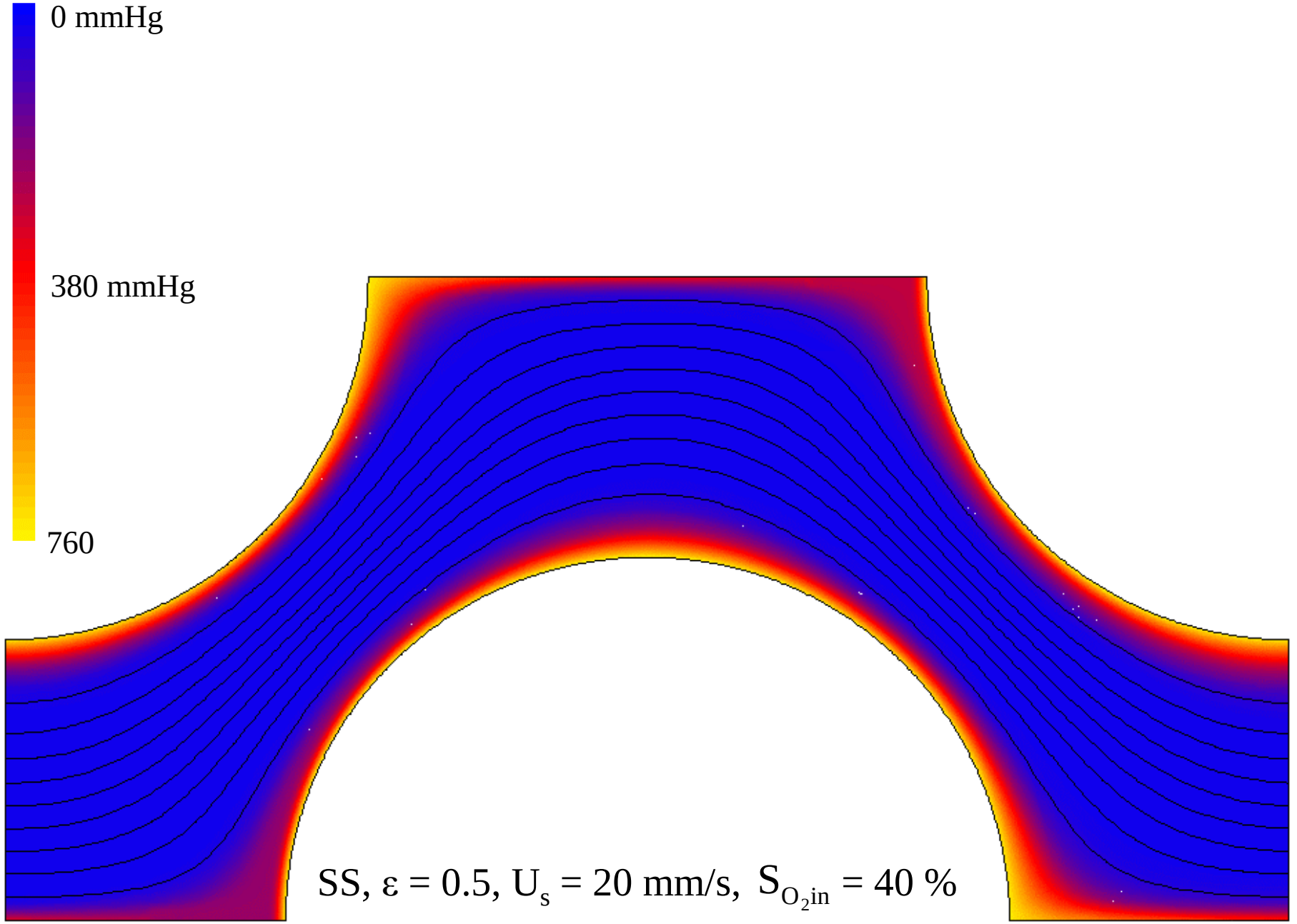
0 mmHg
380 mmHg
760
SS, ε = 0.5, U_s = 20 mm/s, $S_{O_2 in}$ = 40 %

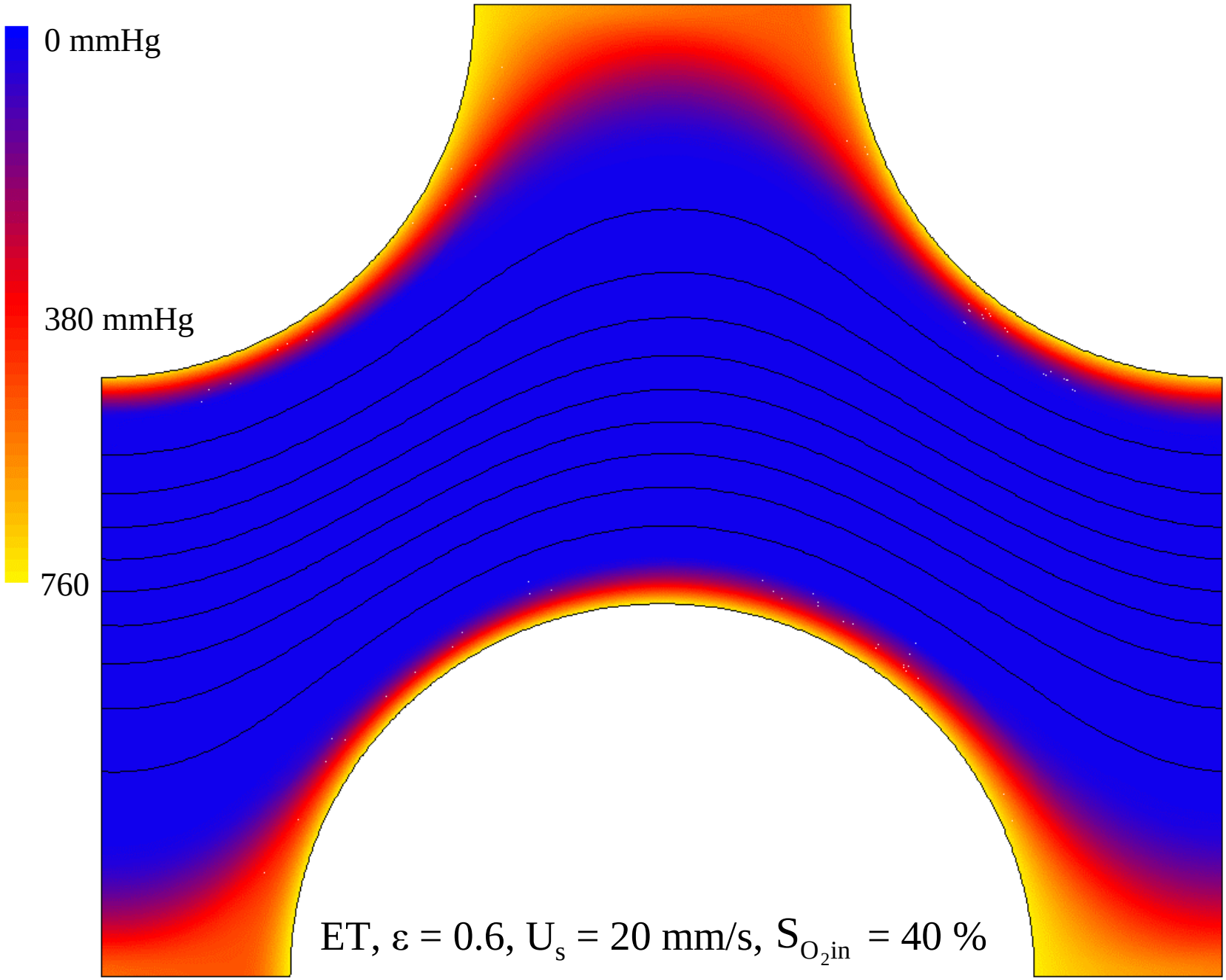
0 mmHg
380 mmHg
760
ET, ε = 0.6, U_s = 20 mm/s, $S_{O_2 in}$ = 40 %

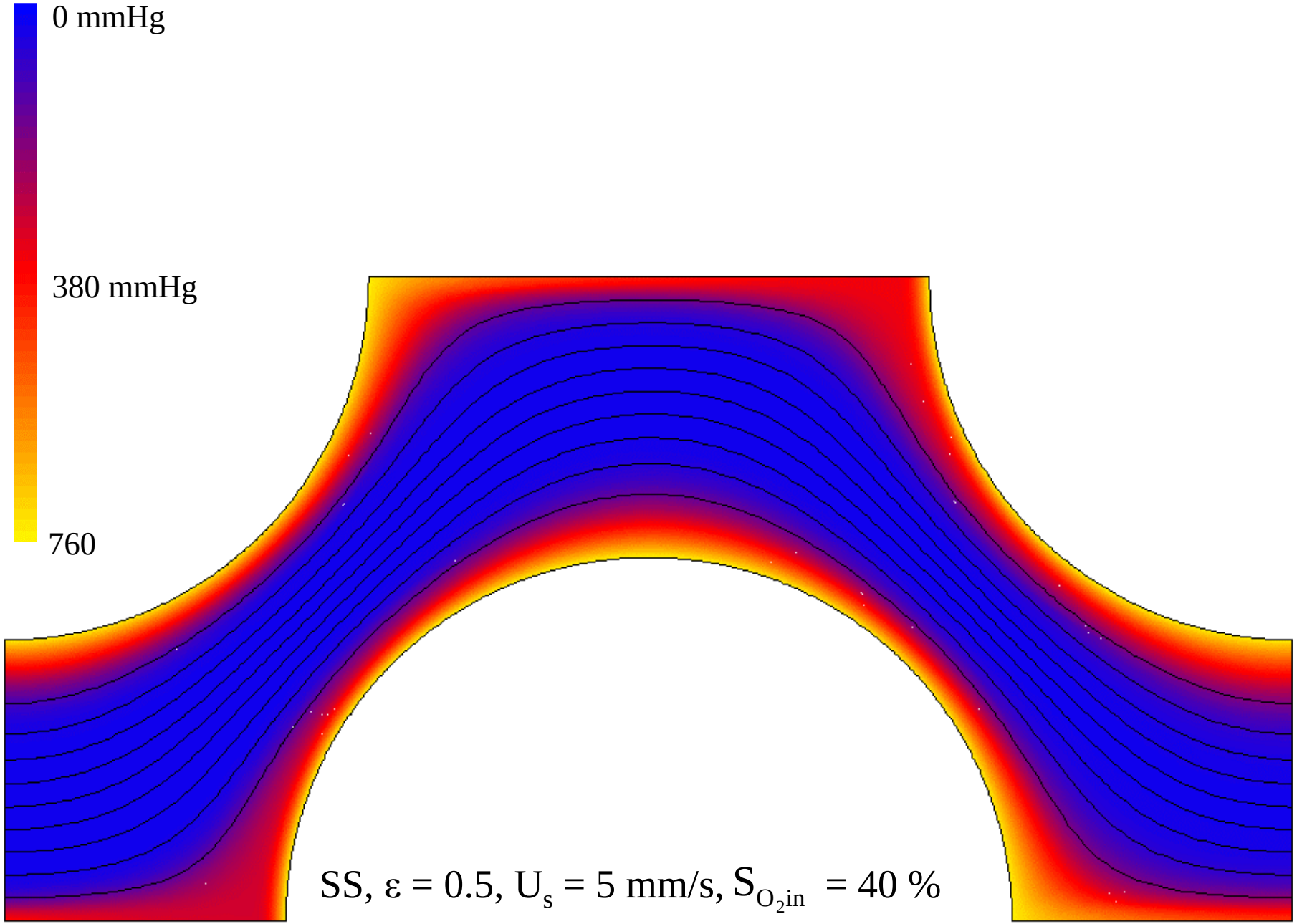
0 mmHg
380 mmHg
760
SS, ε = 0.5, U_s = 5 mm/s, $S_{O_2 in}$ = 40 %

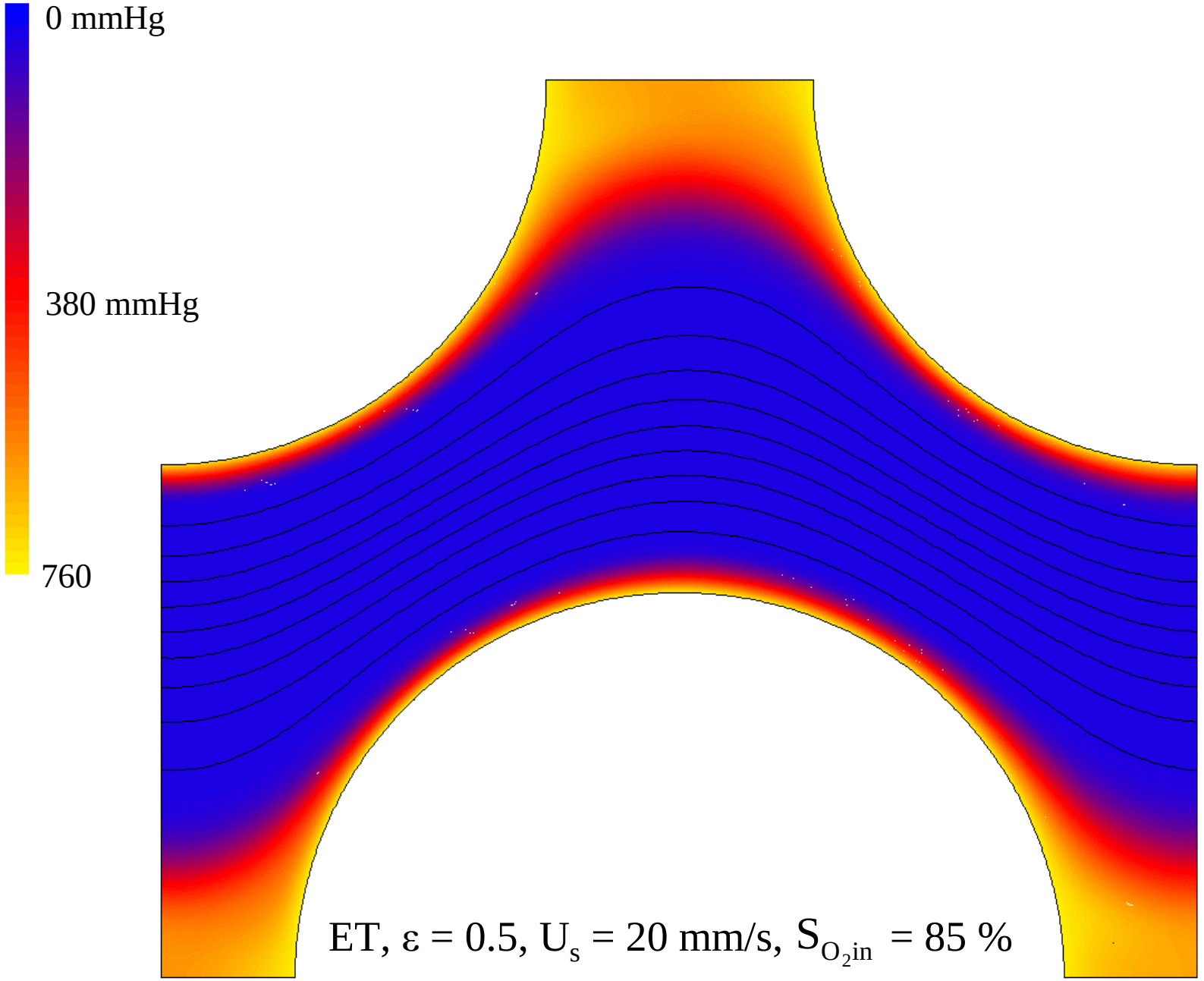

ET, $\varepsilon = 0.5$, $U_s = 20$ mm/s, $S_{O_2 in} = 85$ %

b) Oxygen saturation

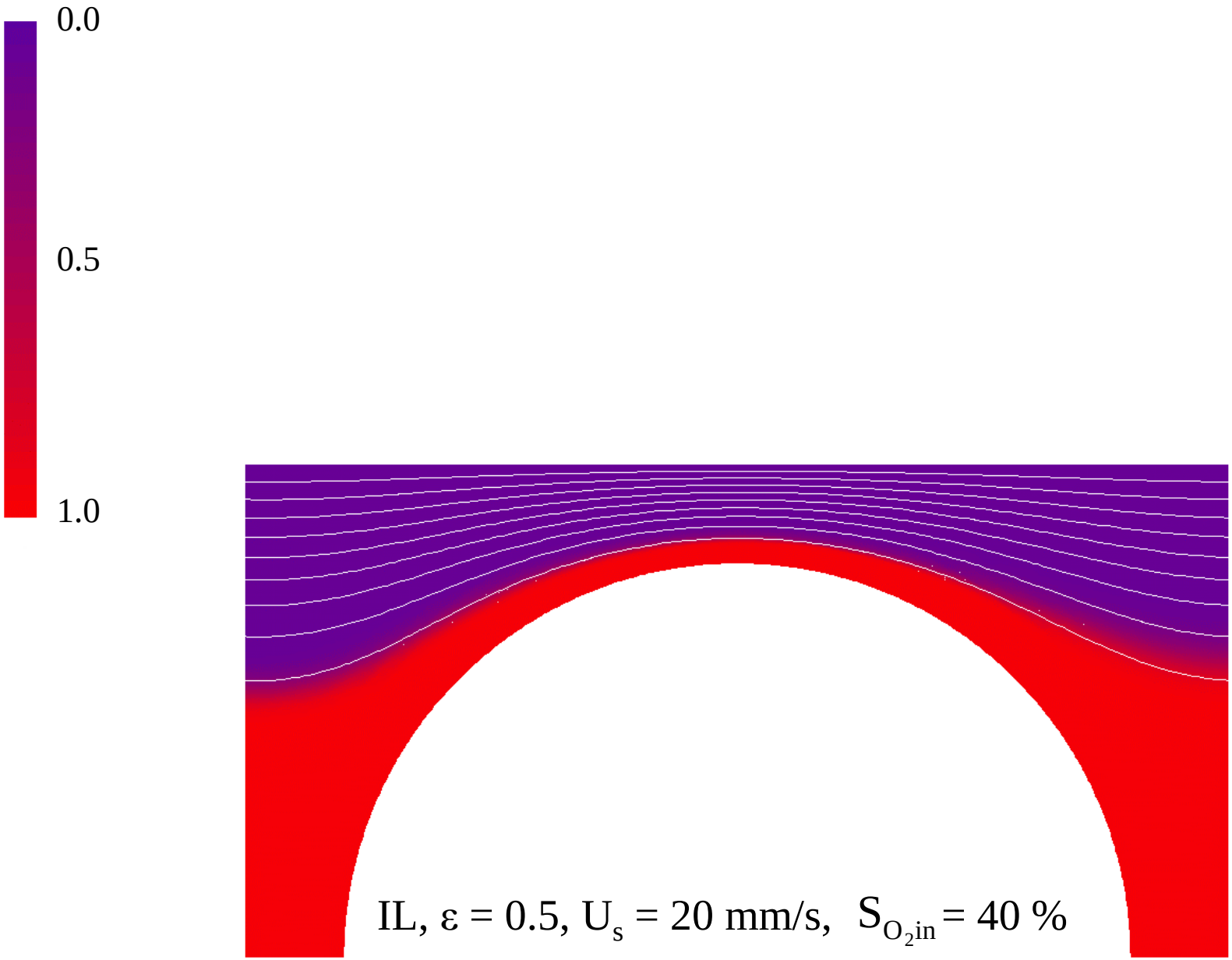

IL, ε = 0.5, U_s = 20 mm/s, $S_{O_2 in}$ = 40 %

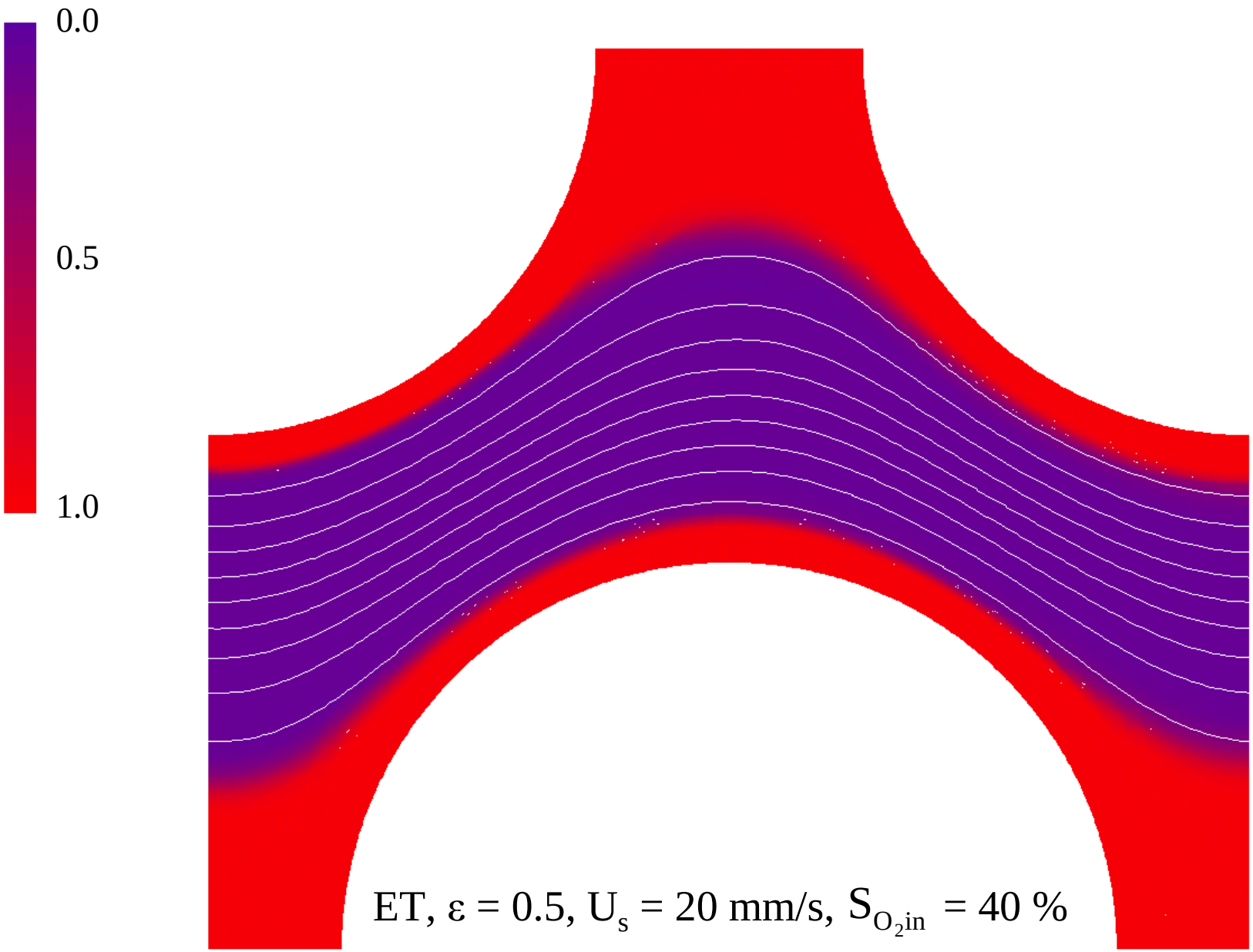

ET, $\varepsilon = 0.5$, $U_s = 20$ mm/s, $S_{O_2 in} = 40$ %

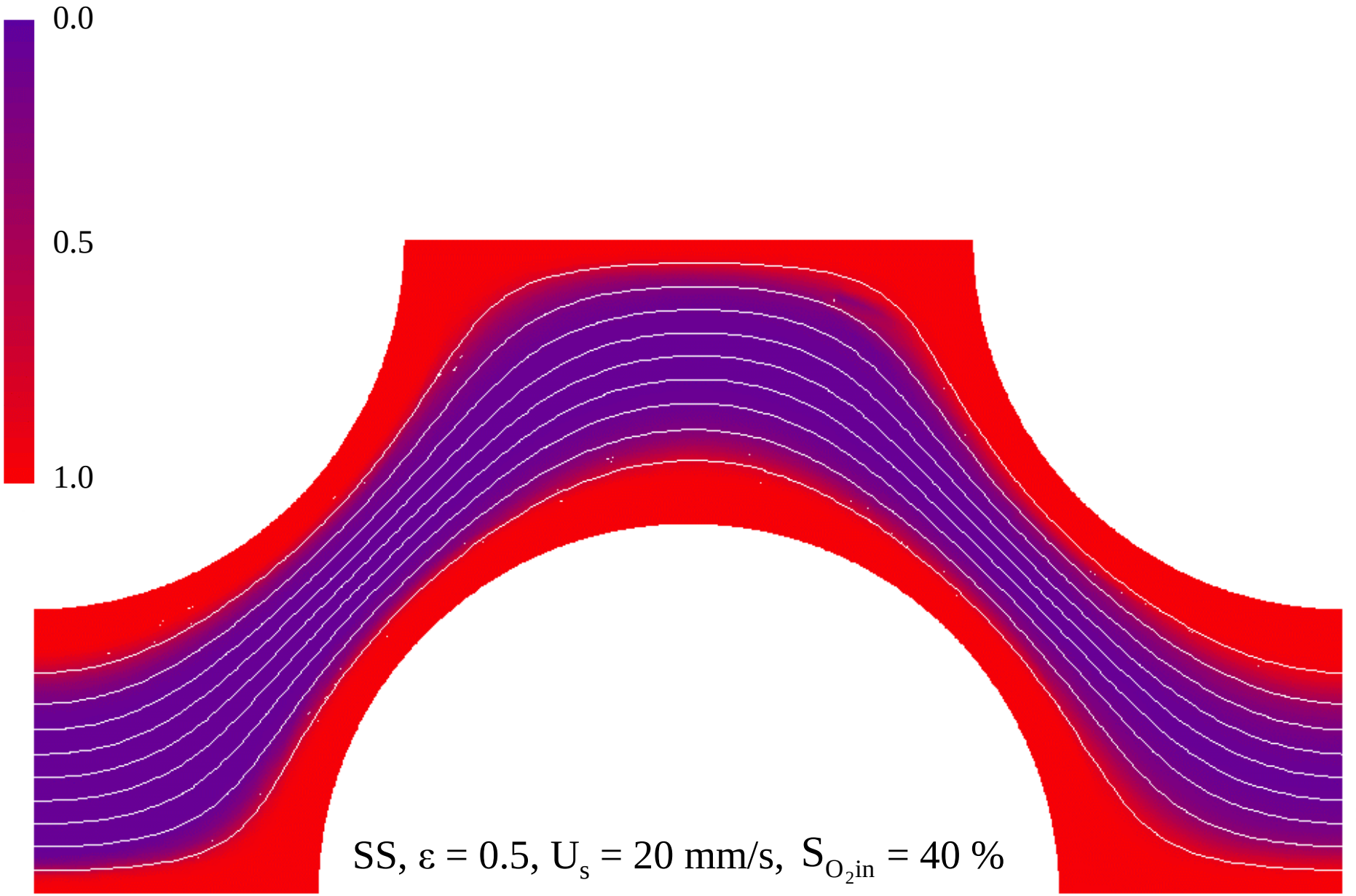

SS, $\varepsilon = 0.5$, $U_s = 20$ mm/s, $S_{O_2 in} = 40$ %

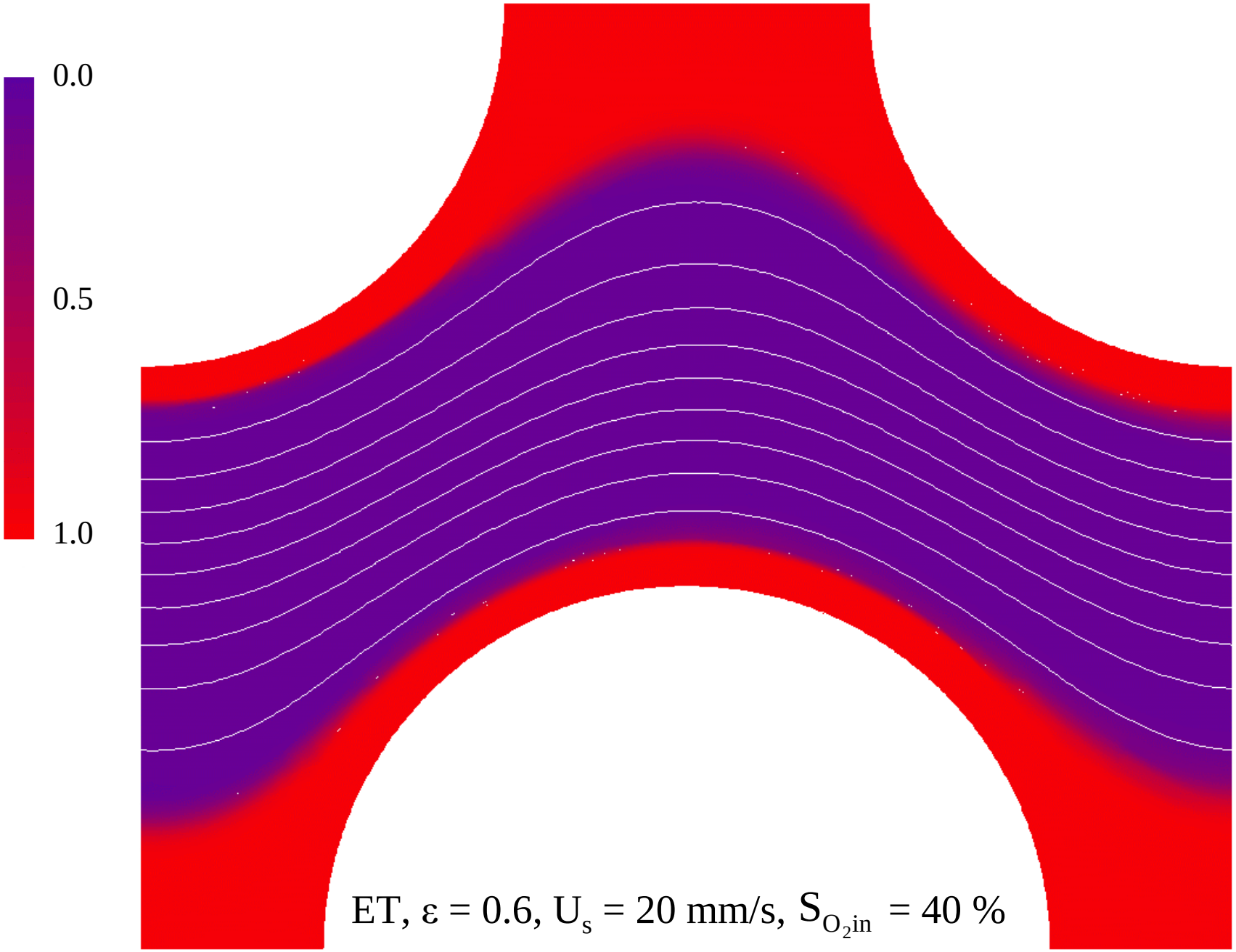

ET, ε = 0.6, U_s = 20 mm/s, $S_{O_2 in}$ = 40 %

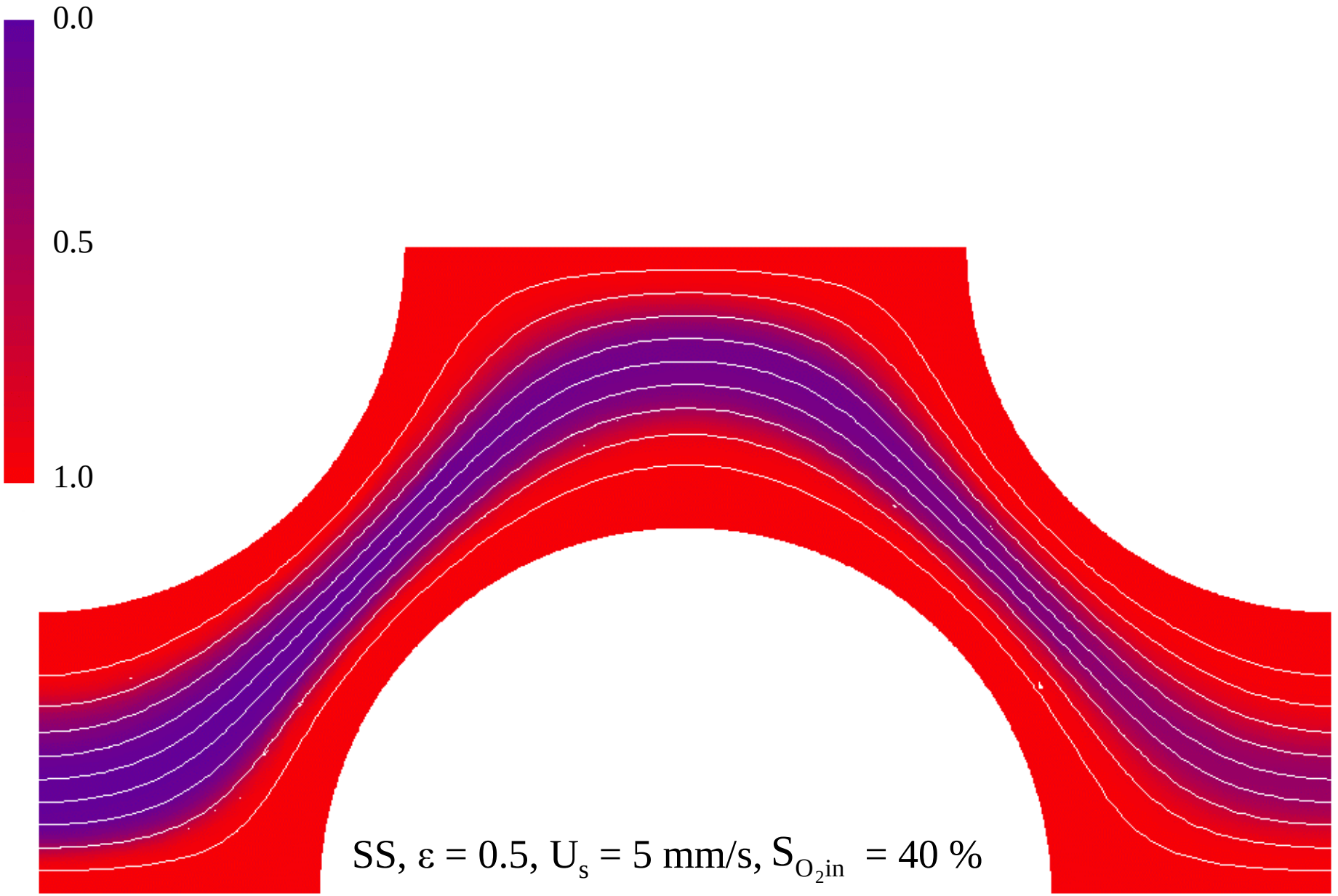

SS, $\varepsilon = 0.5$, $U_s = 5$ mm/s, $S_{O_2 in} = 40$ %

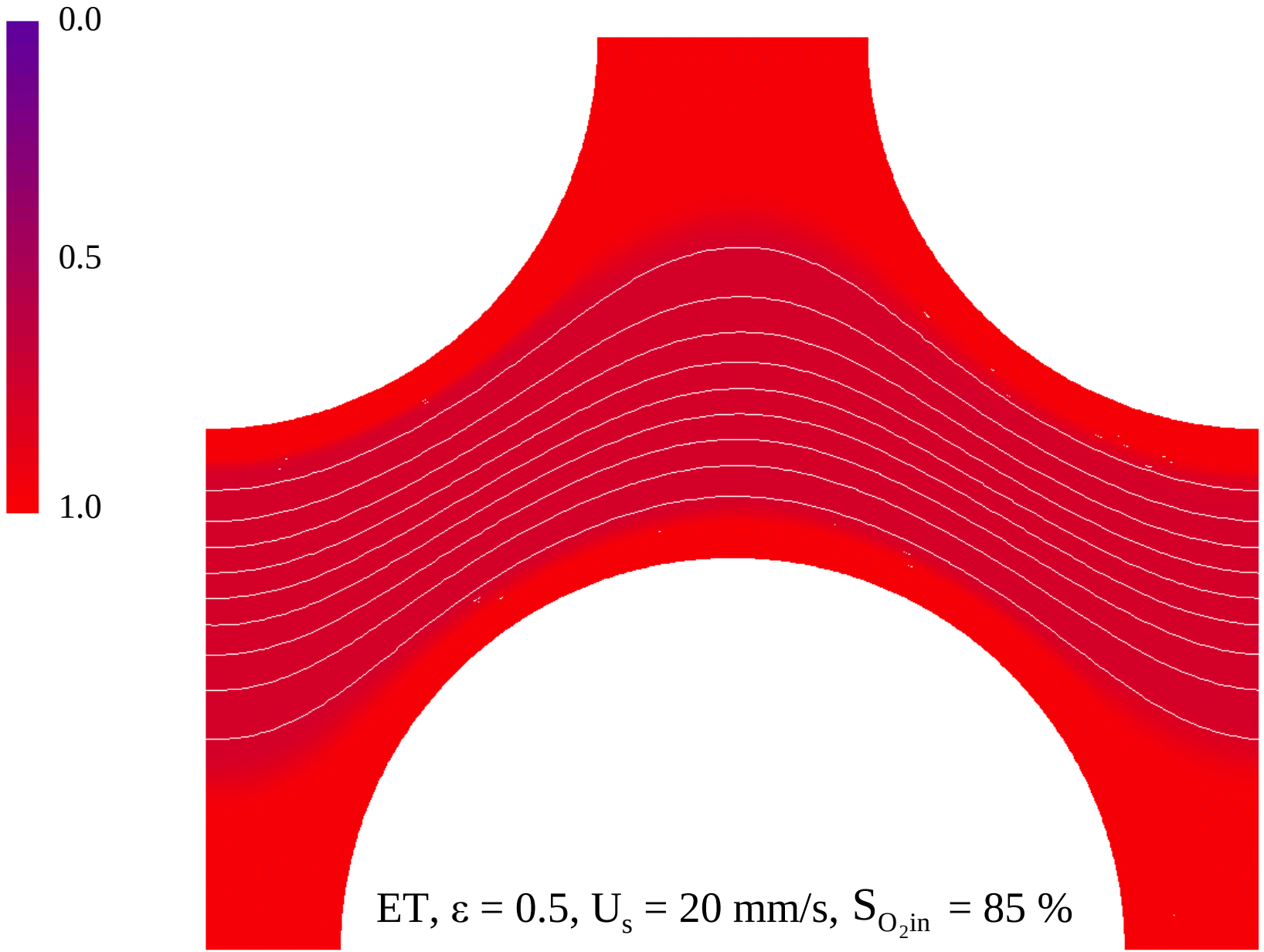

ET, ε = 0.5, U_s = 20 mm/s, $S_{O_2 in}$ = 85 %

Bloedstroming en gastransport in een kunstlong:
in numero en in vitro analyse

Blood flow and gas transport in artificial lungs:
in numero and in vitro analysis

ir. Peter Dierickx

Academiejaar 2000 – 2001